

PARITY-VIOLATING AND  
PARITY-CONSERVING BERRY PHASES  
FOR HYDROGEN AND HELIUM  
IN AN ATOM INTERFEROMETER

Martin-Isbjörn Trappe

Heidelberg, 2nd November 2012



DISSERTATION

SUBMITTED TO THE

COMBINED FACULTIES OF THE NATURAL SCIENCES AND MATHEMATICS  
OF THE RUPERTO-CAROLA-UNIVERSITY OF HEIDELBERG, GERMANY,

FOR THE DEGREE OF

DOCTOR OF NATURAL SCIENCES

PUT FORWARD BY

**DIPL.-PHYS. MARTIN-ISBJÖRN TRAPPE**

BORN IN LEIMEN, GERMANY

ORAL EXAMINATION: 19.12.2012



PARITY-VIOLATING AND  
PARITY-CONSERVING BERRY PHASES  
FOR HYDROGEN AND HELIUM  
IN AN ATOM INTERFEROMETER

Referees: Prof. Dr. Thomas Gasenzer  
Prof. Dr. Dirk Dubbers



## **Paritätsverletzende und paritätserhaltende Berry-Phasen für Wasserstoff und Helium in einem Atomstrahlinterferometer**

In der vorliegenden Arbeit werden Berry-Phasen für metastabile Zustände von Wasserstoff und Helium in äußeren elektromagnetischen Feldern untersucht. Ein wesentliches Ziel ist die Herleitung einer paritätsverletzenden Observable, die vom elektroschwachen Mischungswinkel abhängt. Die entsprechende Ausarbeitung erfolgt im Hinblick auf ein zur Verfügung stehendes hochpräzises Atomstrahl-Spinocho-Interferometer und im Hinblick auf den theoretisch sehr genau bekannten Aufbau von Wasserstoff. Wir bestimmen die strukturellen Eigenschaften paritätsverletzender sowie paritätserhaltender Berry-Phasen und ihrer Flussdichtevektorfelder, die durch ihr unterschiedliches Verhalten unter eigentlichen und uneigentlichen Rotationen charakterisiert sind. Dies erlaubt weitreichende analytische Untersuchungen sowie die Überprüfung unserer numerischen Berechnungen. Im Falle von Wasserstoff weisen wir geometrieabhängige Lebensdauer-Modifikationen durch imaginäre Berry-Phasen nach. Über die zeitliche Entwicklung der atomaren Wellenpakete wird eine Beschreibung des Atominterferometers eingeführt. Ein analytischer Ausdruck für das experimentell leicht zugängliche Spinochosignal wird entwickelt und numerisch ausgewertet, um paritätsverletzende Signale zu extrahieren. Wir diskutieren die Bedeutung der so berechneten paritätsverletzenden Effekte für interferometrische Präzisionsbestimmungen der schwachen Ladungen des Protons. Desweiteren wird das Konzept der Heisenberg-limitierten Atominterferometrie zur Erhöhung der Messgenauigkeit bezüglich Berry-Phasen skizziert. Abschließend präsentieren wir Vorhersagen zu paritätserhaltenden Berry-Phasen für metastabile Heliumzustände, die im Heidelberger Experiment untersucht werden.

## **Parity-Violating and Parity-Conserving Berry Phases for Hydrogen and Helium in an Atom Interferometer**

In the present thesis Berry phases for metastable states of hydrogen and helium exposed to external electromagnetic fields are investigated. One main goal is the derivation of a parity-violating observable incorporating the electroweak mixing angle. The study is done in view of an available high-precision atomic beam spin echo interferometer and with respect to the theoretically very well-known structure of hydrogen. We determine the general properties of parity-violating and parity-conserving Berry phases and their flux-density vector fields distinguished by their behaviour under proper and improper rotations. This allows for extensive analytical investigations and cross-checks of our numerical computations. Regarding hydrogen, we reveal geometry-dependent modifications of atomic lifetimes due to parity-conserving imaginary Berry phases. Deriving the evolution of the atomic wave packets, we establish the theoretical description of an atom interferometer. An analytical expression for the spin echo signal, easily accessible in experiment, is presented and numerically evaluated to extract parity-violating signals. We discuss the implications of the computed parity-violating effects on interferometric precision measurements of the proton's weak charges. Moreover, we outline the concept of Heisenberg-limited atom interferometry to improve the resolution for measurements of Berry phases. Finally, we present predictions for parity-conserving Berry phases of metastable helium states studied in the Heidelberg experiment.



# Contents

<b>1</b>	<b>Introduction</b>	<b>1</b>
<b>2</b>	<b>Foundations, Motivations, and Historical Overview</b>	<b>9</b>
2.1	Parity Violation in Quantum Physics . . . . .	9
2.2	The Parity-Violating Atomic Hamiltonian . . . . .	17
2.3	Present Status of the Electroweak Mixing Angle . . . . .	22
2.4	Parity Violation in Heavy Atoms . . . . .	24
2.5	Parity Violation in Light Atoms . . . . .	30
2.6	Adiabatic Theorem and Berry Phases . . . . .	37
2.6.1	Geometrical Properties of Berry Phases . . . . .	42
2.6.2	Experimental Observations of Berry Phases . . . . .	45
<b>3</b>	<b>Berry Phases for Hydrogen</b>	<b>47</b>
3.1	Wigner-Weisskopf Approximation . . . . .	49
3.2	Hydrogen in External Fields . . . . .	51
3.2.1	Adiabaticity Conditions . . . . .	52
3.2.2	The Parity-Violating Mass Matrix of Hydrogen . . . . .	55
3.2.3	Structure of Degeneracies of Hydrogen . . . . .	56
3.2.4	Chirality of Hydrogen in Electromagnetic Fields . . . . .	58
3.3	Geometric Phases for Atoms at Rest . . . . .	60
3.4	Numerical Computation of Berry Phases . . . . .	62
3.5	Geometric Flux Densities . . . . .	63
3.5.1	Representations and General Properties . . . . .	64
3.5.2	General Structure of Flux Densities for Hydrogen . . . . .	68
3.6	Flux Densities in Mixed Parameter Spaces for Hydrogen . . . . .	74
3.6.1	A Pure Magnetic Field $\mathcal{B}$ . . . . .	74
3.6.2	An Electric Field $\mathcal{E}$ together with a Constant Magnetic Field . . . . .	77
3.6.3	The Parameter Space $\{\mathcal{E}_1, \mathcal{E}_3, \mathcal{B}_3\}$ with a Constant $\mathcal{B}_2$ -Field . . . . .	80
3.6.4	Systematic Analysis of Flux-Density Vector Fields . . . . .	85
3.7	Berry Phases for Specific Field Configurations . . . . .	90
<b>4</b>	<b>Hydrogen in an Interferometer</b>	<b>97</b>
4.1	lABSE Experiments . . . . .	98
4.2	The Effective Schrödinger Equation in the Adiabatic Limit . . . . .	101
4.3	Interference of Two Internal States: Total Integrated Flux . . . . .	106

<b>5</b>	<b>Spin Echo Signals</b>	<b>109</b>
5.1	Perturbative Expansion of the Total Integrated Flux . . . . .	109
5.2	Summed Spin Echo Signals . . . . .	111
5.3	A Parity-Violating Spin Echo Signal . . . . .	113
5.4	An Experimentally Realised Field Configuration . . . . .	119
5.5	Error Estimates and Implications for the Standard Model . . . . .	122
5.6	Atom Interferometry Below the Standard Quantum Limit . . . . .	124
5.6.1	Spin Squeezing . . . . .	126
5.6.2	Applications for LABSE Experiments . . . . .	127
<b>6</b>	<b>Berry Phases for Helium</b>	<b>133</b>
6.1	Energies and Decay Rates . . . . .	133
6.2	Parity-Conserving Berry Phases . . . . .	137
<b>7</b>	<b>Conclusions and Future Prospects</b>	<b>139</b>
<b>A</b>	<b>Notations and Definitions</b>	<b>145</b>
A.1	Values for Quantities Related to $n = 2$ Hydrogen . . . . .	146
A.2	The Matrix Representations of $\underline{\tilde{\mathcal{M}}}_0$ , $\underline{\mathcal{D}}$ , and $\underline{\mu}$ for Hydrogen . . . . .	151
A.3	Notations and Matrix Representations of $\underline{\tilde{\mathcal{M}}}_0$ , $\underline{\mathcal{D}}$ , and $\underline{\mu}$ for Helium . . . . .	158
<b>B</b>	<b>Flux-Density Vector Fields</b>	<b>167</b>
B.1	Relations for the Geometric Flux Densities . . . . .	167
B.2	Useful Expressions for Parity-Violating Fluxes . . . . .	170
B.3	Detailed Calculations of Specific Flux-Density Vector Fields . . . . .	172
<b>C</b>	<b>Derivation of the Non-Relativistic Parity-Violating Hamiltonian</b>	<b>175</b>
<b>D</b>	<b>The Numerical Software QABSE</b>	<b>185</b>
	<b>Bibliography</b>	<b>189</b>

# 1 Introduction

Symmetries have been proven to be abundantly fruitful in the description of our physical world. Their investigation allowed for the development of well-confirmed theories as the Standard Model of elementary particle physics and the theory of relativity, that is, the cornerstones of today's fundamental physical laws. It is widely accepted that the combined symmetry CPT of the discrete transformations of charge conjugation (C), parity (P), and time reversal (T), is respected by all laws of nature [1–3]. However, the individual symmetries may be, and indeed are, broken.

Until 1957 nature was believed to be invariant under space inversion, that is, all physical phenomena were regarded to respect space-reflection symmetry just as rotational and translational symmetry. In 1956 T.-D. Lee and C. N. Yang proposed that the weak interactions could violate parity [4]. After that analysis, C. S. Wu and collaborators observed parity violation in nuclear beta decay [5]. This profound discovery of an unusual geometric property of the nuclear forces deepened our understanding of many physical processes in many fields of research ranging from elementary particle physics at high energies to atomic and nuclear properties at low energies. For a selection of reviews see [6–12]. Parity violation has even been discussed in the realm of chiral biological molecules [7,13,14], although the estimates are debated controversially and a rigorous quantitative analysis has not been achieved so far.

In the 1960s Glashow, Weinberg, and Salam formulated the unification of the electromagnetic and weak forces [15–17]. Today, this electroweak theory is included in the Standard Model and constitutes the basis for all parity-violating physical processes. The charged W-bosons mediate processes like nuclear beta decay where the identity of the involved particles is changed. In contrast, the neutral Z-bosons, first observed at CERN in 1973 [18] in form of the so-called weak neutral currents, mediate P-violating processes in stable atoms. The Z-bosons couple differently to left- and right-handed Standard Model fermions, thereby establishing P-violating interactions within inert matter. In the low-energy regime of atomic physics the weak neutral currents are incorporated in the P-violating Hamiltonian forming the foundation of our investigation of parity violation in atomic systems, including hydrogen.

In the realm of atomic physics the weak neutral currents constitute the basis of parity violation in terms of Z-boson exchange between electrons and nuclei. A first discussion of weak neutral current interactions between electrons and protons was started by Y. B. Zel'dovich in 1959 [19]. Already in these early days of atomic parity violation, hydrogen was proposed as a candidate to exhibit P-violating effects [19,20]. The first verification of atomic parity violation was, however, achieved in 1978 by means of a P-violating optical rotation in an experiment on bismuth [21].

At this point we want to put forward another geometric phenomenon which lies at the heart of quantum mechanics. In 1984, M. V. Berry found that the wave functions of quantum mechanical systems can exhibit, besides the dynamic phases, geometric phases which depend on the evolution of the system in a non-local way. The simplest case is an adiabatic evolution in an at least two-dimensional parameter space [22]. These now after Berry named geometric phases show a dependence on the closed path which the state passes through in the underlying parameter space. Berry demonstrated that quantum mechanics is, at a fundamental level and under very general circumstances, endowed with a non-local geometric structure. As a prime example it was then pointed out that the Aharonov-Bohm effect [23] can be interpreted in terms of geometric phases. Berry phases have been studied extensively during the past decades entering numerous areas of research. Reviews addressing geometric phases can, for instance, be found in [24,25]. Besides the investigation of quantum mechanical particles like electrons and neutrons in external fields, geometric phases also play an important role in such diverse fields as solid state physics, topological insulators, mathematical physics, and quantum information; see, for example, [26–31].

Berry’s phase also emerges for atoms exposed to external electric and magnetic fields varying in time which form a six-dimensional parameter space. P violation (PV) in such physical systems manifests itself in P-violating<sup>1</sup> contributions to Berry’s phase. These contributions can be divided into nuclear-spin independent and nuclear-spin dependent parts, following from the derivation of the PV Hamiltonian  $H_{PV}$  from first principles.

The main goal of this thesis is the exploration of possibilities to reveal PV signatures in terms of Berry phases for  $n = 2$  hydrogen states exposed to electromagnetic fields in an atom interferometer. The idea is to combine one of the theoretically best-known atomic species, hydrogen, with interferometry which is known for its potential to allow high-precision measurements [32, 33]. We aim at the derivation of a physical observable which is easily accessible in an atom interferometry experiment. One particularly suitable experimental setup for the investigation of Berry phases is a longitudinal atomic beam spin echo (LABSE) scheme. The investigation of spin echos dates back to the 1950s [34]. The basic idea is to apply subsequent magnetic fields, oriented antiparallel to each other, to spin-polarised particles, thereby reversing their accumulated dynamic phase and establishing an ‘echo’ of polarisation. In 1995, Dubbers et. al. developed a high-precision atomic beam spin echo setup and measured Berry phases for  $^3\text{He}$  propagating in magnetic fields [35, 36]. In the present thesis, we theoretically describe a similar apparatus which is presently used and further developed in the group of M. DeKieviet [32, 33, 37–39]. We investigate the properties of Berry phases for metastable 2S states of hydrogen [40]. They live long enough for feasible interferometry experiments and possess a weak admixture of 2P states of hydrogen due to  $H_{PV}$ , thereby allowing for PV Berry phases to be observed in interference patterns. In the present thesis we aim at the determination of maximal magnitudes of PV Berry phases by exploring suitable regions of the electromagnetic parameter space.

---

<sup>1</sup>In the following, we will abbreviate ‘P-violating’ the same way as ‘P violation’.

---

Through the PV observables we have, in principle, access to the electroweak mixing angle  $\theta_W$ , a fundamental parameter of the Standard Model (SM), the numerical value of which is not predicted theoretically within the SM. It rather has to be determined experimentally. The most precise data have been acquired at large momentum transfers in collider experiments [41, 42]. A value of  $\sin^2 \theta_W$  measured at high-energy can be connected to values at lower energies by use of renormalisation group theory. In the low-energy limit the running of the coupling constant  $\sin^2 \theta_W$  is predicted to saturate at  $\sin^2 \theta_W = 0.23867(16)$  [43]. Due to very few experimental data in the low-energy regime, a cross-check of hitherto found results for the running of  $\sin^2 \theta_W$  would be most welcome, complementary to high-energy physics. Moreover, a high-precision determination of  $\sin^2 \theta_W$  may constrain alternative models of weak interactions or indicate physics beyond the SM if deviations from the SM-predictions are found.

Atomic parity violation (APV) experiments offer the possibility to determine  $\sin^2 \theta_W$  at low energies. Much effort has been put in observing PV effects in heavy atoms which have a high nuclear charge  $Z$ . In general, such atomic species are favoured compared to light atoms due to the so-called  $Z^3$ -law [44–46]. This was derived in 1974 by M.-A. Bouchiat and C. Bouchiat who predicted a strong enhancement of PV effects with growing nuclear charge. Several physical phenomena have been investigated in the context of APV. To date, the most prominent and most precise example is the measurement of P-violating  $6S \rightarrow 7S$  transitions in caesium, conducted in the group of C. E. Wieman [47]. Summaries and reviews of APV can, for instance, be found in [7, 8, 11, 12]. The most severe constraint regarding APV experiments is the necessity to extract desired observables like  $\sin^2 \theta_W$  from experimental outcomes by comparison with theory which involves demanding atomic-structure calculations. See, for example, [8] and references therein for the sophisticated computations to retrieve high-accuracy APV predictions for heavy atoms with many electrons and complicated nucleon configurations.

In contrast, the lightest atoms such as hydrogen and deuterium can be regarded as ideal candidates to study APV due to their structural simplicity, at least from the theoretical point of view. Summaries of the present status for PV in hydrogen and deuterium are given in [48, 49]. Until now, PV experiments with these atomic species have not been competitive with investigations of heavy atoms, cf. [50] for a brief review. In fact, the most precise experiment was done by C. C. W. Fehrenbach at the University of Michigan in 1993 [51]. There, a  $\sin^2 \theta_W$ -dependent PV observable, determined from a P-violating  $2S \rightarrow 2S'$  transition in hydrogen, was reported with a combined error of 1500%.

In the theoretical description of APV, the electroweak mixing angle is directly related to the weak charges [44] which are proportionality constants for the weak PV interaction of the nucleus. The nuclear-spin independent weak charge  $Q_W^{(1)}$  incorporates only  $\sin^2 \theta_W$ , the nuclear charge, and the neutron number. Therefore,  $\sin^2 \theta_W$  can be determined most clearly via  $Q_W^{(1)}$ , not taking into account the absolute size of the PV effects. On the other hand, the nuclear-spin dependent weak charge  $Q_W^{(2)}$  also

involves the total polarisations  $\Delta q + \Delta \bar{q}$  of a nucleus carried by the quark species  $q$  and  $\bar{q}$ , see, e.g., [52]. As a part of the so-called spin crisis of the proton [52–54], the experimental determination of the  $s$ -quark contribution  $\Delta s + \Delta \bar{s}$  is not entirely conclusive to date [55–59]. Thus, a measurement of  $Q_W^{(2)}$  would offer the possibility to significantly contribute to the knowledge of the proton’s spin structure.

Apart from PV Berry phases the parameter space of electric ( $\mathcal{E}$ ) and magnetic ( $\mathcal{B}$ ) fields first of all provides for P-conserving (PC) Berry phases which are, in general, much larger than PV ones. Here, the external fields  $\mathcal{E}$  and  $\mathcal{B}$  couple to the atom’s electric and magnetic dipole operators  $\underline{D}$  and  $\underline{\mu}$ , respectively. Moreover, the instability of the  $n = 2$  hydrogen states effectively yields complex eigenenergies of the Hamiltonian in the corresponding subspace. As a consequence of the non-hermitian Hamiltonian, both PC and PV complex Berry phases can emerge for the metastable 2S states in suitable electromagnetic field configurations. For geometric phases of systems being subject to non-hermitian Hamiltonians see, for instance, [60–66]. Particularly emphasising the role of metastable states, geometric phases and their relation to the adiabatic theorem were discussed in [67, 68]. In the present work we find complex Berry phases for hydrogen in suitable electromagnetic fields giving rise to geometry-dependent modifications of the atomic lifetimes. This intriguing effect has not been observed experimentally so far.

As already pointed out by Berry, the geometric phases arising from a closed line integral in parameter space can be rewritten in terms of an oriented surface integral over a flux-density vector field [22]. The investigation of Berry phases can then be done in terms of these vector fields.

In this thesis we analyse the flux-density vector fields of metastable atomic states [40]. Thereby, we retrieve formulae of the vector field components and their derivatives proving to be useful for analytical as well as numerical analysis. The visualisation of three-dimensional flux-density vector fields serves as a convenient tool to explore the electromagnetic parameter space. In that way, it becomes possible to search for Berry phases with tailored properties, such as pure PV Berry phases or imaginary parts of Berry phases.

Studying the behaviour of the external-field-dependent flux-density vector fields under proper and improper rotations, we gain expansions of these vector fields in terms of functions which are invariant under those rotations. With these expansions, analytical expressions for the global structure of the vector fields in specific parameter spaces are derived, enabling consistency checks of our numerical calculations. Furthermore, this structure analysis reveals relations like a high sensitivity of specific flux-density vector fields to the electric dipole operator  $\underline{D}$  in the case of hydrogen. Considering more complex atomic species with less accurately known dipole operators, analogous findings could be valuable for determining  $\underline{D}$  and  $\underline{\mu}$ , respectively, via measurements of adequate Berry phases connected to those flux-density vector fields.

We gain access to the Berry phases, which are incorporated in the evolution of the atomic wave packet, by deriving the total flux  $\mathcal{F}$  of longitudinally propagating atoms that arrive at the detector for given electromagnetic field configurations. The

---

observable  $\mathcal{F}$  represents the interference pattern as a function of the applied external fields. Our analysis culminates in the detailed investigation of spin echo signals  $\mathcal{F}$  under realistic conditions. We retrieve PC as well as PV spin echo signals and discuss their implications on precision measurements of the proton's weak charges.

Regarding precision enhancement of atom-interferometric measurements, we investigate the possibility to use squeezed  $N$ -particle states instead of single atoms. Here, the crucial feature of squeezed states is the decreased variance of one observable of interest at the expense of the variance of the conjugate observable. For example, squeezed atomic states were investigated in the group of D. J. Wineland to reduce projection noise in spectroscopy [69]. There, the total-spin fluctuations  $\Delta J_y$  of an initial state are decreased in  $y$ -direction while increased in  $x$ -direction. The total spin  $\langle \mathbf{J} \rangle$  with the corresponding error spheroid is then rotated according to a Ramsey-type spectroscopy scheme such that the initial  $\Delta J_y$  ends up to be the decreased error of a  $J_z$ -measurement. Exploiting squeezed states, the resolution of interference patterns could be pushed beyond the standard quantum limit of product states, i.e., of a sequence of uncorrelated single atoms, by a factor up to  $\sqrt{N}$ . Extensive literature is available on that subject; see [69–76] for a selection in view of this thesis.

Finally, we present results for Berry phases of metastable helium which is currently used in the IABSE apparatus built by M. DeKieviet and collaborators. Compared to metastable hydrogen, metastable helium states have the advantage to be detectable with very high efficiency [77]. Many of the results in this thesis are valid for a wide class of physical systems. To be more precise, we can treat any system with adiabatically evolving metastable states obeying an effective Schrödinger equation with an effective Hamiltonian which couples the system linearly<sup>2</sup> to external parameters. This includes  $n = 2$  helium exposed to electromagnetic fields. In particular, we calculate PC Berry phases for one metastable 2S state of  $^4\text{He}$ . In principle, this result can be checked immediately in experiment. The required matrix elements of the magnetic and electric dipole operators and the PV contribution to the mass matrix were calculated by M. Puchalski [78].

The present work is in line with an extended sequence of projects [39, 67, 68, 79–83] and aims to connect to existing experiments in a concrete way. The main findings of this thesis include the discussions and results published in [40] and [32]. It is organised as follows.

In Chapter 2 we review, after several general remarks on parity violation in Section 2.1, the foundations and motivations for the investigation of atoms, especially hydrogen, in the realm of APV. In the course of that, the derivation of the PV Hamiltonian is outlined in Section 2.2 starting from the Lagrangian of quantum flavour dynamics. Moreover, we present the current status of research regarding the electroweak mixing angle in Section 2.3. Although the present work focusses on PV in hydrogen, we give

---

<sup>2</sup>We derive several properties and relations which hold for non-linear couplings as well.

## Chapter 1. Introduction

---

an overview of PV in heavy atoms in Section 2.4 as an instructive prelude, thereby emphasising the main differences between PV in light and heavy atoms. Besides introducing the general properties and principal quantities of atomic parity mixing used throughout the subsequent chapters, we address the advantages of PV investigations with hydrogen in Section 2.5. There, hitherto proposals and efforts to measure PV in hydrogen are discussed as well.

We present the concept of Berry's phase and its connection to the adiabatic theorem in Section 2.6. There, we give the straightforward extension to the case of non-hermitian Hamiltonians as needed in this work. Furthermore, the common textbook-illustration of geometric phases which emerge for parallel-transported vectors on a sphere is elucidated by explicitly connecting it to the quantum mechanical derivation of Berry's phase. We close Chapter 2 by citing several experimental observations of geometric phases.

Chapter 3, based on [40], is devoted to one main subject of this thesis. We aim at the computation, classification, and structural analysis of Berry phases and their flux-density vector fields for metastable states. We provide means for the investigation and generation of tailored Berry phases, in particular for atomic systems in external fields and especially for hydrogen.

First, the Wigner-Weisskopf approximation is outlined in Section 3.1 yielding an effective description of the exponential decay of the  $n = 2$  hydrogen states in terms of a non-hermitian Hamiltonian or mass matrix. In Section 3.2 we discuss hydrogen exposed to electromagnetic fields in view of the requirements to determine PV Berry phases. General remarks and notations regarding Berry phases for atoms at rest are given in Section 3.3. Our approach of their numerical computation is briefly summarised in Section 3.4. A rigorous analysis of the structure of geometric flux-density vector fields via their transformation properties under proper and improper rotations is presented in Section 3.5. Those findings can be utilised to preselect interesting parameter space regions and compute Berry phases as well as the according flux-density vector fields. Furthermore, that analysis allows for convenient consistency-checks of the numerically derived geometric phases in view of the exceedingly large parameter space of electric and magnetic fields. Besides giving several remarks on the systematic analysis of flux-density vector fields, we illustrate our results for their properties with concrete examples for hydrogen in Section 3.6. Berry phases for specific electromagnetic field configurations are determined in Section 3.7. There, both real and imaginary parts of PC and PV Berry phases are evaluated.

At this point, we connect to a realistic experimental scheme which ought to enable measurements of the Berry phases found so far. The evolution of hydrogen wave packets in LABSE experiments is described in Chapter 4, based on [32]. After defining the basic experimental parameters in Section 4.1, we introduce the effective Schrödinger equation in the adiabatic limit and its solutions in Section 4.2. Specialising to Gaussian wave packets, the interference effects of two internal 2S states are derived in Section 4.3. As a result, we obtain an analytical expression of the interference pattern  $\mathcal{F}$  which corresponds to a spin echo signal in case of a spin echo field configuration.

---

In Chapter 5 we derive specific spin echo signals comprising the theoretical machinery, developed in the preceding chapters, and realistic experimental parameters. Due to the small magnitude of PV mixing in hydrogen, a perturbative expansion of  $\mathcal{F}$  with respect to its PV part is in order. In Section 5.1 we present this expansion allowing for separate analysis of PC and PV spin echo signals such that the PV signal is not masked by numerical errors of the PC signal. The further treatment of two spin echo signals, following from a chiral field configuration and its space-reflected version, is described in Section 5.2. There, we aim for the extraction and interpretation of the PV signal. An example of such a PV interference pattern is discussed in detail in Section 5.3, thereby noting several subtleties which have to be accounted for in the numerical implementation. After calculating PC spin echo signals for an already manufactured field configuration in Section 5.4, we estimate the theoretical uncertainties of our PV spin echo signals in Section 5.5. As a result and based on the uncertainties of all physical quantities relevant for the PV signals, achievable accuracy limits for the proton's weak charges and their constituents are retrieved.

In Section 5.6 we investigate, from the theoretical point of view, the possibility of using squeezed states to improve the sensitivity of the LABSE scheme. The concept of spin squeezing is introduced and an approach for the application to LABSE experiments is formulated.

Berry Phases for the  $n = 2$  states of  ${}^4\text{He}$  are addressed in Chapter 6. As a prerequisite for further investigations, the complex eigenenergies in electromagnetic fields are calculated in Section 6.1. We present a first result on a PC Berry phase of a meta-stable helium state in magnetic field parameter space in Section 6.2. In principle, this finding could be checked immediately with the currently available LABSE apparatus.

We conclude in Chapter 7 by summarising our results and accounting for several ideas and future directions of research regarding PV phases in light atoms.

In Appendix A we give notations and definitions used throughout the thesis. Values and quantities related to the hydrogen mass matrix are noted in Appendix A.1. There, the labelling scheme of the  $n = 2$  states is introduced. We furthermore derive the decay matrix as used in the Wigner-Weisskopf approximation. In Appendix A.2 we present the mass matrix for the  $n = 2$  states of hydrogen. The labelling scheme and the mass matrix for the  $n = 2$  states of  ${}^4\text{He}$  are given in Appendix A.3.

Detailed calculations of several relations regarding the flux-density vector fields discussed in Chapter 3 are presented in Appendix B.

In Appendix C we give the detailed derivation of the non-relativistic PV Hamiltonian, as outlined in Section 2.2.

The numerical computations presented in this thesis are carried out with the numerical software QABSE. Its main features are noted and commented in terms of a pseudo-code in Appendix D.



## 2 Foundations, Motivations, and Historical Overview

In this chapter we discuss the main aspects of the physical framework underlying the work presented in this thesis, in particular atomic parity (P) violation and Berry phases.

The notion of P violation (PV) and its implications on physical quantities are introduced in Section 2.1 with emphasis on concepts referred to in the subsequent chapters.

To date, P violation in atoms is understood in terms of the weak neutral currents within the electroweak sector of the Standard Model (SM). In Section 2.2 we present the derivation of the PV contribution of the atomic non-relativistic Hamiltonian  $H_{\text{PV}}$  from first principles. Besides the familiar P-conserving electromagnetic Hamiltonian  $H_{\text{PC}}$ , the P-violating contribution  $H_{\text{PV}}$  is the basis for the calculations of PV Berry phases in this thesis.

The determination of fundamental electroweak parameters such as the Weinberg angle  $\theta_W$  is one of the main objectives in the realm of atomic parity violation (APV). In Section 2.3 we summarise the current state of knowledge concerning the electroweak mixing angle  $\theta_W$ . The angle is directly related to the weak charges of atoms. Major successes have been achieved with APV experiments on heavy atoms, especially caesium. Because of their importance for the low-energy regime of electroweak physics and the connections to APV in light atoms, we collect the physical foundations and main findings of PV experiments with heavy atoms in Section 2.4.

In Section 2.5 we focus on the general properties of PV in hydrogen and the advantages hydrogen provides compared to heavy atoms. We also give a brief review of hitherto existing proposals for PV measurements on hydrogen.

The main part of the present thesis is devoted to the calculation and classification of P-conserving and P-violating Berry phases. Like parity violation, the quantum mechanical Berry phase constitutes a fundamental geometrical property of our world. It was shown by M. V. Berry in 1984 [22] that quantum mechanics exhibits, under very general conditions, a non-local geometric structure which manifests itself, e.g., in terms of geometric phases. We discuss this profound property of a quantum system in Section 2.6.

### 2.1 Parity Violation in Quantum Physics

In this section we introduce the fundamental characteristics of the P transformation, necessary for the understanding of the chiral properties of hydrogen atoms in external

electromagnetic fields. In the course of that, we will also briefly quote a few experiments concerning PV, highlight APV and mention different areas of research where PV experiments would allow new insight. More detailed discussions of APV in general and PV in hydrogen in particular are provided in Sections 2.4 and 2.5, respectively.

### Parity Transformation

The P transformation is defined by

$$P : \mathbf{x} \rightarrow P \mathbf{x} = -\mathbf{x} , \quad (2.1)$$

where  $P$  is the representation of P in three-dimensional spatial space switching sign of the coordinate vector  $\mathbf{x}$ , i.e., switching between left- and right-handed coordinate systems. Mirror symmetry is often investigated in the same physical context as space-reflection symmetry. This is justified since parity is the combination of mirror reflection and an appropriate  $\pi$ -rotation of the coordinate system – and, to date, every fundamental law of physics is understood to be rotationally invariant. Of course, one has to be aware of the difference between mirror reflection and P transformation when it comes to specific experimental situations which aim to detect the chiral properties of a physical system. Chirality is the intrinsic handedness of a system. A system is called chiral if it cannot be transformed into its mirror image by rotations or any other transformation which corresponds to a symmetry of the system, e.g., Lorentz boosts. A system is chiral or it is not. On the other hand, the handedness of a system denotes its property of being left- or right-handed. And this property is not conserved in general. One often cited example is the sign-changing helicity<sup>1</sup> of a spin-particle under a suitable Lorentz boost.

The symmetry of parity is said to be violated in a physical system if the space reflected version of an experiment on the system leads to a different outcome than the non-transformed experiment. In the following, we want to clarify the meaning of this statement since in the literature this core idea of P violation experiments is often presented in a fragmented or even inconclusive way.

### Left-Right-Asymmetry

A general way of describing the behaviour of a system under a P transformation is the investigation of the left-right-asymmetry

$$A_{LR} = \frac{\sigma_L - \sigma_R}{\sigma_L + \sigma_R} , \quad (2.2)$$

where  $\sigma_{L/R}$  denote the outcomes of an experiment L and of the space reflected experiment R, respectively. The quantity (2.2) is at the heart of P violation experiments. Of course, the experimental outcomes  $\sigma_{L/R}$  in (2.2) have to be numbers, e.g., counting rates, angles, or spatial distances. If  $\sigma_{L/R}$  are exact images of one another under P transformation, parity is conserved for the underlying physical process, i.e.,  $A_{LR} = 0$ .

---

<sup>1</sup>The helicity operator of a particle with spin  $\mathbf{S}$  and momentum  $\mathbf{p}$  is defined as  $h = \mathbf{S} \cdot \mathbf{p}$ .

## 2.1. Parity Violation in Quantum Physics

---

If, on the other hand,  $A_{LR} \neq 0$ , then the symmetry of parity is violated. There is extensive literature available on this subject, see for instance [8, 84, 85] for the realm of atomic physics. However, we want to stress aspects which are particularly relevant for the present thesis and therefore give a customised summary of the fundamental arguments involved in the investigation of P violation.

### Chiral Observables

For the correct P transformation of experiment L the behaviour of the involved components under space inversion has to be known. Otherwise, one may not be able to distinguish between a P-violating effect and false assumptions on the experimental setup. For example, treating the polar vector of the electric field as an axial vector, i.e., not reversing its sign for experiment R, can result in a false left-right asymmetry. That is, by performing experiment L and experiment R we test parity only under the assumption that the chiral properties of the experimental setup are known. The behaviour of any observable with respect to a P transformation has to be determined by experiment via space reflecting the experimental apparatus. For example, an electric field  $\mathbf{E}$  can be produced by some apparatus A, then, by P-transforming A, i.e., by space reflecting all the components which A is built from, one finds

$$\mathbf{E} \xrightarrow{P} -\mathbf{E} . \quad (2.3)$$

Conversely, the classical electromagnetic theory implies, for instance,

$$\mathbf{E} = -\nabla\phi - \partial_t\mathbf{A} \xrightarrow{P} -(-\nabla)\phi - \partial_t(-\mathbf{A}) = -\mathbf{E} \quad (2.4)$$

for an electric potential  $\phi$  and a magnetic vector potential  $\mathbf{A}$ . Hence, one has to P-transform all quantities involving a spatial dependence. We note that the electric field itself is not chiral since  $-\mathbf{E}$  is transformed into  $\mathbf{E}$  via a  $\pi$ -rotation. Considering (2.3), the electric field is said to be P-odd. Conversely, a physical quantity like the magnetic field  $\mathbf{B}$  is said to be P-even as it does not change sign under a P transformation. With non-chiral constituents like  $\mathbf{E}$  and  $\mathbf{B}$  one can devise experiments which possess chirality and P-transform them in a well-defined way. We list some basic physical quantities in Table 1 together with their behaviour under P transformation.

P-odd	P-even
spatial vector $\mathbf{x}$	time $t$
momentum $\mathbf{p}$	energy $E$
force $\mathbf{F}$	mass $m$
electric field $\mathbf{E}$	magnetic field $\mathbf{B}$
electric current density $\mathbf{j}$	electric charge density $\rho$
magnetic vector potential $\mathbf{A}$	electric potential $\phi$
helicity $h$	angular momentum $\mathbf{L}$ and spin $\mathbf{S}$

**Table 1:** Behaviour of some basic physical quantities under P transformation.

An essential requirement for testing parity is the chirality of the experimental setup. If it possesses no handedness, the P-transformed setup can simply be rotated into the non-transformed one leading to the same physics. Eventually, a definite chirality of the experimental setup is not sufficient for finding different measurement results with the P-reflected setup.

### Parity in Quantum Mechanics

We now connect the discussion of P violation with the notion of symmetry in quantum mechanics. The parity operator is hermitian and unitary and has the spatial representation  $\langle \mathbf{x} | P | \mathbf{x}' \rangle = \langle \mathbf{x} | -\mathbf{x}' \rangle = \delta^3(\mathbf{x} + \mathbf{x}')$  implying that  $\langle \mathbf{x} | P | \psi \rangle = \psi(-\mathbf{x})$  for the spatial wave function of an arbitrary state  $|\psi\rangle$ . Thus, the state  $P|\psi\rangle$  in spatial representation describes a system obtained from the spatial representation of  $|\psi\rangle$  by space reflection. Considering a physical system described by the Hamiltonian  $H = H^{\text{even}} + H^{\text{odd}}$  containing parts which are even and odd under a P transformation, respectively, then parity is not conserved because of

$$P^{-1}HP = H^{\text{even}} - H^{\text{odd}} \neq H \quad \Rightarrow \quad [H, P] \neq 0 . \quad (2.5)$$

For a time independent Hamiltonian  $[H, P] \neq 0$  implies  $[U, P] \neq 0$ , where  $U$  is the time evolution operator. That is, if  $|\psi\rangle$  is an eigenstate of  $P$ , then  $U|\psi\rangle$  is in general not. Thus, for the transition rates  $\Gamma$  between two states  $|\phi\rangle$  and  $|\psi\rangle$  and their mirror states  $|\phi'\rangle = P|\phi\rangle$  and  $|\psi'\rangle = P|\psi\rangle$ , respectively, one finds

$$\Gamma(\psi' \rightarrow \phi') = |\langle \phi' | U | \psi' \rangle|^2 = |\langle \phi | P^{-1} U P | \psi \rangle|^2 \neq |\langle \phi | U | \psi \rangle|^2 = \Gamma(\psi \rightarrow \phi) . \quad (2.6)$$

### Enantiomers

One source for intuitively accessible chiral experiments are enantiomers, i.e., left- and right-handed versions of chiral molecules which are transformed into each other by a mirror reflection. They cannot be transformed into each other by a proper rotation. As an example we show the chemical structure of lactic acid in Figure 2.1. Experiment L consists of an experimental setup L in the laboratory coordinate system  $K$ , where the left-handed molecule interacts with light polarised in  $z$ -direction while travelling in  $x$ -direction. The result of L is the rotation of the plane of polarisation by an angle  $\phi$  in the  $y$ - $z$ -plane. The setup R in the  $x$ - $z$ -mirror-reflected coordinate system  $K'$  then consists of the right-handed molecule interacting with photons polarised in  $z$ -direction. The angles of rotation  $\phi$  and  $\phi'$  have opposite signs in  $K$ , but the same sign when regarding them in their respective coordinate systems. That is, the optical rotations  $\sigma_L$  and  $\sigma_R$  are exact mirror images of one another<sup>2</sup> and the left-right asymmetry is expected to be

$$A_{\text{LR}} = \frac{\sigma_L - \sigma_R}{\sigma_L + \sigma_R} = \frac{\phi - \phi'}{\phi + \phi'} = 0 . \quad (2.7)$$

---

<sup>2</sup>The experiment R looks the same as experiment L seen in the  $x$ - $z$ -mirror.

## 2.1. Parity Violation in Quantum Physics

Thus, in this example of chiral molecules inducing optical rotation no P violation is present. In fact, experiments detected the rotation of the plane of polarisation in opposite direction by the same amount. The first one was performed in 1848 by Louis Pasteur [86] discovering molecular chirality, and modern experiments yield opposite rotations of equal magnitude within the given accuracy, cf. references given in [87]. Different angles of rotation would indicate P violation in chiral molecules. In fact, there are experiments and proposals for detecting P-violating effects in enantiomers, see for example [87–89], or [7] and references therein. Due to the electroweak interaction incorporated in the Hamiltonian  $H$  the two versions of an enantiomer are generally not expected to have the same energies according to

$$E_{\psi'} = \langle \psi | P^{-1} H P | \psi \rangle \neq \langle \psi | H | \psi \rangle = E_{\psi} , \quad (2.8)$$

where  $|\psi\rangle$  is some energy eigenstate of  $H$ . Of course, detecting this difference and tracing it back to the weak interaction may be even more difficult than in experiments with single atoms. Although chemical reactions are usually regarded to fall in the realm of the (P-conserving) electromagnetic interaction, there are debated attempts to trace back the chiral features of biological molecules such as proteins and DNA to the neutral currents of electroweak interaction. Discussions of these issues and related questions of P violation in biologically relevant molecules can for instance be found in [7, 13, 14].

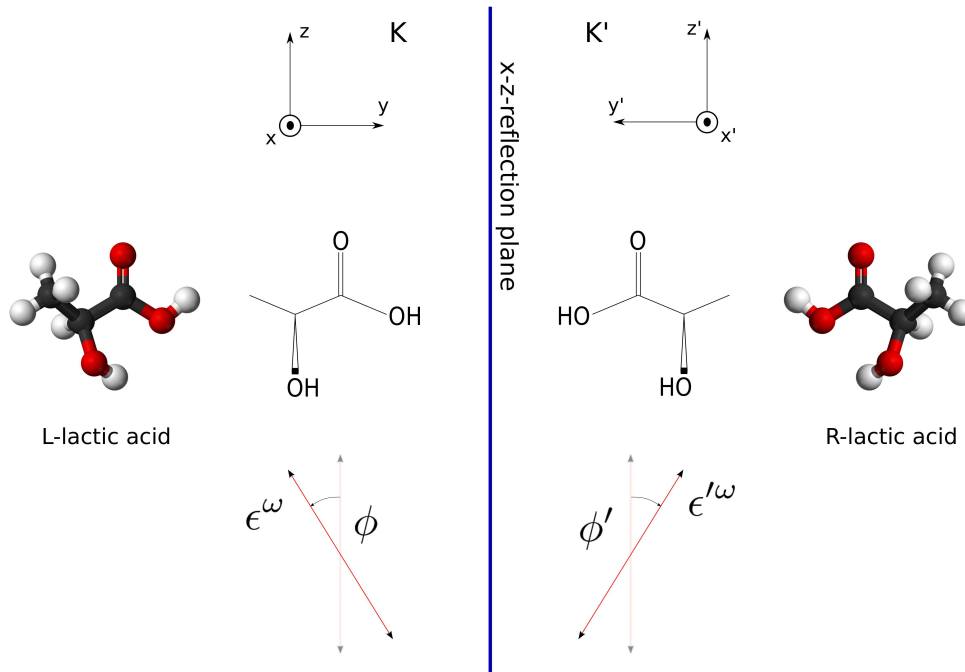


**Figure 2.1:** Lactic acid rotates the plane of polarisation of linearly polarised light  $\epsilon^\omega$ . In the laboratory frame K the rotation angle has different signs when considering the two types of enantiomers. The illustration of the three-dimensional lactic acid molecule is adopted from <http://knol.google.com/k/organic-and-biomaterials-chemistry-lecture-32#>.

### Energy Shifts due to $H_{\text{PV}}$

Equation (2.8) holds for P-violating Hamiltonians in general. However, the energy shifts may not be large enough for feasible experiments since the P-violating part  $H_{\text{PV}}$  of the Hamiltonian  $H = H_0 + H_{\text{PV}}$  of a non-degenerate system does not contribute to the energy levels in first-order perturbation theory in  $H_{\text{PV}}$ . This is due to  $[H_0, P] = 0$ , implying  $H_0 P|\psi_0\rangle = E_0 P|\psi_0\rangle$  and  $P|\psi_0\rangle = e^{i\eta}|\psi_0\rangle$ , with  $\eta \in \mathbb{R}$ , leading to

$$\langle \psi_0 | H_{\text{PV}} | \psi_0 \rangle = \langle P\psi_0 | P H_{\text{PV}} P | P\psi_0 \rangle = - \langle \psi_0 | H_{\text{PV}} | \psi_0 \rangle = 0 , \quad (2.9)$$

i.e., a vanishing first-order contribution. Thus, in the case of non-degenerate 2S states of hydrogen their energy shifts are at least of second order in perturbation theory,

$$E_{\psi'} - E_{\psi} = \frac{|\langle 2P_{1/2} | H_{\text{PV}} | 2S_{1/2} \rangle|^2}{E(2S_{1/2}) - E(2P_{1/2})} = \frac{|\delta_i L|^2}{L} = |\delta_i|^2 L \lesssim 10^{-25} L , \quad (2.10)$$

where  $L$  is the Lamb shift. The zeroth-order contributions to  $E_{\psi}$  and  $E_{\psi'}$  cancel. For the other quantities involved in (2.10) see Appendices A.1 and A.2. Clearly, the observation of such small energy shifts is exceedingly difficult. However, larger energy shifts may be obtained in the case of degenerate eigenstates of  $H_0$ . As shown in [81,82], the application of suitable chiral electric field configurations can yield energy shifts proportional to  $\delta_i$  or even to  $\sqrt{\delta_i}$ , respectively, representing a huge enhancement of the PV effect compared to (2.10).

### P-Violating Light Absorption by Atoms

We now address a P-violating effect actually observed in atoms. For simplicity, we suppose an experimental setup L, where an atom absorbs only the left-polarised ( $\sigma_{\text{L}}$ ) component of linearly polarised photons travelling in  $x$ -direction. This absorption property of the atom provides a PV effect, as we will see in the following. Since there are no left- or right-handed versions of atoms, the atom does not need to be replaced to obtain a version of the experiment which is mirror-reflected with respect to the  $x$ - $z$ -plane. By the same token, the incoming beam of linearly polarised light consisting of left- and right-polarised light in equal shares stays the same. That is, the setup R obtained from setup L by reflection at the  $x$ - $z$ -plane is not modified at all compared to setup L. Consequently, its absorption properties stay the same, i.e., again only left-polarised photons are absorbed. But the atom of experiment R should absorb only mirror-reflected  $\sigma_{\text{L}}$ -light, that is,  $\sigma_{\text{R}}$ -light, if mirror reflection symmetry is supposed to hold. As a result parity symmetry is not respected in the absorption process. Here, the left-right asymmetry is

$$A_{\text{LR}} = \frac{\rho_{\sigma_{\text{L}}} - \rho_{\sigma_{\text{R}}}}{\rho_{\sigma_{\text{L}}} + \rho_{\sigma_{\text{R}}}} = 1 , \quad (2.11)$$

where  $\rho_{\sigma_{\text{L/R}}}$  are the absorption rates of left- and right polarised light. The P-violating absorption properties of atoms were investigated and a non-vanishing left-right asymmetry was found in 1978 in Novosibirsk in an experiment using bismuth vapour [21]. This was the first observation of parity violation in atoms.

### Role of the Standard Model

At this point, the question arises of how to predict the behaviour of a physical system under space reflection. An asymmetry with respect to parity simply has to be built into the theory right from the beginning. The Standard Model of particle physics provides a description of most P-violating processes observed so far. For a counterexample we refer to [47, 90, 91] where a discrepancy between experiment and theory is reported for a PV observable. We will address this issue more detailed in Section 2.4.

We want to mention the very first experiment finding a violation of space-reflection symmetry. It was the measurement of the angular distribution of electrons emitted from polarised cobalt nuclei in  $\beta^-$ -decay in 1957 by C. S. Wu and collaborators [5]. This experiment was conducted a few months after Lee and Yang posed the question of P violation due to weak interactions [4]. The two versions of the chiral experimental setup are shown schematically in Figure 2.2.

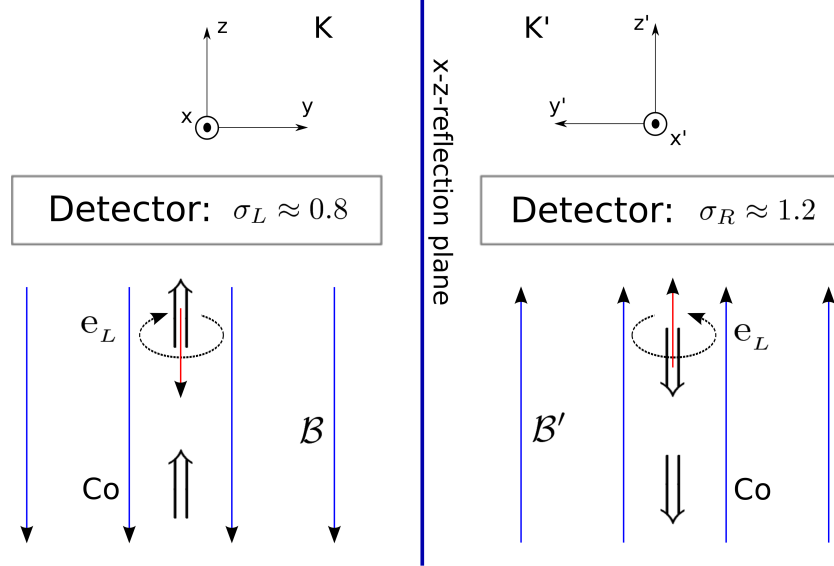


**Figure 2.2:** Illustration for the  $\beta^-$ -decay experiment [5] viewed in the mirror reflected coordinate systems  $K$  and  $K'$ . The spins of the cobalt nuclei, indicated by broad arrows, are aligned antiparallel to the magnetic field  $\mathcal{B}$  and  $\mathcal{B}'$  (blue arrows), respectively. Due to angular momentum conservation in the process (2.12), the electron spin is also aligned antiparallel to the magnetic field. The  $z$ -components of the electron momenta are indicated by red arrows for the preferred electron helicities as observed in the experiment. That is, preferably left-handed electrons in terms of helicity, i.e., left-helicity electrons, are emitted in both experimental setups, illustrated by the curved arrows. This is a direct verification of P violation in the process of  $\beta^-$ -decay.

According to [5] the decay



is observed at a small temperature to ensure sufficient polarisation of the cobalt sample due to the magnetic field  $\mathbf{B} \parallel \mathbf{e}_z$ . The two experimental realisations are mirror images of

one another, obtained by mirror reflection at the  $x$ - $z$ -plane. However, the experimental outcomes  $\sigma_L$  and  $\sigma_R$ , which are the ratios of the counting rates of the electrons at low and high temperature<sup>3</sup>, were found not to be mirror images of one another. In terms of helicity the emitted electrons are preferably left-handed in both cases while the mirror reflection of the left-handed electron in  $K$  ought to result in a right-handed electron in  $K'$  if parity was conserved. In fact, the W-bosons of the Standard Model involved in  $\beta$ -decay couple only to left-handed fermions and right-handed anti-fermions, i.e., parity is maximally broken in  $\beta$ -decay. Note that left-handed particles in the SM actually are meant to be left-chiral ones, not left-helicity particles. The notation  $\mathbf{e}_L$  in Figure 2.2 indicates left-helicity electrons, whereas in the context of the SM the notation  $\mathbf{e}_L$  is usually used for the left-chiral part of the electron  $\mathbf{e} = \mathbf{e}_L + \mathbf{e}_R$ . However, having clarified that aspect, we will adopt the SM notation from this point forward. The left-right asymmetry of the  $\beta$ -decay experiment is

$$A_{\text{LR}} = \frac{\sigma_L - \sigma_R}{\sigma_L + \sigma_R} = \frac{\sigma_L - 0}{\sigma_L + 0} = 1, \quad (2.13)$$

under ideal experimental conditions. Of course, the left-helicities of the electrons could be switched by a Lorentz boost resulting in right-helicity electrons. But the detectors would be boosted in the same direction leading to the same detection asymmetry between both versions of the experiment.

Until 1968, the Cabibbo-Theory [92] of weak charged currents described all weak decays. P violation in stable atoms was not supposed to be possible. Nowadays, P violation in the SM is introduced via the Glashow-Weinberg-Salam model of electroweak interaction [15–17], formulated in 1968 and unifying electromagnetic and weak interactions. As a consequence, a new neutral gauge boson called the Z- or  $Z^0$ -boson was predicted, followed from the discovery of the weak neutral currents in 1973 [18]. The Z-boson coupling to fundamental fermions is different for left- and right-handed fermions, thereby yielding the possibility of inert matter like atoms to exhibit P violation for various observables. In contrast to the maximal left-right-asymmetry of  $\beta$ -decay, the left-right asymmetry from interference between P-conserving and P-violating amplitudes in atoms is many orders of magnitude smaller, see Section 2.4. Here, the electromagnetic interactions dominate over the weak PV interactions. Estimates for a measurable left-right asymmetry of the order of  $10^{-6}$  are retrieved for heavy atoms. In Section 2.3 we will also quote, besides those APV experiments, several high-energy experiments aiming at the detection of P violation.

In the following section, we outline those parts of the electroweak theory which are relevant for APV, in particular for hydrogen. The bottom-line observation is the intrinsic chirality of atoms.

---

<sup>3</sup>At high temperature the polarisation of the cobalt nuclei is lost resulting in equal counting rates  $\sigma_L = \sigma_R$ .

## 2.2 The Parity-Violating Atomic Hamiltonian

To put our theoretical basis of atomic PV into the context of the SM, we introduce the Lagrangian  $\mathcal{L}_{\text{QFD}}$  of quantum flavour dynamics as the starting point for the derivation of the P-violating part of atomic Hamiltonians. We proceed with the discussion of the low-energy limit of those terms in  $\mathcal{L}_{\text{QFD}}$  relevant for atoms and perform a non-relativistic reduction of the obtained Hamiltonian suitable for the investigation of light atoms such as hydrogen. In the course of that, we discuss the foundations of P violation in electroweak theory, especially the role of vector- and axial-vector couplings. We give a detailed derivation of the PV part of the atomic Hamiltonian in Appendix C. The presentation given here and in Appendix C is based on [93] where a more extensive discussion can be found.

### The Lagrangian of Quantum Flavor Dynamics

$\mathcal{L}_{\text{QFD}}$  is the basis for the derivation of the non-relativistic PV atomic Hamiltonian from first principles. As outlined in Appendix C, the Lagrangian reads, after introduction of the fermion and gauge boson masses via the spontaneously broken Higgs field:

$$\begin{aligned} \mathcal{L}_{\text{QFD}} = & -\frac{1}{2} \text{Tr} \left( \mathbf{W}_{\lambda\rho} \mathbf{W}^{\lambda\rho} \right) - \frac{1}{4} \mathbf{B}_{\lambda\rho} \mathbf{B}^{\lambda\rho} \\ & + \mathbf{W}_\lambda^+ \mathbf{W}^{-\lambda} m_W^2 \left( 1 + \frac{\rho'}{\rho_0} \right)^2 + \frac{1}{2} \mathbf{Z}_\lambda \mathbf{Z}^\lambda m_Z^2 \left( 1 + \frac{\rho'}{\rho_0} \right)^2 + \frac{1}{2} (\partial_\lambda \rho') (\partial^\lambda \rho') \\ & - \frac{1}{2} m_{\rho'}^2 \rho'^2 \left[ 1 + \frac{\rho'}{\rho_0} + \frac{1}{4} \left( \frac{\rho'}{\rho_0} \right)^2 \right] - \bar{\psi} \mathbf{M} \psi \left( 1 + \frac{\rho'}{\rho_0} \right) + \bar{\psi} i \gamma^\lambda \partial_\lambda \psi + \mathcal{L}_{\text{Int}} , \end{aligned} \quad (2.14)$$

where

$$\mathcal{L}_{\text{Int}} = -e \left\{ \mathbf{A}_\lambda \mathcal{J}_{\text{em}}^\lambda + \frac{1}{\sqrt{2} \sin \theta_W} \left( \mathbf{W}_\lambda^+ \mathcal{J}_{\text{CC}}^\lambda + \mathbf{W}_\lambda^- \mathcal{J}_{\text{CC}}^{\lambda\dagger} \right) + \frac{1}{\sin \theta_W \cos \theta_W} \mathbf{Z}_\lambda \mathcal{J}_{\text{NC}}^\lambda \right\} , \quad (2.15)$$

$$\mathcal{J}_{\text{em}}^\lambda = \bar{\psi} \gamma^\lambda (\mathbf{T}_3 + \mathbf{Y}) \psi , \quad (2.16)$$

$$\mathcal{J}_{\text{NC}}^\lambda = \bar{\psi} \gamma^\lambda \mathbf{T}_3 \psi - \sin^2 \theta_W \mathcal{J}_{\text{em}}^\lambda , \quad (2.17)$$

$$\mathcal{J}_{\text{CC}}^\lambda = \bar{\psi} \gamma^\lambda (\mathbf{T}_1 + i \mathbf{T}_2) \psi . \quad (2.18)$$

The Lagrangian (2.14) and its constituents are motivated and defined in Appendix C. In the remainder of this section we want to focus on the weak neutral currents  $\mathcal{J}_{\text{NC}}^\lambda$  responsible for PV effects in atoms.

Considering Table C.1 of Appendix C and the currents (2.16)-(2.18), one finds that the W-bosons couple to left-handed fermions only – in contrast to the Z-boson which couples to both left- and right-handed fermions, but with different coupling strengths due to different third components  $T_3$  of the weak isospin  $T$ .

### Low Energy Limit for Atomic Physics

We are interested in the fermion couplings of (2.15)-(2.18) to describe the interaction between quarks and electrons in atoms. From  $\mathcal{L}_{\text{QFD}}$  one can deduce Feynman rules, e.g., for the quark-electron interaction at tree-level via Z-boson exchange and photon exchange, respectively, see Figure 2.3. We take the low-energy limit for the Z-boson propagator  $Z(q)$  by demanding the squared four-momentum transfer  $q^2$  to be much smaller than  $m_Z^2$ . This yields

$$Z(q) \equiv \frac{-i \left( g_{\rho\lambda} - \frac{q_\rho q_\lambda}{m_Z^2} \right)}{q^2 - m_Z^2} \xrightarrow{q^2 \ll m_Z^2} \frac{i g_{\rho\lambda}}{m_Z^2}, \quad (2.19)$$

where  $g_{\rho\lambda}$  is the metric tensor. This constant propagator in momentum space corresponds to a  $\delta$ -distribution in real space. Thus, the effective lepton-quark interaction via Z-boson exchange in the low-energy limit can be regarded as a point-like 4-fermion interaction. We can write this interaction as an effective current-current-coupling

$$\begin{aligned} \mathcal{L}_{\text{int,eff}}^Z &= -\frac{e^2}{2m_W^2 \sin^2 \theta_W} \mathcal{J}_{\text{NC}}^\lambda g_{\lambda\rho} \mathcal{J}_{\text{NC}}^\rho \quad (2.20) \\ &= -\frac{2G}{\sqrt{2}} \left\{ \left( -\frac{1}{2} + 2 \sin^2 \theta_W \right) \bar{e} \gamma^\lambda e + \frac{1}{2} \bar{e} \gamma^\lambda \gamma_5 e \right\} \\ &\quad \times \left\{ \left( \frac{1}{2} - \frac{4}{3} \sin^2 \theta_W \right) \bar{u} \gamma_\lambda u - \frac{1}{2} \bar{u} \gamma_\lambda \gamma_5 u \right. \\ &\quad \left. + \left( -\frac{1}{2} + \frac{2}{3} \sin^2 \theta_W \right) (\bar{d} \gamma_\lambda d + \bar{s} \gamma_\lambda s) + \frac{1}{2} (\bar{d} \gamma_\lambda \gamma_5 d + \bar{s} \gamma_\lambda \gamma_5 s) \right\}. \quad (2.21) \end{aligned}$$

The expression (2.21) is explicitly deduced in Appendix C.

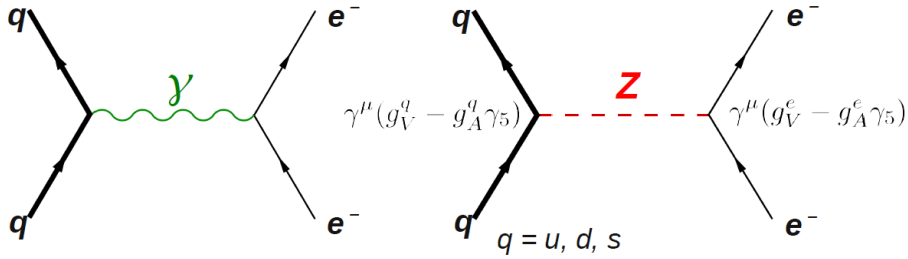


**Figure 2.3:** The diagrammatically depicted electromagnetic and weak amplitudes for the electron-quark interaction corresponding to a photon exchange and a Z-boson exchange, respectively. Here,  $q$  stands for the three light quarks  $u, d, s$ . In case of the low-energy interaction between quarks and electron in the hydrogen atom these fundamental tree-level Feynman graphs are replaced by an effective four-fermion interaction. We assume that contributions from the heavy quarks  $c, t$ , and  $b$  can be neglected. The couplings of the Z-boson to quarks and electron are indicated. It turns out that only the couplings between vector(V-) and axial-vector(A-)terms contribute to the effective PV interaction described in the present section. The indicated neutral-current couplings can be read off directly from (C.28)-(C.32) in Appendix C – hence the notion (V–A)-theory.

## 2.2. The Parity-Violating Atomic Hamiltonian

Since we are interested in the P-violating interactions induced by the neutral currents, we present the transformation properties of the terms in (2.21) under a P reflection. A detailed discussion of these transformation properties can for example be found in [94]. We use the abbreviation  $P$  for the unitary operator  $U(P)$  acting on the field operators of a Dirac field  $\psi(x)$ . We obtain the transformation property

$$U^\dagger(P)\psi(\mathbf{x},t)U(P) = P\psi(\mathbf{x},t)P = \eta\gamma^0\psi(-\mathbf{x},t) \quad (2.22)$$

where  $\eta$  is a phase factor which drops out when P transformations of Dirac field bilinears are considered. With (2.22) we easily obtain

$$P\bar{\psi}(\mathbf{x},t)P = \eta^*\bar{\psi}(-\mathbf{x},t)\gamma^0, \quad (2.23)$$

$$P\bar{\psi}(\mathbf{x},t)\psi(\mathbf{x},t)P = \bar{\psi}(-\mathbf{x},t)\psi(-\mathbf{x},t), \quad (2.24)$$

$$P\bar{\psi}(\mathbf{x},t)\gamma^\mu\psi(\mathbf{x},t)P = \begin{cases} \bar{\psi}(-\mathbf{x},t)\gamma^\mu\psi(-\mathbf{x},t), & \mu = 0 \\ -\bar{\psi}(-\mathbf{x},t)\gamma^\mu\psi(-\mathbf{x},t), & \mu = 1, 2, 3 \end{cases}, \quad (2.25)$$

$$Pi\bar{\psi}(\mathbf{x},t)\gamma_5\psi(\mathbf{x},t)P = -i\bar{\psi}(-\mathbf{x},t)\gamma_5\psi(-\mathbf{x},t), \quad (2.26)$$

$$P\bar{\psi}(\mathbf{x},t)\gamma^\mu\gamma_5\psi(\mathbf{x},t)P = \begin{cases} -\bar{\psi}(-\mathbf{x},t)\gamma^\mu\gamma_5\psi(-\mathbf{x},t), & \mu = 0 \\ \bar{\psi}(-\mathbf{x},t)\gamma^\mu\gamma_5\psi(-\mathbf{x},t), & \mu = 1, 2, 3 \end{cases}. \quad (2.27)$$

Thus, the products of, for instance, two vector-currents  $(\bar{\psi}_1\gamma^\mu\psi_1)(\bar{\psi}_2\gamma_\mu\psi_2)$  or two axial-vector currents  $(\bar{\psi}_1\gamma^\mu\gamma_5\psi_1)(\bar{\psi}_2\gamma_\mu\gamma_5\psi_2)$ , respectively, are P-invariant. But the product  $(\bar{\psi}_1\gamma^\mu\psi_1)(\bar{\psi}_2\gamma_\mu\gamma_5\psi_2)$  of a vector current (V) with an axial-vector current (A) changes sign under P transformation. Therefore, the PV part  $\mathcal{L}_{\text{int,eff}}^{Z,\text{PV}}$  of  $\mathcal{L}_{\text{int,eff}}^Z$  incorporates only the (V-A)-couplings. Since  $\mathcal{L}_{\text{int,eff}}^{Z,\text{PV}}$  does not include any derivative-couplings, the corresponding Hamiltonian reads

$$\begin{aligned} H_{\text{PV}} &= - \int d^3x \mathcal{L}_{\text{int,eff}}^{Z,\text{PV}} = H_{\text{PV}}^{(1)} + H_{\text{PV}}^{(2)} \\ &= -\frac{G}{\sqrt{2}} \int d^3x 2g_A^e \bar{\mathbf{e}}\gamma^\lambda\gamma_5\mathbf{e} \left( \sum_{q=u,d,s} g_V^q \bar{\mathbf{q}}\gamma_\lambda\mathbf{q} \right) \\ &\quad - \frac{G}{\sqrt{2}} \int d^3x 2g_V^e \bar{\mathbf{e}}\gamma^\lambda\mathbf{e} \left( \sum_{q=u,d,s} g_A^q \bar{\mathbf{q}}\gamma_\lambda\gamma_5\mathbf{q} \right). \end{aligned} \quad (2.28)$$

The couplings  $g_{V/A}^\psi$  are given in Table 2.

$\psi$	$g_V^\psi$	$g_A^\psi$
$\mathbf{e}$	$-\frac{1}{2} + 2\sin^2\theta_W$	$-\frac{1}{2}$
$\mathbf{u}$	$\frac{1}{2} - \frac{4}{3}\sin^2\theta_W$	$\frac{1}{2}$
$\mathbf{d}, \mathbf{s}$	$-\frac{1}{2} + \frac{2}{3}\sin^2\theta_W$	$-\frac{1}{2}$

**Table 2:** The weak neutral current couplings  $g_{V/A}^\psi$  in  $H_{\text{PV}}$ , see (2.28).

## Chapter 2. Foundations, Motivations, and Historical Overview

---

As we will see in the following,  $H_{\text{PV}}^{(1)}$  is the nuclear-spin independent part of  $H_{\text{PV}}$  for atoms while  $H_{\text{PV}}^{(2)}$  depends on the nuclear spin. In principle, the P-conserving part of the Hamiltonian deduced from  $\mathcal{L}_{\text{int,eff}}^Z$  can lead to small energy shifts. But due to uncertainties in the dominating part of an atomic Hamiltonian, namely the part connected to photon exchange, these shifts are very hard to detect [95].

### Non-Relativistic Reduction of the P-Violating Hamiltonian

For now, we have calculated the atomic PV Hamiltonian of electron-quark interaction via Z-boson exchange in the low-energy limit of (relativistic) QFD. The next step is a non-relativistic (NR) reduction of  $H_{\text{PV}}$  to obtain more feasible expressions for the calculation of the hydrogen Hamiltonian. In contrast to heavy atoms the NR reduction for light atoms like hydrogen is a good approximation, see [7]. Here, the crucial quantity for a NR approximation is the ratio between the typical momentum transfer  $|\mathbf{p}_{\text{PV}}|$  for the electroweak interaction in hydrogen and the electron mass  $m_e$  which is of the order  $\frac{|\mathbf{p}_{\text{PV}}|}{m_e} \approx \frac{1/r_B}{m_e} = \frac{\alpha m_e}{m_e} \approx 1/137 \ll 1$ , with Bohr radius  $r_B$  and fine structure constant  $\alpha$ , see [96]. This leads to a valid NR reduction by demanding

$$|\mathbf{p}_{\text{PV}}| \ll m_e \Rightarrow p_{\text{PV},0} = \sqrt{m_e^2 + \mathbf{p}_{\text{PV}}^2} \approx m_e + \frac{\mathbf{p}_{\text{PV}}^2}{2m_e} \approx 511 \text{ keV} + 0.01 \text{ keV} \approx m_e . \quad (2.29)$$

Normalised states  $|Z, N, I, I_3\rangle$  of the nucleus can be represented by the quantum numbers of atomic number  $Z$ , number of neutrons  $N$ , nuclear spin  $I$ , and its third component  $I_3$ , with  $\langle Z, N, I, I'_3 | Z, N, I, I_3 \rangle = \delta_{I'_3 I_3}$ . Regarding a single atomic species, we employ the abbreviation  $|I, I_3\rangle$  for  $|Z, N, I, I_3\rangle$ .

The general one-electron states according to the Dirac theory are

$$|\psi_e\rangle = \int \frac{d^3p}{(2\pi)^3 \sqrt{2p_0}} \sum_{s=\pm\frac{1}{2}} \tilde{\psi}_s(\mathbf{p}) \mathbf{a}_s^\dagger(\mathbf{p}) |0\rangle . \quad (2.30)$$

The lepton operator of the electron can in general be written as

$$\mathbf{e}(x) = \sum_s \int \frac{d^3k}{(2\pi)^3 2k_0} \left[ \mathbf{b}_s^\dagger(\mathbf{k}) v_s(k) e^{ikx} + \mathbf{a}_s(\mathbf{k}) u_s(k) e^{-ikx} \right] . \quad (2.31)$$

The NR reduction can be performed by approximating the involved Dirac spinors employing (2.29). The general expressions for Dirac spinors are

$$u_s(p) = \sqrt{p^0 + m} \begin{pmatrix} \chi_s \\ \frac{\boldsymbol{\sigma} \cdot \mathbf{p}}{p^0 + m} \chi_s \end{pmatrix} \quad (2.32)$$

and  $\bar{u}_{s'}(p') = u_{s'}^\dagger(p') \gamma^0$ , with  $\chi_{\frac{1}{2}} = \begin{pmatrix} 1 \\ 0 \end{pmatrix}$  and  $\chi_{-\frac{1}{2}} = \begin{pmatrix} 0 \\ 1 \end{pmatrix}$ . That way, we derive the matrix elements  $\langle \psi'_{e'}, I, I'_3 | H_{\text{PV}} | \psi_e, I, I_3 \rangle$  explicitly in Appendix C.

## 2.2. The Parity-Violating Atomic Hamiltonian

---

Our final expression for  $H_{\text{PV}}^{(1)}$  in the non-relativistic reduction, acting on states  $|\psi_e, I, I_3\rangle$  in the combined electron-nucleus Hilbert space, reads

$$H_{\text{PV}}^{(1)} = \frac{G}{4\sqrt{2}m_e} Q_W^{(1)} \left( \delta^3(\mathbf{x}) \boldsymbol{\sigma} \cdot \vec{\mathbf{p}} + \boldsymbol{\sigma} \cdot \overleftarrow{\mathbf{p}} \delta^3(\mathbf{x}) \right) \quad (2.33)$$

for  $I'_3 = I_3$ . The nuclear-spin independent weak charge is defined as

$$Q_W^{(1)}(Z, N) = -4g_A^e \left[ (2g_V^u + g_V^d) Z + (g_V^u + 2g_V^d) N \right]. \quad (2.34)$$

and find with Table 2

$$Q_W^{(1)} = (1 - 4 \sin^2 \theta_W) Z - N. \quad (2.35)$$

The Pauli-matrix vector and the electron momentum operator are denoted as  $\boldsymbol{\sigma}$  and  $\mathbf{p}$ , respectively. We formally write  $\vec{\mathbf{p}}$  and  $\overleftarrow{\mathbf{p}}$  acting as derivative operators to the right and to the left, respectively, cf. Appendix C for details. In view of its role as a fundamental quantity of electroweak interaction in atoms, the weak charge of an atomic nucleus was introduced by M.-A. Bouchiat and C. Bouchiat [44] in analogy to the electric charge of the nucleus. The expression (2.35) is valid only at tree level, but corrections due to higher-order electroweak effects do not exceed the 1% level, see [8].

The nuclear-spin dependent part of  $H_{\text{PV}}$  is

$$H_{\text{PV}}^{(2)} = \frac{G}{4\sqrt{2}m_e} Q_W^{(2)} \left( \delta^3(\mathbf{x}) (\boldsymbol{\sigma} \cdot \mathbf{I})(\boldsymbol{\sigma} \cdot \vec{\mathbf{p}}) + (\boldsymbol{\sigma} \cdot \overleftarrow{\mathbf{p}})(\boldsymbol{\sigma} \cdot \mathbf{I}) \delta^3(\mathbf{x}) \right). \quad (2.36)$$

Here,

$$\begin{aligned} Q_W^{(2)}(Z, N) &= 4g_V^e \sum_{q=u,d,s} g_A^q G_A^{(q)}(Z, N) \\ &= -\frac{1}{I} (1 - 4 \sin^2 \theta_W) [\Delta u + \Delta \bar{u} - (\Delta d + \Delta \bar{d}) - (\Delta s + \Delta \bar{s})], \end{aligned} \quad (2.37)$$

where  $\Delta q + \Delta \bar{q} = I G_A^{(q)}(Z, N)$  are the total polarisations of the nucleus carried by the quark species  $q$ , and  $G_A^{(q)}(Z, N)$  are the directly related axial form factors of the nucleus for the quark species  $q$ .

As discussed in [52] using the quark parton model, that part of the proton spin carried by the quarks  $q$  and  $\bar{q}$  is

$$\frac{1}{2}(\Delta q + \Delta \bar{q}) = \frac{1}{2} \int_0^1 [q^+(x) - \bar{q}^-(x) + \bar{q}^+(x) - q^-(x)] dx. \quad (2.38)$$

Here,  $q^{+(-)}(x)$  are the distribution functions of the quark  $q$  carrying the fraction  $x$  of the total momentum of the proton. The superscripts  $+$  ( $-$ ) refer to the parton having the same (opposite) helicity as the proton. For the experimental values of  $\Delta q + \Delta \bar{q}$  we refer to Table A.1 of Appendix A.1. The value for  $\Delta s + \Delta \bar{s}$  is not very well known at present. We employ the interval  $-0.12 \leq \Delta s + \Delta \bar{s} \leq 0$ , leading to  $-0.1259 \leq Q_W^{(2)} \leq -0.1151$ . The combined error from the other constituents of  $Q_W^{(2)}$  remains below the 2% level. That is, a measurement of  $Q_W^{(2)}$  below the 7% level would already provide a substantial contribution towards a more precise determination of  $\Delta s + \Delta \bar{s}$ , and, hence, towards the understanding of the proton spin.

### 2.3 Present Status of the Electroweak Mixing Angle

As we will discuss in Chapter 3 the physical quantities for the investigation of P violation as proposed in this thesis are proportional to the weak charges  $Q_W^{(i)}$  ( $i = 1, 2$ ), see (2.35) and (2.37), which both include  $\sin^2 \theta_W$ . The electroweak mixing angle can be regarded as one of the fundamental parameters of the Standard Model, cf. (C.20)-(C.23) in Appendix C. Given the SM-prediction of  $\sin^2 \theta_W$ , its high-precision experimental extraction in the low-energy regime provides valuable information about the electroweak interaction at very low energies. As one result of the present thesis we will find the possibility to determine  $\sin^2 \theta_W$  at the 0.05% level using hydrogen since the theoretical calculations can be employed with an according accuracy. In the case of heavier atoms which promise larger PV effects such an accuracy, which is limited by the precision of atomic structure calculations, cannot be taken for granted. A 0.05%-determination of  $\sin^2 \theta_W$  at low momentum transfer would render the uncertainties from experiment and theory comparable. In this section we give the current status of experiments measuring  $\sin^2 \theta_W$ .

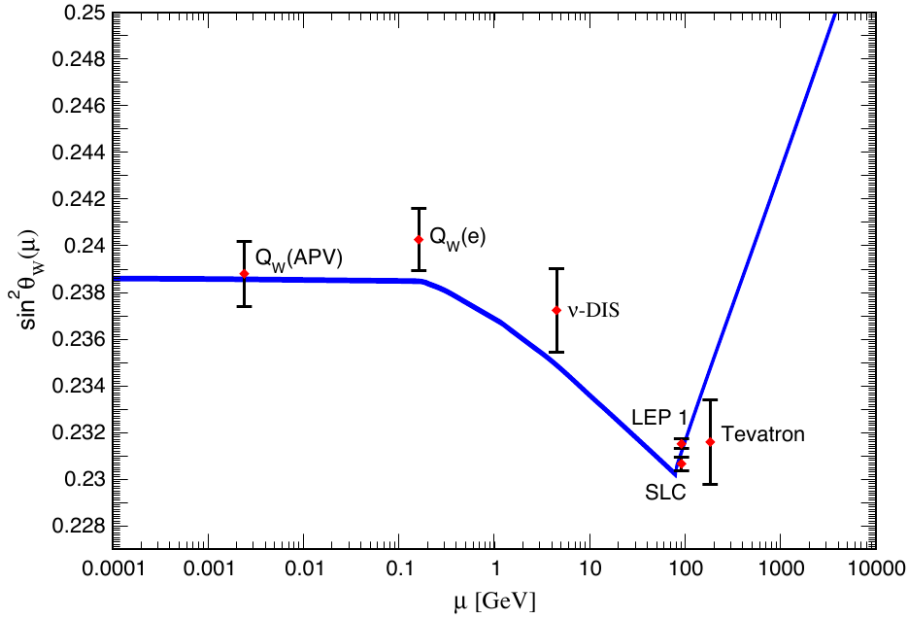


**Figure 2.4:** The dependence of the electroweak mixing angle  $\sin^2 \theta_W$  in the  $\overline{\text{MS}}$  scheme depending on the renormalisation scale parameter  $\mu = \sqrt{|q^2|}$  with  $q^2$  being the four-momentum transfer squared. The minimum of the curve is located at  $\mu = m_W$ . Each kink of the curve is a result of matching the effective field theories which arise by integrating out the SM particles with lower and lower masses. Theory uncertainties of the curve are given by the width of the curve. The Tevatron result is regarded as additional Z pole data at  $\mu = m_Z = 91.1876(21)$  GeV [12], but shifted to the right for presentational purposes. A more precise access to the low-energy parameter region can in principle be provided by PV experiments with hydrogen. The figure is taken from [97], based on [43].

### 2.3. Present Status of the Electroweak Mixing Angle

So far, not exceedingly many experiments regarding the measurement of  $\sin^2 \theta_W$  – in particular at low energies – have been performed. The most accurate values of  $\sin^2 \theta_W$  were obtained at the Z factories LEP 1 and SLC at the Z scale; for a summary see [12,97] and references therein. This value is used to fix the  $\beta$ -function  $\beta(\mu) = \partial \sin^2 \theta_W / \partial \ln \mu$  for the running of  $\sin^2 \theta_W$  in the modified minimal subtraction ( $\overline{\text{MS}}$ ) renormalisation scheme, see for example [94]. Recent overviews for the running of  $\sin^2 \theta_W$  are given by the particle data group [12,97]. We show the corresponding graph in Figure 2.4 which is based on the most recent analysis of the theoretical low-energy limit of  $\sin^2 \theta_W$  in [43], which is found to be

$$\sin^2 \theta_W(\mu \rightarrow 0) = 0.23867(16) . \quad (2.39)$$

This value, saturating at low momentum transfers, is used in the discussion of PV in atoms. The numerical value (2.39) results in a high sensitivity of the weak charges  $Q_W^{(i)}$  on  $\sin^2 \theta_W$  in the case of hydrogen because, for the proton, both are proportional to  $(1 - 4 \sin^2 \theta_W)$ . In fact, an accuracy of e.g.  $\Delta Q_W^{(1)} / Q_W^{(1)} = 4\%$  corresponds to a relative error of  $\Delta \sin^2 \theta_W / \sin^2 \theta_W = 0.3\%$ .

#### Collider Experiments

In Figure 2.4 six data points regarding the measurement of  $\sin^2 \theta_W$  are shown. The Tevatron result [98,99] is, on the one hand, based on the investigation of the reaction  $p\bar{p} \rightarrow e^+e^-$ , mediated primarily by Z-bosons at momentum transfers of the order of the Z-boson mass  $m_Z$ . There, the forward-backward asymmetry  $A_{\text{FB}}$  of  $e^+e^-$  is related to  $\sin^2 \theta_W$ . On the other hand,  $\sin^2 \theta_W$  is extracted by determination of the W-boson mass<sup>4</sup>  $m_W$  from the decay  $W \rightarrow e^{-(+)} + \nu$ . At the SLC the electroweak mixing angle is extracted from the measurement of the left-right cross-section asymmetry  $A_{\text{LR}}$  for Z production via  $e^+e^-$  collisions, see [41]. The data point labelled LEP 1 combines the results of various lepton asymmetry measurements sensitive to  $\sin^2 \theta_W$ , see [42]. Another possibility of measuring  $\sin^2 \theta_W$  is neutrino deep inelastic scattering ( $\nu$ -DIS) off nucleons. There, the cross-sections of reactions like  $\nu_\mu N \rightarrow \nu_\mu X$  and  $\nu_\mu N \rightarrow \mu^- X$  are linked to  $\sin^2 \theta_W$ . For a review on precision measurements with neutrino beams, including  $\nu$ -DIS, see for example [100]. The data point labelled  $\nu$ -DIS in Figure 2.4 is a combined value of several  $\nu$ -DIS experiments including the NuTeV measurement [101]. In the SLAC E158 experiment [102], labelled  $Q_W(e)$ , longitudinally polarised electrons at  $\mu = 0.16 \text{ GeV}$  are scattered off (unpolarised) valence electrons of a fixed hydrogen target. The electroweak mixing angle is involved in the measured asymmetry  $A_{\text{LR}} = (\sigma_{\text{R}} - \sigma_{\text{L}}) / (\sigma_{\text{R}} + \sigma_{\text{L}})$  of the cross-sections  $\sigma_{\text{L}}$  and  $\sigma_{\text{R}}$ , related to left- and right-handed beam electrons, respectively.

The proton's weak charge  $Q_W^{(1)}(1, 0) = 1 - 4 \sin^2 \theta_W$  is proposed to be measured with 4% accuracy at Jefferson Lab for  $\mu^2 = 0.026 \text{ GeV}^2$ , see [103]. There, the relevant observable is a PV asymmetry  $A_{\text{LR}}$  for elastically scattered electrons off protons,

<sup>4</sup> $m_W = m_Z \cos^2 \theta_W$ , see Equation (C.23) in Appendix C.

with leading term proportional to  $Q_W^{(1)}(1,0)\mu^2$ . The asymmetry arises from different scattering rates depending to the electron beam helicities.

### APV Experiments

Besides the collider experiments there have been performed APV experiments measuring the weak charges (2.35) at low momentum transfers. The typical momentum transfer for the electron in hydrogen can be estimated from the inverse Bohr radius corresponding to  $\alpha m_e \approx 4 \text{ keV}$ . To date, no APV experiments with hydrogen or other light atoms can be regarded satisfying. Nevertheless, we will discuss the hitherto existing proposals for measuring APV in hydrogen in Section 2.5. The most precise APV experiments are those with caesium, see [47] and [104]. The experimental uncertainty of  $\sin^2 \theta_W$  reported in [47] is at the 0.5%-level, noted as  $Q_W(\text{APV})$  in Figure 2.4. Together with a more detailed presentation of the caesium experiments we will discuss the principal advantages and disadvantages of measuring PV in heavy atoms in Section 2.4.

## 2.4 Parity Violation in Heavy Atoms

In this thesis we primarily deal with P violation in hydrogen. But much effort has been put forward in the field of P violation in heavy atoms during the past decades. Hence, many fundamental considerations have been pursued in that direction some of which can also be adopted to hydrogen. We therefore give a brief discussion about the main investigations concerning P violation in heavy atoms. We also point out the disadvantages of APV investigations of heavy atoms, in particular in view of APV in light atomic species.

### The Left-Right-Asymmetry

In general, weak amplitudes  $A_W$  interfere with the electromagnetic amplitude  $A_{\text{em}}$  of a transition in a usual APV experiment yielding a left-right asymmetry  $A_{\text{LR}}$  for the transition probabilities  $\sigma_{\text{L/R}}$  which are of the form

$$\sigma_{\text{L/R}} = |A_{\text{em}} \pm A_W|^2 = |A_{\text{em}}|^2 + |A_W|^2 \pm 2 \text{Re}\{A_{\text{em}}A_W^*\} . \quad (2.40)$$

We note that a vanishing electromagnetic amplitude would imply  $\sigma_{\text{L}} = \sigma_{\text{R}}$ , i.e., no P violation could be detected directly. At first glance, this may be puzzling because electromagnetically (parity-)forbidden transitions with  $A_{\text{em}} = 0$  become allowed through  $A_W \neq 0$ . Though, detecting a signal for such a transition first of all is a sign for a nonvanishing amplitude due to the weak interaction. If or if not the symmetry of space reflection is broken in that transition, based on  $A_W$ , cannot be determined directly in that case since the whole experimental setup is invariant under P-transformation. Nevertheless, parameters of the electroweak interaction, including parameters which are important for the understanding of parity violation like  $\sin^2 \theta_W$ , can in principle be determined.

For  $|A_{\text{em}}| \gg |A_{\text{W}}|$  one finds

$$A_{\text{LR}} = \frac{\sigma_{\text{L}} - \sigma_{\text{R}}}{\sigma_{\text{L}} + \sigma_{\text{R}}} = \frac{2 \operatorname{Re}\{A_{\text{em}}A_{\text{W}}^*\}}{|A_{\text{em}}|^2 + |A_{\text{W}}|^2} \approx \frac{2 \operatorname{Re}\{A_{\text{em}}A_{\text{W}}^*\}}{|A_{\text{em}}|^2}. \quad (2.41)$$

As indicated by (2.41) small P-conserving amplitudes  $A_{\text{em}}$ , such as the  $6\text{S}_{1/2} \rightarrow 7\text{S}_{1/2}$  transition, are favoured as long as experiments can handle the background. Enlarging the ratio (2.41) by exploiting favourable physical circumstances is usually referred to as enhancement of the P-violating effect. As outlined e.g. in [84], increasing the asymmetry by decreasing  $|A_{\text{em}}|$  is favourable because of systematics competing with the asymmetry due to the weak amplitude. However, lowering  $|A_{\text{em}}|$  eventually brings the signal in competition with the background while not improving the signal-to-noise ratio  $S/N \propto A_{\text{LR}} R/\sqrt{R}$ , where, approximately,  $R = \frac{1}{2}(\sigma_{\text{L}} + \sigma_{\text{R}}) \propto |A_{\text{em}}|^2$  is the mean rate, and  $A_{\text{LR}} \propto |A_{\text{em}}|^{-1}$ .

### The $Z^3$ -law

The main advantage of investigating the effects of PV in heavy atoms is their cubic dependence on the nuclear charge, the so-called  $Z^3$ -law [44–46]. A qualitative explanation is, for instance, provided in [10]. For a probability amplitude  $A_{\text{W}}$  of a transition, mediated by a particle of mass  $M$  and being proportional to  $g^2/(M^2 + q^2)$  with coupling  $g$  and squared momentum transfer  $q^2$ , one finds in the case of comparable couplings for  $A_{\text{em}}$  and  $A_{\text{W}}$  the relation

$$A_{\text{LR}} \propto \frac{2q^2}{M^2 + q^2} \approx \frac{2q^2}{M^2} \quad (2.42)$$

while the approximate expression holds for low momentum transfers. Since the Bohr radius corresponding to an unscreened Coulomb potential of charge  $Z$ , as seen by the nucleus-penetrating electron orbitals involved in the short-range weak interaction, is of the order of  $r_{\text{B}}/Z$  we find the according momentum transfer squared  $|q|^2$  to grow like  $Z^2$ . Hence, we obtain  $A_{\text{LR}} \propto Z^2$ . The third factor of  $Z$  can be traced back to the coherent contribution of all nucleons interacting with the electron.

### Physics beyond the Standard Model

Taking into account (2.42), the masses of additional neutral gauge bosons can be constrained by measuring  $A_{\text{LR}}$ . More precisely, by observing a certain  $A_{\text{LR}}$ , a lower bound for the mass of a neutral gauge boson can be extracted from (2.42), in case it couples the involved particles of the observed process in a way comparable to the Z-boson. Actually, the lower bound for the mass of such a  $Z'$  boson is reported to be  $1.3 \text{ TeV}/c^2$  at 84% confidence level, improving the limit from investigations at Tevatron, see [105]. In return, given a mass range of  $Z'$ , there is also the possibility to constrain the type of its coupling to quarks and electrons, i.e., probing vector- or axial-vector couplings of  $Z'$ .

Furthermore, (2.42) allows for the existence of a light but weakly coupled neutral gauge boson, the so-called  $U$  boson, mediating an interaction between dark matter

particles and regular matter. For example, the decay  $U \rightarrow e^+e^-$  had been suggested as an explanation of the 511 keV  $\gamma$ -line observed from the galactic bulge [106]. The according investigation in the realm of APV is, e.g., pursued in [107, 108].

In general, APV can reveal or constrain alternatives to the weak neutral-current sector of the SM at low energies. That way, APV may in the end also be valuable in the search for a theory unifying all fundamental interactions.

### The Caesium Experiments

Highly forbidden transitions are in principle appropriate for the investigation of P-violating effects in heavy atoms. For instance, the  $7S_{1/2} \rightarrow 6S_{1/2}$  transition of caesium ( $Z = 55$ ) is forbidden by electromagnetic parity selection rule, the so-called Laporte rule. This rule is broken by the weak interaction, where the S states get a small admixture of P states leading to eigenstates  $6\hat{S}$  and  $7\hat{S}$  of non-definite parity. Thereby, a small P-violating electric dipole amplitude  $\langle 6\hat{S} | \mathbf{D} | 7\hat{S} \rangle$  of the electric dipole operator  $\mathbf{D}$  is introduced. We point out that a left-right asymmetry, based on (2.40), can neither be observed in the case of a pure P-conserving nor in the case of a pure P-violating amplitude. Usually, the P-conserving amplitude  $A_{\text{em}}$  considered in APV experiments is a magnetic dipole amplitude or an additional (Stark) transition amplitude introduced via a small external electric field. In either case the interference between the P-conserving and the P-violating amplitude gives rise to a left-right asymmetry according to (2.41). As reported in [85] and [8], an asymmetry of the order of  $10^{-5}$  for the  $6S_{1/2} \rightarrow 7S_{1/2}$  transition rates can be expected for caesium.

One main disadvantage of heavy atoms regarding PV experiments which aim for the weak charges is the need for an accurate calculation of the involved electron orbitals to connect the measurements with theoretical predictions. Therefore, a prudent choice are alkali atoms like caesium due to their comparably simple electronic structure of just one valence electron. The impact of large atomic numbers  $Z$  has already been mentioned above.

The most accurate determination of the weak charge in the realm of atomic physics experiments has been achieved with caesium. To illustrate the basic considerations involved in APV experiments of heavy atoms, we focus on an approach which utilises a parity-forbidden transition, where interference of a Stark induced electric dipole (E1) amplitude with an electroweak amplitude breaks the parity selection rule.

Figure 2.5 shows the schematic experimental setup of the Paris experiment at ENS [109]. There, the Cs atoms are, within a constant electric (Stark) field  $\mathbf{E}$ , excited to the  $7S_{1/2}$  state via counter-propagating light beams with circular polarisations  $\pm\xi$  and wave vectors  $\pm\mathbf{k}$ . The circular polarisation  $\xi_f$  of fluorescence light from the allowed  $7S_{1/2} \rightarrow 6P_{1/2}$  transition, emitted in direction  $\mathbf{k}_f$ , was measured. This circular polarisation is related to the electronic polarisation  $\mathbf{P} = \langle \boldsymbol{\sigma} \rangle = \mathbf{P}_{\parallel} + \mathbf{P}_{\perp} \propto -\xi\beta\mathbf{k} - \frac{\xi\text{Im}E1^{\text{PV}}}{|\mathbf{E}|^2}\mathbf{k} \times \mathbf{E}$  of the caesium atoms prior to their decay. Unlike  $\mathbf{P}_{\parallel}$ , which is the polarisation component parallel to the light beam, the additional component  $\mathbf{P}_{\perp} \propto \xi\mathbf{k} \times \mathbf{E}$ , predicted due to the electroweak interaction, does not transform like an axial vector under P transformation.

## 2.4. Parity Violation in Heavy Atoms

The PV contribution can be revealed due to the chiral arrangement of the vectors and axial vectors as depicted in Figure 2.5(b). The electronic polarisation results in a non-vanishing photon polarisation  $\xi_f$ , and the according left-right asymmetry can be written as the ratio  $|\mathbf{P}_\perp|/|\mathbf{P}_\parallel|$ . It is reported as

$$A_{\text{LR}} = \frac{|A_{\text{W}}|}{|A_{\text{em}}|} = \frac{|\mathbf{P}_\perp|}{|\mathbf{P}_\parallel|} = \frac{\text{Im} \mathbf{E} \mathbf{1}^{\text{PV}}}{\beta |\mathbf{E}|} = (-1.56 \pm 0.17(\text{stat.}) \pm 0.12(\text{syst.})) \times 10^{-5}, \quad (2.43)$$

obtained with typical electric fields  $|\mathbf{E}| = 100 \text{ V/cm}$ , where  $\beta$  is the vector transition polarisability, see [110]. Taking into account the reported accuracy, the value (2.43) agrees with the theoretical prediction of  $(-1.61 \pm 0.07(\text{stat.}) \pm 0.20(\text{syst.})) \times 10^{-5}$ . Thus, already in 1983, one validation of the Glashow-Weinberg-Salam model at low energies using an atomic physics experiment at low energies was successful. As a result of a refined version of this experiment [104] the updated value for the left-right asymmetry is  $A_{\text{LR}} = (-1.538 \pm 0.040) \times 10^{-5}$ .

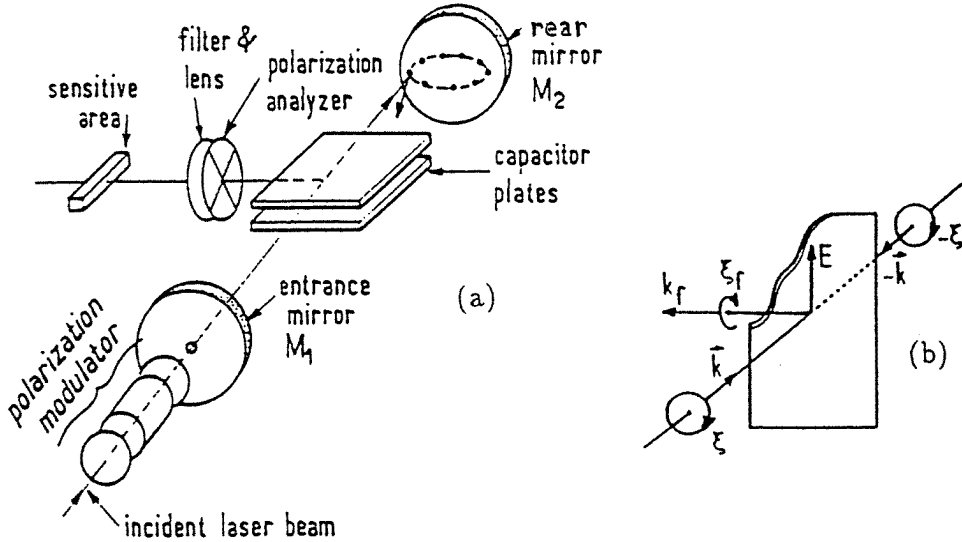


**Figure 2.5:** (a) The schematic setup of the Paris experiment [109] and (b) the involved configuration of vectors  $\mathbf{E}$ ,  $\mathbf{k}$  and axial vectors, here represented by the photon helicities  $\xi$ , in the interaction region between the capacitor plates. A non-vanishing circular polarisation  $\xi_f$  of the fluorescence light breaks the mirror symmetry of the chiral system. The picture is adopted from [8] with permission.

The at present still most precise APV experiment was conducted for caesium in the group of C. E. Wieman at Boulder, Colorado, in 1997 [47], with an experimental setup in principle similar to that depicted in Figure 2.5. Again, the signature of P violation arises from  $6S \rightarrow 7S$  transitions, more precisely from transitions between states of total angular momentum  $F = 3$  and  $F = 4$ , respectively. The applied external fields provide

## Chapter 2. Foundations, Motivations, and Historical Overview

---

several possibilities of spatial transformations leading to redundant measurements of the P-violating signal. The final result is reported as

$$\frac{\text{Im } E1^{\text{PV}}}{\beta 100 \text{ V/cm}} = \begin{cases} 1.6349(80) & 6\text{S}(F=4) \rightarrow 7\text{S}(F=3) \\ 1.5576(77) & 6\text{S}(F=3) \rightarrow 7\text{S}(F=4) \end{cases} \quad (2.44)$$

for the two indicated hyperfine transitions. The difference of 0.077(11) between both values is expected to originate mainly from the nuclear anapole moment, see Appendix C.

In order to extract from experiment a numerical value for the weak charge the quantity

$$E1^{\text{PV}} = \langle 7\hat{\text{S}}_{1/2} | \mathbf{D} | 6\hat{\text{S}}_{1/2} \rangle = \sum_n \left( \frac{\langle 7\text{S}_{1/2} | \mathbf{D} | n\text{P}_{1/2} \rangle \langle n\text{P}_{1/2} | H_{\text{PV}} | 6\text{S}_{1/2} \rangle}{E(6\text{S}_{1/2}) - E(n\text{P}_{1/2})} + \frac{\langle 7\text{S}_{1/2} | H_{\text{PV}} | n\text{P}_{1/2} \rangle \langle n\text{P}_{1/2} | \mathbf{D} | 6\text{S}_{1/2} \rangle}{E(7\text{S}_{1/2}) - E(n\text{P}_{1/2})} \right) \quad (2.45)$$

has to be calculated [111]. Here,  $|n\text{S}_J\rangle$  and  $|n\text{P}_J\rangle$  denote the states of principal quantum number  $n$ , total angular momentum  $J$ , and orbital angular momenta  $L=0$  and  $L=1$ , respectively, in absence of P-violating contributions. As well as the electric dipole operator  $\mathbf{D}$ , the P-violating Hamiltonian  $H_{\text{PV}}$  mixes S and P states. The states resulting from that PV admixture are denoted as  $|n\hat{L}_J\rangle$ . Since  $H_{\text{PV}}$  is proportional to the weak charge, a measurement of  $E1^{\text{PV}}$  and a calculation of the sum in (2.45) gives access to  $Q_W$ . That way, the nuclear-spin independent weak charge of Cs is extracted and found to be  $Q_W = -72.06(28)_{\text{exp}} (34)_{\text{theo}}$ , from an updated version of the experiment [111]. While deviating from the SM prediction by  $2.5\sigma$ , a reconsideration of the involved atomic theory calculations brought experiment and prediction to agreement, see [105] and references therein. As a result, the combined value of theory and experiment is reported as  $Q_W = -73.16(29)_{\text{exp}} (20)_{\text{theo}}$ .

Presently, the only high-precision experimental knowledge regarding the nuclear-spin dependent contribution to the weak charge is deduced from the Boulder experiment [47]. The ratio  $r$  of the two measured  $E1^{\text{PV}}$  amplitudes from (2.44) gives  $r_{hf}^{\text{exp}} = r - 1 = (4.8 \pm 0.7) \times 10^{-2}$ , where a non-vanishing value of  $r_{hf}^{\text{exp}}$  indicates a nuclear-spin dependent PV effect. But the obtained  $r_{hf}^{\text{exp}}$  is not in accordance with the theoretical prediction  $r_{hf}^{\text{theo}} = (1.6 \pm 0.3) \times 10^{-2}$ , see [90,91]. For now, this discrepancy does not allow for a concluding interpretation. Although it is expected that this nuclear-spin dependent PV effect can be traced back to the nuclear-spin dependent weak charge within the framework of the Standard Model, experimental and theoretical re-evaluations, respectively, may eventually suggest otherwise.

### Other Heavy Atoms, Isotopes, and Ions

The largest left-right asymmetry in APV experiments so far was detected for a forbidden transition in ytterbium ( $Z=70$ ) [112]. In agreement with theory, the asymmetry is reported to be of the order of  $10^{-4}$ , but its accuracy of 16% is not yet sufficient to discuss

## 2.4. Parity Violation in Heavy Atoms

---

impacts on nuclear-spin dependent effects. However, improvements of the experimental setup are claimed to be underway which could yield a determination of isotope effects as well as the detection of the respective anapole moments. Via measurements of different isotopes the uncertainties of the electronic structure are expected to cancel.

A promising possibility for detecting P violation was found in the  $6P_{1/2} \rightarrow 6P_{3/2}$  magnetic dipole (M1) transition in thallium ( $Z = 81$ ), see [113, 114], where a small E1 amplitude due to the weak interaction is mixed into the M1 transition. Bismuth ( $Z = 83$ ) [115] and lead ( $Z = 82$ ) [116] were also studied. The theoretical uncertainties in the case of thallium are at the 3%-level [117] while the uncertainties for lead and bismuth are even larger due to their more complicated electronic structures.

A further intriguing approach is the investigation of isotopes. There, uncertainties of nuclear and electronic structure calculations can cancel when considering ratios of the weak charges for different isotopes. For instance, it is argued in [118] that in the case of samarium the only remaining uncertainty for  $[Q_W^{(2)}(^{154}\text{Sm}) - Q_W^{(2)}(^{144}\text{Sm})]/Q_W^{(2)}(^{144}\text{Sm}) = (2 + 24.8 \sin^2 \theta_W)^{-1}$  is due to different nuclear radii of the isotopes. However, theoretical as well as experimental difficulties in the realm of PV experiments with isotopes still persist, see for instance [119, 120], not yet allowing for accuracies competitive with those of the Cs experiments.

Another route of investigation is offered by ions, e.g.,  $\text{Ba}^+$  [121],  $\text{Ra}^+$  [122], or  $\text{Yb}^+$  [123], combining a wealth of stable isotopes with a comparably simple electronic structure and small energy splittings of the parity-mixed states. Just as in the case of neutral atoms appropriate transitions in appropriate environments are examined to deduce PV data. However, the reported accuracies of theoretical calculations regarding PV amplitudes range from 3% for  $\text{Ba}^+$  and  $\text{Ra}^+$  up to 50% for  $\text{Yb}^+$ , see for instance [124].

There are also efforts to measure APV at GSI, Darmstadt [125–129]. For example, a circularly polarised laser can induce a PV E1-transition between the  $^1S_0$  state and the  $^3S_1$  state of helium-like ions which are injected in storage rings [129]. The interference with the M1 amplitude accounts for an asymmetry in the transition cross section when using left- and right-polarised light, respectively.

Ions can offer even larger enhancement effects than the  $Z^3$ -law for neutral atoms. As pointed out in [7], the PV Hamiltonian of hydrogen-like ions scales with  $Z^5$ . This is, however, a statement about the generic magnitude of the PV effect. Other important ingredients like energy separation or applicability of external fields in realistic experiments may effectively diminish those enhancements. This has always to be taken into account when proposing concrete experimental realisations for measuring PV effects. For instance, decreased denominators in the sum of (2.45) generically increase the PV effect, but only as long as the nominators do not decrease to the same extent. The summands may also cancel, at least partially.

### Disadvantages of Heavy Atoms

The determination of the nuclear-spin dependent weak charge using PV experiments with heavy atoms is difficult since the P-violating effects grow only with  $Z^2$ , see [85]. The reason is that  $Q_W^{(1)}$  is of the order of  $N$  which is of the order of  $Z$ , but  $Q_W^{(2)} \propto Z^0 = 1$ , cf. (2.35) and (2.37). Furthermore, an extraction of the associated couplings  $C_p^2$  and  $C_n^2$  from experiment is in need of a nuclear physics calculation of heavy nuclei. That is a much more severe constraint on accuracy than the corresponding derivations for the proton. And even these can be regarded as unsatisfactory to date due to the difficulties in determining the total polarisations of the quarks, see Section 2.2. Nevertheless, comparing heavy and light atoms from a theoretical point of view, the investigation of the proton axial-vector coupling  $C_p^2$  is most promising regarding hydrogen PV experiments where the least nuclear physics uncertainties are anticipated.

A further drawback of heavy atoms can be the lack of knowledge concerning the number and properties of states of many-electron atoms which actually contribute to parity mixing and could possibly lead to cancellations of P-violating effects.

Already this short historical abstract hints at the enormous effort and state-of-the-art atomic-physics as well as nuclear-physics calculations necessary for a reliable test of the electroweak theory using heavy atoms. Especially, the nuclear-spin dependent effects obtained with the Boulder experiment need of cross-checking. One way to circumvent the difficulties for heavy atoms and still obtain a competitive accuracy for  $\sin^2 \theta_W$  and other electroweak parameters may be the investigation of hydrogen due to its simple electronic structure.

## 2.5 Parity Violation in Light Atoms

Despite longstanding efforts a determination of P-violating observables of hydrogen is still to come. In light of the very limited number of high-precision APV experiments and their drawbacks one should hesitate to consider the implications for the Standard Model as well established. Besides additional experiments using heavy atoms and ions, an investigation of hydrogen or other light atoms may as well be considered. Due to the theoretically well-known structure of hydrogen [130], corrections to the coulomb interaction such as the neutral-current weak amplitude for electron-quark interaction can be investigated directly, that is, without having to rely on complex atomic or nuclear physics calculations with limited accuracy.

The present thesis is mainly devoted to the investigation of hydrogen. We therefore focus on that atomic species in the following, whereas general remarks regarding other light atoms and isotopes will be given as well.

### General Properties of Parity Mixing in Hydrogen

The P-violating Hamiltonian  $H_{\text{PV}}$ , see (2.33) and (2.36), involves spatial singularities of the form  $\delta^3(\mathbf{x}) \boldsymbol{\sigma} \cdot \mathbf{p}$ , where  $\mathbf{p}$  represents a spatial derivative. Therefore, in this approximation of a point-like nucleus, only states with non-vanishing wave function or derivative at the nucleus allow for parity mixing, see, for example, [84]. In addition, the matrix elements for states with angular momentum  $J > 1/2$  vanish, as shown in [7]. As in [80] we neglect PV mixing of states with different principal quantum number. Hence, the only states of interest concerning parity mixing in  $n = 2$  hydrogen are the  $S_{1/2}$  and  $P_{1/2}$  states. Regarding the P-odd  $H_{\text{PV}}$  as perturbation of the underlying hydrogen Hamiltonian  $H_0$  of the P-even Coulomb interaction, the unperturbed states  $|2S\rangle$  and  $|2P\rangle$  with different – but definite – parity can be mixed by  $H_{\text{PV}}$ , leading to perturbed states  $|2\hat{S}\rangle$  and  $|2\hat{P}\rangle$  with non-definite parity. The matrix elements of  $H_{\text{PV}}$  with respect to the unperturbed states of the same parity are spatial integrals over a P-odd function and therefore vanish identically. Assuming non-degeneracy,  $H_{\text{PV}}$  mixes states  $|\psi\rangle$  and  $|\chi_n\rangle$  of different parity according to

$$|\psi\rangle \longrightarrow |\hat{\psi}\rangle = |\psi\rangle + \sum_n |\chi_n\rangle \frac{\langle \chi_n | H_{\text{PV}} | \psi \rangle}{E(\psi) - E(\chi_n)} \quad (2.46)$$

in first-order perturbation theory. From (2.46) the transition amplitude between two states  $|\hat{\psi}_1\rangle$  and  $|\hat{\psi}_2\rangle$  can be written as

$$\langle \hat{\psi}_2 | T_{\text{EM}} | \hat{\psi}_1 \rangle = \langle \psi_2 | T_{\text{EM}} | \psi_1 \rangle + \sum_n \left\{ \frac{\langle \psi_2 | T_{\text{EM}} | \chi_n \rangle \langle \chi_n | H_{\text{PV}} | \psi_1 \rangle}{E(\psi_1) - E(\chi_n)} + \frac{\langle \psi_2 | H_{\text{PV}} | \chi_n \rangle \langle \chi_n | T_{\text{EM}} | \psi_1 \rangle}{(E(\psi_2) - E(\chi_n))^*} \right\}, \quad (2.47)$$

with  $T_{\text{EM}}$  being the electromagnetic transition operator. Assuming for example  $|\psi_1\rangle$  and  $|\psi_2\rangle$  to have the same parity, the P-even part of  $T_{\text{EM}}$ , i.e., the magnetic dipole operator  $\boldsymbol{\mu} = -\mu_B(\mathbf{L} + g\mathbf{S})$ , leads to a non-vanishing magnetic dipole amplitude contained in the unperturbed amplitude  $\langle \psi_2 | T_{\text{EM}} | \psi_1 \rangle$ . But, since in this case  $H_{\text{PV}}$  couples  $|\psi_{1,2}\rangle$  only with states  $|\chi_n\rangle$  having a parity opposite to that of  $|\psi_{1,2}\rangle$ ,  $\boldsymbol{\mu}$  does not induce a PV amplitude. On the other hand, the P-odd part of  $T_{\text{EM}}$ , i.e., the electric dipole operator  $\mathbf{D}$ , leads to non-vanishing  $H_{\text{PV}}$ -induced electric dipole amplitudes via the sum in (2.47). This sum over intermediate states can be difficult to compute for heavy atoms, but in the case of hydrogen the sum in (2.46) reduces to

$$|2\hat{S}_{1/2}\rangle = |2S_{1/2}\rangle + |2P_{1/2}\rangle \frac{\langle 2P_{1/2} | H_{\text{PV}} | 2S_{1/2} \rangle}{E(2S_{1/2}) - E(2P_{1/2})} \quad (2.48)$$

for the 2S states, which can be calculated with high precision.

### $H_{\text{PV}}$ for Single-Electron Atoms

With (2.33)-(2.37) and employing Coulomb wave functions one finds the matrix elements

$$\langle 2S_{1/2}, F', F_3 | H_{\text{PV}}^{(1)} | 2P_{1/2}, F, F_3 \rangle = -i\delta_1(Z, N)L(Z, N) \delta_{F', F} \delta_{F_3', F_3}, \quad (2.49)$$

$$\begin{aligned} \langle 2S_{1/2}, F', F_3 | H_{\text{PV}}^{(2)} | 2P_{1/2}, F, F_3 \rangle &= -i\delta_2(Z, N)L(Z, N) [F(F+1) - I(I+1) - \frac{3}{4}] \\ &\times \delta_{F', F} \delta_{F_3', F_3}, \end{aligned} \quad (2.50)$$

with  $|I - \frac{1}{2}| \leq F, F' \leq I + \frac{1}{2}$  and

$$\langle 2S_{1/2}, F', F_3 | H_{\text{PV}}^{(1)} | 2P_{3/2}, F, F_3 \rangle = 0, \quad \langle 2S_{1/2}, F', F_3 | H_{\text{PV}}^{(2)} | 2P_{3/2}, F, F_3 \rangle = 0, \quad (2.51)$$

where  $|I - \frac{1}{2}| \leq F' \leq I + \frac{1}{2}$ ,  $|I - \frac{3}{2}| \leq F \leq I + \frac{3}{2}$ , see [80]. In (2.49) and (2.50) we define, as in (19) of [68], the PV parameters

$$\delta_i(Z, N) = -\frac{\sqrt{3}G}{64\pi\sqrt{2}m_e r_B^4(Z) L(Z, N)} Q_W^{(i)}(Z, N) \quad (2.52)$$

$$= -2.6882933(14) \cdot 10^{-17} \frac{Z^4 Q_W^{(i)}(Z, N)}{L(Z, N)} \text{ eV}, \quad (i = 1, 2). \quad (2.53)$$

Here  $r_B(Z) = (Z\alpha m_e)^{-1} = Z^{-1}r_B$  is the first Bohr radius and  $L(Z, N)$  is the Lamb shift for a hydrogen-like atom with proton number  $Z$  and neutron number  $N$ . The numerical factor in (2.53) was obtained using the values for Fermi's constant  $G$ , Bohr radius  $r_B$ , and electron mass  $m_e$  from [12]. The numerical values of  $\delta_{1,2}$  and  $Q_W^{(1,2)}$  for hydrogen are given in Table A.1 of Appendix A.1. In Section 3.2.2 we will explicitly introduce the full mass matrix of hydrogen including  $H_{\text{PV}}$ .

It is instructive to recapitulate the  $Z$ -scalings of several quantities for nuclei with general  $Z$  and  $N$  as given in [80], see Table 3. The quantities presented there differ only slightly for deuterium and tritium. The PV parameters  $\delta_i$  for these hydrogen isotopes are given by  $\delta_i(Z, N) = -6.14 \times 10^{-12} Q_W^{(i)}(1, N)$ . In the case of deuterium we have  $\delta_1 = 5.653 \times 10^{-12}$ , which is one order of magnitude larger than for hydrogen, cf. Table A.1 of Appendix A.1. The constant  $\delta_2$  largely depends on the value of  $\Delta s + \Delta \bar{s}$ . For  $-0.12 \leq \Delta s + \Delta \bar{s} \leq 0$  one obtains  $5.82 \times 10^{-14} \geq \delta_2(1, 1) \geq 0$ , cf. [131].

	$Z = 1, N = 0$	<b>Table 3:</b> Approximate scaling laws for the fine structure splitting $\Delta(Z, N) = E(2P_{3/2}) - E(2P_{1/2})$ , hyperfine splitting $\mathcal{A}(Z)$ , Lamb shift $L(Z, N) = E(2S_{1/2}) - E(2P_{1/2})$ , as well as the total decay rates $\Gamma_P$ and $\Gamma_S$ in vacuum for hydrogen-like atoms and ions.
$\Delta(Z, N) \simeq Z^4 \Delta$	$\Delta = 45.36431 \mu\text{eV}$	
$\mathcal{A}(Z) \simeq Z^3 \mathcal{A}$	$\mathcal{A} = 5.874326 \mu\text{eV}$	
$L(Z, N) \simeq Z^4 L$	$L = 4.374891 \mu\text{eV}$	
$\Gamma_P(Z, N) \simeq Z^4 \Gamma_P$	$\Gamma_P = 6.264883 \text{ s}^{-1}$	
$\Gamma_S(Z, N) \simeq Z^6 \Gamma_S$	$\Gamma_S = 8.2203 \text{ s}^{-1}$	

### Advantages of Hydrogen

We have already mentioned the high sensitivity of hydrogen experiments with respect to  $\sin^2 \theta_W$  in Section 2.3. Compared to heavy atoms hydrogen offers a cleaner access to the  $s$ -quark contribution for the proton spin, see Section 2.2. Furthermore, a fortunate circumstance in hydrogen is the small energy difference, the lamb shift, between the  $2S_{1/2}$  and  $2P_{1/2}$  states. The magnitudes of the mixing matrix elements

$$\frac{\langle 2S_{1/2} | H_{PV} | 2P_{1/2} \rangle}{E(2S_{1/2}) - E(2P_{1/2})} \quad (2.54)$$

are therefore enhanced and become comparable to the parity mixings in heavy atoms. In fact, the mixing for the  $6S \rightarrow 7S$  transition of caesium is of the order of  $0.8 \times 10^{-11} e r_B$  in atomic units, see [10]. Considering hydrogen, the product of (2.54) and  $\langle 2S_{1/2} | e z | 2P_{1/2} \rangle$  is of the order of  $\sqrt{3} \delta_{1,2} e r_B \approx 10^{-12} e r_B$ , see Tables A.1 and A.4 in Appendix A.1.

Specific  $2P_{1/2}$  states can be made to cross with specific  $2S_{1/2}$  states by applying a suitable magnetic field. This way the energy denominator in (2.54) decreases by a factor of  $|(E(2S_{1/2}) - E(2P_{1/2})) / (\hbar \Gamma_P / 2)| \approx 2\pi L / (\Gamma_P / 2) \approx 21$ , taking the Lamb shift  $L$  from Table A.2 in Appendix A.1 and the decay width  $\Gamma_P$  of the  $2P_{1/2}$  states, see Appendix A.2. Though, as pointed out in [132], proximity of levels involved in (2.54) does not necessarily lead to larger P-violating effects. One rather has to consider all ingredients of the experiment, such as electromagnetic fields, to obtain the parameters for maximal PV signals.

According to (2.35) and (2.37) the spin-independent weak charge is dominant for large  $Z$ , i.e., large  $N$ , due to the closeness of  $\sin^2 \theta_W$  to  $1/4$  while for hydrogen the spin-dependent weak charge is about a factor of three larger. These different magnitudes will, of course, also be reflected in the P-violating observables for hydrogen considered in this thesis.

In order to connect with common literature, see for instance [7, 48, 133], we state an alternative expression of the relativistic P-violating Hamiltonian  $H_{PV} = H_{PV}^{(1)} + H_{PV}^{(2)}$  with

$$H_{PV}^{(1)} = \frac{G}{\sqrt{2}} \sum_i \bar{\psi}_e \gamma_\lambda \gamma_5 \psi_e (C_{1p} \bar{\psi}_{p_i} \gamma^\lambda \psi_{p_i} + C_{1n} \bar{\psi}_{n_i} \gamma^\lambda \psi_{n_i}) , \quad (2.55)$$

$$H_{PV}^{(2)} = \frac{G}{\sqrt{2}} \sum_i \bar{\psi}_e \gamma_\lambda \psi_e (C_{2p} \bar{\psi}_{p_i} \gamma^\lambda \gamma_5 \psi_{p_i} + C_{2n} \bar{\psi}_{n_i} \gamma^\lambda \gamma_5 \psi_{n_i}) , \quad (2.56)$$

summing over all protons  $p_i$  and neutrons  $n_i$  of the nucleus. Here, all electron-nucleon couplings,  $C_{1p}$ ,  $C_{2p}$ ,  $C_{1n}$ , and  $C_{2n}$ , due to the weak neutral current are incorporated. An investigation of both hydrogen and deuterium can reveal these four fundamental parameters of the proton and the neutron, respectively. The coupling constants  $C_{1p}$  and  $C_{2p}$  are related to the weak charges of the proton as follows, see [7, 48]:

$$Q_W^{(1)}(p) = 2 C_{1p} = -4 C_u^{(1)} - 2 C_d^{(1)} , \quad (2.57)$$

$$Q_W^{(2)}(p) = -4 C_{2p} = -3.74 C_u^{(2)} + 1.44 C_d^{(2)} . \quad (2.58)$$

In heavy atoms  $C_{2p}$  is highly suppressed compared to  $C_{1p}$ . This is not the case for light atoms, and hence, from the theoretical point of view,  $C_{2p}$  can be most conveniently determined with hydrogen.

### Charting the Electroweak Sector with Help from APV

The weak charge (2.35) can be rewritten as

$$\begin{aligned} Q_W^{(1)} &= (2Z + N) Q_W(u) + (Z + 2N) Q_W(d) \\ &= (-4Z - 2N) C_u^{(1)} + (-2Z - 4N) C_d^{(1)} \end{aligned} \quad (2.59)$$

leading to an allowed region in the  $(C_u^{(1)}, C_d^{(1)})$ -plane, defined by

$$C_d^{(1)} = -\frac{Q_W^{(1)} \pm \Delta}{2Z + 4N} - \frac{4Z + 2N}{2Z + 4N} C_u^{(1)}, \quad (2.60)$$

for a given value of  $Q_W^{(1)}$  with an uncertainty  $\Delta$ . Figure 2.6 shows the possibility of complementary determination of the weak charges  $C_u$  and  $C_d$  of the u and d quarks with high-energy collider experiments at, e.g., SLAC and APV experiments, respectively. In contrast to low-energy APV experiments the nucleons at high-energy collider experiments can be disintegrated, leading to an incoherent interaction of all quarks with the electron. The regions in the  $(C_u^{(1)}, C_d^{(1)})$ -plane constraining the weak charges thus come out to be almost orthogonal while meeting at a value of  $\sin^2 \theta_W$  as predicted by the Standard Model. That way, the combined investigation of both high- and low-energy PV experiments results in a determination of  $C_u^{(1)}$  and  $C_d^{(1)}$  which none of both experimental approaches alone can provide. In the case of hydrogen, we obtain  $C_d^{(1)} \approx -0.023 \pm \Delta/2 - 2C_u^{(1)}$  from (2.60), illustrated by a red line in Figure 2.6. We also show a more in-depth illustration in Figure 2.7, cf. [11, 12, 134].

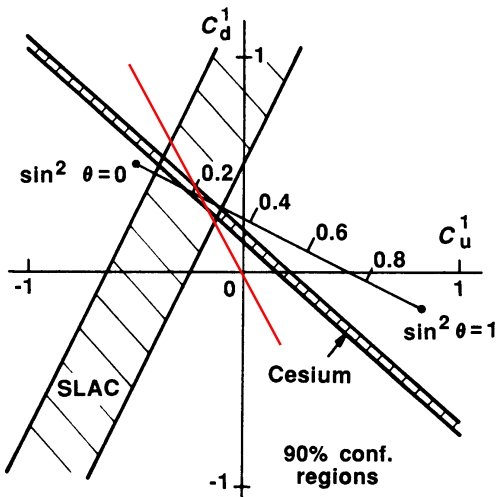


**Figure 2.6:** The 90% confident regions of the measurements of the weak charges of the u and d quarks, as found in the high-energy electron-deuteron scattering experiment at SLAC with momentum transfers of about 1GeV/c [135, 136] and the Cs experiments at Paris in 1982/83, are indicated by the striped areas. The electroweak theory predicts values for  $C_u^{(1)}$  and  $C_d^{(1)}$  as presented by the segmented line for all *a priori* possible values of  $\sin^2 \theta_W$ . The figure is adopted from [85], reprinted with permission from AAAS. The red line represents the corresponding relation of  $C_u^{(1)}$  and  $C_d^{(1)}$  for hydrogen.

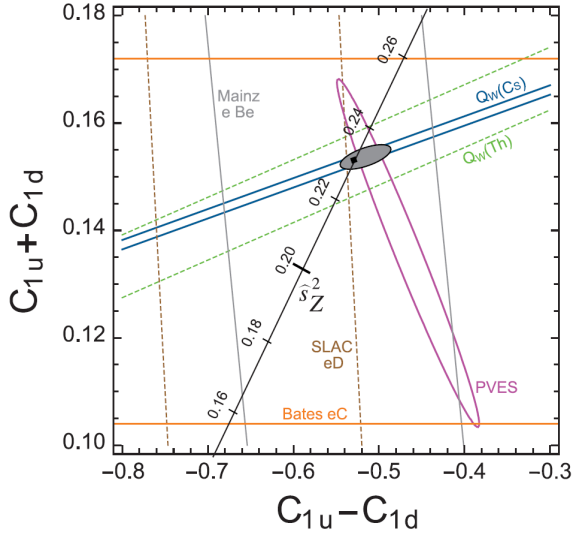


**Figure 2.7:** The constraints of one standard deviation on the couplings  $C_u^{(1)}$  and  $C_d^{(1)}$  from various experimental data. The Cs-data [47] combined with the results from parity-violating electron scattering (PVES) on nucleons, see [134] and references therein, yield a complementary determination of  $C_u^{(1)}$  and  $C_d^{(1)}$ . Further experiments are labelled  $Q_W(\text{Th})$  [113, 114], SLAC eD [136], Mainz e Be [137], and Bates eC [138]. The shaded area represents the 90% confident region by a combination of all results. The SM prediction of the electroweak mixing angle  $\hat{s}_Z^2 = 0.23116$  at the Z-boson mass is indicated. The figure is taken from [12].

### Review of Proposals for Measuring PV in Hydrogen

Actually, the first proposal for APV investigations, especially with hydrogen, was given by Zel'dovich in 1959 [19], even before the introduction of the unified gauge theory of electromagnetism and weak interactions. But the left-right-asymmetry  $A_{LR}$  of the rotation of the plane of polarisation of light due to the weak interaction was estimated to be of the order of  $10^{-20}$  for hydrogen and hence was considered to be unobservable. As one result of the present thesis, we will find P-violating effects in hydrogen with  $A_{LR}$  being ten orders of magnitude larger.

Due to  $2P_{1/2}$  containing a  $2S_{1/2}$  admixture, the emitted photon for the  $2P_{3/2} \rightarrow 2P_{1/2}$  transition of hydrogen was predicted to be circularly polarised with an order of magnitude of  $10^{-7}$ , see [20]. The transition involves a magnetic dipole amplitude M1 and an electric dipole amplitude  $E1^{PV}$ , induced by the weak interaction, leading to a circular polarisation proportional to  $E1^{PV}/M1$ . But due to the short lifetime of the 2P states an according experiment has not been built ever since.

Similarly, the amplitude of the transition  $2S_{1/2} \rightarrow 1S_{1/2}$  contains a strongly suppressed M1 amplitude and the E1 amplitude of  $2P_{1/2} \rightarrow 1S_{1/2}$  because  $2S_{1/2}$  contains an admixture<sup>5</sup>  $i\eta$  of  $2P_{1/2}$ . Thus, the different amplitudes  $A_{\pm} = A(M1) \pm \eta A(E1)$  effectively lead to a circular polarisation

$$p = \frac{I_+ - I_-}{I_+ + I_-} = \frac{|A_+|^2 - |A_-|^2}{|A_+|^2 + |A_-|^2} \propto \eta \frac{A(E1)}{A(M1)} \quad (2.61)$$

of the emitted photons, see [7]. However, as already mentioned in Section 2.4, experiments with rare decays such as the above mentioned M1 amplitude suffer from the difficulty to keep background contributions to the decay smaller than the spontaneous decay rate.

Polarisation rotations<sup>6</sup> of atoms due to  $H_{PV}$  in chiral electric field configurations

<sup>5</sup>Time reversal (T)-invariance yields an imaginary admixture, cf. [7].

<sup>6</sup>Rotations of the total atomic angular momentum  $\langle \mathbf{F} \rangle$ .

$\mathcal{E}(\mathbf{x})$  were studied in [80]. There, the nominal magnitude of rotation were found to be of order  $10^{-8}$ , whereas rotations at the percent level are reported to be achievable with suitable experimental setups. These results for hydrogen-like systems were applied to  ${}^1_1\text{H}$ ,  ${}^4_2\text{He}^+$ , and  ${}^{12}_6\text{C}^{5+}$ .

In [82] P-violating energy shifts depending on chiral electric field configurations were investigated. The predictions for the nominal magnitudes of these  $\delta_i$ -linear shifts range from  $10^{-9}$  Hz to  $10^{-5}$  Hz. However, under specific conditions a proportionality to  $\sqrt{\delta_i}$  can be established which largely increases the energy shifts. For the discussed setups the shifts could be brought up to 1 Hz for  ${}^4_2\text{He}^+$  and up to  $10^{-5}$  Hz for  ${}^1_1\text{H}$ .

### Performed Experiments

Measuring PV in hydrogen cannot be regarded successful so far. There were several proposals to detect PV in hydrogen which lead to experiments at the University of Michigan [51, 84, 139, 140], Yale University [141, 142], and University of Washington [143]. But a sufficient precision could not be reached in any of them, see [50] for a brief review. In fact, the best result is reported to be  $C_{2p} = 1.5 \pm 1.5$  (stat.)  $\pm 22$  (syst.) [51] while the Standard Model predicts  $C_{2p} = 0.036$  as pointed out in [48]. All of these experiments are based on measuring transition rates between 2S states in a chiral interaction region composed of static electric and magnetic fields and a microwave field  $\epsilon^\omega$  driving the transition, see Figure 2.8 as an example.

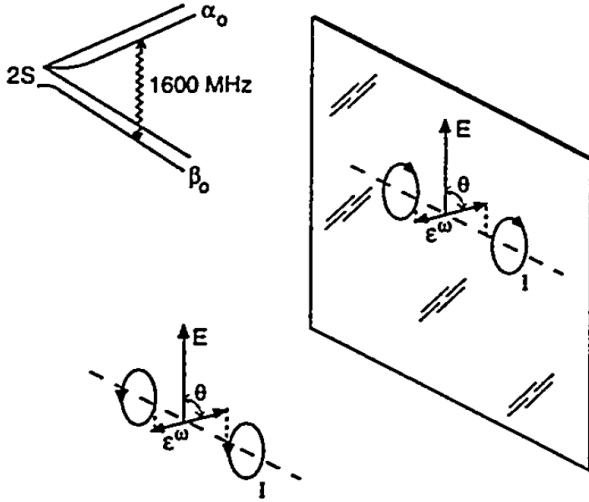


**Figure 2.8:** Illustration of the interaction region of the Michigan experiment [51, 84, 140] on P violation in hydrogen. A microwave field  $\epsilon^\omega$  drives a transition between the 2S states  $\alpha_0$ , corresponding to  $|10\rangle$  of Table A.2 in Appendix A.1, and  $\beta_0$ , corresponding to  $|12\rangle$ . Electric currents  $I$  produce a magnetic field  $\mathbf{B}$  (parallel to the dashed line), and with a static electric field  $\mathbf{E}$  perpendicular to  $\mathbf{B}$  a chiral interaction region is obtained. The Figure is adopted from [50] with permission: *PV in hydrogen. Different prospects using helium-like ions*, R. W. Dunford and Th. Stöhlker; Editors B. Frois and M.-A. Bouchiat, Copyright © 1999, Singapore: World Scientific.

There, the weak-induced amplitude corresponds to a process  $2S \rightarrow 2S'$  of the form

$$|2S_{1/2}\rangle \xrightarrow{\epsilon^\omega} |2P_{1/2}\rangle \xrightarrow{H_{PV}} |2S'_{1/2}\rangle, \quad (2.62)$$

---

## 2.6. Adiabatic Theorem and Berry Phases

while a PC amplitude is either obtained as a M1 transition  $|2S_{1/2}\rangle \xrightarrow{b^\omega} |2S'_{1/2}\rangle$  by a microwave magnetic field  $b^\omega$  or as a Stark induced amplitude, being also of the form (2.62), with  $H_{PV}$  replaced by a static electric field. Then, the amplitude due to PV mixing between 2S and 2P states gives rise to an asymmetry in the transition rate via interference with the PC amplitude.

To stress a generally appreciated feature of precision experiments we note that in the case of the Michigan experiment there are two different possibilities to invert the handedness of the interaction region, namely reversing  $\mathbf{E}$  or  $I$ . This provides a tool to study systematic errors such as stray electric fields which could mimic PV effects.

With these considerations we close the introductory review of parity violation in atoms and lead over to the concept of Berry phases, the second principal topic of this thesis, which turn out to exhibit PV contributions.

## 2.6 Adiabatic Theorem and Berry Phases

One main objective of the present thesis is the calculation and classification of P-violating and P-conserving geometric (Berry-) phases for hydrogen wave functions in external electromagnetic fields. In general, Berry phases can emerge for every time-dependent quantum mechanical system with at least two external parameters and adiabatic time evolution, as revealed by Michael Berry in 1984 [22].

In order to clarify the notion of geometric phases investigated in the present thesis, we briefly review the different types of geometric phases discussed in literature.

Berry's phase [22] is characterised by an adiabatic evolution due to a hermitian cyclic<sup>7</sup> Hamiltonian. In contrast, the Aharonov-Anandan phase [144] emerges for in general non-adiabatic processes and requires cyclic projective states<sup>8</sup> only. Approaching the adiabatic limit, the Aharonov-Anandan phase tends to Berry's phase. Both occur for unitary evolution. An even more general concept of geometric phases is provided by the Pancharatnam phase [145–148]. In general, it includes non-adiabatic, non-cyclic, and non-unitary evolution. That is, Pancharatnam's phase is the most general of the above mentioned geometric phase concepts. An instructive example is provided by the quantum mechanical measurement process, the collapse of the wave function, the action of which can be represented by projection operators. For subsequent projections on the states  $|\psi_3\rangle$ ,  $|\psi_2\rangle$ , and  $|\psi_1\rangle$ , one finds for an initial state  $|\psi_I\rangle = |\psi_1\rangle$  the final state<sup>9</sup>  $|\psi_F\rangle = |\psi_1\rangle \langle\psi_1|\psi_3\rangle \langle\psi_3|\psi_2\rangle \langle\psi_2|\psi_1\rangle$  with a phase factor  $\langle\psi_1|\psi_3\rangle \langle\psi_3|\psi_2\rangle \langle\psi_2|\psi_1\rangle$  which, in general, can be interpreted in geometric terms, see [148].

---

<sup>7</sup>A cyclic Hamiltonian  $H(T) = H(0)$  means that the time-dependent system, initialised with a specific parameter setting at  $t = 0$ , evolves such that it is exposed to the same parameter setting at  $t = T$ .

<sup>8</sup>A projective state  $|\xi\rangle$  is an element of the projective Hilbert space  $\mathcal{H}_p$  consisting of the equivalence classes of the states in the Hilbert space  $\mathcal{H}$ . The projective Hilbert space can be defined by the map  $\pi : \mathcal{H} \rightarrow \mathcal{H}_p$ ,  $\pi(|\psi\rangle) = \{|\phi\rangle : |\phi\rangle = e^{i\varphi}|\psi\rangle, \phi \in \mathbb{R}\}$ .

<sup>9</sup>For simplicity, we omit the time evolution in between the projections.

Berry phases can also be divided into the two classes of Abelian and non-Abelian phases. For example, an adiabatically evolving state  $|\psi_n(t)\rangle$  in the degenerate<sup>10</sup>  $k_n$ -dimensional eigenspace  $V_n$  with basis  $\{|\psi_{a_n}(t)\rangle; a_n = 1, \dots, k_n\}$  can be written as  $|\psi_n(t)\rangle = U_n(t, 0)|\psi_n(0)\rangle$ , where the evolution matrix  $U_n(t, 0)$  in general mixes the initial eigenvectors  $|\psi_{a_n}(0)\rangle$  which compose  $|\psi_n(0)\rangle$ . For  $\dim V_n = 1$ , no degeneracy is encountered, and a Berry phase for the corresponding state  $|\psi_n(t)\rangle$  is an Abelian  $U(1)$  factor  $\exp \oint_{\mathcal{C}} \mathcal{A}$ , with Abelian gauge potential  $\mathcal{A}$ , accumulated along a closed curve  $\mathcal{C}$ . For  $\dim V_n > 1$  the two time evolution matrices  $U_n(t_2, t_1)$  and  $U_n(t_3, t_2)$  do not commute in general, leading to non-Abelian Berry phases contained in the evolved state. This was first discussed by Wilczek and Zee [149] who revealed a non-Abelian gauge structure in terms of a path-ordered time evolution matrix  $U(t) = \mathcal{P} \exp \oint_{\mathcal{C}} \mathcal{A}$ , where  $\mathcal{A}$  does not commute with itself for different points of the closed curve  $\mathcal{C}$ . For further discussions of gauge potentials related to Berry phases see, for example, [25, 150]. An investigation of Abelian and non-Abelian Berry phases for metastable states, related to the situation in the present thesis, can be found in [67]. As pointed out in [25], non-Abelian geometric phases are the generic case for non-adiabatic evolution, although Abelian phases can occur in special cases.

In this thesis we investigate complex adiabatic Abelian geometric phases arising for non-hermitian Hamiltonians while no degeneracies are encountered during the cyclic evolution. In view of the nomenclature of geometric phases given above, those phases occurring for an effectively non-unitary evolution are more appropriately termed Pancharatnam phases rather than Berry phases. The derivation of the latter in [22] does not involve the effective description of unstable systems. However, Berry's derivation, adapted to the case of non-hermitian Hamiltonians, formally goes through unchanged<sup>11</sup>. Hence, we also denote the complex adiabatic geometric phases considered in this thesis as Berry phases. And since we are dealing with these types of Berry phases only, we will also use the term geometric phases synonymously from this point forward.

In the following, we proceed with the discussion of the adiabatic theorem and its connection to Berry phases.

### The Adiabatic Theorem

Let a time-dependent Hamiltonian  $H(t)$  with eigenstates  $|\alpha(t)\rangle$  and discrete spectrum be parametrised by

$$t = \frac{T}{\tau_0} \tau, \quad 0 \leq \tau \leq \tau_0, \quad (2.63)$$

where  $T$  is the total observation time, and  $\tau_0$  is a fixed parameter. One requirement for the derivation of the adiabatic theorem is non-degeneracy of the energy eigenvalues,

---

<sup>10</sup>Non-degeneracy is employed in the derivation of the adiabatic theorem which itself is used in the derivation of Berry's phase. However, this reasoning does not exclude adiabatically evolving systems which encounter degeneracies. The notion of (adiabatic) Berry phases can also be applicable for specific degenerate systems.

<sup>11</sup>We address this issue later in this section.

## 2.6. Adiabatic Theorem and Berry Phases

---

i.e., for all  $\tau$  and for all  $\beta \neq \alpha$  the property

$$E(\alpha, \tau) \neq E(\beta, \tau) \quad (2.64)$$

has to hold. Additionally, the first and second order derivatives  $d\mathbb{P}_\alpha/d\tau$  and  $d^2\mathbb{P}_\alpha/d\tau^2$  of the projection operators  $\mathbb{P}_\alpha = |\alpha(\tau)\rangle\langle\alpha(\tau)|$  have to be well defined and continuous on the interval  $0 \leq \tau \leq \tau_0$ . Then, the adiabatic theorem states the following asymptotic property for the time evolution operator  $U_T(\tau)$ , see for instance [151]:

$$\lim_{T \rightarrow \infty} U_T(\tau) \mathbb{P}_\alpha(0) = \mathbb{P}_\alpha(\tau) \lim_{T \rightarrow \infty} U_T(\tau). \quad (2.65)$$

Equation (2.65) can be illustrated by considering an eigenstate  $|\alpha\rangle$  of  $H(0)$  with eigenvalue  $E(\alpha, 0)$ . In that case, (2.65) together with the relation  $\mathbb{P}_\alpha(0)|\alpha\rangle = |\alpha\rangle$  yields

$$\lim_{T \rightarrow \infty} U_T(\tau)|\alpha\rangle = \mathbb{P}_\alpha(\tau) \lim_{T \rightarrow \infty} U_T(\tau)|\alpha\rangle. \quad (2.66)$$

Due to the projection operator  $\mathbb{P}_\alpha(\tau)$  on the right hand side of (2.66) the state  $U_T(\tau)|\alpha\rangle$  on the left hand side tends, in the limit  $T \rightarrow \infty$ , to a state within the subspace which corresponds to  $E(\alpha, \tau)$ .

It is instructive to follow the intuitive derivation of the adiabatic approximation as given in [152]. Here, we present the corresponding derivation for a non-hermitian Hamiltonian  $\underline{\mathcal{M}}$  as employed for hydrogen described in the Wigner-Weisskopf approximation.

Let the eigenvalue equations for a non-hermitian Hamiltonian  $\underline{\mathcal{M}}$  with diagonalisable matrix representation read

$$\begin{aligned} \underline{\mathcal{M}}(t) |\alpha, t\rangle &= E(\alpha, t) |\alpha, t\rangle, \\ (\widetilde{\alpha}, t | \underline{\mathcal{M}}(t) &= (\widetilde{\alpha}, t | E(\alpha, t), \end{aligned} \quad (2.67)$$

where

$$E(\alpha, t) = E_R(\alpha, t) - \frac{i}{2}\Gamma(\alpha, t), \quad E_R(\alpha), \Gamma(\alpha) \in \mathbb{R}, \quad (2.68)$$

is in general complex. We again assume  $E(\alpha(t)) \neq E(\beta(t))$  for  $\alpha \neq \beta$ . For the non-hermitian Hamiltonian or mass matrix  $\underline{\mathcal{M}}(t)$  right and left eigenvectors have to be distinguished. Here and in the following, the left eigenvectors of the mass matrix are denoted by a tilde. When dealing with internal states of the hydrogen atom, e.g., the eigenstates of  $\underline{\mathcal{M}}(t)$ , we use the bra-ket notation with parentheses  $|\ )$  instead of squared brackets  $|\ )$  which are reserved for total wave functions. Besides the orthogonality relation between left and right eigenvectors, we employ the common normalisation for the right eigenvectors

$$(\widetilde{\alpha}(t) | \beta(t)) = \delta_{\alpha\beta}, \quad (2.69)$$

$$(\alpha(t) | \alpha(t)) = 1, \text{ (no summation over } \alpha \text{)}, \quad (2.70)$$

## Chapter 2. Foundations, Motivations, and Historical Overview

---

The general solution of the Schrödinger equation

$$i\partial_t |\psi(t)\rangle = \underline{\mathcal{M}}(t)|\psi(t)\rangle \quad (2.71)$$

can be written as

$$|\psi(t)\rangle = \sum_{\beta} c_{\beta}(t) e^{-i\phi_{\beta}(t)} |\beta(t)\rangle, \quad (2.72)$$

with differentiable complex functions  $c_{\beta}(t)$  and  $\phi_{\beta}(t) = \int_0^t dt' E_{\beta}(t')$ . In the following, we omit the time dependence for abbreviation. A dot indicates a time derivative. Inserting (2.72) into (2.71) and projecting onto  $(\tilde{\alpha}|$ , one finds

$$i \sum_{\beta} \left\{ \dot{c}_{\beta} e^{-i\phi_{\beta}} |\beta\rangle - i c_{\beta} \dot{\phi}_{\beta} e^{-i\phi_{\beta}} |\beta\rangle + c_{\beta} e^{-i\phi_{\beta}} \partial_t |\beta\rangle \right\} = \sum_{\beta} c_{\beta} e^{-i\phi_{\beta}} E_{\beta} |\beta\rangle \quad (2.73)$$

$$\Rightarrow i \dot{c}_{\alpha} e^{-i\phi_{\alpha}} + c_{\alpha} E_{\alpha} e^{-i\phi_{\alpha}} + i \sum_{\beta} c_{\beta} e^{-i\phi_{\beta}} (\tilde{\alpha}| \partial_t |\beta\rangle) = c_{\alpha} e^{-i\phi_{\alpha}} E_{\alpha} \quad (2.74)$$

$$\Leftrightarrow \dot{c}_{\alpha} = -c_{\alpha} (\tilde{\alpha}| \partial_t |\alpha\rangle) - \sum_{\beta \neq \alpha} c_{\beta} e^{-i(\phi_{\beta} - \phi_{\alpha})} (\tilde{\alpha}| \partial_t |\beta\rangle). \quad (2.75)$$

The time derivative of  $\underline{\mathcal{M}}|\beta\rangle = E_{\beta}|\beta\rangle$  reads  $\underline{\dot{\mathcal{M}}}| \beta\rangle + \underline{\mathcal{M}}\partial_t |\beta\rangle = \dot{E}_{\beta}|\beta\rangle + E_{\beta}\partial_t |\beta\rangle$ . From that we find for  $\beta \neq \alpha$

$$\begin{aligned} (\tilde{\alpha}| \underline{\dot{\mathcal{M}}}| \beta\rangle) + E_{\alpha} (\tilde{\alpha}| \partial_t |\beta\rangle) &= \dot{E}_{\beta} \delta_{\alpha\beta} + E_{\beta} (\tilde{\alpha}| \partial_t |\beta\rangle) \\ \Rightarrow \frac{(\tilde{\alpha}| \underline{\dot{\mathcal{M}}}| \beta\rangle)}{E_{\beta} - E_{\alpha}} &= (\tilde{\alpha}| \partial_t |\beta\rangle). \end{aligned} \quad (2.76)$$

Substituting (2.76) into (2.75) yields

$$\dot{c}_{\alpha} = -c_{\alpha} (\tilde{\alpha}| \partial_t |\alpha\rangle) - \sum_{\beta \neq \alpha} c_{\beta} e^{-i(\phi_{\beta} - \phi_{\alpha})} \frac{(\tilde{\alpha}| \underline{\dot{\mathcal{M}}}| \beta\rangle)}{E_{\beta} - E_{\alpha}}. \quad (2.77)$$

At this point, the adiabatic approximation neglects the second term on the r.h.s. of (2.77), effectively demanding

$$(\tilde{\alpha}| \partial_t |\beta\rangle) \propto \delta_{\alpha\beta}. \quad (2.78)$$

It becomes evident from (2.76) that the adiabatic approximation holds for large enough energy separations and sufficiently slow variations of  $\underline{\mathcal{M}}$ , respectively.

### Berry's Phase

With (2.78), we can easily integrate (2.77) and obtain

$$c_{\alpha}(t) = c_{\alpha}(0) \exp \left\{ - \int_0^t dt' (\widetilde{\alpha}(t') | \partial_{t'} |\alpha(t')\rangle) \right\}. \quad (2.79)$$

## 2.6. Adiabatic Theorem and Berry Phases

---

Then, an initial state  $|\psi(0)\rangle = |\alpha(0)\rangle$ , i.e.,  $c_\alpha(0) = 1$  and  $c_\beta(0) = 0$  for all  $\beta \neq \alpha$ , (2.79) leads to

$$|\psi(t)\rangle = e^{-i\phi_\alpha(t)} e^{i\gamma_\alpha(t)} |\alpha(t)\rangle, \quad (2.80)$$

where

$$\gamma_\alpha(t) = i \int_0^t dt' (\widetilde{\alpha(t')} | \partial_{t'} |\alpha(t')) \quad (2.81)$$

and

$$\dot{\gamma}_\alpha(t) = i (\widetilde{\alpha(t)} | \partial_t |\alpha(t)) . \quad (2.82)$$

According to (2.80) the basis states at time  $t$  are the basis states at  $t = 0$  up to a phase, thereby inheriting the initial labelling of the basis states.

Besides the familiar dynamical phase  $\phi_\alpha(t)$ , which is also present for time-independent Hamiltonians, the phase  $\gamma_\alpha(t)$  emerging in (2.80) can be interpreted in geometric terms and is therefore called geometric phase, as will be discussed in the next section.

Let  $\mathcal{C} : [0, T] \rightarrow R$  be a closed curve in the at least two-dimensional<sup>12</sup> parameter space  $R$ , with elements  $\mathbf{R}$ , of a time-dependent system with no degeneracy along  $\mathcal{C}$ . Then, the adiabatically evolving system ends up at the same parameter configuration it started from, picking up the geometric phase

$$\begin{aligned} \gamma_\alpha(T) &= \gamma_\alpha(\mathcal{C}) = i \oint_{\mathcal{C}} dt' (\widetilde{\alpha(t')} | \partial_{t'} |\alpha(t')) \\ &= i \oint_{\mathcal{C}} d\mathbf{R} (\widetilde{\alpha(\mathbf{R})} | \nabla_{\mathbf{R}} |\alpha(\mathbf{R})) \\ &=: \oint_{\mathcal{C}} \mathbf{A} \cdot d\mathbf{R} \end{aligned} \quad (2.83)$$

in addition to the dynamical phase.  $\nabla_{\mathbf{R}}$  denotes the generalised nabla operator in the parameter space  $R$ . The initial and final phases of the wave function are linked via the specific adiabatic evolution the system runs through in parameter space. The geometric phase (2.83) is called Berry phase. In contrast to the dynamical phase which provides information about the evolution of the system in time, Berry's phase is time-independent and reflects the geometrical structure of the underlying parameter space. As demonstrated by Berry in [22], the line integral (2.83) can be transformed into a surface integral over a vector field  $\mathbf{V}$  via Stokes' theorem. In the case of a non-hermitian effective Hamiltonian or mass matrix, one finds

$$\begin{aligned} \gamma_\alpha(\mathcal{C}) &= \oint_{\partial\mathcal{F}=\mathcal{C}} \mathbf{A} \cdot d\mathbf{R} =: \int_{\mathcal{F}} \mathbf{V} \cdot d\mathbf{f} \\ &= i \sum_{\beta \neq \alpha} \int_{\mathcal{F}} \frac{(\widetilde{\alpha(\mathbf{R})} | d_{\mathcal{M}}(\mathbf{R}) |\beta(\mathbf{R})) (\widetilde{\beta(\mathbf{R})} | d_{\mathcal{M}}(\mathbf{R}) |\alpha(\mathbf{R}))}{(E_\beta(\mathbf{R}) - E_\alpha(\mathbf{R}))^2}, \end{aligned} \quad (2.84)$$

---

<sup>12</sup>A system  $H_1(\lambda)$  depending on one parameter  $\lambda$  is a special case of a system  $H_2(\lambda, \mu)$  when  $\mu$  gets fixed. Therefore, an area in the  $\lambda$ - $\mu$ -parameter space automatically shrinks to zero for a fixed  $\mu$ , resulting in a vanishing Berry phase, see (2.84).

see [39]. Of course, (2.84) only holds if the eigenenergies are non-degenerate along  $\mathcal{C}$  and on  $\mathcal{F}$ . In Section 3.5 we will formulate further useful representations of the geometric flux densities, i.e., the integrands of the surface integral of (2.84).

For a non-hermitian mass matrix  $\underline{\mathcal{M}}$ , which effectively incorporates a decay matrix  $\Gamma$ , the Berry phases are in general complex. This feature can be traced back to the fact that the left and right eigenvectors of the non-hermitian mass matrix differ in general, see [39]. If they are equal, as for the case of a hermitian Hamiltonian, it can be shown that the Berry phases are real. Moreover, the complex Berry phase tends to the Berry phase described in [22] for  $\Gamma \rightarrow 0$ , which can be seen as follows. Let  $\langle \tilde{n} | = {}^{(0)}\langle n | + {}^{(\Gamma)}\langle n |$  and  $|n\rangle = |n\rangle^{(0)} + |n\rangle^{(\Gamma)}$  be the left and right eigenvectors of  $\underline{\mathcal{M}}$ , respectively, obeying  $\langle \tilde{n} | m \rangle = \delta_{nm}$  and  $\langle n | n \rangle = 1$ . Demanding

$$\begin{pmatrix} |n\rangle \\ \langle \tilde{n} | \end{pmatrix} \xrightarrow{\Gamma \rightarrow 0} \begin{pmatrix} |n\rangle^{(0)} \\ {}^{(0)}\langle n | \end{pmatrix}, \quad (2.85)$$

we find

$$\dot{\gamma} = i \left( {}^{(0)}\langle n | + {}^{(\Gamma)}\langle n | \right) \partial_t \left( |n\rangle^{(0)} + |n\rangle^{(\Gamma)} \right) = i {}^{(0)}\langle n | \partial_t |n\rangle^{(0)} + f(\Gamma) \quad (2.86)$$

for the corresponding Berry phase  $\gamma$ , while  $f(\Gamma) \xrightarrow{\Gamma \rightarrow 0} 0$ .

### 2.6.1 Geometrical Properties of Berry Phases

The emergence of Berry phases can be illustrated by parallel transport of a tangent vector along a closed curve on the sphere, representing the parameter space  $M$ , see Figure 2.9. At every point  $p$  of the sphere there is a two-dimensional tangent space  $T_p M$  which can be interpreted as a  $U(1)$  degree of freedom if the direction of vectors in  $T_p M$  can be chosen freely.

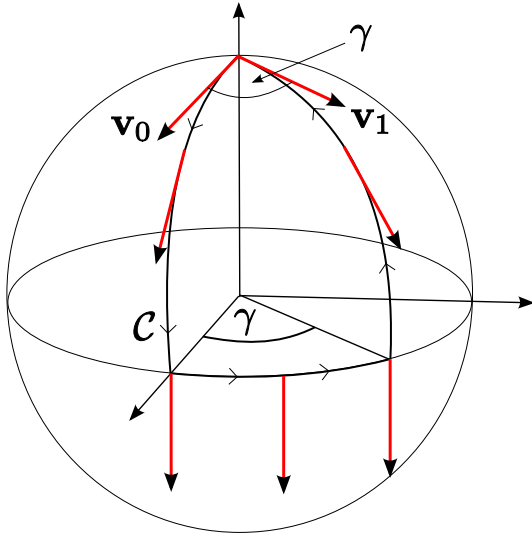


**Figure 2.9:** Parallel transport of a vector on the sphere as an example for the appearance of Berry phases in the case of non-vanishing curvature of the parameter space along the path  $\mathcal{C}$ . This situation illustrates the geometric phases emerging for a spin-1-particle in a magnetic field, see (2.89).

## 2.6. Adiabatic Theorem and Berry Phases

---

The starting vector  $\mathbf{v}_0$  at the north pole of the sphere is parallel transported along geodesics ending up as vector  $\mathbf{v}_1$ . The vector  $\mathbf{v}_1$  is again an element of the local tangential plane at the north pole, i.e., the system is exposed to the same parameters as initially, but  $\mathbf{v}_1$  does not coincide with the starting vector. In this example the angle between  $\mathbf{v}_0$  and  $\mathbf{v}_1$  is a geometric phase angle  $\gamma$  that gets picked up during the transport along  $\mathcal{C}$ . In flat parameter spaces the curvature always vanishes, and Berry phases will not occur. Considering parallel transport on a curved surface, the emergence of Berry phases is easy to grasp. However, a discussion of why to parallel-transport vectors through a curved parameter space in the first place is in order. In the following, we show that the defining condition for Berry's phase is equivalent to the condition obtained for the phase of a quantum mechanical states vector which is parallel-transported along geodesics in parameter space.

### Spin- $J$ -Particle in a Magnetic Field

Before proceeding with the discussion of interpreting Berry's phase in terms of geometry, we present the standard example of a geometric phase. In the following, we will see that a spin- $J$ -system in a magnetic field represents the case  $M = S^2$ . A more detailed investigation can for instance be found in [25]. The Hamiltonian

$$H(\mathbf{R}) = H(\theta, \varphi) = \omega_0 \frac{\mathbf{B}(\theta, \varphi)}{B} \cdot \mathbf{J} = \omega_0 e^{-i\varphi(t)J_z} e^{-i\theta(t)J_y} J_z e^{i\theta(t)J_y} e^{i\varphi(t)J_z} \quad (2.87)$$

is defined on the sphere  $S^2$ . The instantaneous eigenstates of (2.87) are

$$|\eta_m(\mathbf{R})\rangle := |\eta_m(\varphi, \theta)\rangle = e^{-i\varphi(J_z - m)} e^{-i\theta J_y} |m\rangle, \quad (2.88)$$

where  $|m\rangle$  are the eigenstates of  $J_z$ . The corresponding eigenvalues are denoted as  $E_m(\mathbf{R})$ . Together with (2.84) and (2.87) one finds  $\mathbf{V}_m = -m \mathbf{B}/B^3$  leading to

$$\gamma_m(\mathcal{C}) = \oint_{\partial\mathcal{F}=\mathcal{C}} \mathbf{A} \cdot d\mathbf{R} = \int_{\mathcal{F}} \mathbf{V}_m \cdot d\mathbf{f} = -m \int_{\mathcal{F}} \sin\theta \, d\theta d\varphi = -m \Omega(\mathcal{C}), \quad (2.89)$$

where  $\mathcal{F} \subset S^2$  and  $\Omega(\mathcal{C})$  being the solid angle encircled by  $\mathcal{C}$ . The contour  $\mathcal{C}$  in (2.89) is chosen such that  $\Omega(\mathcal{C}) \geq 0$ . For the reversed cycling direction  $\gamma_m(\mathcal{C})$  switches sign. As discussed in [25], the dependence of  $\gamma_m(\mathcal{C})$  on the solid angle is directly connected to the Dirac monopole singularity at  $\mathbf{B} = \mathbf{0}$  being an isolated point of degeneracy for the spin- $J$ -system. For  $m = 1$  a full equatorial circuit gives a phase change of  $4\pi/2 = 2\pi$ , while  $m = 1/2$  leads to a phase change of  $\pi$ .

### Parallel transport of quantum mechanical states

To reveal the connection between parallel transport and Berry's phase, we consider the sphere of the preceding section as the parameter space  $M$  of some quantum mechanical system. Imposing an adiabatic evolution, the quantum mechanical state vector

$$|\phi(t)\rangle = e^{i\varphi(t)} |n(\mathbf{R}(t))\rangle, \quad (2.90)$$

## Chapter 2. Foundations, Motivations, and Historical Overview

---

with  $\varphi(0) = 0$ , can be represented as an element of a one-dimensional complex space  $\mathbb{C}$  at every value of  $t$  with base vector  $|n(\mathbf{R}(t))\rangle$ . Let the set of parameters  $\mathbf{R}(t)$ ,  $t \in [0, T]$ , represent a smooth curve  $\alpha : [0, T] \rightarrow M$ . Then, we can identify  $|\phi(t)\rangle$  with a smooth complex scalar function  $\phi(t) \in \mathbb{C}$ . But we can also identify  $|\phi(t)\rangle$  as an element of the tangent space  $T_{\mathbf{R}(t)}M \simeq \mathbb{R}^2$  at  $\mathbf{R}(t) \simeq \alpha(t) \in M$ , where  $\varphi(t)$  represents the phase of the vector in  $T_{\mathbf{R}(t)}M \simeq \mathbb{C}$ . Hence, we may eventually identify  $\phi(t)$ , up to a phase, with the tangent vector field  $\dot{\alpha}(t) = \frac{d}{dt} = \frac{dx^\mu(\alpha(t))}{dt} \frac{\partial}{\partial x^\mu} \Big|_{\alpha(t)}$  living in the tangent space.

The affine connection  $\nabla_V U$  of a vector field  $U$ , defined on  $M$ , is a derivative in the direction of  $V \in T_p M$  at a point  $p \in M$ . The curve  $\alpha(t)$  is called a geodesic if  $\nabla_{\dot{\alpha}(t)} \dot{\alpha}(t) = 0$ . The latter equation is the defining property of a parallel transport of the tangent vector  $V = \dot{\alpha}(t)$  along  $\alpha(t)$ . For a scalar function like  $\dot{\alpha}(t)$  the affine connection is the ordinary derivative  $\frac{d}{dt}$ . For the present case this leads to the parallel transport condition  $0 \stackrel{!}{=} \nabla_{\dot{\alpha}(t)} \dot{\alpha}(t) = \frac{d}{dt} \phi(t)$  or  $0 \stackrel{!}{=} \frac{d}{dt} |\phi(t)\rangle$ , respectively. Therefore, we obtain

$$\begin{aligned} 0 = \frac{d}{dt} |\phi(t)\rangle &\Leftrightarrow 0 = \frac{d}{dt} (e^{i\varphi(t)} |n(\mathbf{R}(t))\rangle) \Leftrightarrow 0 = i\dot{\varphi}|n\rangle + \partial_t |n\rangle \\ &\stackrel{13}{\Leftrightarrow} i\dot{\varphi} \delta_{mn} = -\langle m | \partial_t |n\rangle \stackrel{14}{\Leftrightarrow} \dot{\varphi} = i \langle n | \partial_t |n\rangle . \end{aligned} \quad (2.91)$$

Comparing (2.91) with the already deduced condition for the geometric phase (2.82), we find  $\varphi(t) = \gamma_n(t)$ . That is, the parallel transport of (2.90) along geodesics implies a condition for the choice of phases of the state vector along the curve in  $M$ . It is the same condition derived for Berry's phase using Schrödinger's equation and adiabaticity. Conversely, observing a Berry phase – which requires adiabaticity per definition – implies a parallel transport according to the reasoning in (2.91).

We note that not the full state vector

$$|\psi_n(t)\rangle = e^{-\frac{i}{\hbar} \int_0^t E_n(\mathbf{R}(t')) dt'} e^{i\gamma_n(t)} |n(\mathbf{R}(t))\rangle , \quad (2.92)$$

obeying the Schrödinger equation, is parallel transported along  $\alpha$  but only (2.90). Of course, the condition  $\frac{d}{dt} |\psi_n(t)\rangle = 0$  for a parallel transport of  $|\psi_n(t)\rangle$  cannot be fulfilled since this would imply a vanishing Hamiltonian because of  $|n(\mathbf{R}(t))\rangle$  being an arbitrary basis ket of the full Hilbert space. Instead, the parallel transported state vector  $|\phi(t)\rangle$  is the solution of a modified Schrödinger equation with quantum number  $n$

$$\begin{aligned} (H - E_n(t))|\phi(t)\rangle &= i \frac{d}{dt} |\phi(t)\rangle \Leftrightarrow (H - E_n) e^{i\gamma_n} |n\rangle = i \frac{d}{dt} (e^{i\gamma_n} |n\rangle) \\ &\Leftrightarrow (E_n - E_n)|n\rangle = i(i\dot{\gamma}_n |n\rangle + \partial_t |n\rangle) \Leftrightarrow \dot{\gamma}_n = i \langle n | \partial_t |n\rangle \end{aligned} \quad (2.93)$$

which holds since  $\gamma_n$  is Berry's phase. Thus, only (2.90), what one could call the geometric part of the total wave function, is parallel transported in parameter space.

---

<sup>13</sup>The equivalence is based on  $\{|m\rangle\}$  being a basis.

<sup>14</sup>Adiabatic evolution enforces  $\langle m | \partial_t |n\rangle = 0$ , for  $m \neq n$ , and hence  $i\dot{\varphi} \delta_{mn} = -\langle m | \partial_t |n\rangle \Leftrightarrow 0 = 0$ , for  $m \neq n$ .

More generally, Berry phases can be put into context with the geometry of the underlying parameter space using the concept of principal fibre bundles, see for instance [30, 150]. This connection was first pointed out in [29]. The curvature of the parameter space manifold  $M$  at a point  $p \in M$  is related to the holonomy group, a set of automorphisms of all closed curves starting and ending at  $p$ . Therefore, in essence, the choice of a specifically curved parameter space for visualising the emergence of Berry's phase can be considered as a result of deriving the solutions of the differential equation (2.91). The geometry of the parameter space can be deduced from the actually realised parallel transport on  $M$  by evaluating all possibilities of (2.91) to be fulfilled.

### 2.6.2 Experimental Observations of Berry Phases

One of the first experiments measuring Berry's phase was a spin-rotation experiment with polarised neutrons carried out by T. Bitter and D. Dubbers [153, 154] in 1987. This experiment is closely related to the longitudinal atomic beam spin echo experiment we describe in Section 4.1. In the neutron experiment the spin rotation angle of the polarised neutrons precessing around a helical magnetic field arrangement came out to include the solid angle enclosed by the magnetic field vector as predicted by M. V. Berry.

Berry's phase also emerges in the realm of nuclear magnetic resonance spectroscopy. There, the levels of two nuclear-spin states split in a magnetic field applied along the  $z$ -axis, and the transition between them is excited by a circularly polarised radio frequency field with magnetic amplitude in the  $x$ - $y$ -plane. Effectively, this leads to a conical circuit of the total magnetic field and, therefore, to an additional rotation angle of the nuclear magnetisation for each circuit. A corresponding experiment has been performed in 1987 confirming the solid-angle dependence of Berry's phase in this situation, see [155].

Another prominent realisation of a Berry phase is present in the Aharonov-Bohm effect [23] where the electromagnetic gauge translates into a phase factor of the wave function, measurable in an interference experiment [156]. This phase factor can be interpreted in terms of a geometric phase when, e.g., an electron in a box is carried around an isolated magnetic flux, see for instance [157]. For a selection of further experiments on geometric phases we refer to [158–163].

To our knowledge, imaginary parts of Berry phases have not been measured so far. In Section 3.7 we describe imaginary Berry phases for hydrogen of in principle measurable magnitude. As will be worked out in the Chapters 3 and 5 the observation of P-violating Berry phases can be expected challenging due to their small absolute values. However, the present thesis focuses on Abelian Berry phases for hydrogen in electromagnetic fields, thereby covering wide, though selected, parts of the parameter space. Larger PV effects may be revealed in regions of parameter space which are not explored yet or in the realm of non-Abelian Berry phases.



### 3 Berry Phases for Hydrogen

In the preceding chapter we formulated the conceptual foundations of this work. We introduced parity violation the concept of Berry phases. In the present chapter we will work out the emergence of Berry phases for hydrogen exposed to adiabatically varying electromagnetic fields. Our goals are a convenient description and classification of P-conserving and P-violating Berry phases for arbitrary systems which obey an effective Schrödinger equation

$$i\frac{\partial}{\partial t}|t\rangle = \underline{\mathcal{M}}(K(t))|t\rangle, \quad (3.1)$$

with  $N \times N$  non-hermitian Hamiltonian matrices<sup>1</sup>  $\underline{\mathcal{M}}(K)$  possessing metastable eigenstates. The parameter vector  $K$  can include any number of components. The investigations in this chapter are mainly based on [40]. The general results obtained here will be explicitly applied to hydrogen and helium.

Section 3.1 is devoted to the Wigner-Weisskopf approximation which accounts for the decay of unstable states leading to an effective time evolution according to (3.1). The decay matrix incorporated in  $\underline{\mathcal{M}}(K(t))$  is derived explicitly for the case of  $n = 2$  hydrogen.

The behaviour of hydrogen in external fields is discussed in Section 3.2. We derive the adiabaticity conditions in Section 3.2.1 necessary for establishing adiabatic Berry phases. The P-violating mass matrix of hydrogen is defined in Section 3.2.2. Its degeneracies in the presence of arbitrary external fields are investigated in Section 3.2.3 in order to define the parameter space regions which are suitable for the search of Abelian Berry phases. Illuminating the role of electric and magnetic fields, an analysis of chiral configurations of hydrogen in external fields is provided in Section 3.2.4.

In view of the adiabatic theorem we introduce notations and general properties of the adiabatically evolving wave functions in Section 3.3.

The approach of numerical computation of geometric phases in the context of this work is briefly summarised in Section 3.4, based on [83].

Eventually, Section 3.5 comprises the analysis of geometric flux-density vector fields. We derive expressions for flux-density vector fields in Section 3.5.1 that generalise those in (2.84) and are notably convenient for numerical implementation. This analysis is carried out in a general framework, that is, not limited to hydrogen, but including all systems following (3.1). We also deduce general expressions for the derivatives of geometric flux densities enabling cross-checks of the numerical algorithms and their accuracy. From the transformation behaviour of the hydrogen mass matrix under

---

<sup>1</sup>The effective Hamiltonian  $\underline{\mathcal{M}}(K)$  is also called mass matrix.

## Chapter 3. Berry Phases for Hydrogen

proper and improper rotations we derive the general structure of flux densities for the metastable states of hydrogen in Section 3.5.2. There, an expansion of the geometric flux densities in terms of invariant functions is obtained which provides for convenient comparisons between numerical and analytical calculations.

In Section 3.6 we present and discuss our numerical and analytical results for the geometric flux-density vector fields by means of instructive examples.

Specific Berry phases will be computed in Section 3.7 for selected external field configurations. Especially, we illustrate the impact of imaginary P-conserving Berry phases on the lifetimes of metastable atomic states and give an example of a P-violating geometric phase.

The results for Berry phases in the present chapter will be used to calculate spin echo signals in Chapter 5. There we consider geometric phases in further field configurations and explore the conditions for their generation in more detail.

### The $n = 2$ Subspace of Hydrogen

In the present chapter we shall consider in particular  $n = 2$  hydrogen atoms at rest subjected to slowly varying electric and magnetic fields. The subspace of hydrogen with principal quantum number  $n = 2$  has complex dimension 16. As a set of basis vectors we choose coupled states of nuclear spin  $|I, I_3\rangle$ , electron spin  $|\frac{1}{2}, S_3\rangle$  and electron orbital angular momentum  $|n, L, L_3\rangle$ . We denote these basis states by  $|nL_J, F, F_3\rangle$  where  $J$  is the total angular momentum of the electron and  $F, F_3$  are the quantum numbers for the total angular momentum of the atom. Their energy levels in vacuum are shown in Figure 3.1. We use a numbering scheme  $\alpha = 1, \dots, 16$  as explained in Appendix A.1, Table A.2.

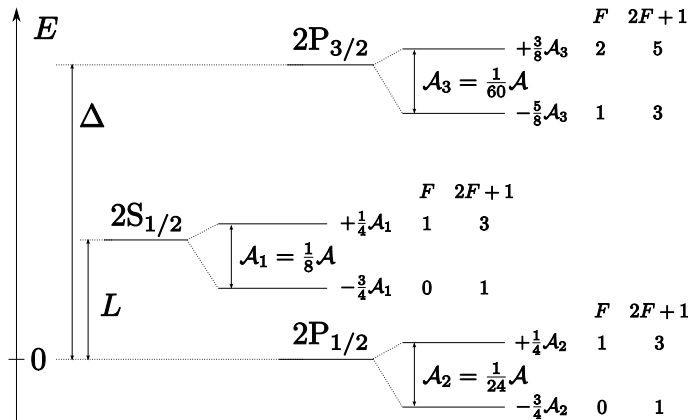


**Figure 3.1:** Energy levels of the hydrogen states with principal quantum number  $n = 2$  in vacuum. The numerical values of the fine structure splitting  $\Delta$ , the Lamb shift  $L$  and the ground state hyperfine splitting energy  $\mathcal{A}$  are given in Table A.1 of Appendix A.1.

### 3.1 Wigner-Weisskopf Approximation

Since we will consider atomic hydrogen travelling through electromagnetic fields for a certain time interval, and since we are especially interested in the metastable 2S states, which have large enough lifetimes for measurements in an atom interferometer, we have to account for their decay in our formalism.

In vacuum the 2S states of hydrogen are metastable and decay by two-photon emission to the ground state. The 2P states decay to the ground state by one-photon emission. We do not take into account energetically allowed radiative transitions from one  $n = 2$  state to another. This will be justified by explicitly calculating the decay matrix in the  $n = 2$  subspace below. Omitting off-diagonal transitions remains valid when we consider the  $n = 2$  states in an external, slowly varying, electromagnetic field in the adiabatic limit. There, by definition, the variation of the external fields has to be slow enough such that no transitions between the  $n = 2$  levels are induced. In this situation we can apply the standard Wigner-Weisskopf method, see [164]. The derivation of this method and its limitations are discussed in many textbooks and articles, see for instance [79, 80, 93, 165–168]. A derivation starting from quantum field theory can be found in [169, 170]. Let us note that for more complex situations than discussed in the present thesis, for instance if radiative transitions are induced between the  $n = 2$  states by an external field, we would have to use other methods, master equations, the optical Bloch equation etc.; see [166].

Following [93], we briefly discuss the Wigner-Weisskopf approximation in general and its applicability for hydrogen in particular. We start with a Hamiltonian  $H = H_0 + H'$ , where  $H_0$  is the unperturbed Hamiltonian and  $H'$  is a small perturbation causing the instability of the eigenstates. The eigenstates of  $H_0$  are supposed to consist of  $n$  degenerate<sup>2</sup> discrete states  $|\alpha\rangle$  and a continuum of states  $|\beta\rangle$ :

$$H_0|\alpha\rangle = E_0|\alpha\rangle, H_0|\beta\rangle = E_\beta|\beta\rangle. \quad (3.2)$$

When  $H'$  is switched on, the discrete states can decay into the continuum states. In the case of the metastable 2S states of hydrogen the decay will lead to continuum states that are composed of 1S states and photon states. Any state  $|t\rangle$  at time  $t$  can be expanded in terms of the eigenstates of  $H_0$ :

$$|t\rangle = \sum_{\alpha=1}^n \psi_\alpha(t)|\alpha\rangle + \sum_{\beta} c_\beta(t)|\beta\rangle. \quad (3.3)$$

The aim is to gain the full evolution of the wave functions  $\psi_\alpha(t)$  given an initial state

$$|t = 0\rangle = \sum_{\alpha=1}^n \psi_\alpha(0)|\alpha\rangle. \quad (3.4)$$

---

<sup>2</sup>Of course, for a system of non-degenerate states each degenerate subsystem can be treated separately as long as it is decoupled from the others.

## Chapter 3. Berry Phases for Hydrogen

---

In the Dirac picture the equation of motion reads

$$i\partial_t|t\rangle_W = H'(t)|t\rangle_W \quad (3.5)$$

with

$$|t\rangle_W = \exp(iH_0t)|t\rangle = \sum_{\alpha=1}^n a_\alpha(t)|\alpha\rangle + \sum_{\beta} b_\beta(t)|\beta\rangle \quad (3.6)$$

and

$$H'(t) = \exp(iH_0t)H' \exp(-iH_0t) . \quad (3.7)$$

Written in components, (3.5) reads

$$i\partial_t a_\alpha(t) = \sum_{\alpha'=1}^n \langle\alpha|H'|\alpha'\rangle a_{\alpha'}(t) + \sum_{\beta} \exp(i(E_0 - E_\beta)t) \langle\alpha|H'|\beta\rangle b_\beta(t) , \quad (3.8)$$

$$\begin{aligned} i\partial_t b_\beta(t) &= \sum_{\alpha'=1}^n \exp(i(E_\beta - E_0)t) \langle\beta|H'|\alpha'\rangle a_{\alpha'}(t) \\ &+ \sum_{\beta'} \exp(i(E_\beta - E_{\beta'})t) \langle\beta|H'|\beta'\rangle b_{\beta'}(t) . \end{aligned} \quad (3.9)$$

As a first approximation, the transition matrix elements  $\langle\beta|H'|\beta'\rangle$  are neglected. In the case of hydrogen this means that the decay products, i.e., the  $n = 1$  states are stable and do not repopulate the  $n = 2$  states via non-zero amplitudes  $\langle\beta|H'|\beta'\rangle$ . In that way, the Schrödinger equation can be solved with the initial conditions  $a_\alpha(0) = \psi_\alpha^{(0)}$  and  $b_\beta(0) = 0$ . Further approximations discussed in [93] result in the amplitudes of the discrete states

$$\psi(t) = \begin{pmatrix} \psi_1(t) \\ \psi_2(t) \\ \vdots \\ \psi_n(t) \end{pmatrix} = e^{-i\mathcal{M}_0 t} \psi(0) \quad (3.10)$$

where  $\mathcal{M}_0 = E_0 - \frac{i}{2}\Gamma$  is the non-hermitian mass matrix corresponding to a hermitian Hamiltonian in the case of solely stable eigenstates. It can be shown that  $\psi_\alpha(t)$  in (3.10) decays exponentially while the eigenstates  $|\alpha\rangle$  of  $\mathcal{M}_0$  exhibit  $\Gamma(\alpha)$  as decay rates. The norm of  $|t\rangle$  is preserved and the decreasing norms of the amplitudes  $\psi_\alpha(t)$  are compensated by the increasing norms of the continuum states.

### The Decay Matrix

To connect the preceding discussion of the Wigner-Weisskopf approximation with hydrogen, we consider the decay of the  $n = 2$  states of hydrogen in more detail. The hermitian part of  $\mathcal{M}_0$ , that is,  $(\mathcal{M}_0 + \mathcal{M}_0^\dagger)/2$  is given by the known energy levels

## 3.2. Hydrogen in External Fields

---

of the  $n = 2$  hydrogen states; see Appendices A.1 and A.2. For the decay matrix  $\underline{\Gamma} = i(\underline{\mathcal{M}}_0 - \underline{\mathcal{M}}_0^\dagger)$  we have (for atoms at rest), see for instance (3.13) of [80],

$$(2L'_{J'}, F', F'_3 | \underline{\Gamma} | 2L_J, F, F_3) = 2\pi \sum_X \langle X | \mathcal{T} | 2L'_{J'}, F', F'_3 \rangle^* \times \delta(E_X - E_2) \langle X | \mathcal{T} | 2L_J, F, F_3 \rangle. \quad (3.11)$$

Here,  $|X\rangle$  denotes the decay states, the atom in a 1S state plus photons, and  $\mathcal{T}$  is the transition matrix. The matrix  $\underline{\Gamma}$  must be diagonal in  $(F, F_3)$  due to rotational invariance<sup>3</sup>. We shall neglect P violation in the decay. Then, the non-diagonal matrix elements between S and P states must be zero<sup>4</sup>. The only non-diagonal matrix elements (3.11) which could be non-zero are, therefore, those for  $L = L' = 1$ ,  $F = 1$ , and  $(J', J) = (1/2, 3/2)$  or  $(J', J) = (3/2, 1/2)$ , respectively. But calculating these matrix elements inserting the usual formulae for E1 transitions on the r.h.s. of (3.11) we get zero. See Appendix A.1 for a detailed derivation. Thus, neglecting higher-order corrections, the matrix  $\underline{\Gamma}$  (3.11) is diagonal.

## 3.2 Hydrogen in External Fields

We want to investigate the emergence of Berry phases for hydrogen in an interferometer which employs spatially varying electromagnetic fields. From a theoretical point of view, this situation is equivalent to the emergence of Berry phases for an atom at rest subjected to electromagnetic fields varying in time. To be more precise, we neglect relativistic effects for the external fields, which are supposed to be the external fields in the rest frame of the atom. We also neglect relativistic time dilatation affecting the decay rates in the laboratory frame. For an atomic velocity of 3000 m/s the relevant quantities to estimate these relativistic effects are  $\beta = v/c \approx 10^{-5}$  and  $\gamma = (1 - \beta^2)^{-1/2} \approx 1 + 0.5 \times 10^{-10}$ .

In the scope of the present work, the external fields form the parameter space for Berry's phase. We consider Berry phases for adiabatic evolution. At this point, the only required experimental parameter for setting up the adiabaticity conditions in Section 3.2.1 is the time of flight for the interferometry experiment, being of the order of 1 ms [77].

The hydrogen atom couples to the electric field  $\mathcal{E}$  via the electric dipole operator  $\underline{D}$  and to the magnetic field  $\mathcal{B}$  via the magnetic dipole operator  $\underline{\mu}$ . The according terms in the mass matrix are  $-\underline{D} \cdot \mathcal{E}$  and  $-\underline{\mu} \cdot \mathcal{B}$ , respectively. The underlines indicate matrices in the  $n = 2$  subspace of hydrogen. See Appendix A.2 for explicit representations of  $\underline{D}$  and  $\underline{\mu}$  in the basis  $\{|2L_J, F, F_3\rangle\}$  of total atomic angular momentum eigenstates of hydrogen for vanishing external fields and without the P-violating mixing. The notations for the eigenstates are given in Appendix A.1.

---

<sup>3</sup>A transition between different  $(F, F_3)$  would violate the conservation of total angular momentum, deduced from rotational invariance.

<sup>4</sup>Without PV admixtures of P states to S states the amplitude  $\langle X | \mathcal{T} | 2S, F, F_3 \rangle$  is an integral over an odd function and hence vanishes.

### 3.2.1 Adiabaticity Conditions

In this section we provide the conditions for the adiabatic evolution of the 2S states.

#### Lifetimes

As an overlying condition we want a sufficient fraction of the involved states not to decay during the experiment. The lifetimes of the 2S and 2P states in vacuum are [171, 172]

$$\begin{aligned}\tau_S &= \Gamma_S^{-1} = 0.12165(1) \text{ s} , \\ \tau_P &= \Gamma_P^{-1} = 1.596199(6) \times 10^{-9} \text{ s} .\end{aligned}\tag{3.12}$$

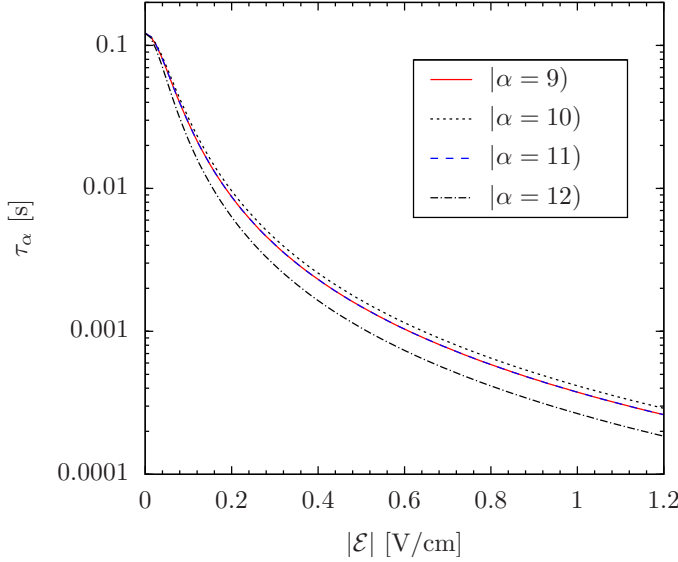


**Figure 3.2:** Lifetimes of the mixed  $2S_{1/2}$  states of hydrogen in the external electric field  $\mathcal{E} = \mathcal{E}e_3$  as a function of  $|\mathcal{E}|$ . The numbering scheme of the states ( $\alpha = 9, \dots, 12$ ) is given in Table A.2 of Appendix A.1.

Here,  $\Gamma_{S,P}$  are the decay rates. An electric field  $\mathcal{E}$  mixes the 2S states with the 2P states. As shown in Figure 3.2, the lifetimes of the 2S states decrease with increasing magnitude of  $|\mathcal{E}|$ . Given a time of flight of the atom through the interferometer of the order of 1 ms, we require as a rough condition an average lifetime for the metastable 2S states of

$$\tau_S(\mathcal{E}) \gtrsim 1 \text{ ms}\tag{3.13}$$

to gain a sufficient flux of metastable 2S states at the detector of the interferometer. According to Figure 3.2 this implies an allowed average for the electric field of

$$|\mathcal{E}(z)|_{\text{av}} \leq 0.60 \text{ V/cm} .\tag{3.14}$$

Here,  $z$  is the parameter of a path

$$\mathcal{C}: z \rightarrow \mathbf{L}(z) , 0 \leq z \leq 1 , \mathbf{L}(0) = \mathbf{L}(1)\tag{3.15}$$

### 3.2. Hydrogen in External Fields

in the parameter space  $\mathbf{L}$ . Of course, it can be appropriate to extend the limit (3.14) for the sake of more promising results sensitive to geometric phases, although the flux of metastable states at the end of the interferometer is reduced. However, the electric field strength should not exceed 250 V/cm to ensure sufficient decoupling of the 2P states from the 2S states which is a necessity for adiabatic evolution of the 2S states. This restriction was discussed in [68], and we will briefly address to the explanation therein. In Figure 3.3 one recognises the quick destabilisation of the mixed  $2S_{1/2}$  states of hydrogen for an increasing external electric field. As was pointed out in [68], a ratio

$$\tau_S/\tau_P \gtrsim 5 \quad (3.16)$$

of lifetimes for the mixed  $2S_{1/2}$  states and any of the 2P states should be sufficient for the decoupling of the 2S states from the 2P states. The reason for this can be found in the correction terms of the expanded amplitudes of the eigenstates in the limit of large observation time  $T$ . They are calculated in [67] and yield a suppression of the corrections to the adiabatic evolution with a factor of  $1/(T\Delta\Gamma_{min})$ , where  $\Delta\Gamma_{min}$  is the minimal difference of decay rates fulfilling  $0 \leq \Delta\Gamma_{min} \leq \Gamma_P - \Gamma_S$ . We suppose that, in a realistic experiment,  $T$  cannot greatly exceed the lifetime  $\tau_S$  of the investigated metastable states. Thus, with  $T$  fixed, a large enough  $\Delta\Gamma_{min}$  has to ensure the suppression of the corrections to a sufficient degree. An increasing ratio of lifetimes (3.16) leads to an increasing  $\Delta\Gamma_{min}$  since we have with  $\tau_S \approx T$ :

$$\Delta\Gamma_{min} \lesssim \Gamma_P - \Gamma_S \Leftrightarrow \Delta\Gamma_{min} T \lesssim \frac{\tau_S}{\tau_P} - 1. \quad (3.17)$$

In that way, an increased ratio  $\tau_S/\tau_P$  leads to an improvement of the adiabatic approximation. Therefore, one may set the limit of  $|\mathcal{E}| \lesssim 250$  V/cm or (3.16), respectively, see [68].

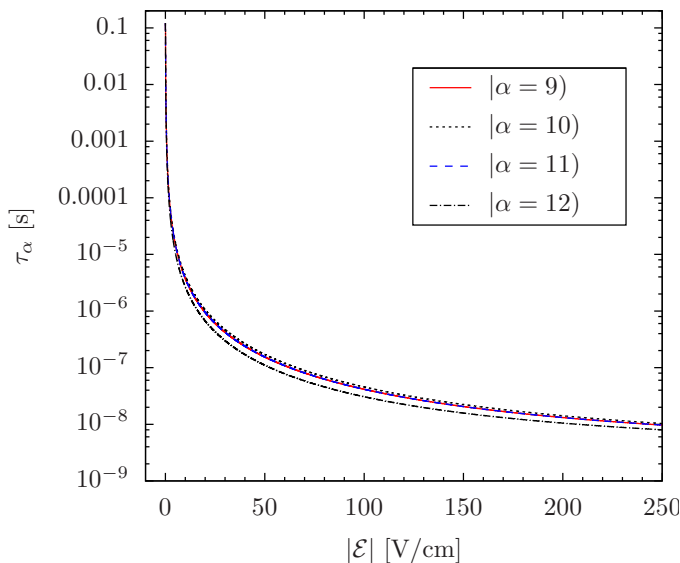


**Figure 3.3:** Lifetimes of the mixed  $2S_{1/2}$  states of hydrogen in the external electric field  $\mathcal{E} = \mathcal{E}\mathbf{e}_3$  as function of  $|\mathcal{E}|$ . For  $\mathcal{E} \approx 250$  V/cm these mixed states have lifetimes only one order of magnitude larger than  $\tau_P$  of the free 2P states, see (3.12).

### Rates of Change of the External Fields

The line integral (2.83) of Berry's phase accumulates the cycles of a path in parameter space. Thus, we would also like to increase the geometric phases via multiple cyclings of the electromagnetic field configuration. However, the rate of change of the external fields has to stay within certain limits for the adiabatic theorem to hold for our setup. As a consequence, the number of cyclings, which are directly related to the rate of change of the external fields, is also limited. More generally, the allowed rates of change for adiabaticity are discussed in [68] leading to the following conditions:

$$\max_{t \in [0, T]} \frac{1}{\mathcal{E}_0} \left| \frac{\partial \mathcal{E}(t)}{\partial t} \right| < \frac{1}{T} \cong \frac{1}{\tau_S}, \quad (3.18)$$

$$\max_{t \in [0, T]} \frac{1}{\mathcal{B}_0} \left| \frac{\partial \mathcal{B}(t)}{\partial t} \right| < \frac{1}{T} \cong \frac{1}{\tau_P}. \quad (3.19)$$

The constants  $\mathcal{E}_0 = 477.3 \text{ V/cm}$  and  $\mathcal{B}_0 = 43.65 \text{ mT}$  indicate the field strengths where the electric energy and the magnetic energy, respectively, are comparable with the Lamb shift  $L$ .

The relations (3.18) and (3.19) are the conditions for the rate of change of the external fields to assure adiabatic evolution of the eigenstates for a system at rest. Since we want to describe propagating atoms, we perform the transformation  $dt \rightarrow v_z^{-1} dz$ , where  $v_z$  is the velocity of the propagating atoms, leading to

$$\begin{aligned} \left| \frac{\partial \mathcal{E}(t)}{\partial t} \right| &\rightarrow v_z \left| \frac{\partial \mathcal{E}(z)}{\partial z} \right|, \\ \left| \frac{\partial \mathcal{B}(t)}{\partial t} \right| &\rightarrow v_z \left| \frac{\partial \mathcal{B}(z)}{\partial z} \right|. \end{aligned} \quad (3.20)$$

As discussed in [32], setting

$$\begin{aligned} \max \left| \frac{\partial \mathcal{E}(z)}{\partial z} \right| &= \frac{\Delta \mathcal{E}}{\Delta z}, \\ \max \left| \frac{\partial \mathcal{B}(z)}{\partial z} \right| &= \frac{\Delta \mathcal{B}}{\Delta z}, \end{aligned} \quad (3.21)$$

one finds the condition  $\Delta z \gtrsim 50 \mu\text{m}$  for a variation  $\Delta \mathcal{E} = 1 \text{ V/cm}$  and  $\Delta z \gtrsim 10 \mu\text{m}$  for a variation  $\Delta \mathcal{B} = 1 \text{ mT}$ . With these values similar conditions can be specified immediately for other field variations.

### Energy Differences

As depicted in the Breit-Rabi-diagram in Figure 3.4, the individual 2S states ( $\alpha = 9, \dots, 11$ ) are degenerate for vanishing magnetic field. Transitions between those states and the accompanied non-adiabatic evolution can be avoided if the energy differences  $\Delta E$  between the 2S states correspond to frequencies much larger than the frequencies  $\nu = 1/\Delta t$  of variation of the  $\mathcal{E}$ - and  $\mathcal{B}$ -fields. With the corresponding variation  $\Delta z = v_z \Delta t$  in  $z$ -direction we get

$$\Delta E \gg h\nu = \frac{h v_z}{\Delta z} \Rightarrow \Delta z \gg \frac{v_z}{\Delta E/h}. \quad (3.22)$$

### 3.2. Hydrogen in External Fields

Choosing for example  $\mathcal{B} = \mathcal{B}e_3$  with  $\mathcal{B} = 1$  mT for the  $F = 1$  states and  $v_z = 3500$  m/s [77], we obtain  $\Delta E/h \approx 25$  MHz, leading to  $\Delta z \gg 150 \mu\text{m}$ . Note that, for example, smaller  $\mathcal{B}$ -fields lead to smaller energy differences  $\Delta E$  and thus require larger variation lengths  $\Delta z$ .

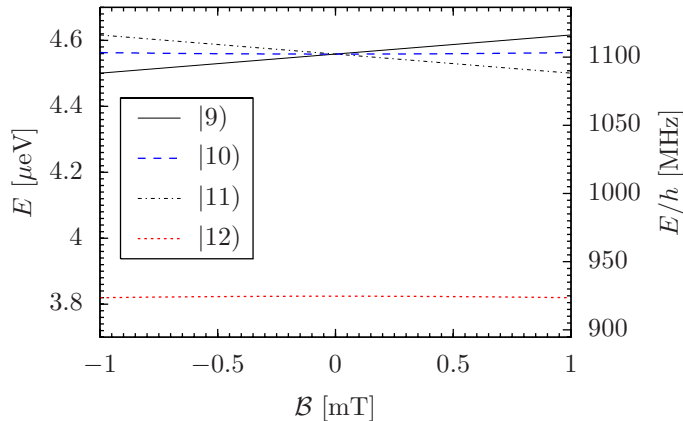


**Figure 3.4:** Breit-Rabi diagram for the 2S states of hydrogen. The magnetic field is  $\mathcal{B} = \mathcal{B}e_3$ . The Zeeman splitting between the states  $\alpha = 9, 10$ , and 11 vanishes for  $\mathcal{B} = 0$ .

Along with the restrictions of the lifetimes, Equations (3.21) and (3.22) constitute the adiabaticity conditions which have to be considered for specific paths in parameter space.

#### 3.2.2 The Parity-Violating Mass Matrix of Hydrogen

We consider the subspace of atomic states with principal quantum number  $n = 2$  of a hydrogen atom at rest exposed to varying external electric and magnetic fields. According to the Wigner-Weisskopf approximation the effective Schrödinger equation reads

$$i\partial_t|t\rangle = \underline{\mathcal{M}}(t)|t\rangle \quad (3.23)$$

where  $\underline{\mathcal{M}}(t)$  is the in general non-hermitian mass matrix, and  $|t\rangle$  is a state vector composed of the discrete undecayed states according to (3.10). Underlined operators denote their representation in the  $n = 2$  subspace.

To gain an explicit representation of  $\underline{\mathcal{M}}$ , we take into account the effective P-violating Hamiltonian (2.28). In light atoms such as hydrogen, the electrons are non-relativistic even near the nucleus and therefore the non-relativistic approximation (2.33) and (2.36) of  $H_{\text{PV}}$  becomes valid for hydrogen.

The mass matrix  $\underline{\mathcal{M}}(t)$  contains contributions from the external fields and  $H_{\text{PV}}$ . We are interested in PC and PV geometric phases, and we want to study them separately. Therefore, we split off a (very small) numerical factor  $\delta$  from the PV part of the mass matrix characterising the intrinsic strength of the PV terms. The mass matrix for

## Chapter 3. Berry Phases for Hydrogen

---

vanishing external fields

$$\begin{aligned}\tilde{\mathcal{M}}_0(\delta_1, \delta_2) &= \mathcal{M}_0 + \delta_1 \mathcal{M}_{\text{PV}}^{(1)} + \delta_2 \mathcal{M}_{\text{PV}}^{(2)} \\ &= \mathcal{M}_0 + \delta \mathcal{M}_{\text{PV}}\end{aligned}\quad (3.24)$$

including the P-odd Hamiltonian (2.28), is given in Table A.3 of Appendix A.2 in terms of the total angular momentum states  $|nL_J, F, F_3\rangle$ . The terms  $\mathcal{M}_{\text{PV}}^{(1)}$  and  $\mathcal{M}_{\text{PV}}^{(2)}$  correspond to the nuclear-spin independent and dependent PV interaction, respectively, cf. [68].

The mass matrix  $\mathcal{M}(t)$  for hydrogen exposed to external fields then reads

$$\mathcal{M}(t) = \mathcal{M}_0 - \underline{\mathbf{D}} \cdot \underline{\mathcal{E}}(t) - \underline{\boldsymbol{\mu}} \cdot \underline{\mathcal{B}}(t) + \delta \mathcal{M}_{\text{PV}} \quad (3.25)$$

in the  $n = 2$  subspace in dipole approximation with

$$\begin{aligned}\delta &= (\delta_1^2 + \delta_2^2)^{\frac{1}{2}} \\ \mathcal{M}_{\text{PV}} &= \sum_{i=1}^2 \frac{\delta_i}{\delta} \mathcal{M}_{\text{PV}}^{(i)},\end{aligned}\quad (3.26)$$

and

$$\delta_i \mathcal{M}_{\text{PV}}^{(i)} = \left( \langle 2L'_{J'}, F', F'_3 | H_{\text{PV}}^{(i)} | 2L_J, F, F_3 \rangle \right), \quad (3.27)$$

see (2.49)-(2.52).  $\underline{\mathbf{D}}$  and  $\underline{\boldsymbol{\mu}}$  are the electric and magnetic dipole operators, respectively. See Tables A.4 and A.5 of Appendix A.1 for their representation in the  $\{|nL_J, F, F_3\rangle\}$ -basis. We denote the mass matrix (3.25) without the P-violating terms by

$$\mathcal{M}^{(0)}(\underline{\mathcal{E}}, \underline{\mathcal{B}}) = \mathcal{M}_0 - \underline{\mathbf{D}} \cdot \underline{\mathcal{E}}(t) - \underline{\boldsymbol{\mu}} \cdot \underline{\mathcal{B}}(t). \quad (3.28)$$

In (3.25) we assume the external electromagnetic fields to be uniform over the atomic dimensions. Furthermore, we assume that  $\mathcal{M}(t)$  is diagonalisable for all times  $t$ , which can be ensured in the case of non-degeneracy for all  $t$ . This yields a complete set of linearly independent right and left eigenvectors for every time  $t$  as in Equation (2.67) with  $\alpha, \beta = 1, \dots, 16$ .

### 3.2.3 Structure of Degeneracies of Hydrogen

For our purposes we want the states evolving along a curve in parameter space to be non-degenerate at all points of the curve. Of course, having chosen an explicit curve, the evolution of the complex energies (2.68) can be tracked numerically to ensure non-degeneracy. But since we want to employ such curves as flexibly as possible, knowledge of these degeneracies is worthwhile to exclude certain regions of parameter space beforehand and to have the possibility of modifying the curves to some degree. The latter aspect is especially valuable for the investigation of spin echo signals.

### Complex Degeneracies

Degeneracies for the  $n = 2$  states of hydrogen occur for  $\mathcal{B} = \mathbf{0}$  with arbitrary  $\mathcal{E}$ . This is a consequence of T invariance. For  $\mathcal{B} = \mathbf{0}$  and  $\mathcal{E} \neq \mathbf{0}$  we can choose the vector  $\mathbf{e}'_3 = \mathcal{E}/|\mathcal{E}|$  as quantisation axis of angular momentum. Then  $F'_3$  is a good quantum number and time reversal invariance implies that there are corresponding eigenstates of  $\mathcal{M}(\mathcal{E}, \mathcal{B} = \mathbf{0})$  with quantum numbers  $F'_3$  and  $-F'_3$  and having the same complex eigenenergies. See Sections 3.3 and 3.4 of [80] for a proof of this result using resolvent methods. We numerically checked that, at least for moderate  $\mathcal{B}$  fields

$$|\mathcal{B}| < 53.8 \text{ mT} \quad (3.29)$$

below the first level crossing in the Breit-Rabi diagram, there are no further degeneracy points or regions.

To illustrate our findings, we present in Figure 3.5 the product of differences of complex eigenenergies in the following way. Defining

$$P(\mathcal{E}, \mathcal{B}) = \mathcal{N} \prod_{\substack{\alpha, \beta=1 \\ \alpha \neq \beta}}^{16} |E(\alpha) - E(\beta)|, \quad (3.30)$$

with suitable normalisation constant  $\mathcal{N}$ , full complex degeneracies correspond to  $P = 0$ . We employ Cartesian grids of  $20^3$  parameter points, thereby also sampling the axes and the origin of three-dimensional parameter spaces which consist of three field components of the external fields, along with fixed values for the remaining three field components. Defining different thresholds  $T_i \geq 0$  successively closer to zero and plotting all points  $(\mathcal{E}, \mathcal{B})$  in the grid which obey  $P(\mathcal{E}, \mathcal{B}) \leq T$ , the pattern of degeneracies can be revealed. Of course, due to numerical errors  $P = 0$  may not be reached even if there is a degeneracy for the according parameter values. Vice versa, the numerics could propose a degeneracy where there is none. However, as we observe in Figure 3.5 the patterns of degeneracies are clearly pronounced. From Figure 3.5 we can state as a result for  $\mathcal{B}$  fields obeying (3.29) that degeneracies occur if and only if  $\mathcal{B} = \mathbf{0}$ .

Omitting the PV part of the mass matrix, we qualitatively obtain the same patterns of degeneracies. That is, besides the case of vanishing  $\mathcal{B}$ -field, we found no further complex degeneracies – not for the 2S states and also not for the 2P states.

### Degeneracies in the Real Part

Moreover, we investigated the parameter spaces for higher magnetic fields including the regions of all crossings in the Breit-Rabi diagram. These crossings are degeneracies of the real part of the complex eigenenergies and are often considered beneficial for the observation of PV effects, see, for instance, [49, 50, 84], since then the denominator in (2.54) becomes comparably small as discussed also in Section 2.5. However, when dealing with Berry phases one has to be aware of the adiabaticity conditions of Section 3.2.1 which demand sufficient splitting in the real parts of the eigenenergies. From the discussion above we find the degeneracies at the high crossings not to be full complex degeneracies.

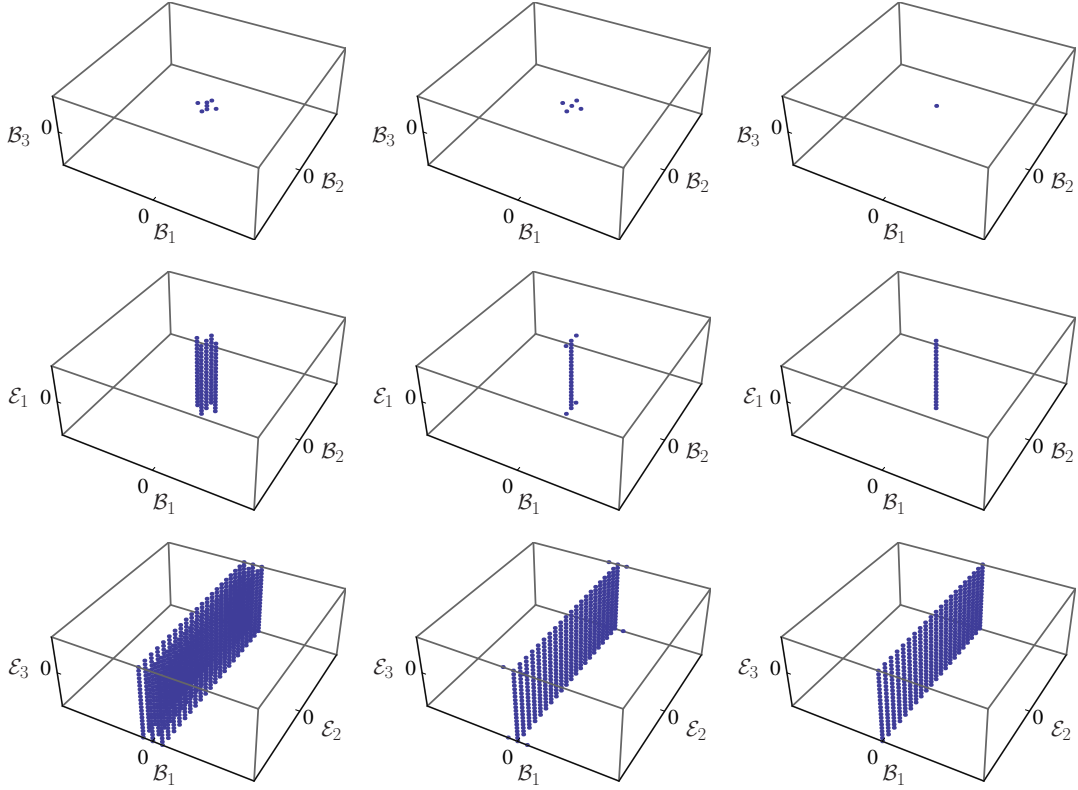


**Figure 3.5:** Representations of (3.30) for the parameter spaces  $\{\mathcal{B}_1, \mathcal{B}_2, \mathcal{B}_3\}$  in the first row,  $\{\mathcal{B}_1, \mathcal{B}_2, \mathcal{E}_1\}$  in the second row, and  $\{\mathcal{B}_1, \mathcal{E}_2, \mathcal{E}_3\}$  in the third row. For the thresholds in the first, second, and third column, respectively, we set  $T_1 > T_2 > T_3 = 0$ . The figures are generated with Mathematica by numerically solving the eigenvalue equation of the effective Hamiltonian (3.25) at  $20^3$  grid points. The employed accuracy is 100 digits. For  $\{\mathcal{B}_1, \mathcal{B}_2, \mathcal{B}_3\}$  we find one point of degeneracy at  $\mathcal{B} = \mathbf{0}$ . In the discretised parameter space regions of  $\{\mathcal{B}_1, \mathcal{B}_2, \mathcal{E}_1\}$  and  $\{\mathcal{B}_1, \mathcal{E}_2, \mathcal{E}_3\}$  we observe 20 degeneracies (for  $\mathcal{B}_1 = \mathcal{B}_2 = 0$ ) and  $20^2$  degeneracies (for  $\mathcal{B}_1 = 0$ ), respectively. Hence, we state that degeneracies occur if and only if  $\mathcal{B} = \mathbf{0}$ . Choosing different edge lengths of the grid for the magnetic as well as electric field strengths, we qualitatively find the same results in terms of the patterns of degeneracies. In the given plots, magnetic and electric field components span the intervals  $[-53.8 \text{ mT}, 53.8 \text{ mT}]$  and  $[-1 \text{ V/cm}, 1 \text{ V/cm}]$ , respectively. The remaining three field components are set to zero. For the parameter space  $\{\mathcal{E}_1, \mathcal{E}_2, \mathcal{E}_3\}$  with  $\mathcal{B} = \mathbf{0}$ , we find numerically  $P \equiv 0$  at every considered parameter value.

### 3.2.4 Chirality of Hydrogen in Electromagnetic Fields

We want to shed some light on the role of electromagnetic fields concerning PV experiments with hydrogen. To actually detect P violation in hydrogen, it is essential that the hydrogen atom interacts with an oriented background because the atom itself is not chiral. In some way, we have to introduce handedness in order to compare two different versions of an experiment. For our system, this background is provided by the external

electric and magnetic fields. Space-reflecting  $\mathcal{E}$  or mirror-reflecting  $\mathcal{B}$  can provide the possibility to perform an experiment which is actually different from the unreflected one. If it were not, we obviously would obtain the same numerical quantities for our observables in both versions of the experiment – no matter how large the contribution from a P-violating part  $\delta\mathcal{M}_{PV}$  of the mass matrix to the those observables is. Note, that if  $\mathcal{E}$  and  $\mathcal{B}$  are orthogonal, the setup is not chiral since the P-transformed setup can be superimposed with the original one by a  $\pi$ -rotation about the magnetic field axis.

### The Mass Matrix

Of course, in addition to such an oriented background we need the mass matrix not to commute with the parity operator P. Thus, additionally to the external field dependence (3.28), the P-violating part  $\delta\mathcal{M}_{PV}$  of the mass matrix (3.25) is required for the symmetry of space reflection to be broken for hydrogen in external fields. We also want to point out that a pure magnetic field cannot give rise to P-violating effects for (3.25) when considering an experimental setup with 2S states where the unperturbed initial and final states have the same parity. The reason in this case is simply that only the electric dipole amplitude is coupled to the PV part of the system in first-order perturbation theory, see (2.46) and (2.47).

On the other hand, the system of atom and pure electric field does not allow for a PV effect either. The  $\mathcal{E}$ -field changes sign under P-transformation but the system can be rotated back to the original situation leaving us with no possibility to distinguish two chiral versions of the experiment. Note that a spatially extended chiral electric field  $\mathcal{E}(\mathbf{x})$  does allow for PV effects, cf. [80, 82]. In contrast, the atoms described by the approximation (3.25) are effectively not exposed such a spatially extended field.

That is, to derive PV effects for our system of hydrogen in external fields we need both electric and magnetic fields.

### The Atomic Motion

For the calculation of P-violating effects in hydrogen, we consider atoms at rest for simplicity of argumentation from Section 3.3 forward. That is, we regard the external fields as functions of time. As in (3.20) the time dependence of the external fields can be transformed into a longitudinal motion of the atoms to provide for the actual experimental conditions of an atom interferometer with stationary electromagnetic fields in the laboratory reference frame. The longitudinal motion of the atoms is not reversed in the space reflected experiment in our case. That is, we are testing parity merely for a subsystem of the whole experiment, namely the hydrogen atom at rest. But nevertheless, this is a valid experiment to test parity in nature since we can calculate the effects which P-violating terms  $\delta\mathcal{M}_{PV}$  in the mass matrix will have on the outcomes although not the whole experiment is P-transformed.

### 3.3 Geometric Phases for Atoms at Rest

The basic theoretical tool for our considerations is the effective Schrödinger equation (3.23) describing the evolution of the undecayed states with state vector  $|t\rangle$  in the Wigner-Weisskopf approximation. In the following, we assume the conditions for adiabatic evolution of the metastable 2S states discussed in Section 3.2.1 to hold. For concrete experimental setups we will calculate the adiabaticity conditions explicitly. In [67,68] the adiabatic theorem and geometric phases for metastable states were studied and in the present work we shall apply and extend the results obtained there. The mass matrix  $\underline{\mathcal{M}}$  in (3.23) depends on the slowly varying parameters  $\mathcal{E}$  and  $\mathcal{B}$ . Thus, we have a six-dimensional parameter space. Geometric phases are connected with the trajectories followed by the field strengths as function of time in this space as discussed in Section 2.6.

#### Notations

We shall, for general discussions, denote  $\mathcal{E}$  and  $\mathcal{B}$  collectively as parameters  $K$ ,

$$\begin{pmatrix} \mathcal{E} \\ \mathcal{B} \end{pmatrix} = \begin{pmatrix} K_1 \\ K_2 \\ K_3 \\ K_4 \\ K_5 \\ K_6 \end{pmatrix} \equiv K . \quad (3.31)$$

Indices  $i, j \in \{1, 2, 3\}$  will be normal space indices, for instance  $\mathcal{E}_i, \mathcal{B}_i$  etc., or refer to any three particular components of  $K$ . Indices  $a, b$  shall refer to the components  $K_a, a \in \{1, \dots, 6\}$ . The mass matrix (3.25) shall be considered as function of the six parameters  $K = K_a$ . Then, the effective Schrödinger equation (3.23) reads, replacing  $(\mathcal{E}, \mathcal{B})$  by  $K$ ,

$$i \frac{\partial}{\partial t} |t\rangle = \underline{\mathcal{M}}(K(t)) |t\rangle . \quad (3.32)$$

With (3.32) and the reduced time  $\tau$ , introduced in (2.63), we write

$$i \partial_\tau |T; \tau\rangle = \frac{T}{\tau_0} \hat{\underline{\mathcal{M}}}(\tau) |T; \tau\rangle \quad (3.33)$$

with  $\hat{\underline{\mathcal{M}}}(\tau) = \underline{\mathcal{M}}(K(t))$  and  $|t\rangle \equiv |T; K(t)\rangle \equiv |T; \tau\rangle$ .

#### Geometric Phases

As discussed in [67] and [68], we get the adiabatic solutions of (3.33), i.e., the solutions in the limit of large  $T$ , for the metastable states as follows. We expand  $|T; \tau\rangle$  in terms of the eigenstates  $|\alpha, \tau\rangle$  of  $\hat{\underline{\mathcal{M}}}(\tau)$ :

$$|T; \tau\rangle = \sum_{\alpha=1}^{16} \psi_\alpha(T; \tau) |\alpha, \tau\rangle . \quad (3.34)$$

### 3.3. Geometric Phases for Atoms at Rest

---

We always suppose slow enough variation of the parameter vector  $K(t)$  and

$$|E_\alpha(K) - E_\beta(K)| \geq c > 0 \quad (3.35)$$

for all  $\alpha \neq \beta$  where  $c$  is a constant. Exceptions where (3.35) is not required to hold will be clearly indicated. Inserting (3.34) into (3.33), we end up with a set of 16 coupled differential equations

$$i\partial_\tau \psi_\alpha(T; \tau) = \frac{T}{\tau_0} E(\alpha, \tau) \psi_\alpha(T; \tau) - \sum_{\beta=1}^{16} (\widetilde{\alpha}, \widetilde{\tau} | i\partial_\tau | \beta, \tau) \psi_\beta(T; \tau) . \quad (3.36)$$

As discussed in [67], these equations partially decouple in the adiabatic limit, i.e., for large  $T$  – which is equivalent to a slowly varying environment if the parameter range  $0 \leq \tau \leq \tau_0$  is fixed. More explicitly, the evolution of the 2S states decouples from that of the 2P states. The evolving metastable states contain only contributions from the instable states that are suppressed by a factor of order  $1/T$ . And those metastable states  $\alpha, \beta$  which are supposed to have equal decay rates  $\Gamma(\alpha, \tau) = \Gamma(\beta, \tau)$  are not coupled any more among each other if the corresponding eigenvalues are non-degenerate. At this point we get the connection to the relation (2.78) which is based on the adiabatic theorem and implies the decoupling discussed above. As found in [67], the four solutions of (3.36) for the metastable 2S states are then

$$\psi_\alpha(T; \tau) = \exp \left[ -i \frac{T}{\tau_0} \varphi_\alpha(\tau) + i \gamma_\alpha(\tau) \right] \left\{ \psi_\alpha(T; 0) + \mathcal{O} \left( \frac{1}{T} \right) \right\} , \quad (3.37)$$

$$(\alpha \in I = \{9, 10, 11, 12\}) , \quad (3.38)$$

where  $T\varphi_\alpha(\tau)/\tau_0$  and  $\gamma_\alpha(\tau)$  are the dynamic and geometric phases, respectively. For metastable states both will in general have real and imaginary parts. Here and in the following, the labels  $\alpha = 9, 10, 11$ , and  $12$  correspond to the states  $|\alpha, K\rangle \equiv |2\hat{S}_{1/2}, F, F_3, \mathcal{E}, \mathcal{B}\rangle$ . These originate from the states  $|2S_{1/2}, F, F_3\rangle$  with  $(F, F_3) = (1, 1), (1, 0), (1, -1)$ , and  $(0, 0)$ , respectively, through the mixing with the 2P states according to the PV, the  $\mathcal{E}$ , and  $\mathcal{B}$  terms in the mass matrix (3.25). This numbering has to be carefully defined, see Appendix A.1, since we have to follow the states in their adiabatic motion along trajectories in parameter space. As explained in Appendix A.1,  $(F, F_3)$  are then only labels of the states, no longer the total angular momentum quantum numbers. Thus, in order to avoid confusion, we shall stick to the labels  $\alpha$  for our states in the following.

In terms of the notations (3.31) and (3.32) we have, for  $t \geq 0$ ,

$$|t\rangle = \sum_{\alpha \in I} \psi_\alpha(t) |\alpha, K(t)\rangle \quad (3.39)$$

where

$$\psi_\alpha(t) = \exp \left[ -i\varphi_\alpha(t) + i\gamma_\alpha(t) \right] \psi_\alpha(0) , \quad (3.40)$$

$$\varphi_\alpha(t) = \int_0^t dt' E_\alpha(K(t')) , \quad (3.41)$$

$$\gamma_\alpha(t) = \int_0^t dt' \langle \alpha, \widetilde{K(t')} | i \frac{\partial}{\partial t'} | \alpha, K(t') \rangle =: i \int_0^t dt' \underline{\mathcal{Q}}_{\alpha\alpha}(t) . \quad (3.42)$$

Below we shall study in detail the geometric phases for metastable states for the case that  $K(t)$  runs through a closed loop in parameter space.

### 3.4 Numerical Computation of Berry Phases

Following Section 3.2.2, the geometric phases in general consist of a P-conserving and two P-violating parts where the latter are nuclear-spin dependent and nuclear-spin independent, respectively. The aim in this section is to get access to these distinguishable contributions. Therefore, a perturbative approach for the computation of the geometric phases is employed, where the perturbations are the P-violating contributions  $\delta_1 \underline{\mathcal{M}}_{\text{PV}}^{(1)}$  and  $\delta_2 \underline{\mathcal{M}}_{\text{PV}}^{(2)}$  to the mass matrix (3.25). Due to their proportionality to  $\delta_1$  and  $\delta_2$  respectively, they are supposed to be sufficiently small.

The derivation was done in [68], and here we will give only the results and notations. With (3.42) one finds

$$\underline{\mathcal{Q}}_{\alpha\alpha}(K(t), \delta_1, \delta_2) = \underline{\mathcal{Q}}_{\text{PC},\alpha\alpha}(K(t)) + \delta_1 \underline{\mathcal{Q}}_{\text{PV},\alpha\alpha}^{(1)}(K(t)) + \delta_2 \underline{\mathcal{Q}}_{\text{PV},\alpha\alpha}^{(2)}(K(t)) + \mathcal{O}(\delta^2) , \quad (3.43)$$

where  $\mathcal{O}(\delta^2)$  is the short-hand notation for  $\mathcal{O}(\delta_1^2, \delta_2^2, \delta_1\delta_2)$  and

$$\underline{\mathcal{Q}}_{\text{PC},\alpha\beta}(K(t)) = \langle \alpha^{(0)}, \widetilde{K(t)} | \frac{\partial}{\partial t} | \beta^{(0)}, K(t) \rangle , \quad (3.44)$$

$$\begin{aligned} \underline{\mathcal{Q}}_{\text{PV},\alpha\alpha}^{(i)}(K(t)) = \sum_{\gamma \neq \alpha} & \left( \frac{\underline{\mathcal{M}}_{\text{PV},\alpha\gamma}^{(i)}(K(t)) \underline{\mathcal{Q}}_{\text{PC},\gamma\alpha}(K(t))}{E(\alpha^{(0)}, K(t)) - E(\gamma^{(0)}, K(t))} \right. \\ & \left. + \frac{\underline{\mathcal{Q}}_{\text{PC},\alpha\gamma}(K(t)) \underline{\mathcal{M}}_{\text{PV},\gamma\alpha}^{(i)}(K(t))}{E(\alpha^{(0)}, K(t)) - E(\gamma^{(0)}, K(t))} \right) , \end{aligned} \quad (3.45)$$

$$\underline{\mathcal{M}}_{\text{PV},\alpha\gamma}^{(i)}(K(t)) = \langle \alpha^{(0)}, \widetilde{K(t)} | \underline{\mathcal{M}}_{\text{PV}}^{(i)} | \gamma^{(0)}, K(t) \rangle , \quad (i = 1, 2) . \quad (3.46)$$

Here,  $|\alpha^{(0)}, K(t)\rangle$  and  $E(\alpha^{(0)}, K(t))$  are the eigenstates and eigenvalues of the unperturbed mass matrix (3.28). We denote the decomposition of the geometric phases as

$$\gamma_\alpha(t, \delta_1, \delta_2) = \gamma_{\text{PC},\alpha}(t) + \delta_1 \gamma_{\text{PV},\alpha}^{(1)}(t) + \delta_2 \gamma_{\text{PV},\alpha}^{(2)}(t) + \mathcal{O}(\delta^2) , \quad (3.47)$$

$$\gamma_{\text{PC},\alpha}(t) = i \int_0^t dt' \underline{\mathcal{Q}}_{\text{PC},\alpha\alpha}(K(t')) , \quad (3.48)$$

$$\gamma_{\text{PV},\alpha}^{(i)}(t) = i \int_0^t dt' \underline{\mathcal{Q}}_{\text{PV},\alpha\alpha}^{(i)}(K(t')) , \quad (i = 1, 2) . \quad (3.49)$$

The eigenvectors  $|\alpha(t)\rangle$  are defined up to a complex phase factor  $e^{i\eta(t)}$ . As shown in [83] the individual contributions (3.48) and (3.49) to the geometric phase are invariant under local phase transformations of the eigenstates  $|\alpha(t)\rangle$  according to

$$\begin{aligned} |\alpha(t)\rangle &\longrightarrow |\alpha(t)\rangle' = e^{i\eta_\alpha(t)} |\alpha(t)\rangle , \\ (\widetilde{\alpha(t)}| &\longrightarrow (\widetilde{\alpha(t)}|' = e^{-i\eta_\alpha(t)} (\widetilde{\alpha(t)}| \end{aligned} \quad (3.50)$$

where  $\eta_\alpha(t)$  has to be real in order to respect (2.69). But since the real phase  $\eta(t)$  can be chosen arbitrarily at the discrete points  $z$  used in the numerical implementation, the scalar product  $(\widetilde{\alpha(t)}|\alpha(t + \Delta t)\rangle)$  connecting successive points is not uniquely determined. Indeed, numerical calculations showed instabilities in the smoothness of the eigenvectors  $|\alpha(t)\rangle$  at successive times  $t$ . The general idea to solve this issue is the introduction of a controlled phase factor  $e^{i\eta_\alpha(t)}$  for the eigenvectors  $|\alpha(t)\rangle$  at every discrete parameter point [173]. With that, one can create a set of uniquely defined eigenvectors at every time  $t$  in order to compute (3.47). The procedural details can be found in [83]. This approach gives access to the geometric phases via an adaptive implementation of Riemann integrals for (3.47).

### 3.5 Geometric Flux Densities

In this section we shall discuss general relations and properties for geometric phases and the corresponding flux densities. These relations hold for any system with time evolution described by an effective Schrödinger equation (3.1). The dependence of  $\underline{\mathcal{M}}$  on  $K$  need not be linear as for  $\underline{\mathcal{M}}(\mathcal{E}, \mathcal{B}) = \underline{\mathcal{M}}(K)$  in Section 3.2.2.

#### Notations

Below we shall make extensive use of the quasi projectors defined as

$$\mathbb{P}_\alpha(K) = |\alpha, K\rangle(\widetilde{\alpha, K}| . \quad (3.51)$$

These satisfy

$$\mathbb{P}_\alpha(K)\mathbb{P}_\beta(K) = \begin{cases} \mathbb{P}_\alpha(K) & \text{for } \alpha = \beta , \\ 0 & \text{for } \alpha \neq \beta , \end{cases} \quad (3.52)$$

$$\sum_\alpha \mathbb{P}_\alpha(K) = \mathbb{1} , \quad (3.53)$$

but, in general, the  $\mathbb{P}_\alpha(K)$  are non-hermitian operators. Furthermore, we shall need the resolvent  $(\zeta - \underline{\mathcal{M}}(K))^{-1}$  where  $\zeta$  is arbitrary complex. With the help of the quasi projectors we get

$$(\zeta - \underline{\mathcal{M}}(K))^{-n} = \sum_\alpha (\zeta - E_\alpha(K))^{-n} \mathbb{P}_\alpha(K) , \quad (n = 0, 1, 2, \dots) , \quad (3.54)$$

see Appendix B.2.

## Chapter 3. Berry Phases for Hydrogen

---

We will consider systems over a time interval  $0 \leq t \leq T$  where the parameter vector  $K(t)$  runs over a closed curve  $\mathcal{C}$

$$\mathcal{C} : t \rightarrow K(t), \quad t \in [0, T], \quad K(T) = K(0) . \quad (3.55)$$

### 3.5.1 Representations and General Properties

The geometric phases (3.42) acquired by the metastable states are then

$$\gamma_\alpha(\mathcal{C}) \equiv \gamma_\alpha(T) = \int_0^T dt' (\widetilde{\alpha, K(t')} | i \frac{\partial}{\partial t'} | \alpha, K(t')) = \int_{\mathcal{C}} (\widetilde{\alpha, K} | i d | \alpha, K) , \quad (3.56)$$

$\alpha \in I$ , where  $I$  is the index set of the metastable states. For our concrete hydrogen case  $I$  is given in (3.38). Here and in the following, we use the exterior derivative calculus; see for instance [174]. Let  $\mathcal{F}$  be a surface with boundary  $\mathcal{C}$ ,

$$\partial \mathcal{F} = \mathcal{C} , \quad (3.57)$$

and suppose that  $\mathcal{M}(K)$  can be diagonalised for all  $K \in \mathcal{F}$ , and (3.35) holds for the eigenvalues. We get then

$$\gamma_\alpha(\mathcal{C}) = i \int_{\partial \mathcal{F}} (\widetilde{\alpha, K} | d | \alpha, K) = i \int_{\mathcal{F}} d(\widetilde{\alpha, K} | d | \alpha, K) = \int_{\mathcal{F}} Y_{\alpha,ab}(K) dK_a \wedge dK_b . \quad (3.58)$$

Here we define the geometric flux densities  $Y_{\alpha,ab}(K)$ , the analogues for the metastable states of the quantities  $\mathbf{V}$  of [22], by<sup>5</sup>

$$\begin{aligned} Y_{\alpha,ab} dK_a \wedge dK_b &= i d(\widetilde{\alpha, K} | d | \alpha, K) , \\ Y_{\alpha,ab}(K) + Y_{\alpha,ba}(K) &= 0 . \end{aligned} \quad (3.59)$$

From (3.59) we get easily<sup>6</sup>

$$\begin{aligned} Y_{\alpha,ab}(K) dK_a \wedge dK_b &= +i (d(\widetilde{\alpha, K} |) \wedge (d | \alpha, K)) \\ &= -i \sum_{\beta \neq \alpha} (\widetilde{\alpha, K} | d | \beta, K) \wedge (\widetilde{\beta, K} | d | \alpha, K) . \end{aligned} \quad (3.60)$$

Here we use

$$(d(\widetilde{\alpha, K} |) | \beta, K) + (\widetilde{\alpha, K} | d | \beta, K) = 0 \quad (3.61)$$

which follows from (2.69). Note that in (3.60)  $\alpha$  is the index of a metastable state,  $\alpha \in I$ , but in the sum over  $\beta$  *all* states with  $\beta \neq \alpha$  have to be included.

---

<sup>5</sup>A symmetric contribution  $Y_{\alpha,ab}^S = Y_{\alpha,ba}^S$  of  $Y_{\alpha,ab} = Y_{\alpha,ab}^S + Y_{\alpha,ab}^A$  has no consequence for  $\gamma_\alpha(\mathcal{C})$  due to  $dK_b \wedge dK_a = -dK_a \wedge dK_b$ . We therefore demand  $Y_{\alpha,ab}$  to be antisymmetric under  $a \leftrightarrow b$ .

<sup>6</sup>We have  $i (d(\widetilde{\alpha} |) \wedge (d | \alpha)) = i \sum_{\beta} (d(\widetilde{\alpha} |) | \beta) \wedge (\widetilde{\beta} | d | \alpha) = -i \sum_{\beta} (\widetilde{\alpha} | d | \beta) \wedge (\widetilde{\beta} | d | \alpha)$ , while  $(\widetilde{\alpha} | d | \alpha) \wedge (\widetilde{\alpha} | d | \alpha) \equiv 0$ .

**Further Representations and Properties for Geometric Flux Densities**

From (2.67) and (2.69) we get for  $\beta \neq \gamma$

$$(\widetilde{\beta}, \widetilde{K} | \underline{\mathcal{M}}(K) | \gamma, K) = 0 . \quad (3.62)$$

Taking the exterior derivative in (3.62) and using (3.61) gives

$$[E_\beta(K) - E_\gamma(K)](\widetilde{\beta}, \widetilde{K} | d | \gamma, K) + (\widetilde{\beta}, \widetilde{K} | (d \underline{\mathcal{M}}(K)) | \gamma, K) = 0 . \quad (3.63)$$

Since we suppose (3.35) to hold for all  $K \in \mathcal{F}$  we get for  $\beta \neq \gamma$

$$(\widetilde{\beta}, \widetilde{K} | d | \gamma, K) = - \frac{(\widetilde{\beta}, \widetilde{K} | (d \underline{\mathcal{M}}(K)) | \gamma, K)}{E_\beta(K) - E_\gamma(K)} . \quad (3.64)$$

Inserting this in (3.60), we obtain<sup>7</sup>

$$\begin{aligned} Y_{\alpha,ab}(K) &= \frac{i}{2} \sum_{\beta \neq \alpha} [E_\alpha(K) - E_\beta(K)]^{-2} (\widetilde{\alpha}, \widetilde{K} | \frac{\partial \underline{\mathcal{M}}(K)}{\partial K_a} | \beta, K) (\widetilde{\beta}, \widetilde{K} | \frac{\partial \underline{\mathcal{M}}(K)}{\partial K_b} | \alpha, K) - (a \leftrightarrow b) \\ &= \frac{i}{2} \sum_{\beta \neq \alpha} [E_\alpha(K) - E_\beta(K)]^{-2} \text{Tr} \left[ \mathbb{P}_\alpha(K) \frac{\partial \underline{\mathcal{M}}(K)}{\partial K_a} \mathbb{P}_\beta(K) \frac{\partial \underline{\mathcal{M}}(K)}{\partial K_b} - (a \leftrightarrow b) \right] \end{aligned} \quad (3.65)$$

where we use the quasi projectors (3.51).

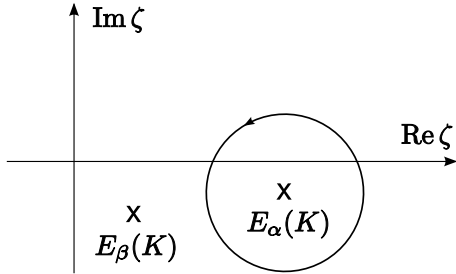


**Figure 3.6:** The complex  $\zeta$  plane with the (schematic) location of the energy eigenvalues  $E_\alpha(K)$  and  $E_\beta(K)$  with  $\beta \neq \alpha$ . The curve  $S_\alpha$  encircles only  $E_\alpha(K)$ .

We shall now derive an integral representation for  $Y_{\alpha,ab}(K)$ . Consider the complex  $\zeta$  plane, see Figure 3.6, where we mark schematically the position of the energy eigenvalues  $E_\alpha(K)$  and  $E_\beta(K)$ ,  $\beta \neq \alpha$ . Since we suppose (3.35) to hold we can choose a closed curve  $S_\alpha$  which encircles only  $E_\alpha(K)$  but where all  $E_\beta(K)$  with  $\beta \neq \alpha$  are outside. The geometric flux densities (3.59), (3.65) are then given as a complex integral

$$Y_{\alpha,ab}(K) = \frac{i}{2} \frac{1}{2\pi i} \oint_{S_\alpha} d\zeta \text{Tr} \left[ \frac{1}{(\zeta - \underline{\mathcal{M}}(K))} \frac{\partial \underline{\mathcal{M}}(K)}{\partial K_a} \frac{1}{(\zeta - \underline{\mathcal{M}}(K))^2} \frac{\partial \underline{\mathcal{M}}(K)}{\partial K_b} \right] . \quad (3.66)$$

The proof of (3.66) is given in Appendix B.1.

<sup>7</sup>We use  $d = \sum_a dK_a \frac{\partial}{\partial K_a}$  and write  $Y_{\alpha,ab}$  such that its antisymmetry with respect to  $a \leftrightarrow b$  is evident. The trace operator is abbreviated as Tr.

### Derivatives of Flux Densities

From (3.66) we get convenient relations for the derivatives of  $Y_{\alpha,ab}(K)$ , see Appendix B.1,

$$\begin{aligned} \frac{\partial}{\partial K_a} Y_{\alpha,bc}(K) &= \frac{i}{2} \frac{1}{2\pi i} \oint_{S_\alpha} d\zeta \left\{ \text{Tr} \left[ \frac{1}{(\zeta - \underline{\mathcal{M}}(K))} \frac{\partial^2 \underline{\mathcal{M}}(K)}{\partial K_a \partial K_b} \frac{1}{(\zeta - \underline{\mathcal{M}}(K))^2} \frac{\partial \underline{\mathcal{M}}(K)}{\partial K_c} \right] \right. \\ &+ \left. \text{Tr} \left[ \frac{1}{(\zeta - \underline{\mathcal{M}}(K))} \frac{\partial \underline{\mathcal{M}}(K)}{\partial K_a} \frac{1}{(\zeta - \underline{\mathcal{M}}(K))} \frac{\partial \underline{\mathcal{M}}(K)}{\partial K_b} \frac{1}{(\zeta - \underline{\mathcal{M}}(K))^2} \frac{\partial \underline{\mathcal{M}}(K)}{\partial K_c} \right] \right\} - (b \leftrightarrow c), \end{aligned} \quad (3.67)$$

which can also be written as

$$\begin{aligned} \frac{\partial}{\partial K_a} Y_{\alpha,bc}(K) &= \frac{i}{2} \left\{ \sum_{\beta \neq \alpha} [E_\alpha(K) - E_\beta(K)]^{-2} \right. \\ &\times \text{Tr} \left[ \mathbb{P}_\alpha(K) \frac{\partial^2 \underline{\mathcal{M}}(K)}{\partial K_a \partial K_b} \mathbb{P}_\beta(K) \frac{\partial \underline{\mathcal{M}}(K)}{\partial K_c} - \mathbb{P}_\alpha(K) \frac{\partial \underline{\mathcal{M}}(K)}{\partial K_c} \mathbb{P}_\beta(K) \frac{\partial^2 \underline{\mathcal{M}}(K)}{\partial K_a \partial K_b} \right] \\ &+ \sum_{\beta \neq \alpha} [E_\alpha(K) - E_\beta(K)]^{-3} \\ &\times \text{Tr} \left[ -2\mathbb{P}_\alpha(K) \frac{\partial \underline{\mathcal{M}}(K)}{\partial K_a} \mathbb{P}_\alpha(K) \frac{\partial \underline{\mathcal{M}}(K)}{\partial K_b} \mathbb{P}_\beta(K) \frac{\partial \underline{\mathcal{M}}(K)}{\partial K_c} \right. \\ &+ \mathbb{P}_\alpha(K) \frac{\partial \underline{\mathcal{M}}(K)}{\partial K_a} \mathbb{P}_\beta(K) \frac{\partial \underline{\mathcal{M}}(K)}{\partial K_b} \mathbb{P}_\alpha(K) \frac{\partial \underline{\mathcal{M}}(K)}{\partial K_c} \\ &+ \left. \mathbb{P}_\beta(K) \frac{\partial \underline{\mathcal{M}}(K)}{\partial K_a} \mathbb{P}_\alpha(K) \frac{\partial \underline{\mathcal{M}}(K)}{\partial K_b} \mathbb{P}_\alpha(K) \frac{\partial \underline{\mathcal{M}}(K)}{\partial K_c} \right] \\ &+ \sum_{\beta, \gamma \neq \alpha} [E_\alpha(K) - E_\beta(K)]^{-1} [E_\alpha(K) - E_\gamma(K)]^{-2} \\ &\times \text{Tr} \left[ \mathbb{P}_\alpha(K) \frac{\partial \underline{\mathcal{M}}(K)}{\partial K_a} \mathbb{P}_\beta(K) \frac{\partial \underline{\mathcal{M}}(K)}{\partial K_b} \mathbb{P}_\gamma(K) \frac{\partial \underline{\mathcal{M}}(K)}{\partial K_c} \right. \\ &+ \mathbb{P}_\beta(K) \frac{\partial \underline{\mathcal{M}}(K)}{\partial K_a} \mathbb{P}_\alpha(K) \frac{\partial \underline{\mathcal{M}}(K)}{\partial K_b} \mathbb{P}_\gamma(K) \frac{\partial \underline{\mathcal{M}}(K)}{\partial K_c} \\ &- \mathbb{P}_\gamma(K) \frac{\partial \underline{\mathcal{M}}(K)}{\partial K_a} \mathbb{P}_\beta(K) \frac{\partial \underline{\mathcal{M}}(K)}{\partial K_b} \mathbb{P}_\alpha(K) \frac{\partial \underline{\mathcal{M}}(K)}{\partial K_c} \\ &- \left. \mathbb{P}_\beta(K) \frac{\partial \underline{\mathcal{M}}(K)}{\partial K_a} \mathbb{P}_\gamma(K) \frac{\partial \underline{\mathcal{M}}(K)}{\partial K_b} \mathbb{P}_\alpha(K) \frac{\partial \underline{\mathcal{M}}(K)}{\partial K_c} \right] \left. \right\} \\ &- (b \leftrightarrow c), \end{aligned} \quad (3.68)$$

see Appendix B.1. As an illustration of (3.68) we will calculate divergence and curl of a specific flux-density vector field in Section 3.6.3.

### Flux Densities in Three-Dimensional Parameter Spaces

In the following sections, we shall use (3.65) and (3.68) to calculate numerically the geometric flux densities and their derivatives for metastable H atoms. We will be especially interested in the flux densities in three-dimensional subspaces of  $K$  space. We will, for instance, consider the cases where the electric field  $\mathcal{E}$  is kept constant and

only a magnetic field  $\mathbf{B}$  varies or vice versa. The geometric flux densities (3.59), (3.65) are then equivalent to three-dimensional complex vector fields. Indeed, let us consider the case that only three components of  $K$ , i.e.,  $K_{a_1}$ ,  $K_{a_2}$ , and  $K_{a_3}$ , are varied. The vectors

$$\mathbf{L} \equiv \begin{pmatrix} L_1 \\ L_2 \\ L_3 \end{pmatrix} = \begin{pmatrix} \kappa_1^{-1} & 0 & 0 \\ 0 & \kappa_2^{-1} & 0 \\ 0 & 0 & \kappa_3^{-1} \end{pmatrix} \begin{pmatrix} K_{a_1} \\ K_{a_2} \\ K_{a_3} \end{pmatrix} \quad (3.69)$$

span the effective parameter space which is now three-dimensional. In (3.69) we multiply the  $K_{a_i}$  with constants  $1/\kappa_i$  which, in the following, will be chosen conveniently. We shall, for instance, always choose the  $\kappa_i$  such that the  $L_i$  have the same dimension for  $i = 1, 2, 3$ . We define the geometric flux-density vectors in  $\mathbf{L}$  space as functions of  $\mathbf{L}$  by

$$J_{\alpha,i}^{(\mathbf{L})}(\mathbf{L}) = \sum_{j,k} \epsilon_{ijk} Y_{\alpha,a_j a_k}(K(\mathbf{L})) \kappa_j \kappa_k, \quad (3.70)$$

$$\mathbf{J}_{\alpha}^{(\mathbf{L})}(\mathbf{L}) = \begin{pmatrix} J_{\alpha,1}^{(\mathbf{L})}(\mathbf{L}) \\ J_{\alpha,2}^{(\mathbf{L})}(\mathbf{L}) \\ J_{\alpha,3}^{(\mathbf{L})}(\mathbf{L}) \end{pmatrix} \quad (3.71)$$

where  $i, j, k \in \{1, 2, 3\}$ .  $K(\mathbf{L})$  may include fixed components  $K_b \notin \{K_{a_1}, K_{a_2}, K_{a_3}\}$ . The curve  $\mathcal{C}$  (3.55) and the surface  $\mathcal{F}$  (3.57) live in  $\mathbf{L}$  space. With the ordinary surface element in  $\mathbf{L}$  space

$$df_i^{\mathbf{L}} = \frac{1}{2} \epsilon_{ijk} dL_j \wedge dL_k \quad (3.72)$$

we get for the geometric phase (3.58)

$$\gamma_{\alpha}(\mathcal{C}) = \int_{\mathcal{F}} \mathbf{J}_{\alpha}^{(\mathbf{L})}(\mathbf{L}) d\mathbf{f}^{\mathbf{L}}. \quad (3.73)$$

### Generalised Divergence Condition

As a further relation following directly from (3.59) we get the generalised divergence condition

$$d(Y_{\alpha,ab}(K) dK_a \wedge dK_b) = i \, dd(\widetilde{\alpha, K} | d|\alpha, K) \equiv 0 \quad (3.74)$$

which implies

$$\frac{\partial}{\partial K_a} Y_{\alpha,bc}(K) + \frac{\partial}{\partial K_b} Y_{\alpha,ca}(K) + \frac{\partial}{\partial K_c} Y_{\alpha,ab}(K) = 0, \quad (3.75)$$

## Chapter 3. Berry Phases for Hydrogen

---

see Appendix B.2. From (3.75) one finds that<sup>8</sup>

$$\operatorname{div} \mathbf{J}_\alpha^{(\mathbf{L})}(\mathbf{L}) = 0 \quad (3.76)$$

wherever (3.35) holds. That is, the vector fields  $\mathbf{J}_\alpha^{(\mathbf{L})}$  can have sources or sinks only at the points where the complex eigenvalues (2.68) of  $\underline{\mathcal{M}}(K)$  become degenerate. More precisely, we see from (3.65) that  $\mathbf{J}_\alpha^{(\mathbf{L})}$  can have such singularities only where  $E_\alpha(K(\mathbf{L}))$  becomes degenerate with another eigenvalue  $E_\beta(K(\mathbf{L}))$  ( $\beta \neq \alpha$ ). This is, of course, well known [22]. From (3.64) we can also calculate the curl of  $\mathbf{J}_\alpha^{(\mathbf{L})}$ :

$$(\operatorname{rot} \mathbf{J}_\alpha^{(\mathbf{L})}(\mathbf{L}))_i = \epsilon_{ijk} \frac{\partial}{\partial L_j} J_{\alpha,k}^{(\mathbf{L})}(\mathbf{L}) = 2 \frac{\partial}{\partial K_{a_j}} Y_{\alpha, a_i a_j}(K(\mathbf{L})) \kappa_i \kappa_j^2. \quad (3.77)$$

Knowledge of both  $\operatorname{div} \mathbf{J}_\alpha^{(\mathbf{L})}$  and  $\operatorname{rot} \mathbf{J}_\alpha^{(\mathbf{L})}$  will allow us an easy understanding of the behaviour of the geometric flux-density vectors for concrete cases in Section 3.6 below.

### 3.5.2 General Structure of Flux Densities for Hydrogen

In this section we shall discuss what we can learn from rotational invariance about the properties of geometric phases and flux densities for the metastable hydrogen states. We will consider the mass matrix  $\underline{\mathcal{M}}(\mathcal{E}(t), \mathcal{B}(t))$  of (3.25). The following analysis can be easily extended to other atomic species obeying a mass matrix of the form (3.25).

#### Proper Rotations

Let  $R \in \operatorname{SO}(3)$  be a proper rotation

$$R : x_i \rightarrow R_{ij} x_j, \quad R = (R_{ij}), \quad \det R = 1. \quad (3.78)$$

We denote by  $R$  and  $\underline{\mathcal{R}}$  its representations in the three-dimensional spatial space and in the  $n = 2$  subspace of the hydrogen atom, respectively. We have then

$$\underline{\mathcal{R}} \underline{\mathcal{M}}(\mathcal{E}, \mathcal{B}) \underline{\mathcal{R}}^{-1} = \underline{\mathcal{M}}(R\mathcal{E}, R\mathcal{B}). \quad (3.79)$$

This shows that  $\underline{\mathcal{M}}(\mathcal{E}, \mathcal{B})$  and  $\underline{\mathcal{M}}(R\mathcal{E}, R\mathcal{B})$  have the same set of eigenvalues<sup>9</sup>. Since we have assumed non-degeneracy of the eigenvalues of  $\underline{\mathcal{M}}(\mathcal{E}, \mathcal{B})$ , see (3.35), the same holds

---

<sup>8</sup>We have

$$\begin{aligned} \operatorname{div} \mathbf{J}_\alpha^{(\mathbf{L})}(\mathbf{L}) &= \sum_i \frac{\partial}{\partial L_i} J_{\alpha,i} = \sum_i \frac{\partial}{\partial K_{a_i}} \kappa_i J_{\alpha,i} = \sum_{ijk} \epsilon_{ijk} \frac{\partial}{\partial K_{a_i}} Y_{\alpha, a_j a_k} \kappa_i \kappa_j \kappa_k =: \sum_{ijk} \epsilon_{ijk} \aleph_{ijk} \\ &= 2 \sum_{\substack{ijk \\ (j < k)}} \epsilon_{ijk} \aleph_{ijk} = 2 \left( \sum_{\substack{ijk \\ (i < j < k)}} \epsilon_{ijk} \aleph_{ijk} + \sum_{\substack{ijk \\ (j < i < k)}} \epsilon_{ijk} \aleph_{ijk} + \sum_{\substack{ijk \\ (j < k < i)}} \epsilon_{ijk} \aleph_{ijk} \right) \\ &= 2 \left( \epsilon_{123} \frac{\partial}{\partial K_{a_1}} Y_{\alpha, a_2 a_3} + \epsilon_{213} \frac{\partial}{\partial K_{a_2}} Y_{\alpha, a_1 a_3} + \epsilon_{312} \frac{\partial}{\partial K_{a_3}} Y_{\alpha, a_1 a_2} \right) \kappa_1 \kappa_2 \kappa_3 \stackrel{(3.75)}{=} 0. \end{aligned}$$

<sup>9</sup>With  $\underline{\mathcal{M}}(\mathcal{E}, \mathcal{B})|\alpha\rangle = E_\alpha|\alpha\rangle$  and  $\underline{\mathcal{M}}' = \underline{\mathcal{M}}(R\mathcal{E}, R\mathcal{B})$  one obtains  $E_\alpha|\alpha\rangle = \underline{\mathcal{R}}^{-1} \underline{\mathcal{M}}' \underline{\mathcal{R}}|\alpha\rangle \Leftrightarrow E_\alpha \underline{\mathcal{R}}|\alpha\rangle = \underline{\mathcal{M}}' \underline{\mathcal{R}}|\alpha\rangle \Leftrightarrow E_\alpha|\alpha'\rangle = \underline{\mathcal{M}}'|\alpha'\rangle$ .

for  $\mathcal{M}(R\mathcal{E}, R\mathcal{B})$ . Moreover,  $\text{SO}(3)$  is a continuous and connected group, therefore the numbering of the eigenvalues, as explained in Appendix A.1, cannot change with  $R$ . Thus, we get

$$E_\alpha(R\mathcal{E}, R\mathcal{B}) = E_\alpha(\mathcal{E}, \mathcal{B}) . \quad (3.80)$$

For the resolvent, cf. (3.54) with  $n = 1$ , we find<sup>10</sup>

$$\underline{\mathcal{R}}(\zeta - \mathcal{M}(\mathcal{E}, \mathcal{B}))^{-1} \underline{\mathcal{R}}^{-1} = (\zeta - \mathcal{M}(R\mathcal{E}, R\mathcal{B}))^{-1} , \quad (3.81)$$

$$\sum_\alpha \frac{\underline{\mathcal{R}} \mathbb{P}_\alpha(\mathcal{E}, \mathcal{B}) \underline{\mathcal{R}}^{-1}}{\zeta - E_\alpha(\mathcal{E}, \mathcal{B})} = \sum_\alpha \frac{\mathbb{P}_\alpha(R\mathcal{E}, R\mathcal{B})}{\zeta - E_\alpha(R\mathcal{E}, R\mathcal{B})} . \quad (3.82)$$

With (3.80) we get from (3.82)

$$\underline{\mathcal{R}} \mathbb{P}_\alpha(\mathcal{E}, \mathcal{B}) \underline{\mathcal{R}}^{-1} = \mathbb{P}_\alpha(R\mathcal{E}, R\mathcal{B}) . \quad (3.83)$$

With the identification of  $(\mathcal{E}, \mathcal{B})$  and  $K$  of (3.31) we can decompose the  $6 \times 6$  flux density matrices  $Y_{\alpha,ab}$  (3.59) into  $3 \times 3$  submatrices corresponding to the  $\mathcal{E}$  and  $\mathcal{B}$  and mixed  $\mathcal{E}, \mathcal{B}$  differential forms (see Appendix C of [68]). With  $\alpha \in I$ , the index of a metastable state, we write<sup>11</sup>

$$\begin{aligned} Y_{\alpha,ab}(K) dK_a \wedge dK_b &= \mathcal{I}_{\alpha,jk}^{(\mathcal{E})}(\mathcal{E}, \mathcal{B}) d\mathcal{E}_j \wedge d\mathcal{E}_k + \mathcal{I}_{\alpha,jk}^{(\mathcal{B})}(\mathcal{E}, \mathcal{B}) d\mathcal{B}_j \wedge d\mathcal{B}_k \\ &\quad + \mathcal{I}_{\alpha,jk}^{(\mathcal{E},\mathcal{B})}(\mathcal{E}, \mathcal{B}) d\mathcal{E}_j \wedge d\mathcal{B}_k , \end{aligned} \quad (3.84)$$

where<sup>12</sup>

$$\mathcal{I}_{\alpha,jk}^{(\mathcal{E})}(\mathcal{E}, \mathcal{B}) + \mathcal{I}_{\alpha,kj}^{(\mathcal{E})}(\mathcal{E}, \mathcal{B}) = 0 , \quad \mathcal{I}_{\alpha,jk}^{(\mathcal{B})}(\mathcal{E}, \mathcal{B}) + \mathcal{I}_{\alpha,kj}^{(\mathcal{B})}(\mathcal{E}, \mathcal{B}) = 0 . \quad (3.85)$$

<sup>10</sup>Using (3.80) and

$$\begin{aligned} \underline{\mathcal{R}}(\zeta - \mathcal{M}(\mathcal{E}, \mathcal{B}))^{-1} \underline{\mathcal{R}}^{-1} &= \sum_\alpha (\zeta - E_\alpha)^{-1} \underline{\mathcal{R}} |\alpha, \mathcal{E}, \mathcal{B}\rangle \langle \alpha, \widetilde{\mathcal{E}}, \widetilde{\mathcal{B}} | \underline{\mathcal{R}}^{-1} \\ &= \sum_\alpha (\zeta - E_\alpha)^{-1} |\alpha, R\mathcal{E}, R\mathcal{B}\rangle \langle \alpha, \widetilde{R\mathcal{E}}, \widetilde{R\mathcal{B}} | = (\zeta - \mathcal{M}(R\mathcal{E}, R\mathcal{B}))^{-1} \end{aligned}$$

we prove (3.82). Note that for the states themselves we can only conclude that  $|\alpha, R\mathcal{E}, R\mathcal{B}\rangle$  and  $\underline{\mathcal{R}}|\alpha, \mathcal{E}, \mathcal{B}\rangle$  must be equal up to a phase factor.

<sup>11</sup>Due to  $Y_{\alpha,ab} = -Y_{\alpha,ba}$  we have  $\mathcal{I}_{\alpha,jk}^{(2)} = -\mathcal{I}_{\alpha,kj}^{(1)}$  in  $(Y_{\alpha,ab}) = \begin{pmatrix} \mathcal{I}_\alpha^{(\mathcal{E})} & \mathcal{I}_\alpha^{(1)} \\ \mathcal{I}_\alpha^{(2)} & \mathcal{I}_\alpha^{(\mathcal{B})} \end{pmatrix}$ .

Hence,  $\mathcal{I}_{\alpha,jk}^{(1)} d\mathcal{E}_j \wedge d\mathcal{B}_k + \mathcal{I}_{\alpha,jk}^{(2)} d\mathcal{B}_j \wedge d\mathcal{E}_k = 2\mathcal{I}_{\alpha,jk}^{(1)} d\mathcal{E}_j \wedge d\mathcal{B}_k$ , leading to  $\mathcal{I}_{\alpha,jk}^{(\mathcal{E},\mathcal{B})} = 2\mathcal{I}_{\alpha,jk}^{(1)}$ .

<sup>12</sup>Equation (3.84) does not exclude contributions to  $\mathcal{I}_{\alpha,jk}^{(\mathcal{E})}$  and  $\mathcal{I}_{\alpha,jk}^{(\mathcal{B})}$  symmetric under  $j \leftrightarrow k$ . Such contributions would simply vanish in the sums of (3.84). To uniquely define  $\mathcal{I}_\alpha^{(\mathcal{E})}$  and  $\mathcal{I}_\alpha^{(\mathcal{B})}$ , the condition (3.85) is employed.

### Chapter 3. Berry Phases for Hydrogen

---

From (3.25), (3.59), (3.65), (3.66), (3.84) and (3.85) we obtain

$$\begin{aligned} \mathcal{I}_\alpha^{(\mathcal{E})}(\mathcal{E}, \mathcal{B}) &= (\mathcal{I}_{\alpha,jk}^{(\mathcal{E})}(\mathcal{E}, \mathcal{B})) , \\ \mathcal{I}_{\alpha,jk}^{(\mathcal{E})}(\mathcal{E}, \mathcal{B}) &= \frac{i}{2} \sum_{\beta \neq \alpha} [E_\alpha(\mathcal{E}, \mathcal{B}) - E_\beta(\mathcal{E}, \mathcal{B})]^{-2} \text{Tr} [\mathbb{P}_\alpha(\mathcal{E}, \mathcal{B}) \underline{D}_j \mathbb{P}_\beta(\mathcal{E}, \mathcal{B}) \underline{D}_k - (j \leftrightarrow k)] \\ &= \frac{i}{2} \frac{1}{2\pi i} \oint_{S_\alpha} d\zeta \text{Tr} \left[ \frac{1}{\zeta - \underline{\mathcal{M}}(\mathcal{E}, \mathcal{B})} \underline{D}_j \frac{1}{(\zeta - \underline{\mathcal{M}}(\mathcal{E}, \mathcal{B}))^2} \underline{D}_k \right] , \end{aligned} \quad (3.86)$$

$$\begin{aligned} \mathcal{I}_\alpha^{(\mathcal{B})}(\mathcal{E}, \mathcal{B}) &= (\mathcal{I}_{\alpha,jk}^{(\mathcal{B})}(\mathcal{E}, \mathcal{B})) , \\ \mathcal{I}_{\alpha,jk}^{(\mathcal{B})}(\mathcal{E}, \mathcal{B}) &= \frac{i}{2} \sum_{\beta \neq \alpha} [E_\alpha(\mathcal{E}, \mathcal{B}) - E_\beta(\mathcal{E}, \mathcal{B})]^{-2} \text{Tr} [\mathbb{P}_\alpha(\mathcal{E}, \mathcal{B}) \underline{\mu}_j \mathbb{P}_\beta(\mathcal{E}, \mathcal{B}) \underline{\mu}_k - (j \leftrightarrow k)] \\ &= \frac{i}{2} \frac{1}{2\pi i} \oint_{S_\alpha} d\zeta \text{Tr} \left[ \frac{1}{\zeta - \underline{\mathcal{M}}(\mathcal{E}, \mathcal{B})} \underline{\mu}_j \frac{1}{(\zeta - \underline{\mathcal{M}}(\mathcal{E}, \mathcal{B}))^2} \underline{\mu}_k \right] , \end{aligned} \quad (3.87)$$

$$\begin{aligned} \mathcal{I}_\alpha^{(\mathcal{E}, \mathcal{B})}(\mathcal{E}, \mathcal{B}) &= (\mathcal{I}_{\alpha,jk}^{(\mathcal{E}, \mathcal{B})}(\mathcal{E}, \mathcal{B})) , \\ \mathcal{I}_{\alpha,jk}^{(\mathcal{E}, \mathcal{B})}(\mathcal{E}, \mathcal{B}) &= i \sum_{\beta \neq \alpha} [E_\alpha(\mathcal{E}, \mathcal{B}) - E_\beta(\mathcal{E}, \mathcal{B})]^{-2} \\ &\quad \times \text{Tr} [\mathbb{P}_\alpha(\mathcal{E}, \mathcal{B}) \underline{D}_j \mathbb{P}_\beta(\mathcal{E}, \mathcal{B}) \underline{\mu}_k - \mathbb{P}_\alpha(\mathcal{E}, \mathcal{B}) \underline{\mu}_k \mathbb{P}_\beta(\mathcal{E}, \mathcal{B}) \underline{D}_j] \\ &= i \frac{1}{2\pi i} \oint_{S_\alpha} d\zeta \text{Tr} \left[ \frac{1}{\zeta - \underline{\mathcal{M}}(\mathcal{E}, \mathcal{B})} \underline{D}_j \frac{1}{(\zeta - \underline{\mathcal{M}}(\mathcal{E}, \mathcal{B}))^2} \underline{\mu}_k \right] . \end{aligned} \quad (3.88)$$

As explained in general in (3.69) ff. we introduce the geometric flux-density vectors  $\mathbf{J}_\alpha^{(\mathcal{E})}(\mathcal{E}, \mathcal{B})$  and  $\mathbf{J}_\alpha^{(\mathcal{B})}(\mathcal{E}, \mathcal{B})$  with components

$$\mathbf{J}_{\alpha,i}^{(\mathcal{E})}(\mathcal{E}, \mathcal{B}) = \epsilon_{ijk} \mathcal{I}_{\alpha,jk}^{(\mathcal{E})}(\mathcal{E}, \mathcal{B}) , \quad \mathbf{J}_{\alpha,i}^{(\mathcal{B})}(\mathcal{E}, \mathcal{B}) = \epsilon_{ijk} \mathcal{I}_{\alpha,jk}^{(\mathcal{B})}(\mathcal{E}, \mathcal{B}) ; \quad (3.89)$$

see also Appendix C of [68].

From (3.84) to (3.88) we get the decomposition of the  $6 \times 6$  matrix  $(Y_{\alpha,ab})$  in terms of  $3 \times 3$  submatrices

$$(Y_{\alpha,ab}) = \left( \begin{array}{c|c} \mathcal{I}_\alpha^{(\mathcal{E})} & \frac{1}{2} \mathcal{I}_\alpha^{(\mathcal{E}, \mathcal{B})} \\ \hline -\frac{1}{2} (\mathcal{I}_\alpha^{(\mathcal{E}, \mathcal{B})})^T & \mathcal{I}_\alpha^{(\mathcal{B})} \end{array} \right) . \quad (3.90)$$

The rotational properties of  $\mathcal{I}_\alpha^{(\mathcal{E})}$ ,  $\mathcal{I}_\alpha^{(\mathcal{B})}$  and  $\mathcal{I}_\alpha^{(\mathcal{E}, \mathcal{B})}$  are easily obtained from (3.79) to (3.83) and (3.86) to (3.88) using<sup>13</sup>

$$\underline{\mathcal{R}}^{-1} \underline{D}_j \underline{\mathcal{R}} = R_{jk} \underline{D}_k , \quad \underline{\mathcal{R}}^{-1} \underline{\mu}_j \underline{\mathcal{R}} = R_{jk} \underline{\mu}_k . \quad (3.91)$$

<sup>13</sup>It is indeed  $\underline{\mathcal{R}}^{-1} \underline{D}_j \underline{\mathcal{R}} = R_{jk} \underline{D}_k$ , not  $\underline{\mathcal{R}} \underline{D}_j \underline{\mathcal{R}}^{-1} = R_{jk} \underline{D}_k$ . The latter would yield  $\underline{\mathcal{R}}' \underline{\mathcal{R}} \underline{D}_j \underline{\mathcal{R}}^{-1} \underline{\mathcal{R}}'^{-1} = \underline{\mathcal{R}}' R_{jk} \underline{D}_k \underline{\mathcal{R}}'^{-1} = R_{jk} \underline{\mathcal{R}}' \underline{D}_k \underline{\mathcal{R}}'^{-1} \Leftrightarrow (\underline{\mathcal{R}}' \underline{\mathcal{R}}) \underline{D}_j (\underline{\mathcal{R}}' \underline{\mathcal{R}})^{-1} = R_{jk} R'_{kl} \underline{D}_l = (RR')_{jl} \underline{D}_l$ , while it should be  $(R'R)_{jl} \underline{D}_l$  on the r.h.s. of the last equation.

We get

$$\begin{aligned}
 R\mathcal{I}_\alpha^{(\mathcal{E})}(\mathcal{E}, \mathcal{B})R^\top &= \mathcal{I}_\alpha^{(\mathcal{E})}(R\mathcal{E}, R\mathcal{B}) , \\
 R\mathcal{I}_\alpha^{(\mathcal{B})}(\mathcal{E}, \mathcal{B})R^\top &= \mathcal{I}_\alpha^{(\mathcal{B})}(R\mathcal{E}, R\mathcal{B}) , \\
 R\mathcal{I}_\alpha^{(\mathcal{E}, \mathcal{B})}(\mathcal{E}, \mathcal{B})R^\top &= \mathcal{I}_\alpha^{(\mathcal{E}, \mathcal{B})}(R\mathcal{E}, R\mathcal{B}) .
 \end{aligned} \tag{3.92}$$

### Improper Rotations

For improper rotations,  $\bar{R} \in O(3)$  with  $\det \bar{R} = -1$ , we have no invariance due to the PV term  $\delta \underline{\mathcal{M}}_{\text{PV}}$  in the mass matrix (3.24). In fact, we are especially interested in PV effects coming from this term. In this subsection we shall decompose the geometric flux densities (3.84) to (3.89) into PC and PV parts.

We consider just one improper rotation<sup>14</sup>, namely the parity transformation  $P : \mathbf{x} \rightarrow P\mathbf{x} = -\mathbf{x}$ . In the  $n = 2$  subspace of the hydrogen atom this is represented by a matrix  $\underline{P}$  which transforms the electric and magnetic dipole operators as follows

$$\underline{P}^{-1} \underline{D}_j \underline{P} = -\underline{D}_j , \quad \underline{P}^{-1} \underline{\mu}_j \underline{P} = \underline{\mu}_j . \tag{3.93}$$

The mass matrix  $\underline{\tilde{\mathcal{M}}}_0$  (3.24) is, of course, not invariant under  $P$  and we have

$$\underline{P} \underline{\mathcal{M}}_0 \underline{P}^{-1} = \underline{\mathcal{M}}_0 , \tag{3.94}$$

$$\underline{P} \underline{\mathcal{M}}_{\text{PV}} \underline{P}^{-1} = -\underline{\mathcal{M}}_{\text{PV}} , \tag{3.95}$$

$$\underline{P} \underline{\tilde{\mathcal{M}}}_0 \underline{P}^{-1} = \underline{P}(\underline{\mathcal{M}}_0 + \delta \underline{\mathcal{M}}_{\text{PV}}) \underline{P}^{-1} = \underline{\mathcal{M}}_0 - \delta \underline{\mathcal{M}}_{\text{PV}} . \tag{3.96}$$

Clearly, since  $\delta \approx 7.57 \times 10^{-13}$  is very small (see Appendix A.1), it is useful to consider the case where it is set to zero, that is, where parity is conserved. We denote the quantities corresponding to this case by  $\underline{\mathcal{M}}^{(0)}$ , see (3.28), and  $E_\alpha^{(0)}$ ,  $\mathbb{P}_\alpha^{(0)}$  etc. From (3.28), (3.93), and (3.94) we find for the PC quantities<sup>15</sup>

$$\underline{P} \underline{\mathcal{M}}^{(0)}(\mathcal{E}, \mathcal{B}) \underline{P}^{-1} = \underline{\mathcal{M}}^{(0)}(-\mathcal{E}, \mathcal{B}) , \tag{3.97}$$

$$E_\alpha^{(0)}(\mathcal{E}, \mathcal{B}) = E_\alpha^{(0)}(-\mathcal{E}, \mathcal{B}) , \tag{3.98}$$

$$\underline{P} \mathbb{P}_\alpha^{(0)}(\mathcal{E}, \mathcal{B}) \underline{P}^{-1} = \mathbb{P}_\alpha^{(0)}(-\mathcal{E}, \mathcal{B}) . \tag{3.99}$$

<sup>14</sup>An improper rotation is a composite operation  $\bar{R} = P \circ R$ . However, due to the rotational invariance of  $\mathcal{I}_\alpha$  (3.92), it is sufficient to consider  $P$  only.

<sup>15</sup>The parity operator  $\underline{P}$  in the  $n = 2$  subspace does not act on the *numbers*  $\mathcal{E}_i$ ,  $\mathcal{B}_i$  of the field components. Of course, switching the sign of  $\underline{D}$  in the mass matrix (3.28) has the same effect as switching the sign of  $\mathcal{E}$ . From (3.97) we see that  $\underline{\mathcal{M}}^{(0)}(\mathcal{E}, \mathcal{B})$  and  $\underline{\mathcal{M}}^{(0)}(-\mathcal{E}, \mathcal{B})$  have the same set of eigenvalues. We still have to check that our numbering scheme leads indeed to (3.98) and (3.99) for every  $\alpha$ . As discussed in Appendix A.1 we consider only  $\mathcal{B} \neq \mathbf{0}$  and vary  $\mathcal{E}$  starting from  $\mathcal{E} = \mathbf{0}$ :  $\mathcal{E}(\lambda) = \lambda \mathcal{E}$ ,  $\lambda \in [0, 1]$ . For  $\lambda = 0$  (3.98) and (3.99) are trivial. Increasing  $\lambda$  continuously, we encounter, due to  $\mathcal{B} \neq \mathbf{0}$ , no level crossings. Therefore, the identification of the eigenvalues and the quasi projectors corresponding to the same index  $\alpha$  for  $(\mathcal{E}(\lambda), \mathcal{B})$  and  $(-\mathcal{E}(\lambda), \mathcal{B})$  is always possible. This proves (3.98) and (3.99).

### Chapter 3. Berry Phases for Hydrogen

---

Due to time reversal invariance<sup>16</sup> and condition (3.35)  $E_\alpha(\mathcal{E}, \mathcal{B})$  gets no contribution linear in  $\delta$ , that is, linear in the PV term  $\delta \underline{\mathcal{M}}_{\text{PV}}$ ; see [82,175]. Neglecting higher order terms in  $\delta$  we have, therefore,

$$E_\alpha(\mathcal{E}, \mathcal{B}) = E_\alpha^{(0)}(\mathcal{E}, \mathcal{B}) = E_\alpha^{(0)}(-\mathcal{E}, \mathcal{B}) . \quad (3.100)$$

Rotational invariance (3.80) implies then that  $E_\alpha(\mathcal{E}, \mathcal{B})$  must be a function of the P-even invariants one can form from  $\mathcal{E}$  and  $\mathcal{B}$ :

$$E_\alpha(\mathcal{E}, \mathcal{B}) \equiv E_\alpha(\mathcal{E}^2, \mathcal{B}^2, (\mathcal{E} \cdot \mathcal{B})^2) . \quad (3.101)$$

Below we will present the analogous analysis in terms of invariants for the geometric flux densities (3.86) to (3.89) which include P violation.

For the case of no P violation we find<sup>17</sup> that  $\mathcal{I}_\alpha^{(\mathcal{E})}(\mathcal{E}, \mathcal{B})$  and  $\mathcal{I}_\alpha^{(\mathcal{B})}(\mathcal{E}, \mathcal{B})$  must be even, whereas  $\mathcal{I}_\alpha^{(\mathcal{E}, \mathcal{B})}(\mathcal{E}, \mathcal{B})$  must be odd under  $\mathcal{E} \rightarrow -\mathcal{E}$ . Writing  $\mathcal{I}_\alpha(\mathcal{E}, \mathcal{B}) = \mathcal{I}_\alpha^{\text{PC}}(\mathcal{E}, \mathcal{B}) + \mathcal{I}_\alpha^{\text{PV}}(\mathcal{E}, \mathcal{B})$ , this allows us to define generally, without any expansion in  $\delta$ , the PC and PV parts of the geometric flux densities as follows<sup>18</sup>

$$\mathcal{I}_\alpha^{(\mathcal{E})\text{PC}}(\mathcal{E}, \mathcal{B}) = \frac{1}{2} \left[ \mathcal{I}_\alpha^{(\mathcal{E})}(\mathcal{E}, \mathcal{B}) + \mathcal{I}_\alpha^{(\mathcal{E})}(-\mathcal{E}, \mathcal{B}) \right] , \quad (3.102)$$

$$\mathcal{I}_\alpha^{(\mathcal{E})\text{PV}}(\mathcal{E}, \mathcal{B}) = \frac{1}{2} \left[ \mathcal{I}_\alpha^{(\mathcal{E})}(\mathcal{E}, \mathcal{B}) - \mathcal{I}_\alpha^{(\mathcal{E})}(-\mathcal{E}, \mathcal{B}) \right] , \quad (3.103)$$

$$\mathcal{I}_\alpha^{(\mathcal{B})\text{PC}}(\mathcal{E}, \mathcal{B}) = \frac{1}{2} \left[ \mathcal{I}_\alpha^{(\mathcal{B})}(\mathcal{E}, \mathcal{B}) + \mathcal{I}_\alpha^{(\mathcal{B})}(-\mathcal{E}, \mathcal{B}) \right] , \quad (3.104)$$

$$\mathcal{I}_\alpha^{(\mathcal{B})\text{PV}}(\mathcal{E}, \mathcal{B}) = \frac{1}{2} \left[ \mathcal{I}_\alpha^{(\mathcal{B})}(\mathcal{E}, \mathcal{B}) - \mathcal{I}_\alpha^{(\mathcal{B})}(-\mathcal{E}, \mathcal{B}) \right] , \quad (3.105)$$

$$\mathcal{I}_\alpha^{(\mathcal{E}, \mathcal{B})\text{PC}}(\mathcal{E}, \mathcal{B}) = \frac{1}{2} \left[ \mathcal{I}_\alpha^{(\mathcal{E}, \mathcal{B})}(\mathcal{E}, \mathcal{B}) - \mathcal{I}_\alpha^{(\mathcal{E}, \mathcal{B})}(-\mathcal{E}, \mathcal{B}) \right] , \quad (3.106)$$

$$\mathcal{I}_\alpha^{(\mathcal{E}, \mathcal{B})\text{PV}}(\mathcal{E}, \mathcal{B}) = \frac{1}{2} \left[ \mathcal{I}_\alpha^{(\mathcal{E}, \mathcal{B})}(\mathcal{E}, \mathcal{B}) + \mathcal{I}_\alpha^{(\mathcal{E}, \mathcal{B})}(-\mathcal{E}, \mathcal{B}) \right] . \quad (3.107)$$

Using the expansion in the small PV parameter  $\delta$  up to linear order we get for the PC fluxes exactly the expressions (3.86) to (3.88) but with  $\underline{\mathcal{M}}(\mathcal{E}, \mathcal{B})$ ,  $\mathbb{P}_{\alpha, \beta}(\mathcal{E}, \mathcal{B})$ ,  $E_\alpha(\mathcal{E}, \mathcal{B})$  replaced by the corresponding quantities for  $\delta = 0$ , that is,  $\underline{\mathcal{M}}^{(0)}(\mathcal{E}, \mathcal{B})$  etc. For the PV fluxes we have to expand the expressions (3.86) to (3.88) up to linear order in  $\delta$ .

---

<sup>16</sup>Here we disregard the T-violating complex phase in the Cabibbo-Kobayashi-Maskawa Matrix. This is justified since we are dealing with a flavour diagonal process.

<sup>17</sup>According to (3.97) the transformation  $\mathcal{E} \rightarrow -\mathcal{E}$  effectively yields terms like  $\underline{\mathcal{P}} \underline{\mathcal{M}}^{(0)}(\mathcal{E}, \mathcal{B}) \underline{\mathcal{P}}^{-1}$  in the denominators of (3.86)–(3.88). Simple algebraic manipulations within the argument of the trace results in terms of the form  $\underline{\mathcal{P}} \underline{\mathcal{D}}_j \underline{\mathcal{P}}^{-1}$  and  $\underline{\mathcal{P}} \underline{\mathcal{M}}_j \underline{\mathcal{P}}^{-1}$ . Then, (3.93) can be used to immediately obtain the behaviour of the quantities  $\mathcal{I}_\alpha(-\mathcal{E}, \mathcal{B})$ , where  $\mathcal{I}_\alpha = \mathcal{I}_\alpha^{(\mathcal{E})}$ ,  $\mathcal{I}_\alpha^{(\mathcal{B})}$  and  $\mathcal{I}_\alpha^{(\mathcal{E}, \mathcal{B})}$ .

<sup>18</sup>Excluding PV, that is, setting  $\mathcal{I}_\alpha^{(\mathcal{E})} = \mathcal{I}_\alpha^{(\mathcal{E})\text{PC}}$ , we find  $\mathcal{I}_\alpha^{(\mathcal{E})}(-\mathcal{E}, \mathcal{B}) = \mathcal{I}_\alpha^{(\mathcal{E})}(\mathcal{E}, \mathcal{B})$  and, hence, (3.102). Consequently, the PV part  $\mathcal{I}_\alpha^{(\mathcal{E})\text{PV}}$ , which was excluded before, has to be odd under  $\mathcal{E} \rightarrow -\mathcal{E}$ , immediately leading to (3.103). Analogous deductions hold for (3.104)–(3.107). For instance, (3.105) directly leads to  $\mathcal{I}_\alpha^{(\mathcal{B})\text{PV}}(\mathcal{E} = \mathbf{0}, \mathcal{B}) \equiv 0$ .

This is easily done and leads to

$$\begin{aligned} \mathcal{I}_{\alpha,jk}^{(\mathcal{E})\text{PV}}(\mathcal{E}, \mathcal{B}) &= \delta \frac{i}{2} \frac{1}{2\pi i} \oint_{S_\alpha} d\zeta \text{Tr} \left[ \frac{1}{\zeta - \underline{\mathcal{M}}^{(0)}(\mathcal{E}, \mathcal{B})} \underline{\mathcal{M}}^{\text{PV}} \right. \\ &\quad \left. \times \frac{1}{\zeta - \underline{\mathcal{M}}^{(0)}(\mathcal{E}, \mathcal{B})} \underline{D}_j \frac{1}{(\zeta - \underline{\mathcal{M}}^{(0)}(\mathcal{E}, \mathcal{B}))^2} \underline{D}_k - (j \leftrightarrow k) \right] \end{aligned} \quad (3.108)$$

and analogous expressions for  $\mathcal{I}_\alpha^{(\mathcal{B})\text{PV}}$  and  $\mathcal{I}_\alpha^{(\mathcal{E}, \mathcal{B})\text{PV}}$ . These, the derivation of (3.108), and further useful expressions for PV fluxes, are given in Appendix B.2.

### Expansions for Flux Densities

At this point, we can write down the expansions for the geometric flux densities (3.86) to (3.88) following from rotational invariance and the parity transformation properties. In these expansions we encounter invariant functions

$$g_r^\alpha \equiv g_r^\alpha(\mathcal{E}^2, \mathcal{B}^2, (\mathcal{E} \cdot \mathcal{B})^2), \quad h_r^\alpha \equiv h_r^\alpha(\mathcal{E}^2, \mathcal{B}^2, (\mathcal{E} \cdot \mathcal{B})^2), \quad (r = 1, \dots, 15), \quad (3.109)$$

which are, in general, complex valued. Our notation is such that the terms with the  $g_r^\alpha$  are the parity conserving (PC) ones, the terms with the  $h_r^\alpha$  the parity violating (PV) ones. We find the following:

$$\begin{aligned} \mathcal{I}_{\alpha,jk}^{(\mathcal{E})}(\mathcal{E}, \mathcal{B}) &\stackrel{19}{=} \frac{1}{2} \epsilon_{jkl} J_{\alpha,l}^{(\mathcal{E})}(\mathcal{E}, \mathcal{B}), \\ \mathbf{J}_\alpha^{(\mathcal{E})}(\mathcal{E}, \mathcal{B}) &= \mathbf{J}_\alpha^{(\mathcal{E})\text{PC}}(\mathcal{E}, \mathcal{B}) + \mathbf{J}_\alpha^{(\mathcal{E})\text{PV}}(\mathcal{E}, \mathcal{B}) \\ &\stackrel{20}{=} \mathcal{E} \left[ (\mathcal{E} \cdot \mathcal{B}) g_1^\alpha + h_1^\alpha \right] + \mathcal{B} \left[ g_2^\alpha + (\mathcal{E} \cdot \mathcal{B}) h_2^\alpha \right] \\ &\quad + (\mathcal{E} \times \mathcal{B}) \left[ (\mathcal{E} \cdot \mathcal{B}) g_3^\alpha + h_3^\alpha \right], \end{aligned} \quad (3.110)$$

$$\begin{aligned} \mathcal{I}_{\alpha,jk}^{(\mathcal{E}, \mathcal{B})}(\mathcal{E}, \mathcal{B}) &= \mathcal{I}_{\alpha,jk}^{(\mathcal{E}, \mathcal{B})\text{PC}}(\mathcal{E}, \mathcal{B}) + \mathcal{I}_{\alpha,jk}^{(\mathcal{E}, \mathcal{B})\text{PV}}(\mathcal{E}, \mathcal{B}) \\ &\stackrel{21}{=} \frac{1}{2} \epsilon_{jkl} \left\{ \mathcal{E}_l \left[ g_4^\alpha + (\mathcal{E} \cdot \mathcal{B}) h_4^\alpha \right] + \mathcal{B}_l \left[ (\mathcal{E} \cdot \mathcal{B}) g_5^\alpha + h_5^\alpha \right] \right. \\ &\quad \left. + (\mathcal{E} \times \mathcal{B})_l \left[ g_6^\alpha + (\mathcal{E} \cdot \mathcal{B}) h_6^\alpha \right] \right\} \\ &\quad + \delta_{jk} \left[ (\mathcal{E} \cdot \mathcal{B}) g_7^\alpha + h_7^\alpha \right] \end{aligned}$$

<sup>19</sup>With (3.89) we get  $\sum_l \frac{1}{2} \epsilon_{jkl} J_{\alpha,l}^{(\mathcal{E})} = \sum_{lmn} \frac{1}{2} \epsilon_{jkl} \epsilon_{lmn} \mathcal{I}_{\alpha,mn}^{(\mathcal{E})} = \frac{1}{2} \sum_{mn} (\delta_{jm} \delta_{kn} - \delta_{jn} \delta_{km}) \mathcal{I}_{\alpha,mn}^{(\mathcal{E})} = \frac{1}{2} (\mathcal{I}_{\alpha,jk}^{(\mathcal{E})} - \mathcal{I}_{\alpha,kj}^{(\mathcal{E})}) = \mathcal{I}_{\alpha,jk}^{(\mathcal{E})}$ .

<sup>20</sup>With  $\mathbf{J}_\alpha$  being a three-dimensional vector depending on  $\mathcal{E}$  and  $\mathcal{B}$ , the most general structure of  $\mathbf{J}_\alpha$  can be written down using all three-dimensional vectors at hand, namely  $\mathcal{E}$ ,  $\mathcal{B}$ , and  $\mathcal{E} \times \mathcal{B}$ . Terms proportional to these vectors involve the functions (3.109). Since, for example, the notion  $g_r$  indicates a PC term, the expression  $\mathcal{E} g_1^\alpha$  which switches sign under  $\mathcal{E} \rightarrow -\mathcal{E}$ , has to be modified such that it becomes P-even. For that, the only possibility is to multiply with the pseudo scalar  $(\mathcal{E} \cdot \mathcal{B})$ . Similar considerations hold for the remaining terms.

<sup>21</sup>Just the way we impose a vector structure on  $\mathbf{J}_\alpha^{(\mathcal{E})}$  and  $\mathbf{J}_\alpha^{(\mathcal{B})}$ , we impose a matrix structure on  $(\mathcal{I}_{\alpha,jk}^{(\mathcal{E}, \mathcal{B})})$  via all objects composed of  $\mathcal{E}$ ,  $\mathcal{B}$ , and  $\mathcal{E} \times \mathcal{B}$ , and carrying two indices.

$$\begin{aligned}
 & + (\mathcal{E}_j \mathcal{E}_k - \frac{1}{3} \delta_{jk} \mathcal{E}^2) [(\mathcal{E} \cdot \mathcal{B}) g_8^\alpha + h_8^\alpha] \\
 & + (\mathcal{B}_j \mathcal{B}_k - \frac{1}{3} \delta_{jk} \mathcal{B}^2) [(\mathcal{E} \cdot \mathcal{B}) g_9^\alpha + h_9^\alpha] \\
 & + (\mathcal{E}_j \mathcal{B}_k + \mathcal{E}_k \mathcal{B}_j - \frac{2}{3} \delta_{jk} (\mathcal{E} \cdot \mathcal{B})) [g_{10}^\alpha + (\mathcal{E} \cdot \mathcal{B}) h_{10}^\alpha] \\
 & + [\mathcal{E}_j (\mathcal{E} \times \mathcal{B})_k + \mathcal{E}_k (\mathcal{E} \times \mathcal{B})_j] [(\mathcal{E} \cdot \mathcal{B}) g_{11}^\alpha + h_{11}^\alpha] \\
 & + [\mathcal{B}_j (\mathcal{E} \times \mathcal{B})_k + \mathcal{B}_k (\mathcal{E} \times \mathcal{B})_j] [g_{12}^\alpha + (\mathcal{E} \cdot \mathcal{B}) h_{12}^\alpha] , \quad (3.111)
 \end{aligned}$$

$$\begin{aligned}
 \mathcal{I}_{\alpha,jk}^{(\mathcal{B})}(\mathcal{E}, \mathcal{B}) &= \frac{1}{2} \epsilon_{jkl} J_{\alpha,l}^{(\mathcal{B})}(\mathcal{E}, \mathcal{B}) , \\
 \mathbf{J}_\alpha^{(\mathcal{B})}(\mathcal{E}, \mathcal{B}) &= \mathbf{J}_\alpha^{(\mathcal{B})\text{PC}}(\mathcal{E}, \mathcal{B}) + \mathbf{J}_\alpha^{(\mathcal{B})\text{PV}}(\mathcal{E}, \mathcal{B}) \\
 &= \mathcal{E} [(\mathcal{E} \cdot \mathcal{B}) g_{13}^\alpha + h_{13}^\alpha] + \mathcal{B} [g_{14}^\alpha + (\mathcal{E} \cdot \mathcal{B}) h_{14}^\alpha] \\
 &\quad + (\mathcal{E} \times \mathcal{B}) [(\mathcal{E} \cdot \mathcal{B}) g_{15}^\alpha + h_{15}^\alpha] . \quad (3.112)
 \end{aligned}$$

In the next sections we shall discuss specific examples where the general expansions (3.110) to (3.112) will prove to be very useful.

## 3.6 Flux Densities in Mixed Parameter Spaces for n=2 States of Hydrogen

In this section we shall illustrate the structures of the geometric flux densities for specific cases. First, we analytically derive the geometric flux densities  $\mathbf{J}_\alpha^{(\mathcal{B})}(\mathcal{E} = \mathbf{0}, \mathcal{B})$  in magnetic field space for vanishing electric field and compare the results with numerical calculations. In that case the flux densities give rise only to P-conserving geometric phases. We then analyse the structure of  $\mathbf{J}_\alpha^{(\mathcal{E})}(\mathcal{E}, \mathcal{B})$  in electric field space together with a constant magnetic field  $\mathcal{B} = \mathcal{B}_3 \mathbf{e}_3$ . Here, we will obtain P-violating geometric phases. As a further example we investigate the geometric flux densities in the mixed parameter space of  $\mathcal{E}_1, \mathcal{E}_3$  and  $\mathcal{B}_3$  together with a constant magnetic field  $\mathcal{B} = \mathcal{B}_2 \mathbf{e}_2$ .

### 3.6.1 A Pure Magnetic Field $\mathcal{B}$

Starting from the general expression (3.112) for  $\mathbf{J}_\alpha^{(\mathcal{B})}(\mathcal{E}, \mathcal{B})$ , we immediately find for  $\mathbf{J}_\alpha^{(\mathcal{B})}(\mathcal{E} = \mathbf{0}, \mathcal{B})$

$$\mathbf{J}_\alpha^{(\mathcal{B})}(\mathbf{0}, \mathcal{B}) = \mathcal{B} g_{14}^\alpha \quad (3.113)$$

where  $g_{14}^\alpha = g_{14}^\alpha(\mathcal{B}^2)$  only depends on the modulus squared of the magnetic field.

Because of (3.76) we have

$$\nabla_{\mathcal{B}} \cdot \mathbf{J}_\alpha^{(\mathcal{B})}(\mathbf{0}, \mathcal{B}) = 0 \quad (3.114)$$

for  $\mathcal{B}^2 \neq 0$ . With  $b := \mathcal{B}^2$  and inserting (3.113) in (3.114), we get

$$0 = \nabla_{\mathcal{B}} \cdot (\mathcal{B} g_{14}^\alpha(b)) = 3 g_{14}^\alpha(b) + 2 b \partial_b g_{14}^\alpha(b) \quad (3.115)$$

### 3.6. Flux Densities in Mixed Parameter Spaces for Hydrogen

---

with the solution<sup>22</sup>

$$g_{14}^\alpha(b) = a^\alpha b^{-\frac{3}{2}} = a^\alpha |\mathcal{B}|^{-3} \quad (3.116)$$

where  $a^\alpha$  is an integration constant. Therefore,

$$\mathbf{J}_\alpha^{(\mathcal{B})}(\mathbf{0}, \mathcal{B}) = a^\alpha \frac{\mathcal{B}}{|\mathcal{B}|^3} . \quad (3.117)$$

This is the field of a Dirac monopole of strength  $a^\alpha$  at  $\mathcal{B} = \mathbf{0}$ . A detailed calculation of  $a^\alpha$  for the 2S states is presented in Appendix B.3. The resulting flux-density vector field comes out to be real and P-conserving. It is has vanishing curl and reads

$$\mathbf{J}_\alpha^{(\mathcal{B})}(\mathbf{0}, \mathcal{B}) = \begin{cases} -\frac{\mathcal{B}}{|\mathcal{B}|^3} , & \text{for } \alpha = 9 , \\ \frac{\mathcal{B}}{|\mathcal{B}|^3} , & \text{for } \alpha = 11 , \\ \mathbf{0} , & \text{for } \alpha = 10, 12 . \end{cases} \quad (3.118)$$

Comparing this exact result with numerical calculations, we can extract an estimate for the error of  $\mathbf{J}_\alpha$  in parameter spaces other than that of the magnetic field. For  $15^3$  equidistant grid points in a cubic parameter space volume  $[-1 \text{ mT}, 1 \text{ mT}]^3$ , at which the vectors  $\mathbf{J}_{11}^{(\mathcal{B})}(\mathbf{0}, \mathcal{B})$  are evaluated, we obtain numerically the following deviations from the vector field structure given in (3.118):

$$\begin{aligned} ||\mathbf{J}_{11}^{(\mathcal{B})}(\mathbf{0}, \mathcal{B})| \cdot |\mathcal{B}|^2 - 1| &\lesssim 5 \times 10^{-12} , \\ \left| \frac{\mathbf{J}_{11}^{(\mathcal{B})}(\mathbf{0}, \mathcal{B})}{|\mathbf{J}_{11}^{(\mathcal{B})}(\mathbf{0}, \mathcal{B})|} \times \frac{\mathcal{B}}{|\mathcal{B}|} \right| &\lesssim 1.5 \times 10^{-12} , \end{aligned} \quad (3.119)$$

see Figure 3.7. Since the data type used for the numerical calculations has a precision of approximately 16 digits, we find the results (3.119) to be in good agreement with the analytical expression (3.118).

Figure 3.8 illustrates the numerical results for  $\mathbf{J}_{11}^{(\mathcal{B})}(\mathbf{0}, \mathcal{B})$  in the  $\mathcal{B}_3 = 0$  plane. Here and in the following, we find it convenient to plot dimensionless quantities. Therefore, we choose reference values for the electric and magnetic field strengths

$$\mathcal{E}_0 = 1 \text{ V/cm} , \quad \mathcal{B}_0 = 1 \text{ mT} . \quad (3.120)$$

We label the axes in parameter space by  $\mathcal{B}_i/\mathcal{B}_0$  and plot the vectors

$$\hat{\mathbf{J}}_\alpha^{(\mathcal{B})} = \eta \mathbf{J}_\alpha^{(\mathcal{B})} \mathcal{B}_0^2 . \quad (3.121)$$

Here  $\eta$  is a rescaling parameter chosen such as to bring the drawn vectors in the plots to a convenient length scale. The dimensionless geometric phases, see (3.56), (3.58), and (3.73), are then given by the flux of this dimensionless vector field (3.121) through a surface in this space of  $\mathcal{B}_i/\mathcal{B}_0$  and divided by  $\eta$ .

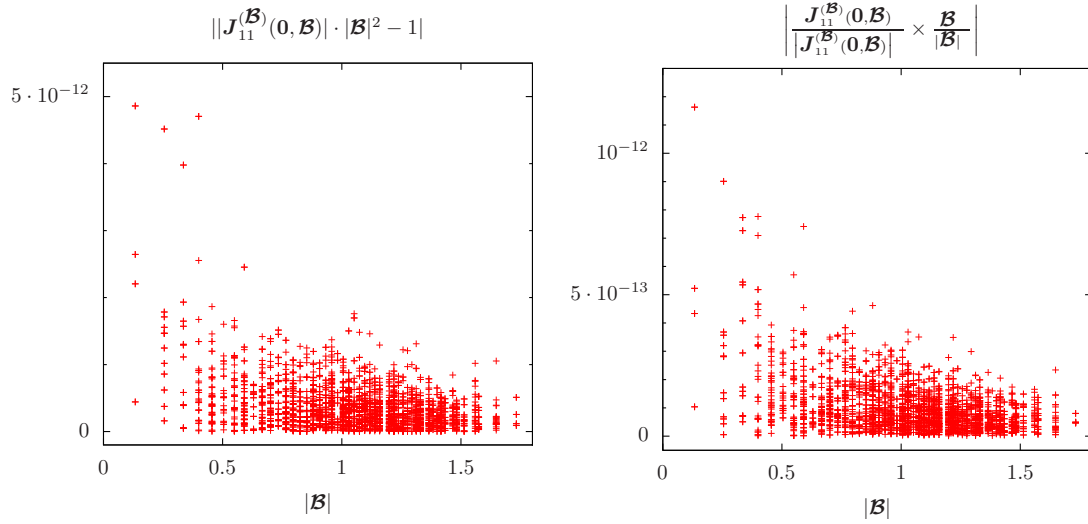


**Figure 3.7:** The two left hand side expressions of (3.119) are shown as a function of  $|\mathcal{B}|$ , allowing a cross-check of the numerical evaluation of (3.118). As a result we can estimate that the relative errors of flux-density vector fields introduced by the numerical implementation are of the order of  $10^{-11}$ .

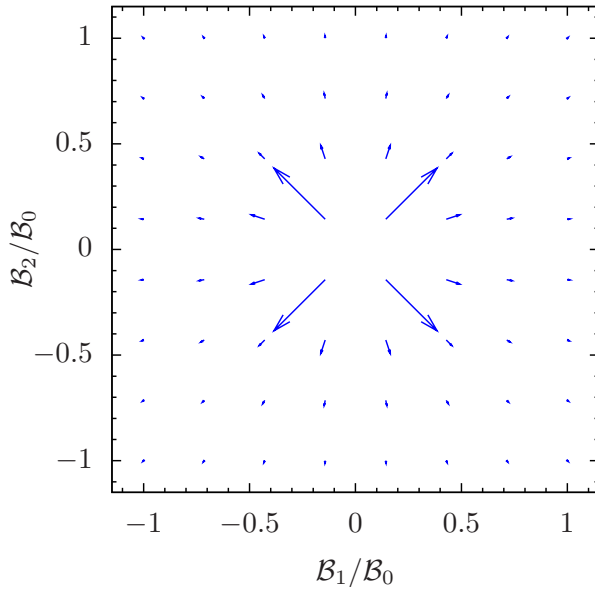


**Figure 3.8:** Visualisation of the P-conserving flux-density vector field  $\hat{\mathbf{J}}_{\alpha}^{(\mathcal{B})PC}(\mathbf{0}, \mathcal{B})$  (3.121) for  $\alpha = 11$  and  $\eta = 0.014$  in magnetic field parameter space at  $\mathcal{B}_3 = 0$ .

### 3.6. Flux Densities in Mixed Parameter Spaces for Hydrogen

---

For any curve  $\mathcal{C} = \partial\mathcal{F}$  in  $\mathcal{B}$  space we get for the Berry phases from (3.73) and (3.118)

$$\gamma_\alpha(\mathcal{C}) = \int_{\mathcal{F}} \mathbf{J}_\alpha^{(\mathcal{B})}(\mathcal{B}) d\mathbf{f}^{(\mathcal{B})} = \begin{cases} -\Omega_{\mathcal{C}} & , \text{ for } \alpha = 9 , \\ +\Omega_{\mathcal{C}} & , \text{ for } \alpha = 11 , \\ 0 & , \text{ for } \alpha = 10, 12 . \end{cases} \quad (3.122)$$

Here  $\Omega_{\mathcal{C}}$  is the solid angle spanned by the curve  $\mathcal{C}$ . Of course, the sign of  $\gamma_\alpha(\mathcal{C})$  depends on the orientation of  $\mathcal{C}$ . This is in accord with the expectation for a spin 1 system; see (2.89) and [29].

Regarding the flux-density vector fields (3.118) emanating from the origin of parameter space, one may view the degeneracy at  $\mathcal{B} = \mathbf{0}$  as the source for  $\mathbf{J}_{11}^{(\mathcal{B})}(\mathbf{0}, \mathcal{B})$  or the sink for  $\mathbf{J}_9^{(\mathcal{B})}(\mathbf{0}, \mathcal{B})$ , respectively. That is, Berry's phase is connected to this degeneracy. However, Berry phases can also emerge in parameter spaces which do not exhibit any degeneracy. We will investigate such an example in the following section.

#### 3.6.2 An Electric Field $\mathcal{E}$ together with a Constant Magnetic Field

We consider the case of geometric flux densities in electric field space with a constant magnetic field  $\mathcal{B} = \mathcal{B}_3 \mathbf{e}_3$  with  $\mathcal{B}_3 > 0$ . Here we find from (3.110)

$$\mathbf{J}_\alpha^{(\mathcal{E})\text{PC}}(\mathcal{E}, \mathcal{B}_3 \mathbf{e}_3) = \mathcal{E} \mathcal{E}_3 \mathcal{B}_3 g_1^\alpha + \mathcal{B}_3 \begin{pmatrix} \mathcal{E}_2 \mathcal{E}_3 \mathcal{B}_3 g_3^\alpha \\ -\mathcal{E}_1 \mathcal{E}_3 \mathcal{B}_3 g_3^\alpha \\ g_2^\alpha \end{pmatrix} , \quad (3.123)$$

$$\begin{aligned} \mathbf{J}_\alpha^{(\mathcal{E})\text{PV}}(\mathcal{E}, \mathcal{B}_3 \mathbf{e}_3) &= \mathcal{E} h_1^\alpha + \mathcal{B}_3 \mathbf{e}_3 \mathcal{E}_3 \mathcal{B}_3 h_2^\alpha + (\mathcal{E}_2 \mathbf{e}_1 - \mathcal{E}_1 \mathbf{e}_3) \mathcal{B}_3 h_3^\alpha \\ &= \mathcal{E} h_1^\alpha + \mathcal{B}_3 \begin{pmatrix} \mathcal{E}_2 h_3^\alpha \\ -\mathcal{E}_1 h_3^\alpha \\ \mathcal{E}_3 \mathcal{B}_3 h_2^\alpha \end{pmatrix} , \end{aligned} \quad (3.124)$$

where  $g_{1,2,3}^\alpha$  and  $h_{1,2,3}^\alpha$  may in general depend on  $\mathcal{E}^2$ ,  $\mathcal{B}_3^2$ , and  $(\mathcal{E}_3 \mathcal{B}_3)^2$ , with  $\alpha \in \{9, 10, 11, 12\}$ . In our case  $\mathcal{B}_3$  is constant. With  $\mathcal{E}_T^2 = \mathcal{E}_1^2 + \mathcal{E}_2^2$  we have, therefore,

$$g_i^\alpha = g_i^\alpha(\mathcal{E}_T^2, \mathcal{E}_3^2) , \quad h_i^\alpha = h_i^\alpha(\mathcal{E}_T^2, \mathcal{E}_3^2) , \quad (i = 1, 2, 3) . \quad (3.125)$$

In the following, we give the results of numerical evaluations of the PC and PV flux-density vectors (3.123) and (3.124), respectively. We split the PV vectors into the contributions from the nuclear-spin independent and dependent PV interactions

$$\mathbf{J}^{(\mathcal{E})\text{PV}} = \mathbf{J}^{(\mathcal{E})\text{PV}_1} + \mathbf{J}^{(\mathcal{E})\text{PV}_2} . \quad (3.126)$$

---

<sup>22</sup>Simply obtained by separation of variables: (3.115)  $\Leftrightarrow -\frac{2}{3} \frac{dg_{14}^\alpha}{g_{14}^\alpha} = \frac{db}{b}$ .

Here the  $\mathbf{J}^{(\mathcal{E})\text{PV}_i}$  are defined as in (3.108) but with  $\delta$  replaced by  $\delta_i$  and  $\mathcal{M}_{\text{PV}}$  replaced by  $\mathcal{M}_{\text{PV}}^{(i)}$  ( $i = 1, 2$ ); see (3.24) and (3.26). Again we shall plot dimensionless vectors

$$\hat{\mathbf{J}}_{\alpha}^{(\mathcal{E})\text{PC}}(\mathcal{E}, \mathcal{B}_3 \mathbf{e}_3) = \eta_{\alpha} \mathbf{J}_{\alpha}^{(\mathcal{E})\text{PC}}(\mathcal{E}, \mathcal{B}_3 \mathbf{e}_3) \mathcal{E}_0^2, \quad (3.127)$$

$$\hat{\mathbf{J}}_{\alpha}^{(\mathcal{E})\text{PV}_i}(\mathcal{E}, \mathcal{B}_3 \mathbf{e}_3) = \eta'_{\alpha,i} \mathbf{J}_{\alpha}^{(\mathcal{E})\text{PV}_i}(\mathcal{E}, \mathcal{B}_3 \mathbf{e}_3) \mathcal{E}_0^2 \quad (3.128)$$

with  $\mathcal{E}_0$  from (3.120) and  $\eta_{\alpha}$  and  $\eta'_{\alpha,i}$  conveniently chosen.

### A PC Flux-Density Vector Field

As an example of a PC flux-density vector field we present in Figure 3.9 the results of a numerical calculation of  $\mathbf{J}_9^{(\mathcal{E})\text{PC}}(\mathcal{E}, \mathcal{B}_3 \mathbf{e}_3)$  for  $\mathcal{B}_3 = 1 \text{ mT}$ . We plot the dimensionless vectors (3.127) with the scaling factor chosen as  $\eta_9 = 2.5 \times 10^4$ . Comparing with (3.123) we see that here the dominant term is the one proportional to  $g_2^9$ :

$$\mathbf{J}_9^{(\mathcal{E})\text{PC}}(\mathcal{E}, \mathcal{B}_3 \mathbf{e}_3) \approx \mathcal{B}_3 g_2^9 (\mathcal{E}_T^2, \mathcal{E}_3^2) \mathbf{e}_3 \quad (3.129)$$

with  $g_2^9(\mathcal{E}_T^2, \mathcal{E}_3^2)$  being practically constant.

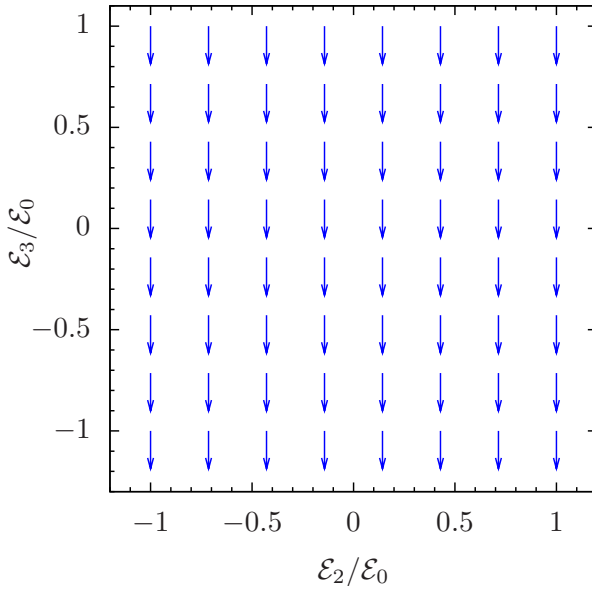


**Figure 3.9:** Visualisation of the real part of the P-conserving flux-density vector field  $\hat{\mathbf{J}}_9^{(\mathcal{E})\text{PC}}(\mathcal{E}, \mathcal{B}_3 \mathbf{e}_3)$  (3.127) in electric field parameter space at  $\mathcal{E}_1 = 1 \text{ V/cm}$ . A constant magnetic field with  $\mathcal{B}_3 = 1 \text{ mT}$  is applied. The scaling factor in (3.127) is chosen as  $\eta_9 = 2.5 \times 10^4$ .

### Sensitivity of Flux-Density Vector Fields to the Electric Dipole Operator

The numerical results shown in Figure 3.9 reveal a large sensitivity of the flux-density vector field  $\mathbf{J}_9^{(\mathcal{E})\text{PC}}$  to the normalisation of the dipole operator  $\underline{\mathbf{D}}$ . Indeed, suppose that we make in our calculations the replacement

$$\underline{\mathbf{D}} \rightarrow \lambda \underline{\mathbf{D}} \quad (3.130)$$

with  $\lambda$  a positive real constant. From  $\mathcal{I}_9^{(\mathcal{E})\text{PC}}$  in (3.86), having the same scaling behaviour as  $\mathbf{J}_9^{(\mathcal{E})\text{PC}}$ , and from the mass matrix (3.25) we find the following scaling behaviour

### 3.6. Flux Densities in Mixed Parameter Spaces for Hydrogen

for  $\mathbf{J}_9^{(\mathcal{E})\text{PC}}$

$$\mathbf{J}_9^{(\mathcal{E})\text{PC}}(\mathcal{E}, \mathcal{B}_3 \mathbf{e}_3) \Big|_{\lambda \underline{\mathbf{D}}} = \lambda^2 \mathbf{J}_9^{(\mathcal{E})\text{PC}}(\lambda \mathcal{E}, \mathcal{B}_3 \mathbf{e}_3) \Big|_{\underline{\mathbf{D}}} . \quad (3.131)$$

Since our calculations show that  $\mathbf{J}_9^{(\mathcal{E})\text{PC}}$  is practically constant for the range of fields explored here we get

$$\mathbf{J}_9^{(\mathcal{E})\text{PC}}(\mathcal{E}, \mathcal{B}_3 \mathbf{e}_3) \Big|_{\lambda \underline{\mathbf{D}}} \approx \lambda^2 \mathbf{J}_9^{(\mathcal{E})\text{PC}}(\mathcal{E}, \mathcal{B}_3 \mathbf{e}_3) \Big|_{\underline{\mathbf{D}}} . \quad (3.132)$$

Therefore, measurements of  $\mathbf{J}_9^{(\mathcal{E})\text{PC}}(\mathcal{E}, \mathcal{B}_3 \mathbf{e}_3)$  for the setup considered in the present section are highly sensitive to deviations of the normalisation of  $\underline{\mathbf{D}}$  from the standard expression as given in Table A.4. By measuring suitable Berry phases, such scalings may prove valuable to determine or cross-check dipole operator representations of more complex atomic species, computed with a lower precision compared to hydrogen.

#### A PV Flux-Density Vector Field

As an example of a PV flux-density vector field we present the numerical results for  $\hat{\mathbf{J}}_9^{(\mathcal{E})\text{PV}_2}$  in Figure 3.10.

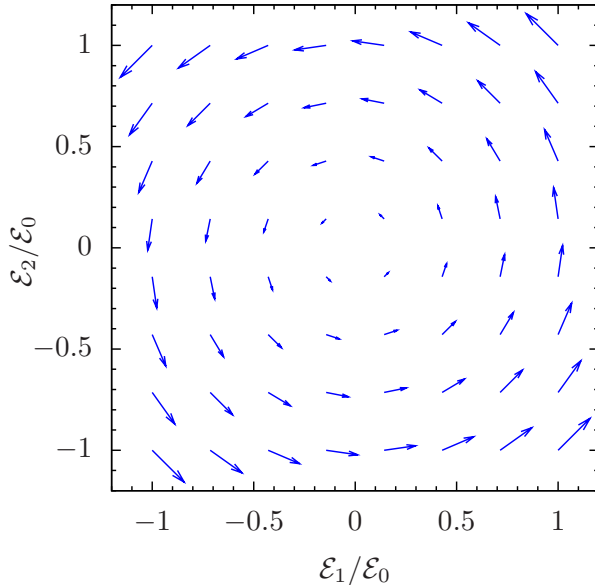


**Figure 3.10:** Visualisation of the real part of the nuclear-spin dependent P-violating flux-density vector field  $\hat{\mathbf{J}}_9^{(\mathcal{E})\text{PV}_2}(\mathcal{E}, \mathcal{B})$  (3.128) in electric field parameter space at  $\mathcal{E}_3 = 1$  V/cm with an additional constant magnetic field  $\mathcal{B} = \mathcal{B}_3 \mathbf{e}_3$ ,  $\mathcal{B}_3 = 1$   $\mu$ T. The scaling factor in (3.128) is chosen as  $\eta'_{9,2} = 400/\delta_2$ .

We find both, the real and the imaginary part of  $\mathbf{J}_9^{(\mathcal{E})\text{PV}_2}(\mathcal{E}, \mathcal{B}_3 \mathbf{e}_3)$  to represent a flow, circulating around the  $\mathbf{e}_3$ -axis, with vanishing third component. That is, in (3.124) for  $\alpha = 9$  the terms involving  $h_1^9$  and  $h_2^9$ , respectively, come out numerically to be negligible compared to the terms involving  $h_3^9$ . We may hence write

$$\mathbf{J}_9^{(\mathcal{E})\text{PV}_2}(\mathcal{E}, \mathcal{B}_3 \mathbf{e}_3) \approx \mathcal{B}_3 h_3^9(\mathcal{E}_T^2, \mathcal{E}_3^2) \begin{pmatrix} \mathcal{E}_2 \\ -\mathcal{E}_1 \\ 0 \end{pmatrix} . \quad (3.133)$$

### Chapter 3. Berry Phases for Hydrogen

---

This is corroborated by numerical studies. For  $|\mathcal{E}_j| \leq \mathcal{E}_0$  ( $j = 1, 2, 3$ ), with  $\mathcal{E}_0$  from (3.120), we find

$$\frac{|\operatorname{Re} e_3 \mathbf{J}_9^{(\mathcal{E})\text{PV}_2}|}{|\operatorname{Re} \mathbf{J}_9^{(\mathcal{E})\text{PV}_2}|} \lesssim 6 \times 10^{-11} \quad (3.134)$$

and

$$\frac{|\mathcal{E}_1 \operatorname{Re} e_1 \mathbf{J}_9^{(\mathcal{E})\text{PV}_2} + \mathcal{E}_2 \operatorname{Re} e_2 \mathbf{J}_9^{(\mathcal{E})\text{PV}_2}|}{|\operatorname{Re} \mathbf{J}_9^{(\mathcal{E})\text{PV}_2}| \sqrt{\mathcal{E}_1^2 + \mathcal{E}_2^2}} \lesssim 2.5 \times 10^{-11}. \quad (3.135)$$

Results similar to (3.134) and (3.135) hold for the imaginary part  $\operatorname{Im} \mathbf{J}_9^{(\mathcal{E})\text{PV}_2}(\mathcal{E}, \mathcal{B}_3 e_3)$  and for  $\mathbf{J}_9^{(\mathcal{E})\text{PV}_1}(\mathcal{E}, \mathcal{B}_3 e_3)$ . Thus, also  $\mathbf{J}_9^{(\mathcal{E})\text{PV}_1}$  has to a good approximation the structure (3.133).

The antisymmetry of  $\operatorname{Re} \mathbf{J}_9^{(\mathcal{E})\text{PV}_2}(\mathcal{E}, \mathcal{B}_3 e_3)$  with respect to  $\mathcal{E} \rightarrow -\mathcal{E}$ , see (3.124), is confirmed numerically at the same level of accuracy. We find

$$\left| \frac{|\operatorname{Re} \mathbf{J}_9^{(\mathcal{E})\text{PV}_2}(\mathcal{E}, \mathcal{B}_3 e_3)|}{|\operatorname{Re} \mathbf{J}_9^{(\mathcal{E})\text{PV}_2}(-\mathcal{E}, \mathcal{B}_3 e_3)|} - 1 \right| \lesssim 2.5 \times 10^{-10} \quad (3.136)$$

and

$$\frac{|\operatorname{Re} \mathbf{J}_9^{(\mathcal{E})\text{PV}_2}(\mathcal{E}, \mathcal{B}_3 e_3) + \operatorname{Re} \mathbf{J}_9^{(\mathcal{E})\text{PV}_2}(-\mathcal{E}, \mathcal{B}_3 e_3)|}{|\operatorname{Re} \mathbf{J}_9^{(\mathcal{E})\text{PV}_2}(\mathcal{E}, \mathcal{B}_3 e_3)|} \lesssim 2.5 \times 10^{-10}. \quad (3.137)$$

Similar numerical results are also obtained for  $\operatorname{Im} \mathbf{J}_9^{(\mathcal{E})\text{PV}_2}(\mathcal{E}, \mathcal{B}_3 e_3)$  and for the real and imaginary parts of  $\mathbf{J}_9^{(\mathcal{E})\text{PV}_1}(\mathcal{E}, \mathcal{B}_3 e_3)$ .

#### 3.6.3 The Parameter Space $\{\mathcal{E}_1, \mathcal{E}_3, \mathcal{B}_3\}$ with a Constant $\mathcal{B}_2$ -Field

In the next example we discuss the parameter space spanned by the vectors

$$\mathbf{L} \equiv \begin{pmatrix} L_1 \\ L_2 \\ L_3 \end{pmatrix} = \begin{pmatrix} \mathcal{E}_0^{-1} & 0 & 0 \\ 0 & \mathcal{E}_0^{-1} & 0 \\ 0 & 0 & \mathcal{B}_0^{-1} \end{pmatrix} \begin{pmatrix} \mathcal{E}_1 \\ \mathcal{E}_3 \\ \mathcal{B}_3 \end{pmatrix}, \quad (3.138)$$

see (3.69) ff. and (3.120). In addition we assume the presence of a constant magnetic field  $\mathcal{B} = 1 \mu\text{T} e_2$ . The values chosen for  $\mathcal{E}_0$  and  $\mathcal{B}_0$  in (3.120) and (3.138) should represent the typical range of electric and magnetic field variations, respectively, for a given experiment. Our choice here is motivated by the discussion of the longitudinal spin echo experiments in [32]. For other experiments different choices of  $\mathcal{E}_0$  and  $\mathcal{B}_0$  will be appropriate.

From (3.69), (3.71), and (3.86) to (3.90) we find

$$\mathbf{J}_\alpha^{(L)}(\mathcal{E}, \mathcal{B}) = \begin{pmatrix} \mathcal{E}_0 \mathcal{B}_0 & 0 & 0 \\ 0 & \mathcal{E}_0 \mathcal{B}_0 & 0 \\ 0 & 0 & \mathcal{E}_0^2 \end{pmatrix} \begin{pmatrix} \mathcal{I}_{\alpha,33}^{(\mathcal{E}, \mathcal{B})}(\mathcal{E}, \mathcal{B}) \\ -\mathcal{I}_{\alpha,13}^{(\mathcal{E}, \mathcal{B})}(\mathcal{E}, \mathcal{B}) \\ 2\mathcal{I}_{\alpha,13}^{(\mathcal{E})}(\mathcal{E}, \mathcal{B}) \end{pmatrix}. \quad (3.139)$$

### 3.6. Flux Densities in Mixed Parameter Spaces for Hydrogen

Here again  $\alpha \in \{9, 10, 11, 12\}$  labels the metastable state to which the geometric flux density corresponds. Inserting in (3.139) the expressions from (3.110) and (3.111) we get for the PC and PV parts of  $\mathbf{J}_\alpha^{(L)}(\boldsymbol{\mathcal{E}}, \boldsymbol{\mathcal{B}})$

$$\mathbf{J}_\alpha^{(L)\text{PC}}(\boldsymbol{\mathcal{E}}, \boldsymbol{\mathcal{B}}) = \begin{pmatrix} \mathcal{B}_3 \mathcal{E}_3 \tilde{g}_1^\alpha + \mathcal{B}_3 \mathcal{E}_1 \tilde{g}_2^\alpha \\ \mathcal{B}_3 \mathcal{E}_3 \tilde{g}_3^\alpha + \mathcal{B}_3 \mathcal{E}_1 \tilde{g}_4^\alpha \\ \tilde{g}_5^\alpha + \mathcal{E}_1 \mathcal{E}_3 \tilde{g}_6^\alpha \end{pmatrix}, \quad (3.140)$$

$$\mathbf{J}_\alpha^{(L)\text{PV}}(\boldsymbol{\mathcal{E}}, \boldsymbol{\mathcal{B}}) = \begin{pmatrix} \tilde{h}_1^\alpha + \mathcal{E}_1 \mathcal{E}_3 \tilde{h}_2^\alpha \\ \tilde{h}_3^\alpha + \mathcal{E}_1 \mathcal{E}_3 \tilde{h}_4^\alpha \\ \mathcal{B}_3 \mathcal{E}_3 \tilde{h}_5^\alpha + \mathcal{B}_3 \mathcal{E}_1 \tilde{h}_6^\alpha \end{pmatrix}, \quad (3.141)$$

where the functions<sup>23</sup>  $\tilde{g}_i^\alpha$  and  $\tilde{h}_i^\alpha$ ,  $i \in \{1, \dots, 6\}$ , may in general depend on  $\mathcal{E}_1^2$ ,  $\mathcal{E}_3^2$  and  $\mathcal{B}_3^2$ ; see Appendix B.3.

For ease of graphical presentation we shall multiply the  $\mathbf{J}_\alpha^{(L)}$  with scaling factors  $\eta$ . Thus we define

$$\hat{\mathbf{J}}_\alpha^{(L)\text{PC}}(\boldsymbol{\mathcal{E}}, \boldsymbol{\mathcal{B}}) = \eta_\alpha \mathbf{J}_\alpha^{(L)\text{PC}}(\boldsymbol{\mathcal{E}}, \boldsymbol{\mathcal{B}}), \quad (3.142)$$

$$\hat{\mathbf{J}}_\alpha^{(L)\text{PV}_i}(\boldsymbol{\mathcal{E}}, \boldsymbol{\mathcal{B}}) = \eta'_{\alpha,i} \mathbf{J}_\alpha^{(L)\text{PV}_i}(\boldsymbol{\mathcal{E}}, \boldsymbol{\mathcal{B}}), \quad (i = 1, 2). \quad (3.143)$$

In the Figures 3.11 to 3.15 we illustrate the results of our numerical calculations of (3.142) and (3.143) for the geometric flux densities of the state with  $\alpha = 9$ . For  $30^3$  grid points in the parameter space volume  $[-\mathcal{E}_0, \mathcal{E}_0]^2 \times [-0.2\mathcal{B}_0, 0.2\mathcal{B}_0]$  we find that numerically

$$|\text{Re } \mathbf{e}_3 \hat{\mathbf{J}}_9^{(L)\text{PC}}| \lesssim 0.2 \left[ (\text{Re } \mathbf{e}_1 \hat{\mathbf{J}}_9^{(L)\text{PC}})^2 + (\text{Re } \mathbf{e}_2 \hat{\mathbf{J}}_9^{(L)\text{PC}})^2 \right]^{\frac{1}{2}}. \quad (3.144)$$

An analogous relation holds for  $\text{Im } \hat{\mathbf{J}}_9^{(L)\text{PC}}(\boldsymbol{\mathcal{E}}, \boldsymbol{\mathcal{B}})$ . This justifies the presentation of these flux-density vector fields in the  $\mathcal{E}_1 - \mathcal{E}_3$  plane as representative vector field structures. Investigating the dependencies of  $\mathbf{J}_9^{(L)}(\boldsymbol{\mathcal{E}}, \boldsymbol{\mathcal{B}})$  on  $\mathcal{E}_1$ ,  $\mathcal{E}_3$  and  $\mathcal{B}_3$  we find our numerical results to be consistent with the analytical structures in (3.140) and (3.141). Note that in Figure 3.15 we have chosen a scaling factor depending on  $\mathcal{B}_3$  since the magnitude of the vector  $\mathbf{J}_9^{(L)\text{PV}_2}(\boldsymbol{\mathcal{E}}, \boldsymbol{\mathcal{B}})$  shows a strong increase towards  $\mathcal{B}_3 = 0$ . This observation is an example of how to provide for the possibility to create enhanced PV Berry phases. We will calculate selected PC and PV Berry phases explicitly in Section 3.7 as well as in the Chapters 5 and 6.

#### Divergence and Curl

From both, (3.67) and (3.68), we can easily check the divergence condition (3.75). We recall from (3.76) that  $\hat{\mathbf{J}}_9^{(L)\text{PC}}$  is divergence free and, thus, generated by a non-vanishing vortex distribution  $\text{rot } \hat{\mathbf{J}}_9^{(L)\text{PC}}$ . Figure 3.16 shows the divergence for  $16^3$  grid points in the parameter space given by (3.138) and  $\boldsymbol{\mathcal{B}} = 1 \mu\text{T } \mathbf{e}_2$ . We find numerically good

<sup>23</sup>The *constant*  $\mathcal{B}_2$  is absorbed in the invariant functions and, hence, does not appear explicitly in (3.140) and (3.141).

agreement with the analytical result of identically vanishing divergence. Calculating the curl of  $\hat{\mathbf{J}}_9^{(L)PC}$  numerically using (3.77), cf. Figure 3.17, we find  $\text{rot } \hat{\mathbf{J}}_9^{(L)PC}$  to be in agreement with a direct Mathematica evaluation using a fit function representing  $\hat{\mathbf{J}}_9^{(L)PC}$ .

The examples of PV flux-density vector fields in Figures 3.13 to 3.15 illustrate the full three-dimensional vector fields which again are divergence free and thus represent flows without sources or sinks.

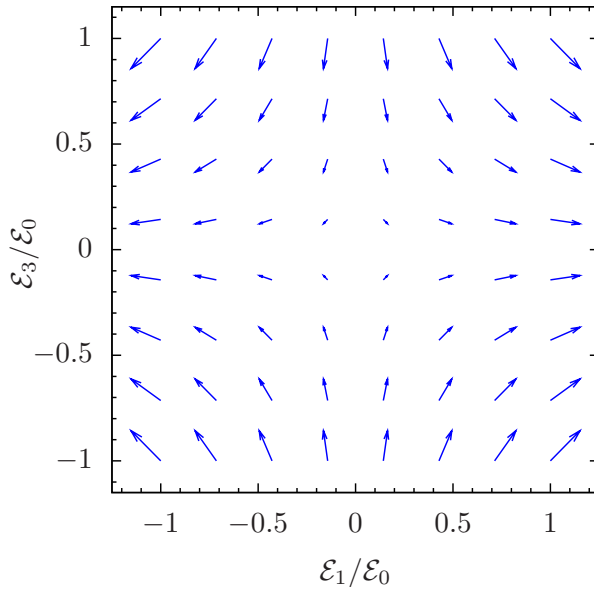


**Figure 3.11:** Visualisation of the 1 and 2 components of the real part of the P-conserving flux-density vector field  $\hat{\mathbf{J}}_9^{(L)PC}(\boldsymbol{\mathcal{E}}, \boldsymbol{\mathcal{B}})$  (3.142) at  $\mathcal{B}_3 = 143 \mu\text{T}$ . The scaling factor is chosen as  $\eta_9 = 2.5 \times 10^4$ .

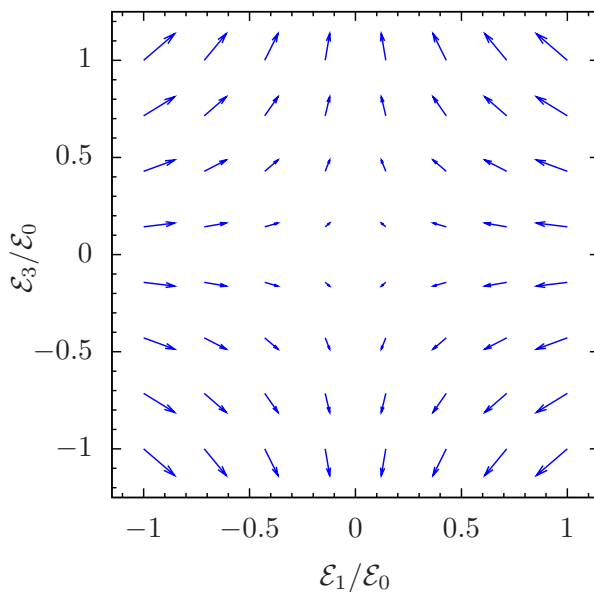


**Figure 3.12:** Visualisation of the 1 and 2 components of the imaginary part of the P-conserving flux-density vector field  $\hat{\mathbf{J}}_9^{(L)PC}(\boldsymbol{\mathcal{E}}, \boldsymbol{\mathcal{B}})$  (3.142) at  $\mathcal{B}_3 = 143 \mu\text{T}$ . The scaling factor is chosen as  $\eta_9 = 2.7 \times 10^5$ .

### 3.6. Flux Densities in Mixed Parameter Spaces for Hydrogen

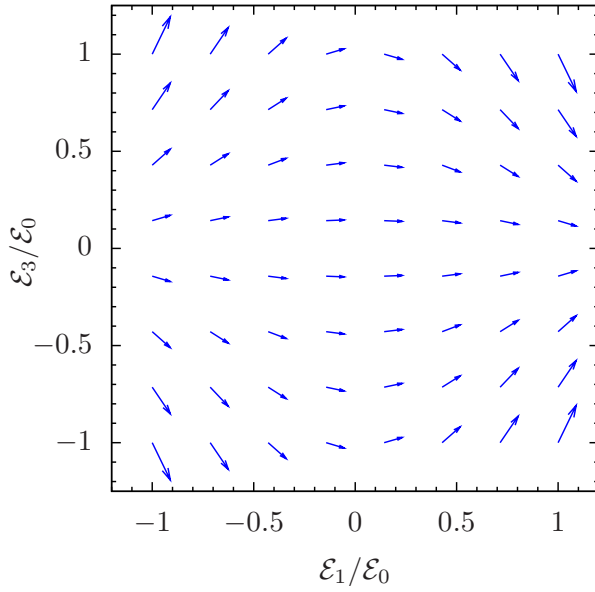


**Figure 3.13:** Visualisation of the 1 and 2 components of the real part of the nuclear-spin dependent P-violating flux-density vector field  $\hat{\mathbf{J}}_9^{(L)PV_2}(\mathcal{E}, \mathcal{B})$  (3.143) at  $\mathcal{B}_3 = 143 \mu\text{T}$ . The scaling factor is chosen as  $\eta'_{9,2} = 10^4/\delta_2$ .

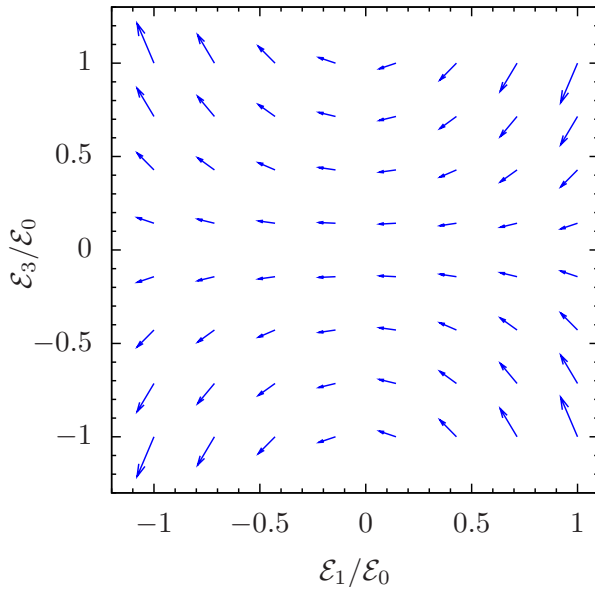


**Figure 3.14:** Visualisation of the 1 and 2 components of the real part of the nuclear-spin dependent P-violating flux-density vector field  $\hat{\mathbf{J}}_9^{(L)PV_2}(\mathcal{E}, \mathcal{B})$  (3.143) at  $\mathcal{B}_3 = 86 \mu\text{T}$ . The scaling factor is chosen as  $\eta'_{9,2} = 4 \times 10^3/\delta_2$ .

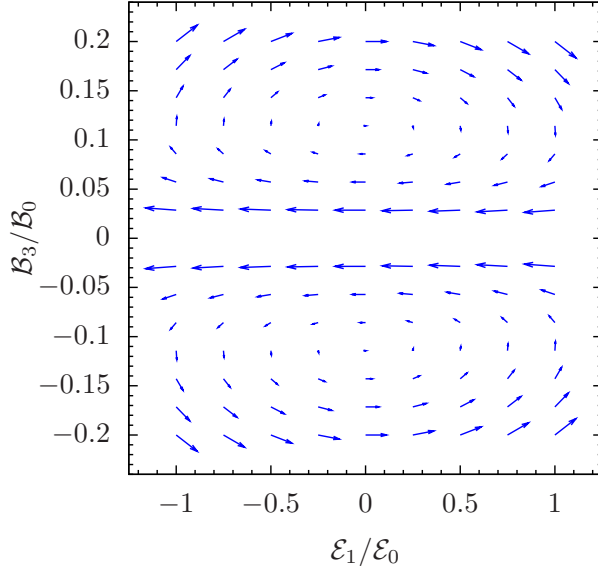


**Figure 3.15:** Visualisation of the 1 and 3 components of the real part of the nuclear-spin dependent P-violating flux-density vector field  $\hat{\mathbf{J}}_9^{(L)PV_2}(\boldsymbol{\mathcal{E}}, \boldsymbol{\mathcal{B}})$  (3.143) at  $\mathcal{E}_3 = 0$ . In order to resolve the structure more clearly the scaling factor is chosen as  $\eta'_{9,2} = 2 \times 10^5 |\mathcal{B}_3/\mathcal{B}_0|^2/\delta_2$ .

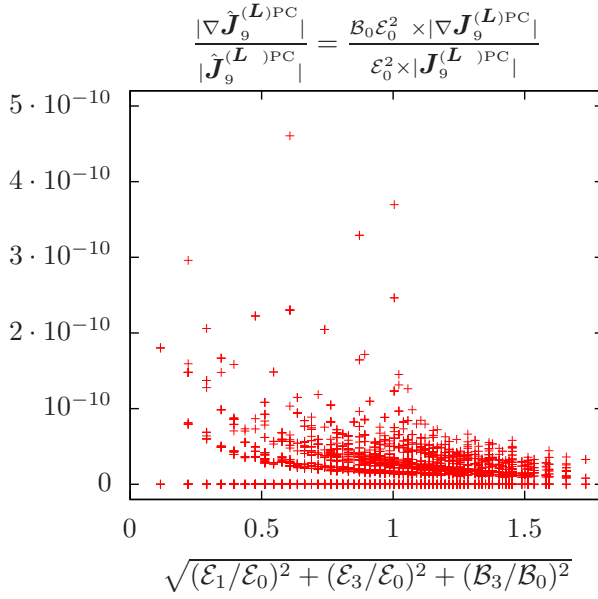


**Figure 3.16:** Numerical evaluation of the divergence of the flux-density vector field (3.142) with  $\alpha = 9$  at  $16^3$  grid points of a cubic grid in the parameter space (3.138) with  $\boldsymbol{\mathcal{B}} = 1 \mu\text{T} \mathbf{e}_2$ . The corresponding values, directly derived from the left hand side of (3.75) via numerical implementation of (3.68), are normalised to  $\frac{\hat{\mathbf{J}}_9^{(L)PC}}{\sqrt{(\mathcal{E}_1/\mathcal{E}_0)^2 + (\mathcal{E}_3/\mathcal{E}_0)^2 + (\mathcal{B}_3/\mathcal{B}_0)^2}}$ .

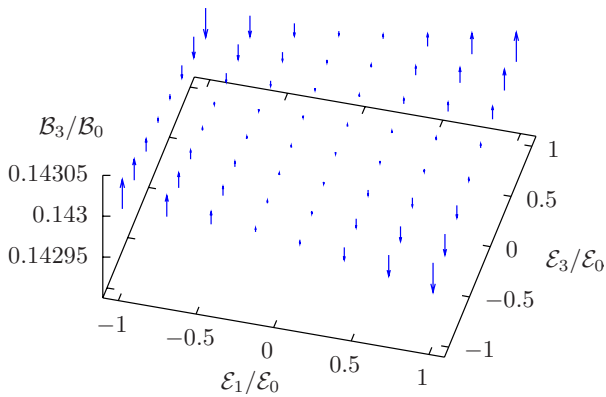


**Figure 3.17:** Numerical evaluation of the curl of the real part of the curl  $(\text{rot } \hat{\mathbf{J}}_9^{(L)PC})_3 = \eta_9 \mathcal{E}_0^2 (\text{rot } \mathbf{J}_9^{(L)PC})_3$  at  $8^2$  grid points of a square grid in the parameter space (3.138) with  $\boldsymbol{\mathcal{B}} = 1 \mu\text{T} \mathbf{e}_2$  at constant  $\mathcal{B}_3 = 143 \mu\text{T}$ . That is, the same parameter grid points as in Figure 3.11 are considered here. We only plot the component of the curl in  $\mathcal{B}_3$ -direction to connect to Figure 3.11. The scaling factor is chosen as  $\eta_9 = 1$ .

### 3.6.4 Systematic Analysis of Flux-Density Vector Fields

To obtain an impression of the plethora of possible flux-density vector fields we present appropriately scaled numerical results of (3.71) for three-dimensional cubic parameter spaces  $\mathbf{L}$  with edge intervals  $[-\mathcal{B}_0, \mathcal{B}_0]$  or  $[-\mathcal{E}_0, \mathcal{E}_0]$ , respectively. However, the resolution of  $6^3$  grid points is not sufficient to reveal all features of the vector fields. For instance, as shown in Section 3.6.3, interesting and valuable structures emerge in regimes of  $\mathcal{B}_3 < 0.2\text{mT}$  in the parameter space  $\{\mathcal{E}_1, \mathcal{E}_3, \mathcal{B}_3\}$  with constant  $\mathcal{B}_2$ , see Figure 3.15. With the grid resolution employed in the present section it were not possible to reveal that structure. An exhaustive exploration of the full six-dimensional parameter space of electric and magnetic fields is left for future work. Though, with the present thesis all necessary theoretical and numerical tools for that task are provided.

The real parts of vector fields  $\hat{\mathbf{j}}_9^{(\mathbf{L})\text{PC}}$  and  $\hat{\mathbf{j}}_9^{(\mathbf{L})\text{PV}_2}$  in parameter spaces  $\mathbf{L}$  are given in Figures 3.18–3.26 in this section. They should be considered as a first illustration of the variety of geometric flux-density vector fields emerging for metastable states of hydrogen exposed to arbitrary combinations of electric and magnetic fields. We note the constant field components and the scaling factors  $\eta_9$  in the titles of the plots. On the left hand sides of the Figures 3.18–3.26 we give the PC part. On the right hand sides the nuclear-spin dependent PV part is shown.

Parameter spaces which effectively yield the same vector field structures are omitted. For instance, the parameter space  $\{\mathcal{E}_1, \mathcal{B}_2, \mathcal{B}_3\}$  with constant  $\mathcal{E}_2$  is presented here, but  $\{\mathcal{E}_1, \mathcal{B}_2, \mathcal{B}_3\}$  with constant  $\mathcal{E}_3$  is not since they are the same modulo a  $\pi/2$ -rotation and a sign in the  $\{\mathcal{B}_2, \mathcal{B}_3\}$ -subspace. We list the considered parameter spaces in Table 1. The constant field components are chosen as  $\mathcal{E}_0$  or  $\mathcal{B}_0$ , respectively. Whenever two constant electric field components  $\mathcal{E}_i$ ,  $i \in \{1, 2, 3\}$ , are involved, we choose  $\mathcal{E}_i = \mathcal{E}_0/\sqrt{2}$ . We have chosen the parameter space volumes such that  $|\mathcal{E}| \lesssim \mathcal{E}_0 = 1\text{V/cm}$ . That way, the field variations can be kept within in the limits for adiabatic evolution, spelled out in Section 3.2.1, for about 1000 cyclings of a curve around the boundary surfaces of the parameter space volumes.

We also show vector fields for those parameter spaces which exhibit only numerical noise instead of a clear structure in order to give error estimates of the used numerical software. In addition, these parameter spaces can be especially useful when working out paths with vanishing PC or PV Berry phases, respectively.

As a prelude of what is still to come regarding the systematic analysis of flux-density vector fields we present selected plots in Figure 3.27 employing parameter space regions differing from those mentioned above. There, we plot the imaginary part of  $\hat{\mathbf{j}}_{11}^{(\mathcal{B})\text{PC}}$  in the magnetic field parameter space  $\{\mathcal{B}_1, \mathcal{B}_2, \mathcal{B}_3\}$  with  $\mathcal{E}_3 = 1\text{V/cm}$ .

variables	constants	numerical error		scaling factor $\eta'_{9,2}$	Figure
		PC	PV <sub>2</sub>		
$\mathcal{B}_1 \mathcal{B}_2 \mathcal{B}_3$	–		✓	$3.0 \times 10^{24}$	3.18
	$\mathcal{E}_3$			$5.0 \times 10^{14}$	3.19
$\mathcal{E}_1 \mathcal{E}_2 \mathcal{E}_3$	$\mathcal{B}_3$			$4.0 \times 10^{17}$	3.20
$\mathcal{E}_1 \mathcal{B}_2 \mathcal{B}_3$	–	✓	✓	$2.0 \times 10^{24}$	3.21
	$\mathcal{B}_1$			$5.0 \times 10^{13}$	
	$\mathcal{E}_2$			$3.0 \times 10^{14}$	
	$\mathcal{B}_1 \mathcal{E}_2$			$5.0 \times 10^{13}$	
$\mathcal{E}_2 \mathcal{B}_2 \mathcal{B}_3$	–	✓		$6.0 \times 10^{12}$	3.22
	$\mathcal{B}_1$			$5.0 \times 10^{13}$	
	$\mathcal{E}_1$			$6.0 \times 10^{12}$	
	$\mathcal{E}_3$	✓		$6.0 \times 10^{12}$	
	$\mathcal{E}_1 \mathcal{E}_3$			$6.0 \times 10^{12}$	
	$\mathcal{B}_1 \mathcal{E}_1$			$5.0 \times 10^{13}$	
	$\mathcal{B}_1 \mathcal{E}_3$			$5.0 \times 10^{13}$	
$\mathcal{B}_1 \mathcal{E}_1 \mathcal{E}_3$			$5.0 \times 10^{13}$		
$\mathcal{E}_1 \mathcal{E}_2 \mathcal{B}_3$	–		✓	$1.0 \times 10^{28}$	3.23
	$\mathcal{B}_1$			$5.0 \times 10^{13}$	3.24
	$\mathcal{E}_3$			$3.0 \times 10^{16}$	
	$\mathcal{B}_1 \mathcal{E}_3$			$5.0 \times 10^{13}$	
$\mathcal{E}_1 \mathcal{E}_2 \mathcal{B}_1$	–	✓		$1.2 \times 10^{16}$	3.25
	$\mathcal{B}_2$	✓		$8.0 \times 10^{12}$	3.26
	$\mathcal{B}_3$			$1.0 \times 10^{13}$	
	$\mathcal{B}_2 \mathcal{B}_3$			$1.0 \times 10^{13}$	
	$\mathcal{E}_3$			$1.5 \times 10^{16}$	
	$\mathcal{E}_3 \mathcal{B}_2$			$8.0 \times 10^{12}$	
	$\mathcal{E}_3 \mathcal{B}_3$			$1.0 \times 10^{13}$	
	$\mathcal{E}_3 \mathcal{B}_2 \mathcal{B}_3$			$1.0 \times 10^{13}$	

**Table 1:** A representative listing of three-dimensional electromagnetic parameter spaces and their basic properties regarding PC and nuclear-spin dependent flux densities. A selection of flux-density vector fields is given in Figures 3.18–3.26. The column ‘variables’ specifies the field components the three-dimensional parameter space is composed of. In the column ‘constants’ the field components which are held at constant values are listed, cf. Section 3.6.4 for details. Wherever a check mark is set in the column ‘numerical error’ we suppose the corresponding PC or PV<sub>2</sub> vector field to vanish but plotted the numerical results nonetheless in order to provide estimates on the errors of our numerical software. For the PV<sub>2</sub> vector fields with an obvious structure we observe a range of five orders of magnitude for the scaling factors  $\eta'_{9,2}$ . The shown dimensionless vector fields  $\hat{J}$  allow for convenient comparisons of the scaling factors, that is, of the expected magnitudes of Berry phases in the employed parameter regions.

### 3.6. Flux Densities in Mixed Parameter Spaces for Hydrogen

**Figure 3.18**

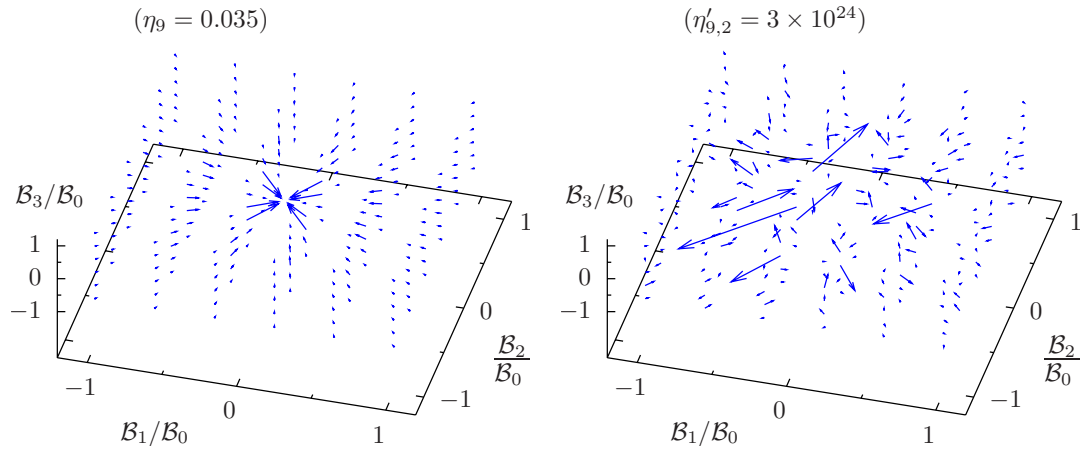


**Figure 3.19**

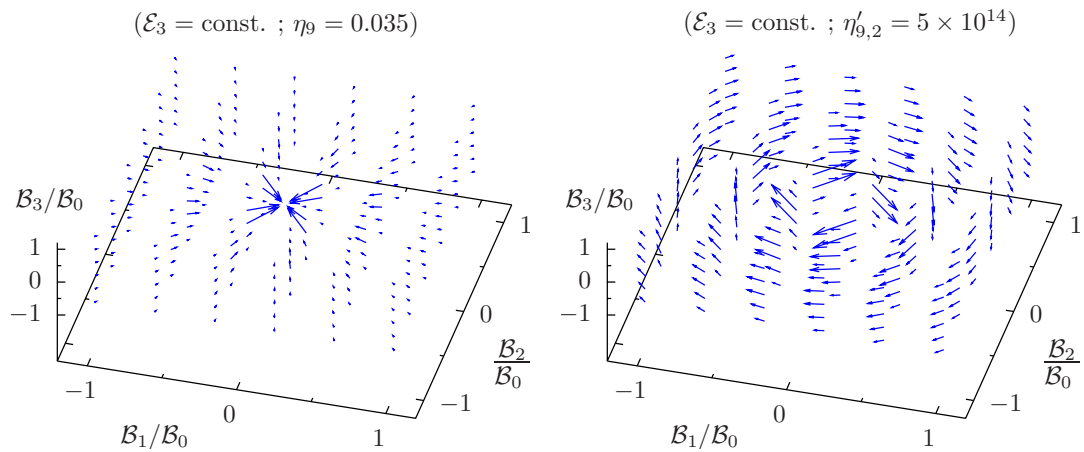


**Figure 3.20**

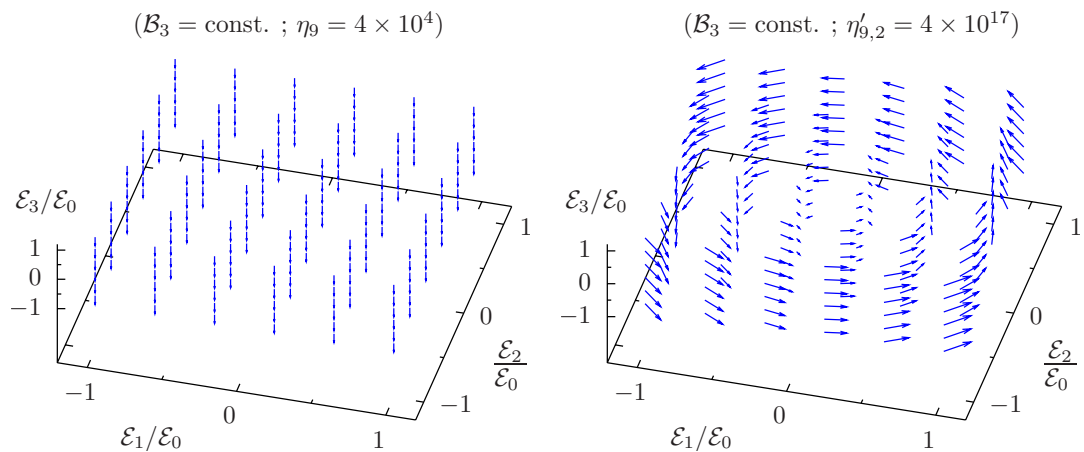


Figure 3.21

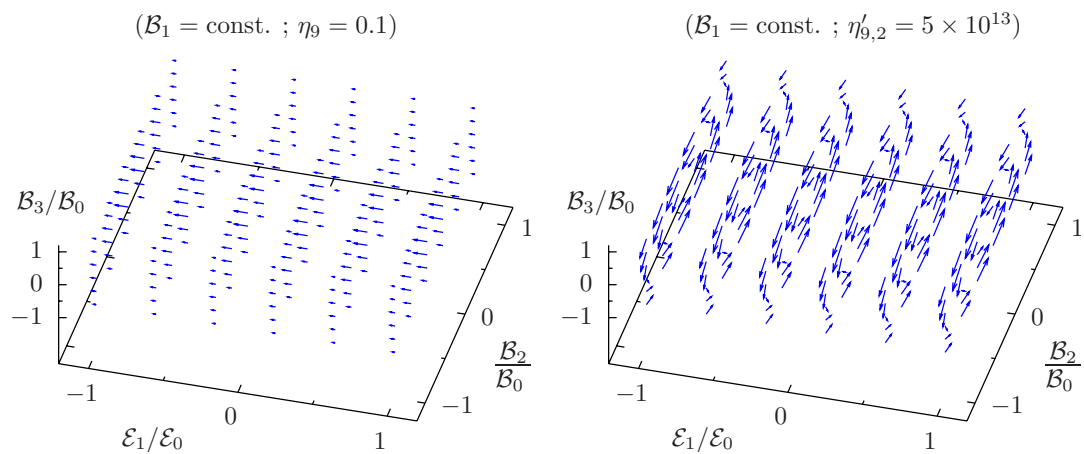


Figure 3.22

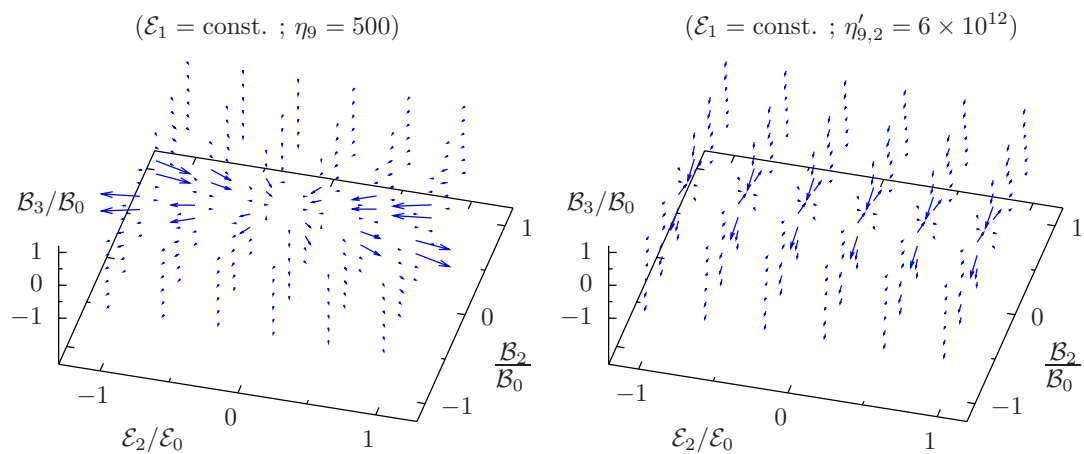
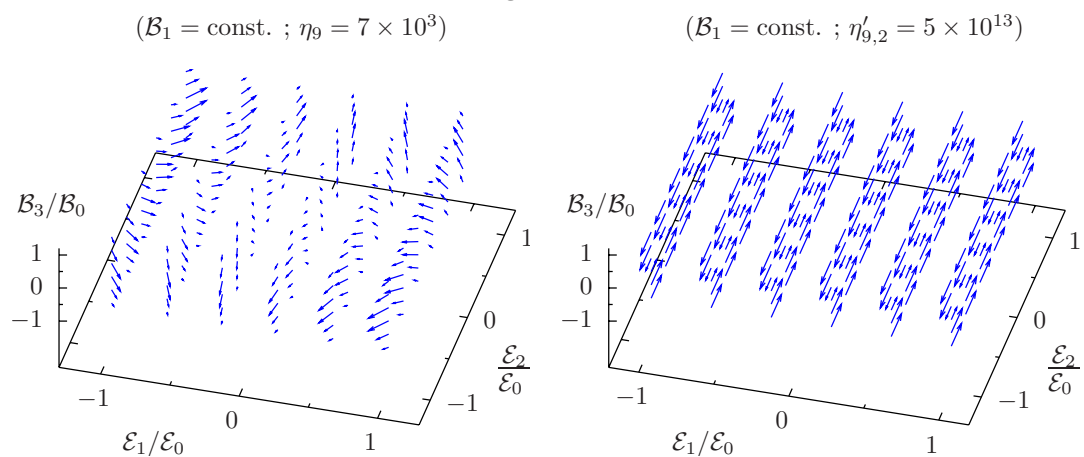
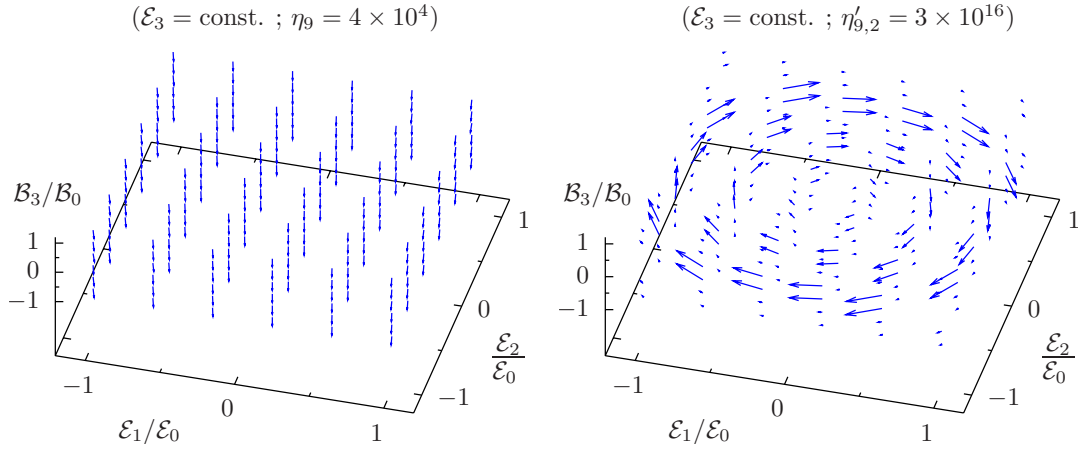


Figure 3.23

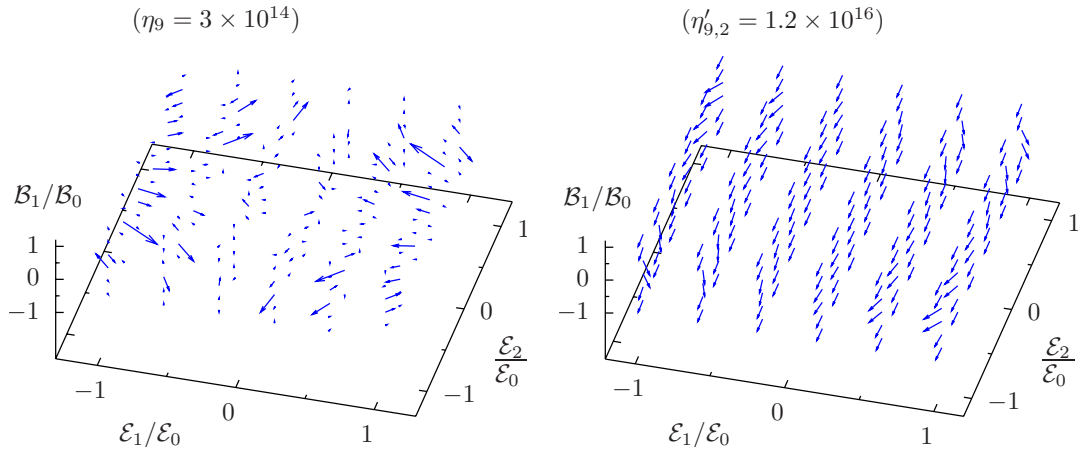


### 3.6. Flux Densities in Mixed Parameter Spaces for Hydrogen

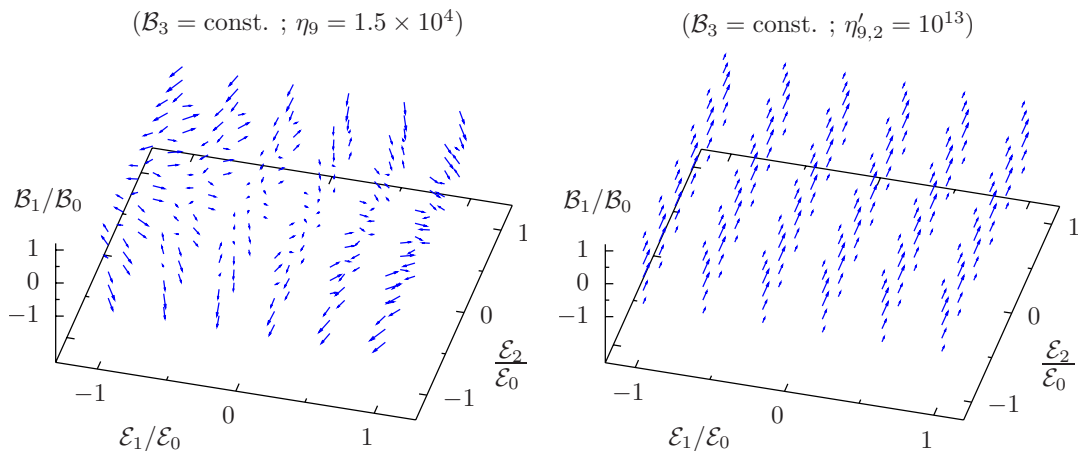
**Figure 3.24**

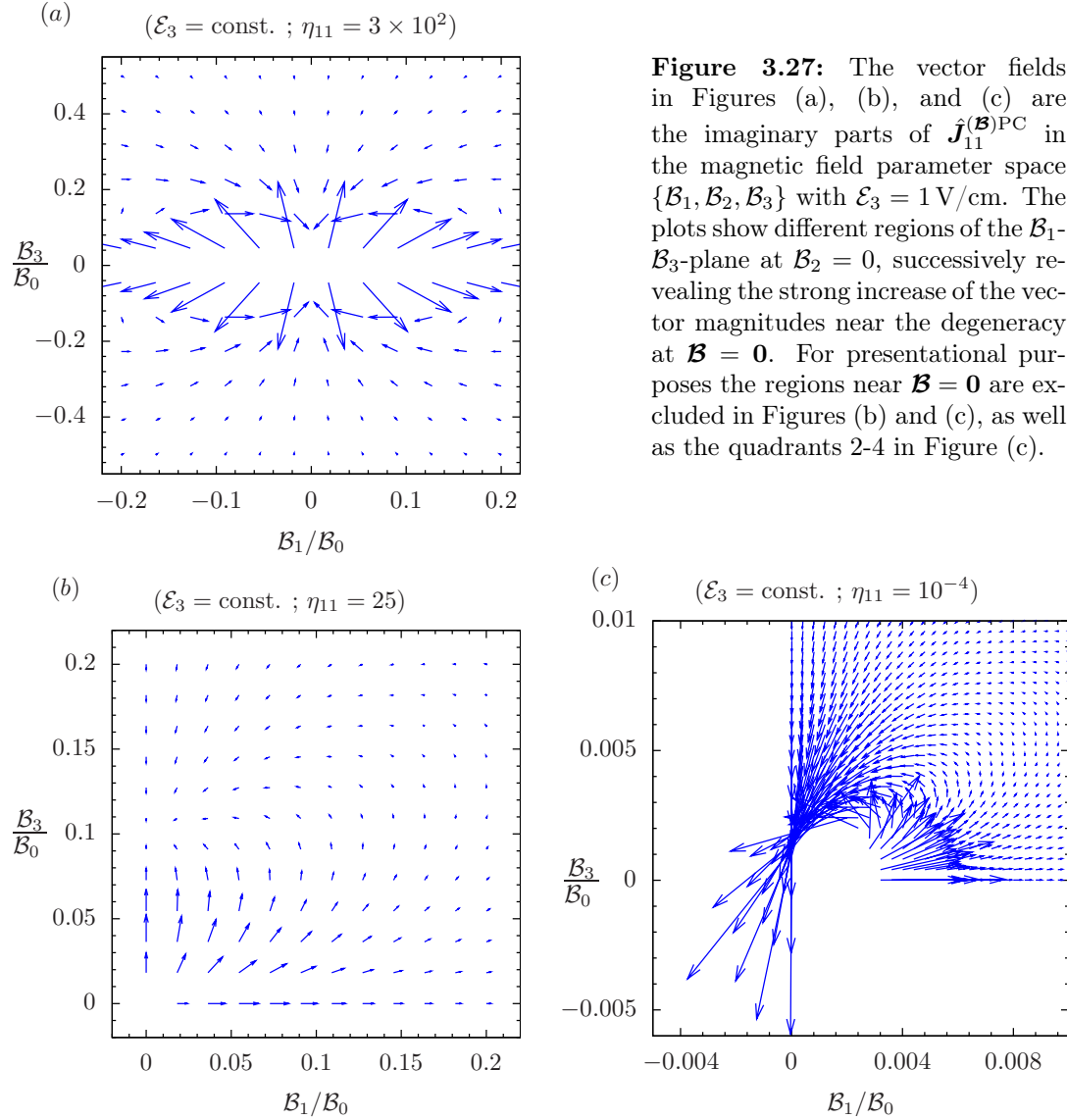


**Figure 3.25**



**Figure 3.26**





### 3.7 Berry Phases for Specific Field Configurations

The analysis of flux-density vector fields in the preceding sections constitutes the basis for preselecting parameter space regions in order to derive Berry phases with tailored properties.

For an adiabatically evolving hydrogen atom the closed path  $\mathcal{C}$  and, therefore, the encircled area  $\mathcal{F}$  in parameter space can, e.g., be chosen such that only PC or PV Berry phases emerge. We are also able to identify parameter space regions where PV geometric phases are enhanced. Of course, we have as well access to both real and imaginary Berry phases.

In the following, we give three instructive examples based on the flux-density vector fields of Section 3.6. The geometric phases are calculated via the line integral repres-

### 3.7. Berry Phases for Specific Field Configurations

entation outlined in Section 3.4. With respect to the labelling of states, that is, the labelling of vector fields as well, there are some subtleties which will be dealt with in Chapter 5. This issue is, however, of no concern in the present section.

#### A PC Geometric Phase

As a first example we calculate the PC geometric phase for the following path in  $\mathcal{E}$  space

$$\mathcal{C}: z \rightarrow \mathcal{E}(z) = \begin{pmatrix} 1.0 + 0.5 \times \sin(200\pi z) \\ 0.5 \times \cos(200\pi z) \\ 1.0 \end{pmatrix} \text{ V/cm}, \quad 0 \leq z \leq 1. \quad (3.145)$$

That is, we consider a path circling 100 times in the  $\mathcal{E}_1$ - $\mathcal{E}_2$ -plane which is orthogonal to the flux direction for  $\alpha = 9$ , see (3.129) and Figure 3.9. For the constant magnetic field chosen there,  $\mathcal{B}_3 = 1 \text{ mT}$ , we obtain for

$$\gamma_9^{\text{PC}}(\mathcal{C}) = 5.89 \times 10^{-4} - 5.25 \times 10^{-5} i. \quad (3.146)$$

Decreasing the constant magnetic field  $\mathcal{B}_3$  we get larger geometric phases. This may seem puzzling at first since the l.h.s of Figure 3.24 suggests no variation of  $\gamma_9^{\text{PC}}(\mathcal{C})$  due to a variation of  $\mathcal{B}_3$ . However, the parameter region of strongly increased magnitudes of  $\mathbf{J}_9^{(\mathcal{E})\text{PC}}(\mathcal{E}, \mathcal{B}_3 \mathbf{e}_3)$  towards the  $\mathcal{B}_3$ -plane is not covered by the grid in Figure 3.24. The scaling factor  $\eta_9 = 4 \times 10^4$  is considerably larger than  $\eta_9 = 450$  in Figure 3.28.

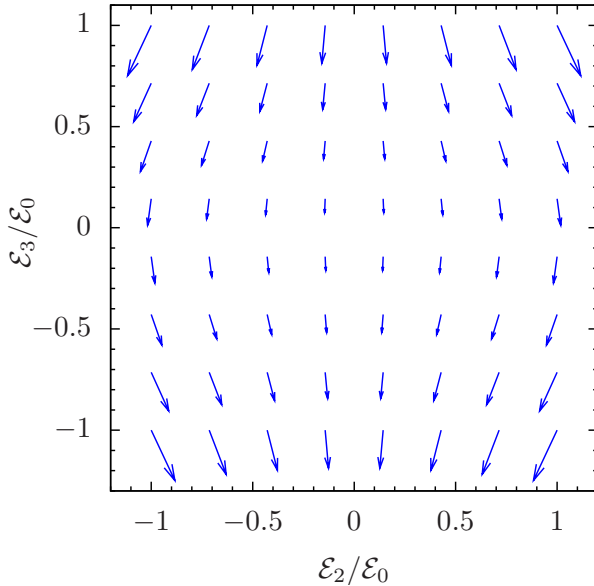


**Figure 3.28:** Visualisation of the real part of the P-conserving flux-density vector field  $\hat{\mathbf{J}}_9^{(\mathcal{E})\text{PC}}(\mathcal{E}, \mathcal{B}_3 \mathbf{e}_3)$  (3.127) in electric field parameter space at  $\mathcal{E}_1 = 1 \text{ V/cm}$ . A constant magnetic field with  $\mathcal{B}_3 = 1 \mu\text{T}$  is applied. The scaling factor in (3.127) is chosen as  $\eta_9 = 450$ .

There, numerical results of the flux-density vector field  $\mathbf{J}_9^{(\mathcal{E})\text{PC}}(\mathcal{E}, \mathcal{B}_3 \mathbf{e}_3)$  for  $\mathcal{B}_3 = 1 \mu\text{T}$  are presented. For the curve (3.145),  $\mathcal{B}_3 = 1 \mu\text{T}$ , and  $\alpha = 9$  we obtain

$$\gamma_9^{\text{PC}}(\mathcal{C}) = 0.0340 - 0.00596 i. \quad (3.147)$$

### Chapter 3. Berry Phases for Hydrogen

---

This example is reminiscent of the need to carefully explore the full parameter space when searching for enlarged Berry phases. Though, the here observed increase is not surprising since the degeneracy at  $\mathbf{B} = \mathbf{0}$  is approached for decreasing  $\mathcal{B}_3$ .

#### Modifying Decay Rates

The emergence of non-vanishing imaginary parts of the flux-density vector fields, see for example Figure 3.12 in  $\mathbf{L}$  space (3.138), leads to an interesting phenomenon. Let us consider a closed curve  $\mathcal{C}$ , being the boundary of a surface  $\mathcal{F}$  in  $\mathbf{L}$  space. We parametrise  $\mathcal{C}$  as

$$\mathcal{C}: z \rightarrow \mathbf{L}(z), \quad 0 \leq z \leq 1, \quad \mathbf{L}(0) = \mathbf{L}(1), \quad (3.148)$$

cf. (3.55), (3.57). Suppose that over a time interval  $[0, T]$  this curve in parameter space is run through by the system in the following way:

$$t \rightarrow z(t) = \frac{t}{T}, \quad 0 \leq t \leq T, \quad \mathcal{C}: t \rightarrow \mathbf{L}(z(t)). \quad (3.149)$$

We consider the adiabatic limit where  $T$  becomes very large. We shall also consider that the system is run through the curve  $\mathcal{C}$  in the reverse direction:

$$t \rightarrow \bar{z}(t) = \frac{T-t}{T} = 1 - z(t), \quad 0 \leq t \leq T, \quad \bar{\mathcal{C}}: t \rightarrow \mathbf{L}(\bar{z}(t)). \quad (3.150)$$

Suppose that we have at  $t = 0$  the atom in the initial state  $\psi_\alpha(0)$ , see (3.40). We change the parameters  $\mathbf{L}$  along the curve  $\mathcal{C}$  as in (3.149). From (3.40) to (3.42) we find the decrease of the norm of the state at time  $T$  to be

$$\frac{|\psi_\alpha(T)|^2}{|\psi_\alpha(0)|^2} = \exp [+2 \operatorname{Im} \varphi_\alpha(T) - 2 \operatorname{Im} \gamma_\alpha(T)]. \quad (3.151)$$

Here,  $2 \operatorname{Im} \varphi_\alpha(T)$  and  $2 \operatorname{Im} \gamma_\alpha(T)$  are the contributions due to the dynamic and geometric phases, respectively,

$$\begin{aligned} 2 \operatorname{Im} \varphi_\alpha(T) &= T \int_0^1 dz E_\alpha(\mathbf{L}(z)), \\ 2 \operatorname{Im} \gamma_\alpha(T) &= 2 \operatorname{Im} \int_{\mathcal{F}} \mathbf{J}_\alpha^{(\mathbf{L})}(\mathbf{L}) d\mathbf{f}^{\mathbf{L}}; \end{aligned} \quad (3.152)$$

see (3.56) and (3.73). From (3.151) we can define an effective decay rate for the state  $\alpha$  under the above conditions as

$$\begin{aligned} \Gamma_{\alpha, \text{eff}}(\mathcal{C}, T) &= \frac{1}{T} [-2 \operatorname{Im} \varphi_\alpha(T) + 2 \operatorname{Im} \gamma_\alpha(T)] \\ &= -2 \operatorname{Im} \int_0^1 dz E_\alpha(\mathbf{L}(z)) + \frac{2}{T} \operatorname{Im} \int_{\mathcal{F}} \mathbf{J}_\alpha^{(\mathbf{L})}(\mathbf{L}) d\mathbf{f}^{\mathbf{L}}. \end{aligned} \quad (3.153)$$

Note that this effective decay rate depends, of course, on the curve  $\mathcal{C}$  and that the geometric contribution is suppressed by a factor  $1/T$  relative to the dynamic contribution. From (3.151) and (3.153) we get for the decrease of the norm of the state  $\alpha$

$$\frac{|\psi_\alpha(T)|^2}{|\psi_\alpha(0)|^2} = \exp [-\Gamma_{\alpha, \text{eff}}(\mathcal{C}, T) T]. \quad (3.154)$$

### 3.7. Berry Phases for Specific Field Configurations

Now we start again with the state  $\psi_\alpha(0)$  at time  $t = 0$  but we change the parameters  $\mathbf{L}$  along the reverse curve  $\bar{\mathcal{C}}$  (3.150). The dynamic term in (3.153) does not change<sup>24</sup> whereas the geometric term changes sign,

$$\Gamma_{\alpha,\text{eff}}(\bar{\mathcal{C}}, T) = -2 \text{Im} \int_0^1 dz E_\alpha(\mathbf{L}(z)) - \frac{2}{T} \text{Im} \int_{\mathcal{F}} \mathbf{J}_\alpha^{(\mathbf{L})}(\mathbf{L}) d\mathbf{f}^{\mathbf{L}} . \quad (3.155)$$

Thus, the effective decay rate depends on the geometry and reversing the sense of the running through our closed curve in parameter space changes the sign of the geometric part.

As a concrete example we choose (3.138) for the  $\mathbf{L}$  space, together with  $\mathbf{B} = 1 \mu\text{T} \mathbf{e}_2$ , and the following curve, illustrated in Figure 3.29,

$$\begin{aligned} \mathcal{C}: z &\rightarrow \mathbf{L}(z) , \quad 0 \leq z \leq 1 , \\ \mathcal{E}_1(z) &= 0.8 \text{ V/cm} , \\ \mathcal{E}_3(z) &= -0.5 \times \sin(4\pi z) \text{ V/cm} , \\ \mathcal{B}_3(z) &= [2 + 2 \times \cos(4\pi z)] \mu\text{T} . \end{aligned} \quad (3.156)$$

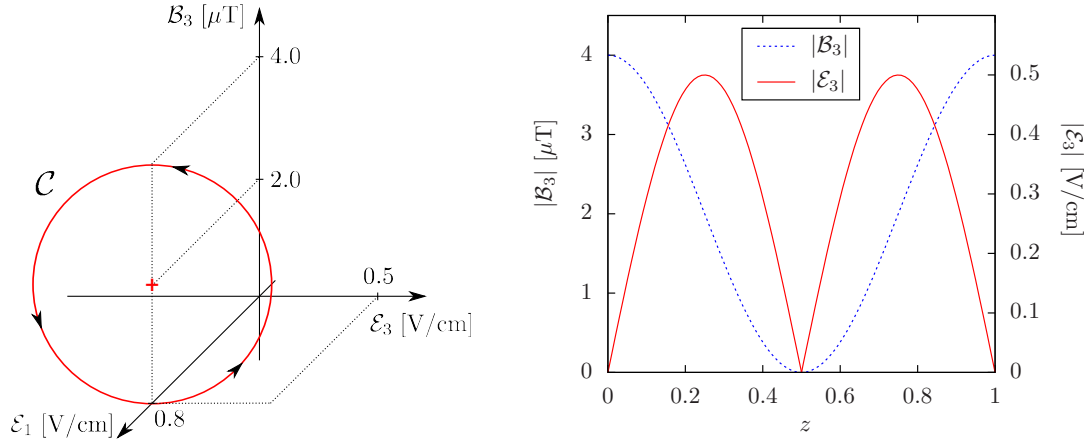


**Figure 3.29:** Left hand side: The curve  $\mathcal{C}$  (3.156) in the parameter space  $\mathcal{E}_1, \mathcal{E}_3, \mathcal{B}_3$ . The circle is run through twice. Right hand side: The evolution of  $|\mathcal{B}_3|$  and  $|\mathcal{E}_3|$  as a function of  $z$  for one cycling starting at  $(\mathcal{B}_3 = 4 \mu\text{T}, \mathcal{E}_3 = 0)$ . The magnitudes of the fields evolve the same way for both directions of the path, indicating the effect of different decay rates for opposite cycling directions to be geometry-dependent rather than depending on the field strengths.

We suppose as in (3.149) that  $\mathcal{C}$  is run through in a time  $T$  with  $z(t) = t/T$ . During this time the path in  $\mathbf{L}$  space makes two loops according to (3.156). With  $T = 1 \text{ ms}$  we can meet the adiabaticity requirements as spelt out in Section 3.2.1. The essential requirement here is that the frequency  $\nu = 2/T$  of the external field variation in (3.156) must be much less than the transition frequencies  $\Delta E/h$  between the Zeeman levels for  $\alpha = 9, 10, 11$ . For the external field of order  $1 \mu\text{T}$  we get  $\Delta E/h \simeq 10 \text{ kHz}$  yielding

<sup>24</sup>The integrated energy merely depends on the field strengths.

## Chapter 3. Berry Phases for Hydrogen

---

the requirement

$$\begin{aligned} \nu &= \frac{2}{T} \ll 10 \text{ kHz} , \\ T &\gg 0.2 \text{ ms} . \end{aligned} \quad (3.157)$$

Calculating the contributions to the effective decay rate (3.153), we find for the state  $\alpha = 9$  the following

$$-2 \operatorname{Im} \int_0^1 dz E_9(\mathbf{L}(z)) = 1935.2 \text{ s}^{-1} , \quad (3.158)$$

$$\frac{2}{T} \operatorname{Im} \int_{\mathcal{F}} \mathbf{J}_9^{(L)}(\mathbf{L}) d\mathbf{f}^L = -1.8 \text{ s}^{-1} . \quad (3.159)$$

This leads to

$$\Gamma_{9,\text{eff}}(\mathcal{C}, T) = 1933.4 \text{ s}^{-1} . \quad (3.160)$$

For the reverse curve  $\bar{\mathcal{C}}$  we find, instead,

$$\Gamma_{9,\text{eff}}(\bar{\mathcal{C}}, T) = 1937.0 \text{ s}^{-1} . \quad (3.161)$$

Thus, under the above conditions the effective decay rates (3.160) and (3.161) differ by 1.9‰ and the corresponding decreases of the norms (3.154) by 3.6‰. We emphasise that this difference has its origin in the PC geometric phase which obeys  $\operatorname{Im} \gamma_\alpha(P(\mathcal{C})) \equiv \operatorname{Im} \gamma_\alpha(\mathcal{C})$ .

The magnitude of this phenomenon should be well within experimental reach. In 1984 M. V. Berry discovered real geometric phases. To our knowledge, imaginary geometric phases, which provide for geometry-dependent lifetime modifications, have not been observed experimentally ever since.

### Example of a P-Violating Phase

To give an example of a PV geometric phase we consider the following curve, again in the parameter space (3.138) with  $\mathbf{B} = 1 \mu\text{T} \mathbf{e}_2$ ,

$$\begin{aligned} \mathcal{C}: z &\rightarrow \mathbf{L}(z) , \quad 0 \leq z \leq 1 , \\ \mathcal{E}_1(z) &= 0 , \\ \mathcal{E}_3(z) &= \mathcal{E}_0 \sin(2\pi z) , \\ \mathcal{B}_3(z) &= 0.1 \mathcal{B}_0 \cos(2\pi z) . \end{aligned} \quad (3.162)$$

For this curve the P-conserving geometric phases vanish<sup>25</sup> due to the antisymmetry of  $\mathbf{e}_1 \cdot \mathbf{J}_\alpha^{(\mathcal{E})\text{PC}}(\mathcal{E}, \mathcal{B}_3 \mathbf{e}_3)$  under  $(\mathcal{E}_1, \mathcal{E}_3) \rightarrow (-\mathcal{E}_1, -\mathcal{E}_3)$ ; see (3.140). Thus, we get here

$$\gamma_\alpha(\mathcal{C}) = \gamma_\alpha^{\text{PV}}(\mathcal{C}) = \gamma_\alpha^{\text{PV}_1}(\mathcal{C}) + \gamma_\alpha^{\text{PV}_2}(\mathcal{C}) . \quad (3.163)$$

---

<sup>25</sup>From  $\mathbf{e}_1 \cdot \mathbf{J}_\alpha^{(\mathcal{E})\text{PC}}(-\mathcal{E}, \mathcal{B}_3 \mathbf{e}_3) = -\mathbf{e}_1 \cdot \mathbf{J}_\alpha^{(\mathcal{E})\text{PC}}(\mathcal{E}, \mathcal{B}_3 \mathbf{e}_3)$  we obtain, due to the specific integration area in the  $\mathcal{E}_3$ - $\mathcal{B}_3$ -plane,  $\gamma_\alpha^{\text{PC}}(P(\mathcal{C})) = -\gamma_\alpha^{\text{PC}}(\mathcal{C}) \Rightarrow \gamma_\alpha^{\text{PC}}(\mathcal{C}) = 0$ . For  $\alpha = 9$  this situation is illustrated by Figure 3.26. There, the parameter space  $\{\mathcal{E}_2, \mathcal{E}_1, \mathcal{B}_1\}$  with constant  $\mathcal{B}_3$  can be transformed into the parameter space of the present section by a proper rotation.

### 3.7. Berry Phases for Specific Field Configurations

---

Numerically we find for  $\alpha = 9$

$$\gamma_9^{\text{PV}_1}(\mathcal{C}') = (0.00467 - 0.000457i) \delta_1 , \quad (3.164)$$

$$\gamma_9^{\text{PV}_2}(\mathcal{C}') = (0.0942 - 0.00421i) \delta_2 . \quad (3.165)$$

Assuming that the curve  $\mathcal{C}$  can be circled  $N$  times, we get as geometric phase  $N\gamma_9(\mathcal{C})$ . Thus, the number of circlings acts as an enhancement factor for the small weak interaction effects in hydrogen. For  $N = 10^3$ , for example, we obtain

$$N\gamma_9^{\text{PV}}(\mathcal{C}) = (4.67 - 0.457i) \delta_1 + (94.2 - 4.21i) \delta_2 . \quad (3.166)$$

With  $\delta_{1,2}$  from Table A.1 this gives a phase of the order of  $10^{-10}$ .

Whether the adiabaticity conditions are met in (3.166) is not worked out here. We will exhaustively elaborate a realistic example in Chapter 5, where a PV spin echo signal is investigated. For that, we first have to introduce the theoretical description of longitudinal atomic beam spin echo experiments that aim at atomic phase measurements.



## 4 Hydrogen in an Interferometer

The prime class of experiments that enable phase measurements are interferometric setups. Dealing with atoms exposed to external electromagnetic fields, we present in this chapter the general formalism describing hydrogen atoms that travel through an atom interferometer. The results can be easily extended to other atomic species. We introduce longitudinal atomic beam spin echo (LABSE) experiments and account for their experimental constraints.

LABSE experiments exploit the fact that the dynamic phase of an atom's wave function built up during the first part of the interferometer can be reversed in the second part by suitable field configurations. Then, the remaining phase is the geometric phase. Furthermore, different dynamic phase evolutions due to different times of flight are each reversed individually. This insensitivity on the non-monochromaticity of the atomic beam is one main advantage of the spin echo concept [35]. Thereby, phase variations due to a modified field configuration can be measured with high precision. In the adiabatic limit the geometric phases do not depend on the time of flight either. That is, LABSE experiments allow for a high-precision measurement of Berry phases like those discussed in the preceding chapter.

In the case of a pure magnetic field configuration a total angular momentum vector  $\langle \mathbf{F} \rangle \parallel \mathbf{B}$  precesses around  $\mathbf{B}$  with the Larmor precession frequency  $\omega_L = \gamma |\mathbf{B}|$ , where  $\gamma$  is the gyromagnetic ratio. Then, the accumulated precession angle of  $\langle \mathbf{F} \rangle$  during time  $T$  corresponds to  $\phi = \gamma \int_0^T |\mathbf{B}| dt$ , see, for example, [35]. A spin echo is achieved when an initially polarised atomic beam depolarises due to a magnetic field configuration and gets polarised again during the reversed process induced by an appropriately flipped magnetic field configuration.

Supposing adiabatic evolution of the internal states of the atoms, we derive the behaviour of the internal states which enables us to create an experimentally well accessible observable that in general contains P-conserving as well as P-violating Berry phases. In Section 4.1 we briefly present the setup of a LABSE experiment for hydrogen being in a superposition of internal states and propagating through external fields. The Berry phases introduced for the non-propagating atoms in Chapter 3 again appear in Section 4.2 as a part of the total phase that emerges for the atomic wave packet in the case of spatially propagating atoms. There, an effective Schrödinger equation in the adiabatic limit for our system and its solutions are discussed.

In Section 4.3 eventually, the evolved state is projected onto an analysing state at the end of the interferometer giving rise to a flux of atomic states which in principle is easily accessible for the experimenter. This total integrated flux is an observable sensitive to Berry phases.

The results recalled and presented here were published in [67], [68], [32], and [33].

## 4.1 IABSE Experiments

During the past years, the group around D. Dubbers and M. DeKieviet has designed and further developed a IABSE experimental scheme [35]. The central parts of one such realisation are shown in Figures 4.1 and 4.2. This apparatus can be used for the detection of geometric phases of atoms propagating through suitable electromagnetic fields.

The atoms are prepared in a certain superposition  $|\psi(z_0)\rangle$  of internal atomic states at position  $z_0$  and propagate in  $z$ -direction through an electromagnetic field configuration. The procedure is schematically shown in Figure 4.3. After passing the external fields, atoms being in the state  $|\psi(z_a)\rangle$ , e.g., in a superposition of the states  $|9\rangle$  and  $|11\rangle$ , are counted at  $z_a$ . For that purpose we introduce the total integrated flux

$$\mathcal{F}_p = \int dt \int d^2x_T j_z(\mathbf{x}_T, z_a, t), \quad (4.1)$$

where  $\mathbf{x} = (\mathbf{x}_T, z) = (x, y, z)$  and  $j_z$  is the  $z$ -component of the probability current. The observable  $\mathcal{F}_p$ , in principle measuring the ratio of beforehand specified incoming and outgoing atomic states, will be discussed in detail in Section 4.3.

One field configuration currently available is produced by two coils that superimpose a constant longitudinal magnetic field in the direction of the beam axis with a transverse spatially rotating magnetic field, see Figures 4.1 and 4.4. The states evolve adiabatically as long as the adiabaticity conditions derived in Section 3.2.1 are satisfied.

While propagating through the field configuration, the atoms accumulate dynamical as well as geometric phases. The internal states of the atom evolve differently leading to a longitudinal separation of the wave packets. This effect can be cancelled by the second coil, the so-called spin echo coil. When the centres of the wave packets meet at the end of the interferometer, one can detect the spin echo signal which essentially is the total integrated flux (4.1).

The following specifications of the experimental setup according to [77] should only be considered as an example. Other configurations can be treated analogously with the methods given in the present thesis. We choose  $l = z_a - z_0 = 1$  m for the length of the interferometer if not explicitly indicated otherwise.

The typical longitudinal velocity  $v_z$ , wave number  $q_z$  and de Broglie wavelength  $\lambda$  of the hydrogen atom in the interferometer at room temperature, 300°K, are  $v_z = \frac{q_z}{m} \approx 3500$  m/s,  $q_z \approx 5.6 \times 10^{10} \text{ m}^{-1}$ , and  $\lambda = \frac{2\pi}{q_z} \approx 1.1 \times 10^{-10}$  m. This gives a kinetic energy  $q_z^2/(2m) \hat{=} 6.5 \times 10^{-2}$  eV corresponding to the longitudinal motion.

At the present stage of the experiment helium atoms with a mean velocity of  $v_z \approx 2000$  m/s are investigated in a magnetic field configuration. The time-of-flight spectrum is taken within 1 ms at a time resolution of 1  $\mu$ s. The magnetic field resolution is in the range of 100 nT. The experiment can be run with about  $10^3$  atoms per second detected at the end of the interferometer [176]. According to [77] it is possible to build atom sources with  $10^{16} - 10^{19}$  atoms per second and sterad leading to  $10^{10}$  metastable atoms per second that can arrive at the detector. The presently used atom source,

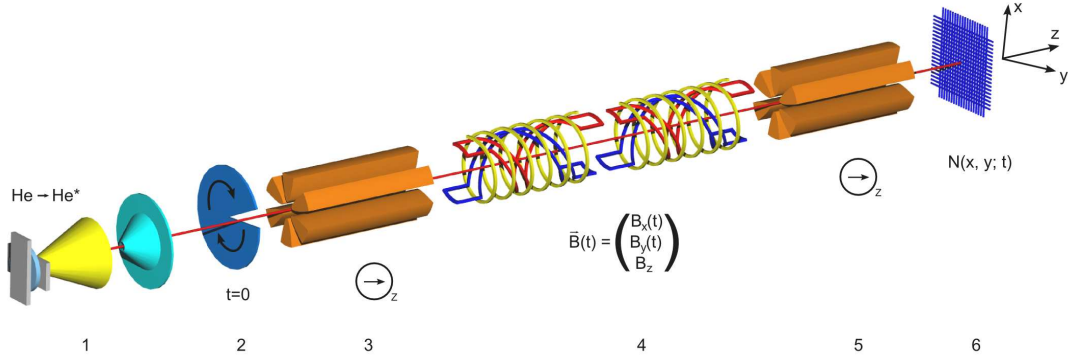


**Figure 4.1:** Schematic view of the longitudinal spin echo interferometer as used in the group of M. DeKieviet. The employed coordinate system is indicated. Currently, the experiment is run with a metastable helium beam exposed to a magnetic field  $\mathbf{B}(t)$ . Metastable helium states propagating in  $z$ -direction are provided at the source (1). A chopper (2) enables a distinct detection of different time-of-flight spectra. The polarisator (3) consists of a sextupole magnetic field vanishing at the  $z$ -axis and a subsequent guide field which is not depicted here for simplicity. The sextupole focusses the (local)  $|F_3 = -1\rangle$  states while defocusing the (local)  $|F_3 = +1\rangle$  states. Here, the local magnetic field, which the atoms off the  $z$ -axis are exposed to, defines the local  $|F_3\rangle$  states. The guide field parallel to  $\mathbf{e}_z$  is then superimposed with the sextupole field, thereby adiabatically creating a global  $z$ -polarisation of the atomic beam. Here, the guide field is aligned along the  $z$ -direction, but other alignments are conceivable as well. Afterwards, the polarised atoms enter the external field configuration (4) – here, it starts with a  $\mathcal{B}_x$ -field. The atoms undergo a non-adiabatic transition into a superposition of polarisations orthogonal to the guide field polarisation. The state created with this procedure is the initial state  $|\psi(z_0)\rangle$  we employ in the present thesis. To be more precise, the quantisation axis used throughout this thesis is the  $z$ -axis which defines the states  $|9\rangle$  and  $|11\rangle$  as  $|F_z = +1\rangle$  and  $|F_z = -1\rangle$ , respectively. In contrast, the initial state according to the field configuration (4) is a superposition of  $|F_x\rangle$  states. Of course, this is just an issue of notation. The resulting final state  $|\psi(z_a)\rangle$  at the end of the field configuration non-adiabatically enters an analysing polarisator (5), i.e., a guide field parallel to  $\mathbf{e}_z$  and a subsequent sextupole field. Depending on the superposition which  $|\psi(z_a)\rangle$  consists of, the non-adiabatic transition due to the guide field results in definite superpositions of  $\sigma_z$ -eigenstates simply by projection on the  $\sigma_z$  eigenbasis. The atoms are then adiabatically guided into the sextupole magnet which defocuses the local  $|F_3 = +1\rangle$  states leaving us with a definite number of local  $|F_3 = -1\rangle$  states. At the end of the apparatus, the time-resolved number  $N(x,y;t)$  of these states, directly related to (4.1), is detected (6). The figure is kindly provided by Peter Augenstein.

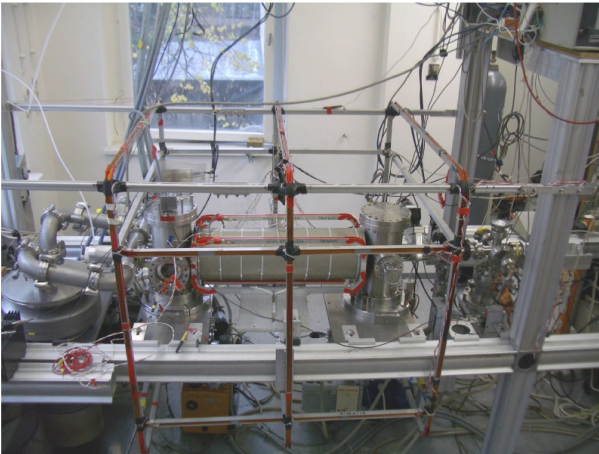


**Figure 4.2:** A picture of the central parts of the spin echo experiment, kindly provided by Peter Augenstein.

which can create both metastable hydrogen and helium, utilises a gas discharge to excite the atoms. Essentially, only the 2S states remain for the experiment due to the short lifetimes of the 2P states. In the case of metastable helium  $\text{He}^*$ , a free electron is produced when the  $\text{He}^*$  hits the earthed detector yielding a measurable current after amplification. Since the source is not perfectly stable over time, an error is introduced when measuring the number of atoms at the detector. This important systematic error can be partly compensated by monitoring the current through the source related to the number of released atoms and by employing sufficiently short measurement times. Another serious systematic error is due to stray fields which can mimic or mask effects of the actual field configuration. Small errors are introduced by the adjustability of the currents through the coils and the alignment of the coils with respect to each other. As already pointed out in Section 3.2, the errors from omitted relativistic effects are clearly negligible compared to the other field uncertainties. Regarding the experimental setup the main approaches towards a higher precision are a more effective shielding of stray fields besides a larger rate of the atom source and an improvement of its stability [176].

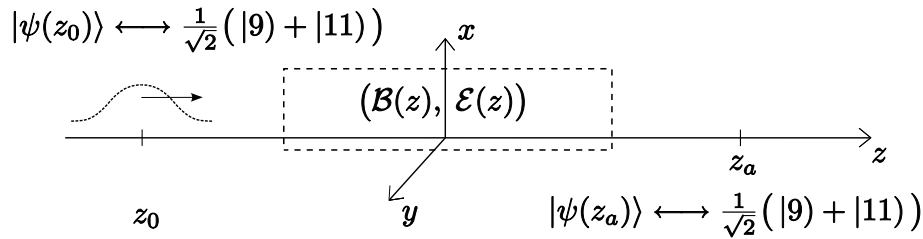


**Figure 4.3:** Scheme of the atom interferometry experiment. The atom is prepared around  $z_0$  and analysed around  $z_a$ . We start with a superposition  $|\psi(z_0)\rangle$  of the two states  $|9\rangle$  and  $|11\rangle$ . After passing the magnetic and electric fields  $\mathcal{B}(z)$  and  $\mathcal{E}(z)$ , the wave function is projected onto an analysing state  $|\psi(z_a)\rangle$ , for example again onto a superposition of the states  $|9\rangle$  and  $|11\rangle$ .

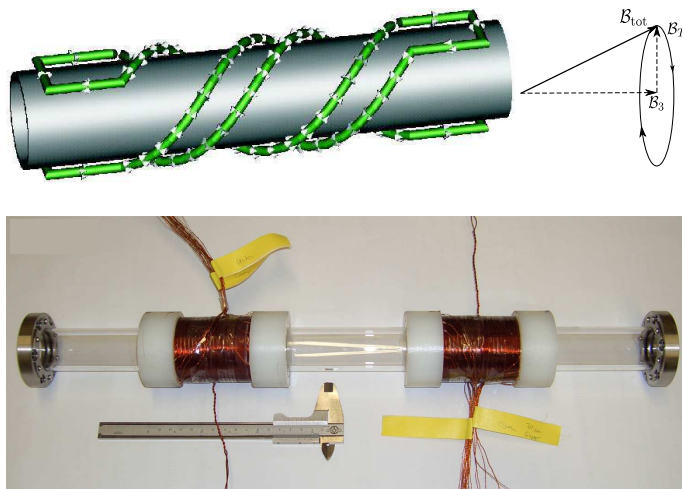


**Figure 4.4:** Upper figure: Schematic view of one spin echo coil producing the transverse part  $\mathcal{B}_T$  of the total magnetic field  $\mathcal{B}_{\text{tot}}$ .

Lower figure: One realisation of a LABSE setup with the  $\mathcal{B}_3$ -coils and the spin echo coils which are mounted on a glass tube.

By varying the currents through the coils, the cone encircled by  $\mathcal{B}_{\text{tot}}$  can be modulated. The illustrations are taken from [37].

## 4.2 The Effective Schrödinger Equation in the Adiabatic Limit

In this section, based on [32], we describe longitudinally propagating atoms in the adiabatic limit. Thus, a kinetic term has to be introduced in the effective Schrödinger equation (3.23). Consequently, the mass matrix then depends on the longitudinal coordinate  $z$  since the electric and magnetic fields are not time dependent in this description but spatially varying.

The full Schrödinger equation describing the undecayed  $n = 2$  states reads

$$i\frac{\partial}{\partial t}|\psi(\mathbf{x}, t)\rangle = \left[ -\frac{1}{2m}\Delta + \underline{\mathcal{M}}(z) + E_0 \right] |\psi(\mathbf{x}, t)\rangle . \quad (4.2)$$

Here  $m$  is the atom's mass and  $\underline{\mathcal{M}}(z)$  is the mass matrix (3.25) with  $t$  replaced by  $z$ . As illustrated in Figure 3.1, the centre of the real parts of the energy levels of the free  $2P_{1/2}$  states was chosen as the (arbitrary) zero for the energy scale. We will see in the following that it is practicable to choose this zero point of the energy differently. Therefore, we introduced a freely selectable real constant  $E_0$  in (4.2).

In the adiabatic limit where the 2S states are decoupled from the 2P states, one finds the effective Schrödinger equation

$$\Delta\hat{\psi}_\alpha(\mathbf{x}, t) + 2im\frac{\partial\hat{\psi}_\alpha}{\partial t}(\mathbf{x}, t) - 2m\mathcal{V}_\alpha(z)\hat{\psi}_\alpha(\mathbf{x}, t) = 0 . \quad (4.3)$$

The quantities in (4.3) are defined as follows. The wave function has the form

$$\hat{\psi}_\alpha(\mathbf{x}, t) = \exp[-i\gamma_\alpha(z)]\psi_\alpha(\mathbf{x}, t) \quad (4.4)$$

where  $\gamma_\alpha(z)$  is the geometric phase

$$\gamma_\alpha(z) = i \int_{z_0}^z dz' (\widetilde{\alpha(z')} | \frac{\partial}{\partial z'} |\alpha(z')\rangle) , \quad (\alpha = 9, \dots, 12) , \quad (4.5)$$

and  $\psi_\alpha(\mathbf{x}, t)$  are the spatial wave functions solving (4.2). The complex effective potential  $\mathcal{V}_\alpha(z) = V_\alpha(z) - \frac{i}{2}\Gamma_\alpha(z)$  in (4.3) is defined by

$$\mathcal{V}_\alpha(z) = E_\alpha(z) + E_0 - \frac{1}{2m} \left[ \left( \frac{\partial\gamma_{\alpha\alpha}(z)}{\partial z} \right)^2 - \frac{\partial(\widetilde{\alpha(z)} | \frac{\partial}{\partial z} |\alpha(z)\rangle)}{\partial z} \right] , \quad (4.6)$$

with the real- and imaginary parts  $V_\alpha(z) = \text{Re}\{\mathcal{V}_\alpha(z)\}$  and  $\Gamma_\alpha(z) = -2\text{Im}\{\mathcal{V}_\alpha(z)\}$ .

### The Adiabatically Propagating Wave Function

In the following, we introduce the solutions of (4.3). The four decoupled differential equations for the 2S states allow for the investigation of one single effective equation for the metastable amplitudes. The index  $\alpha$ , labelling the  $n = 2$  states, can therefore be omitted in the rest of this section. So we write (4.4) as

$$\hat{\psi}(\mathbf{x}, t) = \exp[-i\gamma(z)]\psi(\mathbf{x}, t) , \quad (4.7)$$

and we will derive the solution  $\hat{\psi}$  of the equation

$$\left\{ \frac{\partial^2}{\partial z^2} + 2im\frac{\partial}{\partial t} - 2mV(z) + im\Gamma(z) + \Delta_T \right\} \hat{\psi}(\mathbf{x}, t) = 0, \quad (4.8)$$

corresponding to (4.3), with  $\Delta_T = \frac{\partial^2}{\partial x^2} + \frac{\partial^2}{\partial y^2}$ .

The amplitude  $\hat{\psi}$  can be expanded in powers of  $1/\bar{k}$ , where the typical scale  $\bar{k}$  for the momentum component  $q_z$  in  $z$  direction has an order of magnitude of  $10^4$  eV for our example setup in Section 4.1. We will see that the zero-order term of this expansion already gives a satisfying accuracy for the solution  $\hat{\psi}$ . Then, we will discuss the global behaviour and the structure of  $\hat{\psi}$  representing a well interpretable result.

### Notations

First, we change variables  $(t, z) \rightarrow (\tau, \zeta)$ :

$$\begin{aligned} \tau &= \frac{\bar{k}}{m} t, \\ \zeta &= \int_{z_0}^z dz' \bar{k} / \sqrt{\bar{k}^2 - 2mV(z')}. \end{aligned} \quad (4.9)$$

In SI units,  $\tau$  would be the distance passed by a particle of velocity  $\hbar\bar{k}/m$  during time  $t$ . For a free particle, i.e.  $V(z') \equiv 0$ , the coordinate  $\zeta = \zeta(z)$  is the difference  $z - z_0$  between the starting point  $z_0$  and the current point  $z$  on the  $z$ -axis. For a non-vanishing potential  $V(z')$  the coordinate  $\zeta$  gives a different length compared to the free particle. A positive potential leads to  $\zeta(z) > z - z_0$ . Thus, the particle in the potential has passed a larger effective distance  $\zeta$  than the free one when both have arrived at  $z$ . But we have to keep in mind that both kinds of potentials are located within the same distance  $z - z_0$ , i.e., the particles are always located between  $z_0$  and  $z$  in both cases. We write  $\mathcal{Z}(\zeta) = z$  for the inverse function of  $\zeta(z)$ .

We split off a factor  $\exp[i\phi(z, t)]$  from the wave function  $\hat{\psi}(\mathbf{x}, t)$ , and the remaining amplitude  $\mathcal{A}$  is the envelope function for the wave packet:

$$\hat{\psi}(\mathbf{x}, t) = e^{i\phi(z, t)} \mathcal{A}(\mathbf{x}_T, \zeta, \tau). \quad (4.10)$$

### Expansion of the Wave Function

The amplitude  $\mathcal{A}(\mathbf{x}_T, \zeta, \tau)$  can be expanded as

$$\mathcal{A}(\mathbf{x}_T, \zeta, \tau) = \sum_{n=0}^{\infty} \mathcal{A}^{(n)}(\mathbf{x}_T, \zeta, \tau) = \sum_{n=0}^{\infty} \mathcal{O}(1/\bar{k}^n) \quad (4.11)$$

with the successive terms in (4.11) being suppressed by increasing powers  $1/\bar{k}$  of the inverse momentum. The zero-order term should be a good approximation for large  $\bar{k}$ , and it is given by

$$\mathcal{A}^{(0)}(\mathbf{x}_T, \zeta, \tau) = \varphi(\mathbf{x}_T, \zeta - \tau). \quad (4.12)$$

## 4.2. The Effective Schrödinger Equation in the Adiabatic Limit

---

The proofs of (4.11) and (4.12) are discussed in [32]. Assuming the Gaussian function

$$\chi(\mathbf{x}_T, \zeta) = \mathcal{N}(2\pi)^{-3/4} \sigma_T^{-1} \sigma_L^{-1/2} \exp\left(-\frac{1}{4\sigma_T^2} \mathbf{x}_T^2 - \frac{1}{4\sigma_L^2} \zeta^2\right) \quad (4.13)$$

to be the initial envelope  $\mathcal{A}(\mathbf{x}_T, \zeta, \tau)|_{\tau=0} = \varphi(\mathbf{x}_T, \zeta)$ , with transverse and longitudinal widths  $\sigma_T, \sigma_L > 100 \mu\text{m}$ , we obtain a correction of at most 1% of  $\mathcal{A}^{(0)}$  considering only the first-order term  $\mathcal{A}^{(1)}$ :

$$\left| \frac{\mathcal{A}^{(1)}(\mathbf{x}_T, \zeta, \tau)}{\mathcal{A}^{(0)}(\mathbf{x}_T, \zeta, \tau)} \right| \lesssim 1\% . \quad (4.14)$$

This is shown in [32] besides the case of a general initial wave function. There, the specifications necessary for the above estimate are also provided. They are consistent with the conditions outlined in Sections 4.1 and 3.2.1.

If we start with exactly one atom at  $t = 0$ , the normalisation factor  $\mathcal{N} > 0$  in (4.13) can be obtained from

$$\int d^3x |\psi(\mathbf{x}, t; \bar{k})|^2|_{t=0} = \int d^2x_T \int dz |\chi(\mathbf{x}_T, \zeta(z))|^2 = 1 . \quad (4.15)$$

Realistic widths  $\sigma_L$  of the wave packets, used for the calculations in the present work, are of order 0.4 nm [77], that is, much smaller than those given above. Such wave packets can be formed by appropriate superpositions of (4.7) as will be discussed in Section 4.3.

### Properties of the Wave Packet Envelope

The envelope function (4.12) depends on the difference  $\zeta - \tau$  but not on the independent variables  $\zeta$  and  $\tau$ . Suppose that  $\varphi(\mathbf{x}_T, \zeta - \tau)$  is sharply peaked at  $\mathbf{x}_T = \mathbf{0}$ ,  $z = z_0$ , and at time  $t = 0$ . This corresponds to  $\tau = 0$  and  $\zeta(z_0) = 0$ , according to (4.9). Thus, the initial envelope is characterised<sup>1</sup> by  $\varphi(\mathbf{x}_T, 0)$  and the trajectory of the peak can therefore be obtained via the relation

$$\zeta - \tau = 0 \Leftrightarrow \zeta(z(t)) - \frac{\bar{k}}{m}t = 0 \quad (4.16)$$

$$\Leftrightarrow \int_{z_0}^{z(t)} dz' \frac{m}{\sqrt{\bar{k}^2 - 2mV(z')}} = t \quad (4.17)$$

$$\Leftrightarrow \dot{z}(t) \frac{m}{\sqrt{\bar{k}^2 - 2mV(z(t))}} = \partial_t t = 1, \text{ with } z(0) = z_0 \quad (4.18)$$

$$\Leftrightarrow \frac{1}{2}m\dot{z}^2(t) + V(z(t)) = \frac{\bar{k}^2}{2m}, \text{ with } z(0) = z_0 . \quad (4.19)$$

Obviously, the transverse coordinates  $\mathbf{x}_T$  of the peak do not change while the longitudinal coordinate  $z(t)$  evolves like a classical particle in the potential  $V(z(t))$ , whereas the total energy is  $\bar{k}^2/2m$ . For a trajectory  $z(t)$  of the peak, fulfilling (4.19), the maximum

---

<sup>1</sup>The peak is at  $\mathbf{x}_T = \mathbf{0}$ , but, of course, the whole envelope extends over the plane at  $z = z_0$ .

value of a Gaussian envelope function  $\varphi(\mathbf{x}_T, \zeta - \tau)$  is  $\varphi(\mathbf{x}_T, 0)$  for every time  $t$ . Hence, the shape of the zero-order amplitude remains unaltered. The velocity of propagation in the  $\zeta$  coordinate is constant as one can see from (4.16).

### The Time-Table Model

In order to get a more intuitive understanding of the propagating wave packets in the interferometer, the so-called time-table model is introduced. We want to consider wave packets starting at time  $t = 0$  in the field free region at  $z_0$ . Reversing the functional dependence in (4.17), we define the arrival time  $t(z)$  by

$$t(z) = \int_{z_0}^z dz' \frac{m}{\sqrt{\bar{k}^2 - 2mV(z')}} \quad (4.20)$$

and get the corresponding reduced time  $\tau(z) = \frac{\bar{k}}{m}t(z) = \zeta(z)$  which has dimension of length. In the time-table model these reduced arrival times are compared with those of a free wave packet where  $V(z') \equiv 0$ . The absence of an external potential also implies a vanishing geometric phase  $\gamma(z) \equiv 0$  since the eigenstates do not change in that case. From (4.6) we see that the energy level  $E(z')$  then also satisfies  $\text{Re}\{E(z')\} + E_0 = 0$ . Of course,  $E(z')$  depends on the considered state, and we can select the free state to which we want to compare by choosing  $E_0$  accordingly. For the free state we have  $t_{\text{free}}(z) = \frac{m}{\bar{k}}(z - z_0)$  and  $\tau_{\text{free}}(z) = \frac{\bar{k}}{m}t_{\text{free}}(z) = z - z_0$ . The difference of reduced arrival times

$$\begin{aligned} \Delta\tau(z) &= \tau(z) - \tau_{\text{free}}(z) \\ &= \zeta(z) - (z - z_0) \end{aligned} \quad (4.21)$$

describes the delay ( $\Delta\tau > 0$ ) or advance ( $\Delta\tau < 0$ ) of the arrival of the wave packet peak at coordinate  $z$  in the interferometer compared to the chosen free state. In Figure 4.5 this is shown for the magnetic field as given in Figure 4.6. There, we consider the states  $\alpha = 9$  and  $\alpha = 11$  in a purely longitudinal magnetic field

$$\begin{aligned} \mathcal{B}(z) &= \mathcal{B}(z)\mathbf{e}_3, \quad 0 \leq z \leq 5, \\ \mathcal{B}(z) &= 10 \left( e^{-150(z-0.25)^2} - s \cdot e^{-150(z-0.75)^2} \right) \mu\text{T}, \end{aligned} \quad (4.22)$$

where  $z$  is taken in meters. The factor  $s$  accounts for the detuning of the second  $\mathcal{B}$ -field peak. We compare the evolution of these states with that of the free 2S,  $F = 1$ , states. That is, we set  $E_0 = -L - \mathcal{A}/32$ , see Table A.3 of Appendix A.2. The potentials for the states  $|9\rangle$  and  $|11\rangle$  are then proportional to the third component of the magnetic field in (4.22)

$$\begin{aligned} V_9(z) &= \frac{g\mu_B}{2}\mathcal{B}(z), \\ V_{11}(z) &= -\frac{g\mu_B}{2}\mathcal{B}(z), \end{aligned} \quad (4.23)$$

## 4.2. The Effective Schrödinger Equation in the Adiabatic Limit

see Table A.5 of Appendix A.2. The contributions of the derivatives in (4.6) are neglected here since, numerically, they come out to be small compared to  $-\underline{\mu} \cdot \mathcal{B}(z)$  [83]. We find that in the magnetic field (4.22) the state  $\alpha = 9$  first gets a delay,  $\alpha = 11$  an advance compared to the free state. For  $z$  around 3.75 m, where the magnetic field is reversed, the state  $\alpha = 9$  makes up for the delay, the state  $\alpha = 11$  loses its advance. At  $z = 5$  m they eventually meet again. The overlap of the wave functions, and hence their capability of interfering, depends on their differences of reduced arrival times.

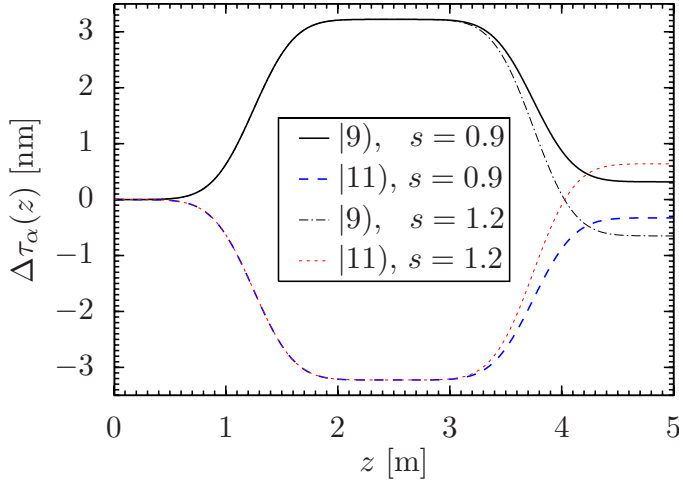


**Figure 4.5:** Example of a time-table plot, i.e., (4.21) as functions of  $z$ , for the states  $\alpha = 9$  and  $\alpha = 11$ . The corresponding potentials, based on the magnetic field  $\mathcal{B}(z)$  from (4.22), are given in (4.23). The Figure is taken from [32].

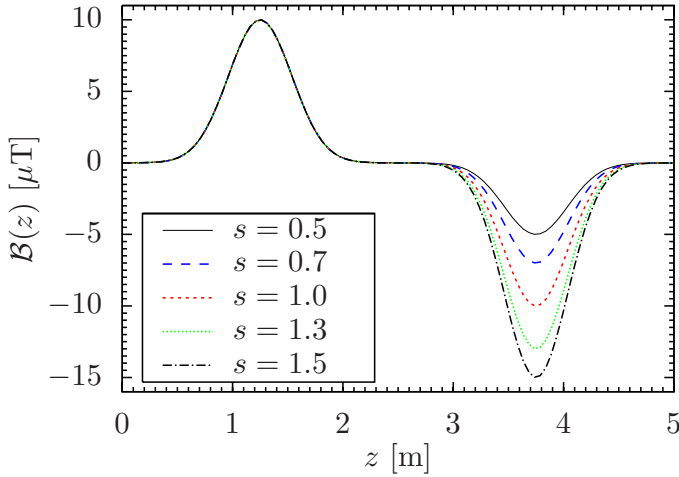


**Figure 4.6:** Example of a magnetic field configuration. The transverse components are chosen as  $\mathcal{B}_1 = \mathcal{B}_2 = 0$ , and the longitudinal component  $\mathcal{B}(z)$  is given in (4.22). The Figure is taken from [32].

### 4.3 Interference of Two Internal States: Total Integrated Flux

We discuss the interference effects of two internal metastable  $n = 2$  states, see [32] for more details. After specifying the initial state of the atom in detail, the propagating wave function can be written down immediately. The evolved wave function is then projected onto an analysing state which gives the flux of atoms at the end of the interferometer.

#### Initial State

We start with two narrow wave packets in the field free region around  $z \approx z_0$  at time  $t = 0$ . There, two metastable 2S states  $|\alpha(z_0)\rangle$  and  $|\beta(z_0)\rangle$ , where  $\alpha, \beta \in I \subset \{9, 10, 11, 12\}$ , are supposed to be superposed coherently. Here,  $I$  is defined as an index set with two elements. Having been prepared in that way, the atom propagates through the interferometer and is analysed at  $z = z_a$ .

For the initial superposition we make the ansatz

$$|\Psi(\mathbf{x}, t = 0)\rangle = \Psi(\mathbf{x}, 0) \sum_{\alpha \in I} c_\alpha |\alpha(z_0)\rangle \quad (4.24)$$

with  $\sum_{\alpha \in I} |c_\alpha|^2 = 1$  and

$$\Psi(\mathbf{x}, 0) = \int \frac{d\bar{k}}{2\pi} f(\bar{k}) \exp[i\bar{k}(z - z_0)] \chi(\mathbf{x}_T, z - z_0). \quad (4.25)$$

We suppose the initial wave function (4.25) to be non-zero only in the region around  $z_0$ . For absence of external fields the initial states  $|\alpha(z_0)\rangle$  with  $\alpha \in I$  are orthonormal since these states have pairwise different values  $(F, F_3)$  which are good quantum numbers for  $\mathcal{E} = \mathcal{B} = \mathbf{0}$ . The envelope amplitude  $\chi(\mathbf{x}_T, z - z_0)$  in (4.25) is supposed to have transverse and longitudinal widths  $\sigma_T, \sigma_L \gtrsim 100 \mu\text{m}$ . We suppose the normalisation condition (4.15) to hold. With  $V(z') = 0$  in the field free region, (4.9) yields  $\zeta(z) = z - z_0$ , and therefore we have  $\int d^2x_T \int dz |\chi(\mathbf{x}_T, z - z_0)|^2 = 1$ . To obtain a realistic shape of the initial wave function, we use a function  $f(\bar{k})$  which is supposed to be sharply peaked at  $\bar{k} = \bar{k}_m$  ( $m$  for maximum) with a width  $\Delta\bar{k} = \sigma_k^{-1}$  satisfying  $0 < \sigma_k \ll \sigma_L$  and  $\bar{k}_m \gg \sigma_k^{-1}$ . To be more specific, we here consider Gaussian functions

$$\chi(\mathbf{x}_T, z - z_0) = (2\pi)^{-3/4} \sigma_T^{-1} \sigma_L^{-1/2} \exp \left[ -\frac{1}{4\sigma_T^2} \mathbf{x}_T^2 - \frac{1}{4\sigma_L^2} (z - z_0)^2 \right], \quad (4.26)$$

$$f(\bar{k}) = (4\pi\sigma_k)^{1/2} (\sigma_k^2 + \sigma_L^2)^{1/4} \exp \left[ -\sigma_k^2 (\bar{k} - \bar{k}_m)^2 \right] \quad (4.27)$$

with  $\sigma_T, \sigma_L \geq 100 \mu\text{m}$  and  $\sigma_k \ll \sigma_L$ .

### 4.3. Interference of Two Internal States: Total Integrated Flux

---

#### Final State

Having specified the initial envelope amplitude  $\chi$ , we obtain the evolution of the initial state (4.24) from the results derived in Section 4.2. In the course of that, we have to reinstate the index  $\alpha$  on the according quantities. In that way the initial state (4.24) leads to the solution

$$|\Psi(\mathbf{x}, t)\rangle = \int \frac{d\bar{k}}{2\pi} f(\bar{k}) \sum_{\alpha \in I} c_\alpha \psi_\alpha(\mathbf{x}, t; \bar{k}) |\alpha(z)\rangle \quad (4.28)$$

where

$$\begin{aligned} \psi_\alpha(\mathbf{x}, t; \bar{k}) &= \exp \left[ -i \frac{\bar{k}^2}{2m} t + i \bar{k} (z - z_0) \right] U_\alpha(z, u; \bar{k}) \Big|_{u=z_\alpha(\zeta_\alpha(z) - (\bar{k}/m)t)} \\ &\times \chi(\mathbf{x}_T, \zeta_\alpha(z) - (\bar{k}/m)t), \end{aligned} \quad (4.29)$$

$$U_\alpha(z, u; \bar{k}) = \exp \left[ -i \int_u^z dz' \left( \frac{2mV_\alpha(z')}{k(z') + \bar{k}} - i \frac{m\Gamma_\alpha(z')}{2k(z')} \right) - \frac{1}{2} \ln \frac{k(z)}{\bar{k}(u)} + i\gamma_\alpha(z) - i\gamma_\alpha(u) \right]. \quad (4.30)$$

#### Total Integrated Flux

When the evolved state (4.28) reaches the end of the interferometer, it is analysed at  $z = z_a$ . In this field free region we suppose  $|\alpha(z)\rangle = |\alpha(z_a)\rangle = |\alpha(z_0)\rangle$  to hold for  $z$  several  $\sigma_L$  around  $z_a$ . We want the state (4.28) to be projected onto

$$|p\rangle = \sum_{\alpha \in I} p_\alpha |\alpha(z_0)\rangle \quad (4.31)$$

where  $\sum_{\alpha \in I} |p_\alpha|^2 = 1$ . The projection results in

$$|\Psi_p(\mathbf{x}, t)\rangle = |p\rangle \langle \tilde{p}| \Psi(\mathbf{x}, t)\rangle = \Psi_p(\mathbf{x}, t) |p\rangle \quad (4.32)$$

with  $\langle \tilde{p}| = \sum_{\alpha \in I} \langle \alpha(z_0) | p_\alpha^*$  and

$$\Psi_p(\mathbf{x}, t) = \langle \tilde{p}| \Psi(\mathbf{x}, t)\rangle = \int \frac{d\bar{k}}{2\pi} f(\bar{k}) \sum_{\alpha \in I} p_\alpha^* c_\alpha \psi_\alpha(\mathbf{x}, t; \bar{k}). \quad (4.33)$$

We suppose that the total integrated flux  $\mathcal{F}_p$  in the above projection is measured at  $z = z_a$ . It is given by

$$\mathcal{F}_p = \int dt \int d^2x_T j_z(\mathbf{x}_T, z_a, t) \quad (4.34)$$

where the  $z$ -component of the probability current is

$$j_z(\mathbf{x}_T, z, t) = \frac{1}{2mi} \Psi_p^*(\mathbf{x}, t) \frac{\partial}{\partial z} \Psi_p(\mathbf{x}, t) + \text{c.c.} \quad (4.35)$$

The observable  $\mathcal{F}_p$  essentially is the ratio of the number of atoms arriving in the desired final state divided by the number of initially prepared atoms. With  $\bar{k} = \bar{k}_m$

## Chapter 4. Hydrogen in an Interferometer

and  $k(z_0) = k(z_a) = \bar{k}_m$  we get from (4.30), up to small corrections discussed in Appendix C of [32], the total phase factors

$$U_\alpha(z_a, z_0; \bar{k}_m) = \exp[-i\phi_{\text{dyn},\alpha} + i\phi_{\text{geom},\alpha}] , \quad (4.36)$$

where the complex dynamical and geometric phases are

$$\phi_{\text{dyn},\alpha} = \frac{m}{\bar{k}_m} \int_{z_0}^{z_a} dz' [V_\alpha(z') - \frac{i}{2}\Gamma_\alpha(z')] , \quad (4.37)$$

$$\phi_{\text{geom},\alpha} = \gamma_\alpha(z_a) - \gamma_\alpha(z_0) . \quad (4.38)$$

(4.37) is obtained from expanding the argument of the exponential function in (4.30) around  $\bar{k}_m$ .

To be able to perform explicit calculations in the following, we insert the Gaussian distributions for  $\chi$  and  $f$ , see (4.26) and (4.27). For this calculation we again refer to [32]. So we obtain the final result for the total integrated flux

$$\mathcal{F}_p = \sum_{\alpha,\beta \in I} p_\beta p_\alpha^* c_\beta^* c_\alpha \exp[-(\Delta\tau_\beta - \Delta\tau_\alpha)^2 / (8\sigma_k'^2)] U_\beta^*(z_a, z_0; \bar{k}_m) U_\alpha(z_a, z_0; \bar{k}_m) . \quad (4.39)$$

As an example we choose the field configuration (4.22). The computation of (4.39) for 1000 values of  $s$  using our numerical software QABSE results in Figure 4.7. Only dynamic phases are present here. At  $s = 1$  the overlap of  $|9\rangle$  and  $|11\rangle$  is maximal. For  $s \neq 1$  the separations  $\Delta\tau_9 - \Delta\tau_{11}$  reduce the overlap leading to a decreased envelope amplitude. The oscillations within the envelope are due to the variations of  $\phi_{\text{dyn},9}$  and  $\phi_{\text{dyn},11}$  as  $s$  is modulated.

We discuss spin echo signals in more detail in the next chapter, where further examples are presented.

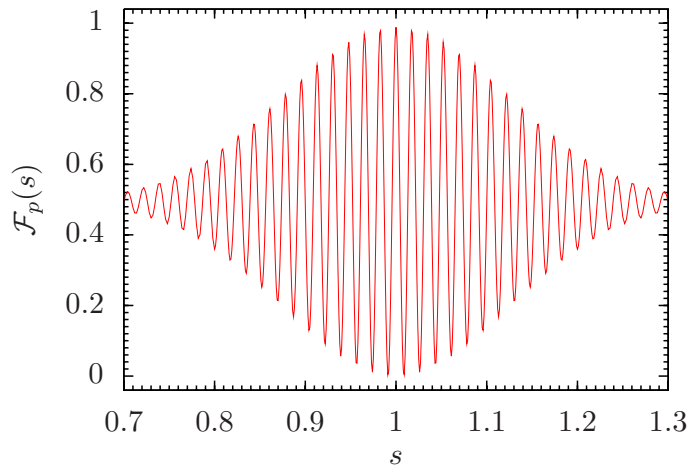


**Figure 4.7:** The experimentally observable spin echo signal for the field configuration (4.22) and the specifications  $c_9 = c_{11} = p_9 = p_{11} = 1/\sqrt{2}$ ,  $\bar{k}_m = q_z = 5.6 \times 10^{10} \text{ m}^{-1}$ ,  $\sigma_L = \sigma_T = 100 \mu\text{m}$ , and  $\sigma_k' = \sigma_k \sigma_L / \sqrt{\sigma_L^2 + \sigma_k^2} = 0.4 \text{ nm}$ . The Figure is taken from [32].

## 5 Spin Echo Signals

At this point all ingredients necessary for the examination of concrete realistic spin echo signals are developed. The total integrated flux  $\mathcal{F}_p$  is the relevant observable including the whole evolution of hydrogen wave packets in LABSE schemes. Derived spin echo signals like that in Figure 4.7 in general depend on the phases (4.37) and (4.38) related to the specific field configurations. The impact of these phases on the spin echo signals is studied in the present chapter.

First, we present in Section 5.1 the expansion of  $\mathcal{F}_p$  in terms of the PV parameter  $\delta$  to obtain independent access to the PC and PV parts of  $\mathcal{F}_p$ . The analysis of PV signals is in need of comparing two chirally different field configurations and their influence on the whole spin echo signal.

Using the  $\delta$ -expansion of  $\mathcal{F}_p$  we work out one way to extract a PV signal in Section 5.2. In the course of that, it becomes apparent how to extract the electroweak mixing angle  $\sin^2 \theta_W$  from the spin echo signal.

In Section 5.3 we elaborate one example of such a PV signal in detail. Several subtleties involved in the actual computation of the interference patterns are accounted for. In the end we arrive at a full analysis of a PV spin echo signal which includes a PV Berry phase of the order of  $10^{-10}$ .

Although Berry phases for hydrogen have not been measured yet with the LABSE apparatus of Section 4.1, the actually available field configuration, constructed in the group of M. DeKieviet and allowing for the measurement of real PC Berry phases, is investigated in Section 5.4 for completeness.

To find uncertainty estimates for spin echo signals, we review the error sources for the theoretical prediction of  $\mathcal{F}_p$  in Section 5.5. There, we also discuss the implications for  $\sin^2 \theta_W$  and estimate the minimum number of measurements necessary to verify or rule out the SM prediction (2.39).

Section 5.6 is devoted to a possibility of improving the resolution of the hitherto used interferometric scheme. We introduce the concept of atom interferometry below the standard quantum limit. It utilises squeezed  $N$ -particle-states as a generalisation of single-atom interferometry, thereby aiming at a  $\sqrt{N}$ -improvement of the experimental accuracy compared to the case of  $N$  independent atoms. We will discuss possible applications to the LABSE scheme.

### 5.1 Perturbative Expansion of the Total Integrated Flux

The small influence of the P-violating part (3.26) of the mass matrix on the total integrated flux  $\mathcal{F}_p$  (4.39) calls for a perturbative expansion of  $\mathcal{F}_p$  in terms of the P-

## Chapter 5. Spin Echo Signals

---

violating parameter  $\delta$ . This way, we get direct access to the P-violating signal  $\mathcal{F}_p^{\text{PV}}$ , which otherwise could be absorbed in the numerical error of the full flux  $\mathcal{F}_p$ . In fact, from the analysis of the flux densities in a pure magnetic field, see Section 3.6.1, the relative numerical error of the Berry phases can be estimated to be at least of the order of  $10^{-12}$  which is approximately at order of  $\delta$ .

As already pointed out in Section 3.5.2 the energies  $E_\alpha(\boldsymbol{\mathcal{E}}, \boldsymbol{\mathcal{B}})$  have no contribution linear in  $\delta$ . Therefore, we find with (4.6), (4.21), and (4.37) for the corrections due to the PV effect:  $V_\alpha(z) \sim \mathcal{O}(\delta^2)$ ,  $\Delta\tau_\alpha \sim \mathcal{O}(\delta^2)$ , and  $\phi_{\text{dyn},\alpha} \sim \mathcal{O}(\delta^2)$ . Thus, we consider the Berry phases  $\phi_{\text{geom},\alpha} \sim \mathcal{O}(\delta)$  to be the only  $\delta$ -dependent contributions to  $\mathcal{F}_p$ . Particularly, all PV effects in this approximation can be eliminated in the numerical calculations by manually setting the P-violating Berry phases to zero.

With the short hand notation

$$k_{\alpha,\beta} = p_\beta p_\alpha^* c_\beta^* c_\alpha \exp[\Delta\tau_{\beta,\alpha}] \exp[i(\phi_{\text{dyn},\beta}^* - \phi_{\text{dyn},\alpha})], \quad (5.1)$$

where  $\exp[\Delta\tau_{\beta,\alpha}] := \exp[-(\Delta\tau_\beta - \Delta\tau_\alpha)^2 / (8\sigma_k'^2)]$ , and the perturbative expansion

$$\begin{aligned} \phi_{\text{geom},\alpha} &:= \phi_{\text{geom},\alpha}^{\text{PC}} + \delta\phi_{\text{geom},\alpha}^{\text{PV}} + \mathcal{O}(\delta^2) \\ &:= \phi_{\text{geom},\alpha}^{\text{PC}} + \delta\left(\frac{\delta_1}{\delta}\phi_{\text{geom},\alpha}^{\text{PV}_1} + \frac{\delta_2}{\delta}\phi_{\text{geom},\alpha}^{\text{PV}_2}\right) + \mathcal{O}(\delta^2) \end{aligned} \quad (5.2)$$

we write the total integrated flux (4.39) to order  $\mathcal{O}(\delta)$  as

$$\begin{aligned} \mathcal{F}_p(\delta) &\equiv \mathcal{F}_p(0) + \delta \left. \frac{\partial \mathcal{F}_p(\delta)}{\partial \delta} \right|_{\delta=0} = \sum_{\alpha,\beta} k_{\alpha,\beta} \exp[-i(\phi_{\text{geom},\beta}^* - \phi_{\text{geom},\alpha})] \Big|_{\mathcal{O}(\delta)} \\ &= \sum_{\alpha,\beta} k_{\alpha,\beta} \exp[-i(\phi_{\text{geom},\beta}^{\text{PC}*} - \phi_{\text{geom},\alpha}^{\text{PC}} + \delta(\phi_{\text{geom},\beta}^{\text{PV}*} - \phi_{\text{geom},\alpha}^{\text{PV}}))] \Big|_{\mathcal{O}(\delta)} \\ &=: \sum_{\alpha,\beta} k_{\alpha,\beta} \exp[-i(\phi_{\beta\alpha}^{\text{PC}} + \delta\phi_{\beta\alpha}^{\text{PV}})] \Big|_{\mathcal{O}(\delta)} = \sum_{\alpha,\beta} k_{\alpha,\beta} \exp[-i\phi_{\beta\alpha}^{\text{PC}}] (1 - i\delta\phi_{\beta\alpha}^{\text{PV}}). \end{aligned} \quad (5.3)$$

Hence, the PV-contributions  $\mathcal{F}_p^{\text{PV}_i}$  for  $\mathcal{F}_p = \mathcal{F}_p^{\text{PC}} + \mathcal{F}_p^{\text{PV}} = \mathcal{F}_p^{\text{PC}} + \mathcal{F}_p^{\text{PV}_1} + \mathcal{F}_p^{\text{PV}_2}$  are

$$\mathcal{F}_p^{\text{PV}_i} = \sum_{\alpha,\beta} k_{\alpha,\beta} \exp[-i\phi_{\beta\alpha}^{\text{PC}}] (-i\delta_i\phi_{\beta\alpha}^{\text{PV}_i}) \quad (5.4)$$

In this section as well as for the Sections 5.2 and 5.3 we employ

$$\phi_{\text{geom},\alpha}^{\text{PC}} = 0 \quad (5.5)$$

for the two metastable states involved in (5.4) which leads to a comparably simple expressions for (5.4). Of course, this requirement has to be checked when the spin echo signal is calculated for specific field configurations. But for that task we have a convenient tool at hand by means of the flux-density vector fields. With

$$\phi_{\beta\alpha}^{\text{PV}_i} = \begin{cases} -2i \text{Im} \phi_{\text{geom},\alpha}^{\text{PV}_i} & , \alpha = \beta \\ \text{Re} \phi_{\text{geom},\beta}^{\text{PV}_i} - \text{Re} \phi_{\text{geom},\alpha}^{\text{PV}_i} - i(\text{Im} \phi_{\text{geom},\beta}^{\text{PV}_i} + \text{Im} \phi_{\text{geom},\alpha}^{\text{PV}_i}) & , \alpha \neq \beta \end{cases} \quad (5.6)$$

## 5.2. Summed Spin Echo Signals

we then obtain for explicit choices of indices  $\alpha, \beta$  and with the phase choice  $\gamma_\alpha(z_0) = \gamma_\beta(z_0) = 0$  in (4.38)

$$\begin{aligned} \mathcal{F}_p^{\text{PV}} = 2\delta \{ & -\text{Re } k_{\alpha,\alpha} \text{Im } \gamma_\alpha^{\text{PV}} - \text{Re } k_{\beta,\beta} \text{Im } \gamma_\beta^{\text{PV}} \\ & + [\text{Re } \gamma_\beta^{\text{PV}} - \text{Re } \gamma_\alpha^{\text{PV}}] \text{Im } k_{\alpha,\beta} - [\text{Im } \gamma_\alpha^{\text{PV}} + \text{Im } \gamma_\beta^{\text{PV}}] \text{Re } k_{\alpha,\beta} \} . \end{aligned} \quad (5.7)$$

Note that we have split off the parameter  $\delta$  from the PV geometric phase. To obtain the two individual contributions  $\mathcal{F}_p^{\text{PV}_i}$ ,  $\delta$  can be replaced by  $\delta_i$ .

In order to extract an intuitively accessible formula for (5.7), we choose the states  $\alpha = 9$ ,  $\beta = 11$ , and employ the following assumptions which actually hold in good approximation for the concrete cases we will consider in later Sections:

$$\text{sgn}(\text{Re } \gamma_9^{\text{PV}}) = \text{sgn}(\text{Re } \gamma_{11}^{\text{PV}}) \stackrel{1}{\iff} \text{sgn}(\text{Im } \gamma_9^{\text{PV}}) = \text{sgn}(\text{Im } \gamma_{11}^{\text{PV}}) , \quad (5.8)$$

$$|\text{Re } \gamma_9^{\text{PV}}| = |\text{Re } \gamma_{11}^{\text{PV}}| , \quad |\text{Im } \gamma_9^{\text{PV}}| = |\text{Im } \gamma_{11}^{\text{PV}}| , \quad (5.9)$$

$$|p_9| = |p_{11}| , \quad |c_9| = |c_{11}| . \quad (5.10)$$

We then find the two cases

$$\textcircled{1} \quad \text{sgn}(\text{Re } \gamma_9^{\text{PV}}) = -\text{sgn}(\text{Re } \gamma_{11}^{\text{PV}}) \implies \mathcal{F}_{p,\textcircled{1}}^{\text{PV}} = 2\delta \text{Re} (\gamma_{11}^{\text{PV}} - \gamma_9^{\text{PV}}) \text{Im } k_{9,11} , \quad (5.11)$$

$$\textcircled{2} \quad \text{sgn}(\text{Re } \gamma_9^{\text{PV}}) = \text{sgn}(\text{Re } \gamma_{11}^{\text{PV}}) \implies \mathcal{F}_{p,\textcircled{2}}^{\text{PV}} = -2\delta \text{Im} (\gamma_9^{\text{PV}} + \gamma_{11}^{\text{PV}}) (\text{Re } k_{9,9} + \text{Re } k_{9,11}) . \quad (5.12)$$

Calculating  $\mathcal{F}_p^{\text{PC}} = \sum_{\alpha,\beta} k_{\alpha,\beta}$  yields

$$\begin{aligned} \mathcal{F}_p^{\text{PC}} = \exp[\Sigma\phi_{11,9}] & (|p_9|^2|p_{11}|^2 + |c_9|^2|c_{11}|^2 + 2 \exp[\Delta\tau_{11,9}] \\ & \times \{ \text{Re}(p_{11}p_9^*c_{11}^*c_9) \cos(\Delta\phi_{11,9}) - \text{Im}(p_{11}p_9^*c_{11}^*c_9) \sin(\Delta\phi_{11,9}) \}) \end{aligned} \quad (5.13)$$

Here, we defined  $\Sigma\phi_{11,9} := \text{Im } \phi_{\text{dyn},11} + \text{Im } \phi_{\text{dyn},9}$  and  $\Delta\phi_{11,9} := \text{Re } \phi_{\text{dyn},11} - \text{Re } \phi_{\text{dyn},9}$ . Equations (5.11)-(5.13) can be evaluated by choosing explicit values for  $c_9$ ,  $c_{11}$ ,  $p_9$ , and  $p_{11}$ .

## 5.2 Summed Spin Echo Signals

In principle, the difference  $\mathcal{F}_p - P(\mathcal{F}_p)$  between the total integrated flux and its space reflected version represents the magnitude of the P-violating effect. However, to track down systematics in an experiment it is often worthwhile to observe the phenomenon in question for different configurations. In the case of APV experiments one convenient approach is the application of different space transformations, i.e., several mirror reflections of the field configuration besides the full parity transformation. For example, the handedness of a field configuration consisting of components  $\mathcal{E}_1$ ,  $\mathcal{E}_3$ , and  $\mathcal{B}_3$  can also be reversed by a mirror reflection  $R_{xz}$  at the  $x$ - $z$ -plane resulting only in a sign change of  $\mathcal{B}_3$ .

---

<sup>1</sup>Here,  $\text{sgn}$  denotes the sign function.

## Chapter 5. Spin Echo Signals

---

We can exploit this procedure to extract a P-violating signal in the following way. First, we suppose absence of the P-violating part of the mass matrix. In this case the reflection  $R_{xz}$  exchanges the roles of  $|9\rangle$  and  $|11\rangle$ . With  $\mathbf{e}_1 = -\frac{1}{\sqrt{2}}(|9\rangle - |11\rangle)$  and  $\mathbf{e}_2 = \frac{i}{\sqrt{2}}(|9\rangle + |11\rangle)$  we denote the 2S states of the  $F = 1$  subspace as

$$|9\rangle = -\frac{1}{\sqrt{2}}(\mathbf{e}_1 + i\mathbf{e}_2), \quad |10\rangle = \mathbf{e}_3, \quad |11\rangle = \frac{1}{\sqrt{2}}(\mathbf{e}_1 - i\mathbf{e}_2). \quad (5.14)$$

At this point we suppose a field configuration with vanishing PC geometric phases. Then, for initial state amplitudes  $c_9 = c_{11} = 1/\sqrt{2}$ , projecting on  $|p\rangle = \mathbf{e}_1$  or  $|p\rangle = \mathbf{e}_2$ , respectively, leads to

$$\mathcal{F}_{\mathbf{e}_{1/2}}^{\text{PC}} = \frac{1}{2} \exp[\Sigma\phi_{11,9}] (1 \mp \exp[\Delta\tau_{11,9}] \cos[\Delta\phi_{11,9}]), \quad (5.15)$$

cf. (5.13). Taking into account  $\text{Re } \phi_{\text{dyn},9/11}|_{-\mathcal{B}_3} = -\text{Re } \phi_{\text{dyn},9/11}|_{\mathcal{B}_3}$ , see (4.23), the quantities  $\mathcal{F}_{\mathbf{e}_{1/2}}^{\text{PC}}$  are invariant under  $R_{xz}$ . According to (5.11) and (5.12) the calculation of  $\mathcal{F}_{\mathbf{e}_{1/2}}^{\text{PV}}$  yields the approximate expressions

$$\mathcal{F}_{\mathbf{e}_{1/2},\textcircled{1}}^{\text{PV}} = \mp \frac{\delta}{2} \text{Re}(\gamma_{11}^{\text{PV}} - \gamma_9^{\text{PV}}) \exp[\Delta\tau_{11,9}] \exp[\Sigma\phi_{11,9}] \sin[\Delta\phi_{11,9}], \quad (5.16)$$

$$\mathcal{F}_{\mathbf{e}_{1/2},\textcircled{2}}^{\text{PV}} = -\frac{\delta}{2} \text{Im}(\gamma_9^{\text{PV}} + \gamma_{11}^{\text{PV}}) \exp[\Sigma\phi_{11,9}] (1 \mp \exp[\Delta\tau_{11,9}] \cos[\Delta\phi_{11,9}]). \quad (5.17)$$

Depending on the concrete situation, the two spin echo signals of different chirality have to be added or subtracted in order to get access to the PV effects hidden in the signal. For instance, we find numerically

$$R_{xy}(\gamma_{9/11}^{\text{PV}}) = -\gamma_{11/9}^{\text{PV}} \quad (5.18)$$

with high precision for a given field configuration. This leads to  $R_{xy}(\text{Re}(\gamma_{11}^{\text{PV}} - \gamma_9^{\text{PV}})) = \text{Re}(\gamma_{11}^{\text{PV}} - \gamma_9^{\text{PV}})$ . Then, the difference  $\mathcal{F}_{\mathbf{e}_{1/2},\textcircled{1}} - R_{xz}(\mathcal{F}_{\mathbf{e}_{1/2},\textcircled{1}})$  for the case  $\textcircled{1}$  enables us to extract the PV effect since  $R_{xz}$  switches the sign of  $\sin[\Delta\phi_{11,9}]$  in (5.16).

Another especially interesting setup is the following. With the projection on  $\mathbf{e}_{45^\circ} := \frac{1}{\sqrt{2}}(\mathbf{e}_1 + \mathbf{e}_2) = \frac{i-1}{2}|9\rangle + \frac{i+1}{2}|11\rangle$  we obtain

$$\mathcal{F}_{\mathbf{e}_{45^\circ}}^{\text{PC}} = \frac{1}{2} \exp[\Sigma\phi_{11,9}] (1 + \exp[\Delta\tau_{11,9}] \sin[\Delta\phi_{11,9}]), \quad (5.19)$$

resulting in  $\mathcal{F}_{\mathbf{e}_{45^\circ}}^{\text{PC}} + R_{xz}(\mathcal{F}_{\mathbf{e}_{45^\circ}}^{\text{PC}}) = \exp[\Sigma\phi_{11,9}]$ . That is, the oscillations within the envelope of the summed PC signal cancel. For  $\mathcal{F}_{\mathbf{e}_{45^\circ}}^{\text{PV}}$  we calculate

$$\text{Re } k_{9,9} = \frac{1}{4} \exp[\Sigma\phi_{11,9}], \quad (5.20)$$

$$\text{Re } k_{9,11} = \frac{1}{4} \exp[\Sigma\phi_{11,9}] \exp[\Delta\tau_{11,9}] \sin(\Delta\phi_{11,9}), \quad (5.21)$$

$$\text{Im } k_{9,11} = -\frac{1}{4} \exp[\Sigma\phi_{11,9}] \exp[\Delta\tau_{11,9}] \cos(\Delta\phi_{11,9}), \quad (5.22)$$

### 5.3. A Parity-Violating Spin Echo Signal

---

leading to

$$\mathcal{F}_{e_{45^\circ}, \textcircled{1}}^{\text{PV}} = \frac{\delta}{2} \text{Re} (\gamma_9^{\text{PV}} - \gamma_{11}^{\text{PV}}) \exp[\Sigma\phi_{11,9}] \exp[\Delta\tau_{11,9}] \cos(\Delta\phi_{11,9}) , \quad (5.23)$$

$$\mathcal{F}_{e_{45^\circ}, \textcircled{2}}^{\text{PV}} = -\frac{\delta}{2} \text{Im} (\gamma_9^{\text{PV}} + \gamma_{11}^{\text{PV}}) \exp[\Sigma\phi_{11,9}] (1 + \exp[\Delta\tau_{11,9}] \sin(\Delta\phi_{11,9})) . \quad (5.24)$$

Assuming again (5.18), we observe that the detection of a PV signal for the case  $\textcircled{1}$  requires the summation of  $\mathcal{F}_{e_{45^\circ}, \textcircled{1}}$  and  $R_{xz}(\mathcal{F}_{e_{45^\circ}, \textcircled{1}})$  instead of taking the difference:

$$\mathcal{F}_{e_{45^\circ}, \textcircled{1}} + R_{xz}(\mathcal{F}_{e_{45^\circ}, \textcircled{1}}) = \exp[\Sigma\phi_{11,9}] (1 + \delta \text{Re} (\gamma_9^{\text{PV}} - \gamma_{11}^{\text{PV}}) \exp[\Delta\tau_{11,9}] \cos(\Delta\phi_{11,9})) , \quad (5.25)$$

$$\mathcal{F}_{e_{45^\circ}, \textcircled{2}} + R_{xz}(\mathcal{F}_{e_{45^\circ}, \textcircled{2}}) = \exp[\Sigma\phi_{11,9}] (1 - \delta \text{Im} (\gamma_9^{\text{PV}} + \gamma_{11}^{\text{PV}}) \exp[\Delta\tau_{11,9}] \sin(\Delta\phi_{11,9})) . \quad (5.26)$$

Equation (5.25) indicates that the PV effect manifests itself, modifying the PC signal  $\exp[\Sigma\phi_{11,9}]$ , as a sinusoidal term which is damped by an increasing separation  $|\Delta\tau_{11,9}|$  of the wave functions of  $|9\rangle$  and  $|11\rangle$ . The order of magnitude of the PV signal, i.e., its maximal amplitude, is given by the PV geometric phases themselves. Because of their comparably simple structure, Equations like (5.25) and (5.26) constitute a convenient semi-analytical<sup>2</sup> testing ground to cross-check the numerical implementation for the spin echo signal.

These examples mentioned above vividly show that we have to process the signals appropriately when choosing specific initial and projection states for concrete field configurations.

### 5.3 A Parity-Violating Spin Echo Signal

In the following, we compare (5.25) with the numerical results for a PV spin echo signal for a path  $\mathcal{C}$  in the  $\mathbf{L} = (\mathcal{E}_3, \mathcal{B}_1, \mathcal{B}_3)$  parameter space. In the course of that we discuss numerous subtleties one has to take into account when calculating spin echo signals. Thereby, we try to illustrate the complex process of finding a suitable spin echo field configuration.

As suggested by the according flux-density vector field in Figure 5.1, we define

$$\mathcal{C}: z \rightarrow \mathbf{L}(z) = \begin{pmatrix} \mathcal{E}_3(z)/\mathcal{E}_0 \\ \mathcal{B}_1(z)/\mathcal{B}_0 \\ \mathcal{B}_3(z)/\mathcal{B}_0 \end{pmatrix}, \quad 0 \leq z \leq 1 , \quad (5.27)$$

$$\begin{aligned} \mathcal{E}_3(z) = \{ & [0.05, 0], [0.075, 40z - 2], [0.175, 1], [0.225, 8 - 40z], [0.325, -1], \\ & [0.35, 40z - 14], [0.55, 0], [0.575, 40z - 22], [0.675, 1], [0.725, 28 - 40z], \\ & [0.825, -1], [0.85, 40z - 34], [1, 0] \} , \end{aligned} \quad (5.28)$$

---

<sup>2</sup>Here, we use the term semi-analytical to emphasise that the formulae (5.25) and (5.26) follow from a perturbative expansion of the analytical expression (4.39), but need numerical input such as the geometric phases or reduced arrival times, respectively.

$$\mathcal{B}_1(z) = \{[0.05, 0.02z], [0.35, 0.001], [0.4, 0.008 - 0.02z], [0.5, 0], [0.55, 0.01 - 0.02z], [0.85, -0.001], [0.9, 0.02z - 0.018], [1.0, 0]\} , \quad (5.29)$$

$$\mathcal{B}_3(z) = \{[0.075, 0.1], [0.175, 0.175 - z], [0.225, 0], [0.325, z - 0.225], [0.4, 0.1], [0.5, 0.9 - 2z], [0.575, -0.1], [0.675, z - 0.675], [0.725, 0], [0.825, 0.725 - z], [0.9, -0.1], [1.0, 2z - 1.9]\} . \quad (5.30)$$

In (5.28)-(5.30) we denote the field value  $f(z)$  for  $x \leq z \leq y$  as  $[y, f(z)]$ , where  $x$  is the upper bound of the preceding interval, initially starting with  $x = 0$ . The electric and magnetic fields are given in V/cm and mT, respectively. For concrete constraints on experimentally feasible field configurations, a smooth path with properties similar to (5.27) can be set up easily.

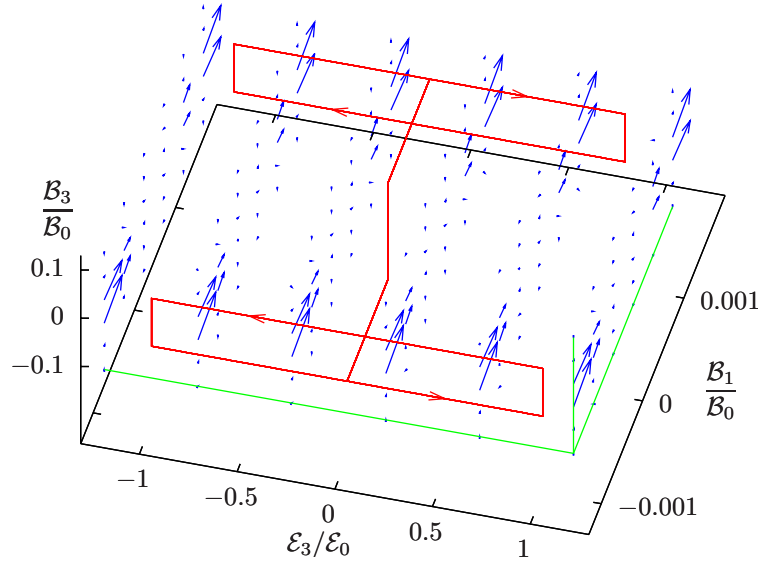


**Figure 5.1:** Visualisation of the real part of the nuclear-spin dependent P-violating flux-density vector field  $\hat{\mathbf{j}}_9^{(L)PV_2}(\mathcal{E}, \mathcal{B})$ . The scaling factor is chosen as  $\eta'_{9,2} = 0.175/\delta_2$ . The drawn vectors start at  $6^3$  base points of a Cartesian grid in the parameter space volume  $[-1.2 \text{ V/cm}, 1.2 \text{ V/cm}] \times [-1.2 \mu\text{T}, 1.2 \mu\text{T}] \times [-0.12 \text{ mT}, 0.12 \text{ mT}]$ . To clarify the structure of the grid, we show three green lines connecting base points along the Cartesian axes. The vectors are essentially parallel to the planes of constant  $\mathcal{E}_3$ . The direction of the red path (5.27), starting and ending at  $(\mathcal{E}_1, \mathcal{B}_1, \mathcal{B}_3) = (0, 0, 0.1 \text{ mT})$ , is indicated by arrows.

A principal requirement for our spin echo experiment is an overlap of the beforehand separated internal states at the detector. In the case of the states |9) and |11) we have to employ a symmetric spin echo configuration in the sense that each section of the path in the magnetic field parameter subspace has to be reversed to a certain degree. Otherwise, for example by choosing only the first loop of (5.27) in the region of  $\mathcal{B}_1, \mathcal{B}_3 > 0$  as full path, the wave packets of |9) and |11) get separated continuously with largest separation at the detector. Of course, small enough asymmetries in the field configuration will still lead to substantial interferences.

### Consistent Labelling of States

At first glance, the path (5.27) should result in a vanishing spin-dependent PV phase  $\gamma_9^{\text{PV}_2}$  since the contributions of the two oriented loops cancel, see Figure 5.1. However, (5.27) runs through  $\mathbf{B} = \mathbf{0}$  giving rise to a non-adiabatic transition as depicted in Figure 5.2. We point out that the Berry phases we consider here emerge for those parts of the curve (5.27) where adiabatic evolution is ensured.

In QABSE the consistent labelling of the states  $|\alpha\rangle$  with the label  $\alpha$  for consecutive steps  $i$  and  $i + 1$  is achieved by demanding<sup>3</sup>  $|\langle \alpha(z_i) | \beta(z_{i+1}) \rangle| = \delta_{\alpha\beta} + \epsilon \approx \delta_{\alpha\beta}$ , with user-specified  $|\epsilon| \ll 1$ . This ensures a continuous developing of the energies for a given label  $\alpha$ . In situations of Figure 5.2 (b), where a degeneracy in principle prohibits adiabatic evolution, we still have conservation of the third component  $F_3$  of the total angular momentum if  $\mathbf{B} \parallel (\pm \mathbf{e}_z)$ . Therefore, we additionally demand<sup>4</sup>  $\langle \alpha(z_i) | F_3 | \beta(z_i) \rangle = F_3 \delta_{\alpha\beta} \approx \langle \alpha(z_{i+1}) | F_3 | \beta(z_{i+1}) \rangle$  to preserve consistent labelling when crossing  $\mathcal{B}_3 = 0$ . As a result, the states |9) and |11) flip their roles, as can be observed by comparing Figures 5.2 (a) and (b). The latter is analogous to the situation for the familiar Breit-Rabi-diagram in Figure 5.2 (c), where the energy of the electron's magnetic moment in the  $\mathbf{B}$ -field flips sign at  $\mathcal{B}_3 = 0$  while keeping the labelling of states. On the other hand, our numerical procedure for the calculation of the flux-density vector fields avoids the degeneracy at  $\mathbf{B} = \mathbf{0}$ , see Appendix A.1. There, the roles of |9) and |11) are not flipped for regions in parameter space which are distinguished by the sign of  $\mathcal{B}_3$ . Hence, (5.27) for the state |9) is set up in such a way that Figure 5.1 holds for  $\mathcal{B}_3 > 0$ , while Figure 5.3 holds for  $\mathcal{B}_3 < 0$ . The contributions of the two loops of (5.27) to  $\gamma_9^{\text{PV}_2}$  therefore add instead of cancel. The same is true for the imaginary parts of  $\hat{\mathbf{J}}_9^{(L)\text{PV}_2}(\mathcal{E}, \mathbf{B})$  and  $\hat{\mathbf{J}}_{11}^{(L)\text{PV}_2}(\mathcal{E}, \mathbf{B})$ .

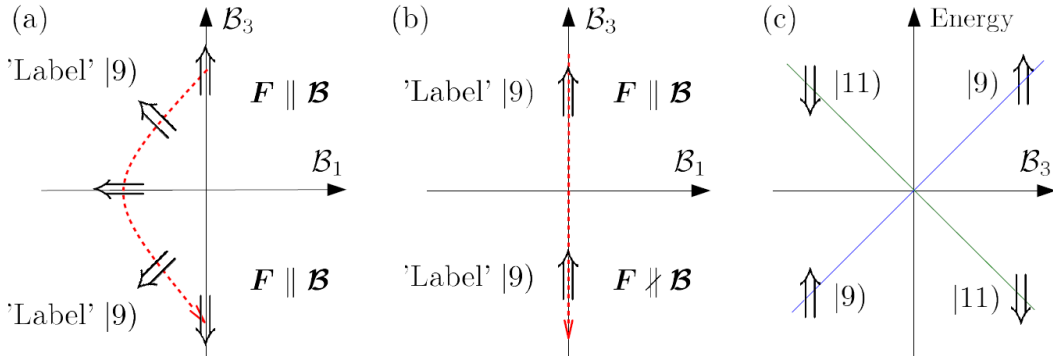


**Figure 5.2:** (a) Avoiding the degeneracy at  $\mathbf{B} = \mathbf{0}$ , we can obtain an adiabatic evolution with  $\mathbf{F} \parallel \mathbf{B}$  at all times, where the total angular momentum  $\mathbf{F}$  is indicated by '⇒'. A fictive path in the parameter space of  $\mathcal{B}_1$  and  $\mathcal{B}_3$  is shown as a dashed red curve. (b) Due to conservation of  $F_3$  in a pure  $\mathcal{B}_3$  field,  $\mathbf{F}$  flips its orientation with respect to the magnetic field  $\mathbf{B}$  when crossing  $\mathcal{B}_3 = 0$ . (c) The Breit-Rabi-diagram for the states |9) and |11).

<sup>3</sup>The absolute value is needed here since the numerical procedure may assign arbitrary phases to the states  $|\beta(z_{i+1})\rangle$ .

<sup>4</sup>The approximation indicates numerical errors which have to be taken into account.

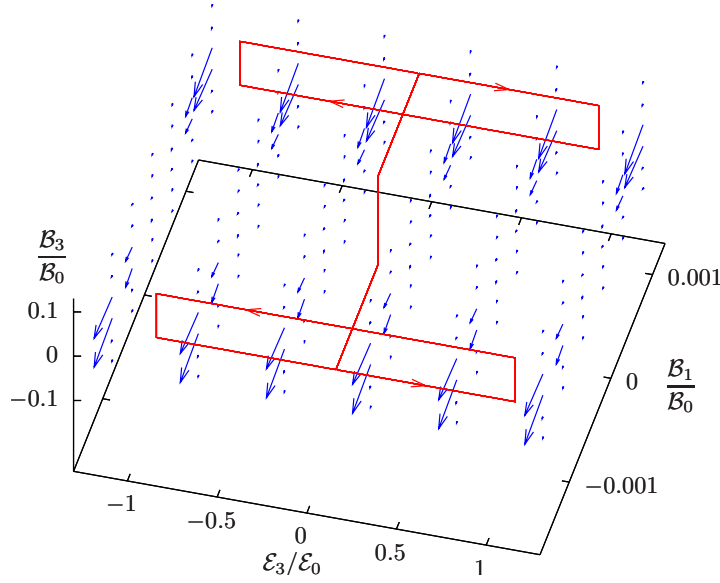


**Figure 5.3:** Visualisation of the real part of the nuclear-spin dependent P-violating flux-density vector field  $\hat{\mathcal{J}}_{11}^{(L)PV_2}(\mathcal{E}, \mathcal{B})$ . The scaling factor is chosen as  $\eta'_{11,2} = 0.175/\delta_2$ .

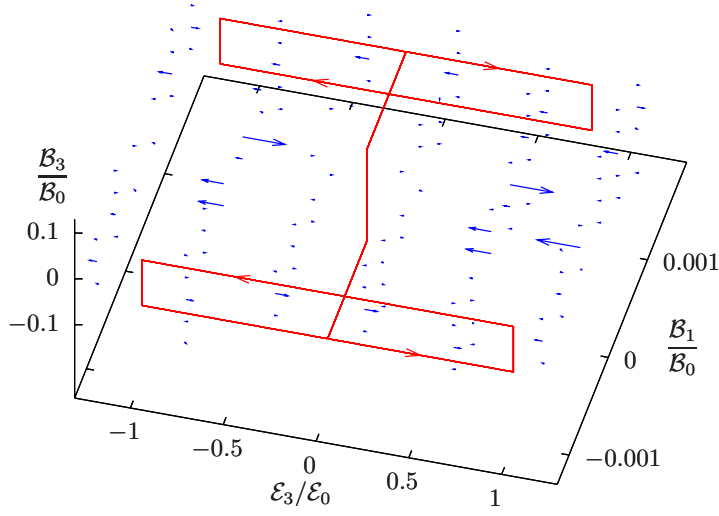
### Discussion of the Result

A part of the PC flux-density vector field for |9) is shown in Figure 5.4. Due to its irregular structure and comparably small absolute values we suppose this vector field to vanish in the presented region of parameter space. That is, we presume Figure 5.4 to show merely numerical noise. Even if we did not suppose that, its contribution would vanish since the vectors have no components orthogonal to the two areas of the path (5.27). The same argumentation holds for the imaginary part and for the PC flux-density vector field for |11). Thus, (5.27) also does not result in a PC geometric phase for |11). Therefore, we may manually set the PC geometric phases to zero in order not to introduce unnecessary numerical errors for the spin echo signal. The approximations (5.8)-(5.10) can be applied for (5.27) where we find the case (5.11).

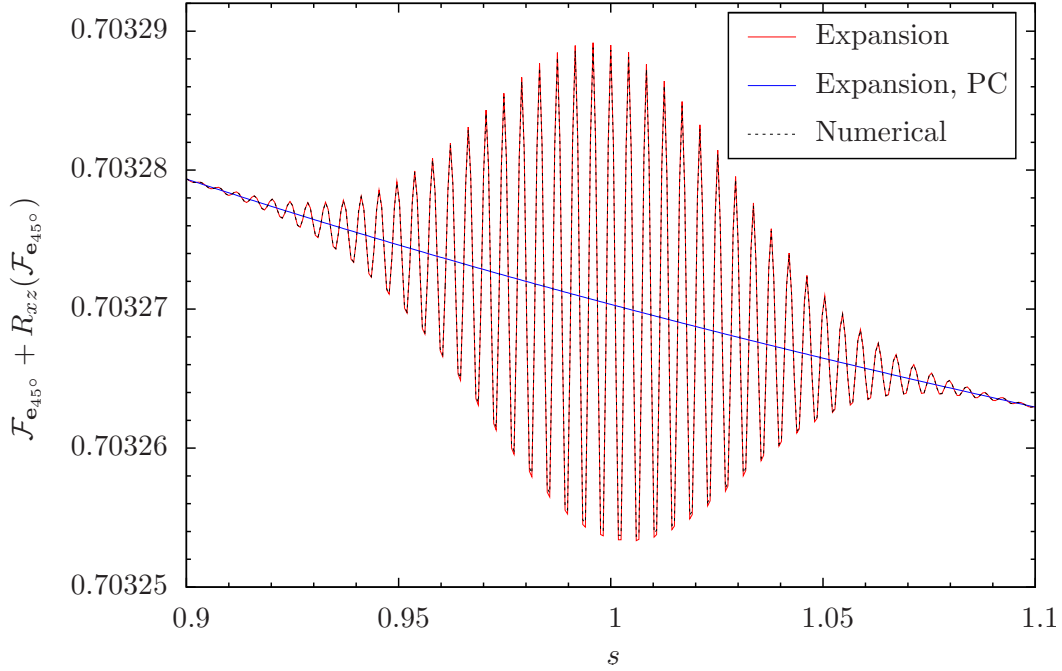
We also manually multiply the PV geometric phases by a factor of  $2 \times 10^8$  before adding the according contribution  $\mathcal{F}_{e_{45^\circ}, \textcircled{1}}^{PV}$  to  $\mathcal{F}_{e_{45^\circ}, \textcircled{1}}^{PC}$ . Otherwise, the numerically obtained values for  $\mathcal{F}_{e_{45^\circ}, \textcircled{1}} + R_{xz}(\mathcal{F}_{e_{45^\circ}, \textcircled{1}})$  would have to be given with an accordingly high precision of about 13 digits. That is, the factor of  $2 \times 10^8$  is not only valuable for presentational purposes but also avoids the introduction of numerical errors due to the double precision variables of the QABSE software. The correct amplitudes of the PV signal can simply be extracted via its division by  $2 \times 10^8$  after the spin echo signals have been processed as desired.

Figure 5.5 shows (5.25) to be consistent with the full numerical calculation of  $\mathcal{F}_{e_{45^\circ}, \textcircled{1}} + R_{xz}(\mathcal{F}_{e_{45^\circ}, \textcircled{1}})$  and, hence, indicates that the approximations (5.8)-(5.10) are indeed acceptable for (5.27). For that field configuration the nuclear-spin independent PV contribution can be regarded negligible. In fact,  $|\gamma_9^{PV_2}| \approx 50 \times |\gamma_9^{PV_1}|$  for (5.27). Evaluating the expansion (5.25) we used the QABSE data of the dynamical phases, the reduced arrival times, and the PV phases of the states |9) and |11).

### 5.3. A Parity-Violating Spin Echo Signal



**Figure 5.4:** Visualisation of the real part of the P-conserving flux-density vector field  $\hat{\mathbf{j}}_9^{(L)PC}(\boldsymbol{\mathcal{E}}, \boldsymbol{\mathcal{B}})$ . The scaling factor is chosen as  $\eta_9 = 5 \times 10^8$ .



**Figure 5.5:** Comparison of the numerical data obtained from QABSE, the expansion (5.25), and its PC part. For the (red-line-)expansion (5.25) only the spin dependent PV part is taken into account. We find very good agreement between the semi-analytical expansion and the numerical data justifying, at least in this particular case, the approximations (5.8)-(5.10).

The enhancement effect for the Berry phases using multiple cyclings requires an accordingly increased number of numerical steps through the whole field configuration to achieve the same numerical precision. To save computing time, it can therefore be worthwhile to calculate the signals for only one cycling of (5.27) and estimate the

signal for the case of multiple cyclings. As an example, the numerical data used to extract the signal in Figure 5.5 has been computed within 30 hours using 16 parallel CPUs. An amplification of the PV signal via multiple path cyclings is achieved via its multiplication with the number of cyclings since the signal scales with the PV phases. Thereby, the number of cyclings  $k = l/\Delta z$  for an interferometer length of  $l = 1$  m is limited by the adiabaticity conditions as discussed in Section 3.2.1. With  $|\mathcal{E}(z)|_{\text{av}} \approx 0.5 \text{ V/cm} \ll 250 \text{ V/cm}$  the lifetime restrictions are met. The limits on the variations of  $\mathcal{E}$  and  $\mathcal{B}$  with respect to  $z$  lead to a maximum of about one cycle per millimetre. The most severe restriction for (5.27) is the minimal energy difference<sup>5</sup> related to  $|\mathcal{B}(z)|_{\text{min}} = 1 \mu\text{T}$  and resulting in the condition  $\Delta z \gg 150 \text{ mm}$ . After all, we find that the number of cyclings of (5.27) should not exceed  $k = 2$ .

In order to fully exhaust the adiabaticity conditions for those regions where adiabatic evolution is needed, we consider the parameter space volume  $[-1 \text{ V/cm}, 1 \text{ V/cm}] \times [-5 \text{ mT}, 5 \text{ mT}]^2$  by multiplying (5.29) and (5.30) with 5000 and 50, respectively. We observe that for the resulting path  $\mathcal{C}'$  the flux-density vector field of e.g. |9) leads to a smaller Berry phase compared to the path  $\mathcal{C}$ . In fact, for one cycling we obtain  $\delta_2 \cdot \text{Re} \gamma_9^{\text{PV}_2}(\mathcal{C}) = 6.634 \times 10^{-14}$ , but  $\delta_2 \cdot \text{Re} \gamma_9^{\text{PV}_2}(\mathcal{C}') = 4.734 \times 10^{-14}$ . In contrast to Figure 5.1 we find the flux-density vectors decreased<sup>6</sup> for larger magnetic field in Figure 5.6. However, the number of cyclings for  $\mathcal{C}'$  can then be increased to  $k = 1000$ , with the adiabaticity conditions still fulfilled. As a result, the PV contribution of the summed spin echo signal reaches maximal amplitudes of  $\delta_2 \cdot \text{Re} (\gamma_9^{\text{PV}_2}(\mathcal{C}') - \gamma_{11}^{\text{PV}_2}(\mathcal{C}')) \approx 10^{-10}$ .

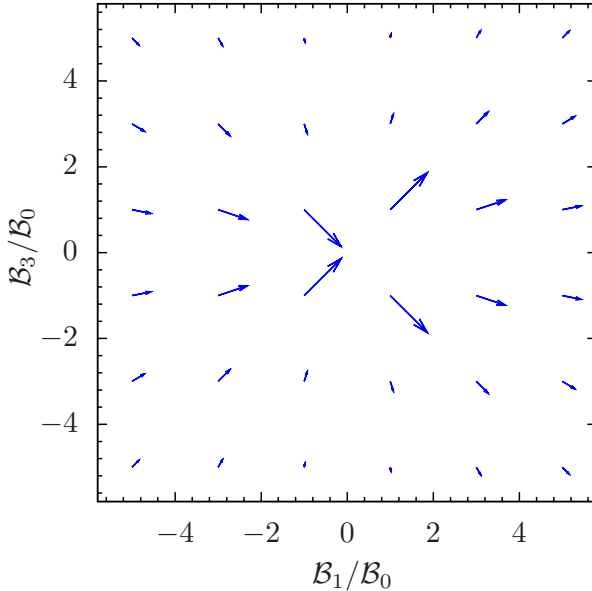


**Figure 5.6:** Visualisation of the real part of the nuclear-spin dependent P-violating flux-density vector field  $\hat{\mathbf{j}}_9^{(L)\text{PV}_2}(\mathcal{E}, \mathcal{B})$  at  $\mathcal{E}_3 = 0$ . The scaling factor is chosen as  $\eta'_{9,2} = 600/\delta_2$ .

<sup>5</sup>The minimal energy difference along  $\mathcal{C}$  is of course zero since the path runs through  $\mathcal{B} = \mathbf{0}$ . But in this regime only the magnetic field in  $z$ -direction is non-zero in the case of which  $F_3$  is conserved. And here we are dealing with the states  $|F_3 = \pm 1\rangle$  only. This situation is under control numerically as depicted in Figure 5.2. Moreover, the according parts of  $\mathcal{C}$  do not contribute to a geometric phase anyway.

<sup>6</sup>This is simply an issue of the different parameter space regions considered.

## 5.4. An Experimentally Realised Field Configuration

---

The excursion in this section vividly demonstrates the subtleties involved in the theoretical design of field configurations appropriate for experimental detection of desired Berry phases. We outlined a way to identify PV Berry phases in spin echo signals, calculated their magnitude for one specific field configuration, and found a PV signal of the order of  $10^{-10}$ . The implications for the electroweak mixing angle resulting from that will be discussed in Section 5.5. Before, we want to present larger (PC) Berry phases for a magnetic field configuration actually available in the present experimental setup.

### 5.4 An Experimentally Realised Field Configuration

A magnetic field configuration suitable for the creation of Berry phases has been built in the group around M. DeKieviet [37]. The experimental data presented here is provided by P. Augenstein [176]. A Mathematica-routine gives  $\chi^2$ -fits to the experimental data as follows:

$$\begin{aligned}
 \mathcal{C}: z &\rightarrow \mathcal{B}(z) , \quad 0 \leq z \leq 0.66 , & (5.31) \\
 \mathcal{B}_1(z)/\mathcal{B}_0 &= -1.09488 \exp[-2251.75 (z - 0.221739)^2] \sin[3.95282 (z - 0.222097)] \\
 &\quad - 0.359245 \exp[-2174.46 (z - 0.457696)^2] \sin[11.8633 (z - 0.193543)] , \\
 \mathcal{B}_2(z)/\mathcal{B}_0 &= 0.230998 \exp[-490.685 (z - 0.222096)^2] \\
 &\quad \times (\cos^2[29.8529 (z - 0.222682)] - 0.894862) \\
 &\quad - 0.249763 \exp[-515.945 (z - 0.458747)^2] \\
 &\quad \times (\cos^2[29.0659 (z - 0.459074)] - 0.901612) , \\
 \mathcal{B}_3(z)/\mathcal{B}_0 &= -0.0534008 \exp[-535.705 (z - 0.451987)^2] \\
 &\quad + 0.0534471 \exp[-566.72 (z - 0.215842)^2] ,
 \end{aligned}$$

where  $z$  is given in meters. For the actual usage in QABSE we tweak the functions in (5.31) as follows. First, we add  $10^{-8}$  T to  $\mathcal{B}_3$  in order to start with a field  $\mathcal{B} \approx \{10^{-8} \text{ T}, 0, 0\}$ , stabilising the numerical procedures which are responsible for correct labelling of the states. Now,  $\mathcal{B}_3$  crosses zero at  $z_c = 0.3338091659$ , where  $\mathcal{B}_1$  is essentially zero, but  $\mathcal{B}_2$  is not. To ensure correct labelling of states with a routine which checks the conservation of the  $F_3$  quantum number in a pure  $\mathcal{B}_3$  field we manually set  $\mathcal{B}_2 = 0$ ,  $0.3167677684 \leq z \leq 0.3622300794$ , while preserving continuity. At  $z_a = 0.66$ , the end of the interferometer, we have to arrive at the same field configuration we started with. That is, we manually set  $\mathcal{B}_2 = 0$  for  $z > 0.5781363795$ . These adjustments surely introduce less errors than the fits (5.31) themselves while simplifying the numerical handling considerably. A comparison of (5.31) and the experimental data is shown in Figure 5.7. The configuration shown there should result in an almost vanishing Berry phase for the 2S states |9) and |11), if adiabatic evolution is employed. However,  $\mathcal{B}_3 = 0$  crosses zero at  $z_c$  yielding a non-adiabatic transition between the states labelled |9) and |11). The flux-density vector fields of |9) and |11) differ in sign,

see (3.118). Therefore, we switch sign of  $\mathcal{B}_1(z)$  for  $z_c \leq z \leq 0.66$  resulting in a Berry phase  $\gamma_9 \approx -0.0112$ .

We modulate  $\mathcal{B}_3(z)$  by multiplication with a parameter  $s$  in the interval  $z_c \leq z \leq 0.66$ . The resulting spin echo signal is shown in Figure 5.8 for the parameter range  $0.5 \leq s \leq 1.5$ . The according variation of  $s$  can be achieved by modulating the current through that part of the second spin echo coil which is responsible for  $\mathcal{B}_3$ , cf. Figure 4.1. In this case, the geometric as well as the dynamic phases are altered with  $s$ . The modulation of  $\mathcal{B}$  by multiplication with  $s$  in the interval  $z_c \leq z \leq 0.66$  leaves the solid angle encircled by  $\mathcal{B}$  invariant. Hence the Berry phase  $\gamma_9$  is invariant, and only the dynamic phases vary. The according spin echo signal is shown in Figure 5.9.

Employing  $c_9 = c_{11} = p_9 = p_{11} = 1/\sqrt{2}$  for the coefficients of the initial and final state, we find the PC part

$$\begin{aligned} \mathcal{F}_p^{\text{PC}} = & \frac{1}{4} \left\{ \exp[2(\text{Im}\phi_{\text{dyn},9} - \text{Im}\phi_{\text{geom},9}^{\text{PC}})] + \exp[2(\text{Im}\phi_{\text{dyn},11} - \text{Im}\phi_{\text{geom},11}^{\text{PC}})] \right. \\ & + 2 \exp[\Delta\tau_{11,9}] \exp[\text{Im}\phi_{\text{dyn},9} + \text{Im}\phi_{\text{dyn},11} - \text{Im}\phi_{\text{geom},9}^{\text{PC}} - \text{Im}\phi_{\text{geom},11}^{\text{PC}}] \\ & \left. \times \cos[\text{Re}\phi_{\text{dyn},11} - \text{Re}\phi_{\text{dyn},9} - \text{Re}\phi_{\text{geom},11}^{\text{PC}} + \text{Re}\phi_{\text{geom},9}^{\text{PC}}] \right\} \quad (5.32) \end{aligned}$$

of the expansion of  $\mathcal{F}_p$  from Section 5.1. The evaluations of (5.32) for the spin echo signals presented in Figures 5.8 and 5.9 are drawn as dashed lines. We find excellent agreement.

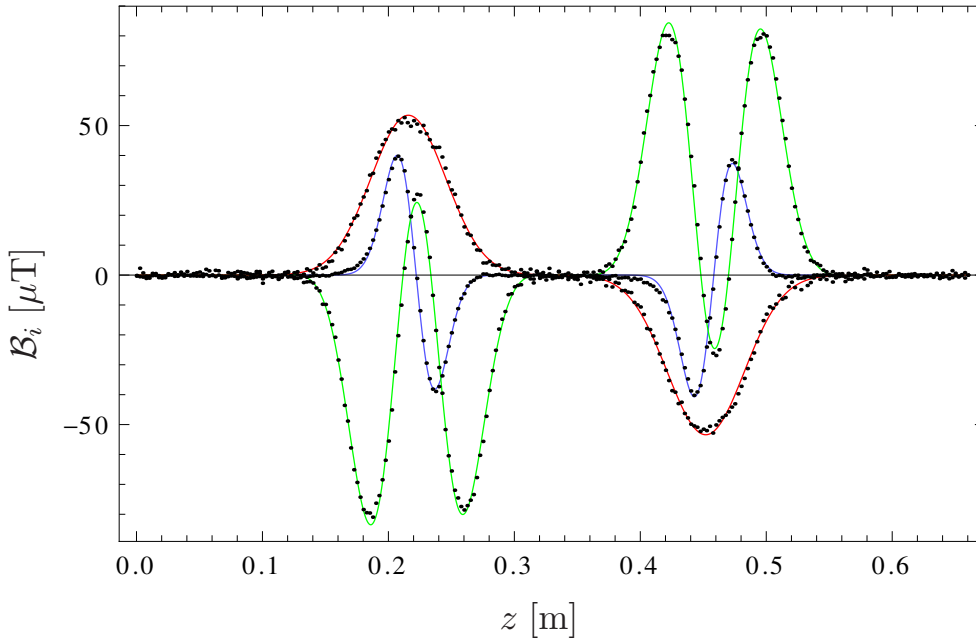


**Figure 5.7:** The field configuration realised in [37]. We show fits of the magnetic field components  $\mathcal{B}_i$ , namely  $\mathcal{B}_1$  (blue line),  $\mathcal{B}_2$  (green line), and  $\mathcal{B}_3$  (red line), to the experimental data which are presented as dots. The fit functions are given in (5.31) and serve as input for our numerical software QABSE.

## 5.4. An Experimentally Realised Field Configuration

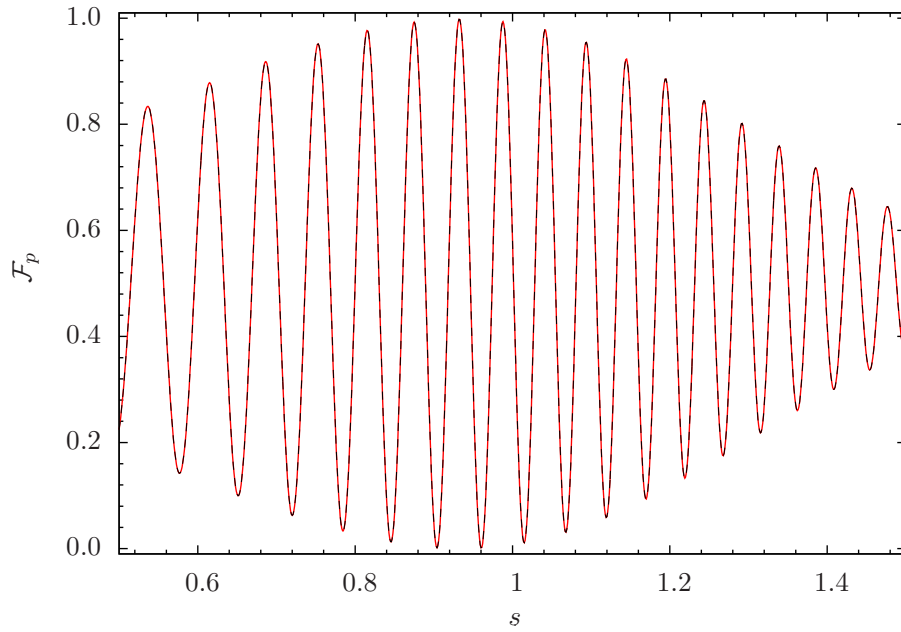


**Figure 5.8:** Spin echo signal (red) for the field configuration (5.31) using hydrogen in the state  $|9\rangle$  and the specifications given in Chapter 4. The graph is generated from 1000 base points  $0.5 \leq s \leq 1.5$ , evaluated within 20 hours of CPU-time using an OpenMP<sup>®</sup> parallel-computing algorithm. The semi-analytical function (5.32) for the presented signal is given as dashed black line.

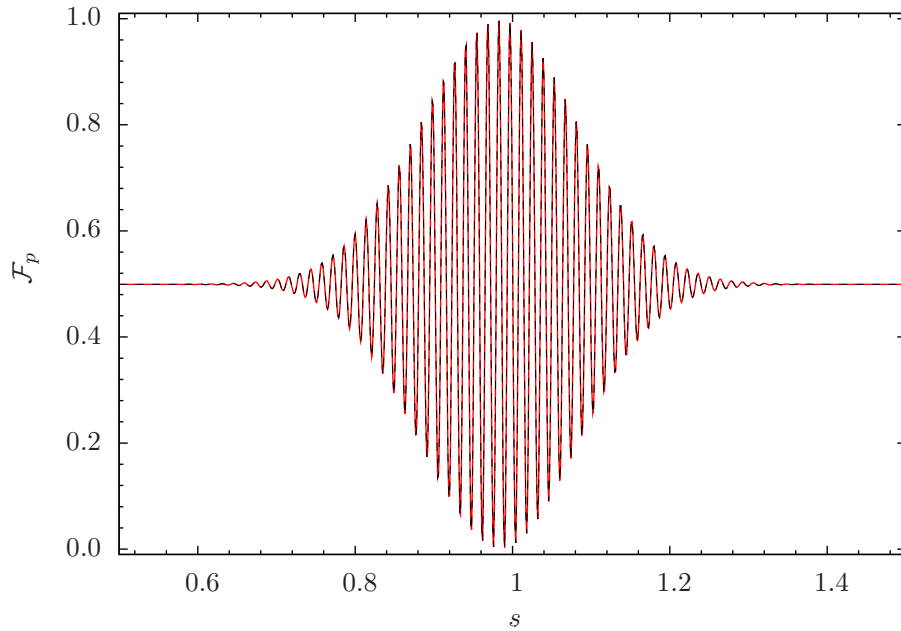


**Figure 5.9:** Spin echo signal (red) for the field configuration (5.31) using hydrogen in the state  $|9\rangle$  and the specifications given in Chapter 4. In contrast to Figure 5.8 not only  $\mathcal{B}_3$  is multiplied by  $s$  in the interval  $z_c \leq z \leq 0.66$  but the whole magnetic field vector  $\mathcal{B}$ . The semi-analytical function (5.32) for the presented signal is given as dashed black line.

## 5.5 Error Estimates and Implications for the Standard Model

It is often regarded as the ultimate goal of atomic PV experiments to gain insight into the electroweak sector, especially the determination of the electroweak mixing angle at low energies. General difficulties of APV experiments are the small magnitudes of the PV effects due to the Coulomb interaction which by far dominates the Z-boson amplitude.

As we have found in the present thesis, this obstacle exists as well for Abelian PV Berry Phases being part of the hydrogen wave functions in external fields. In fact, we have found PV Berry phases of the order of  $10^{-10}$ . Of course, this raises the question of experimental feasibility. On the other hand, further development of technological resources may provide the necessary means in the future. Then, PV effects in hydrogen have the potential for significant advances regarding the knowledge of Standard Model parameters.

To elaborate on that statement we present error estimates for spin echo measurements of PV Berry phases in this section. Thereby, we will not include systematic or statistical experimental errors. The relative errors for the Berry phases introduced through the numerics are of the order of  $10^{-10}$  or less and are therefore negligible. However, the ratio of the PV and PC parts of the spin echo signal  $\mathcal{F}_p$  is of the same order of magnitude. This demands the expansion of  $\mathcal{F}_p$  in terms of the PV parameter  $\delta$  as discussed in Section 5.1. Otherwise, the PV signal would be masked by the numerical errors. Besides the latter, the errors of the mass matrix and the full hydrogen wave functions have to be taken into account. The error estimates for the weak charges due to higher-order electroweak effects, which lead beyond the tree-level expressions (2.35) and (2.37), are below 1%, cf. [8]. Therefore, as indicated in Table A.1 of Appendix A.1, the largest relative errors of physical quantities in the field-free mass matrix are those of the PV parameters  $\delta_{1,2}$  due to the reported error of  $\sin^2 \theta_W$  and the uncertainty of  $(\Delta s + \Delta \bar{s})$ , respectively. The hydrogen energies are much more precisely known, as well as the decay rates (3.12). The wave packet amplitude we use for the calculation of spin echo signals is accurate at the 1%-level, see (4.14). In summary, since we want to extract the PV parameters  $\delta_{1,2}$ , we do not include their errors in our theoretical predictions of spin echo signals. We rather conclude that the dominant error of our PV signal is due to the error of the wave packet amplitude, i.e., of the order of 1%. As pointed out in [32] this accuracy can be further enhanced by taking into account higher orders of (4.11).

The PV spin echo signals are proportional to the weak charges  $Q_W^{(1,2)}$ . Since the weak charges of the proton are proportional to  $(1 - 4 \sin^2 \theta_W)$ , we find that a 1% error of e.g.  $Q_W^{(1)}$  implies an error of 0.05% for  $\sin^2 \theta_W$ . The theoretical prediction according to [43] is  $\sin^2 \theta_W = 0.23867(16)$ , corresponding to a relative error of 0.07%. We may therefore

state that our numerical investigation of PV spin echo signals does not introduce errors larger than the presently known SM error of the electroweak mixing angle. The nuclear-spin dependent weak charge  $Q_W^{(2)}$  merely has to be measured at the 5%-level to improve the current limits on total  $s$ -quark polarisation  $\Delta s + \Delta \bar{s}$ , see Table A.1 of Appendix A.1.

Of course, in an experiment one has to take into account the full signal  $\mathcal{F}_p$  instead of the theoretically derived PV part  $\mathcal{F}_p^{\text{PV}}$  to obtain the left-right asymmetry

$$\mathcal{F}_{p,LR} = \frac{\mathcal{F}_p - P(\mathcal{F}_p)}{\mathcal{F}_p + P(\mathcal{F}_p)}. \quad (5.33)$$

The PV spin echo signal is of the order of the PV Berry phase for which we achieved values up to  $10^{-10}$  so far. A PV-signal accuracy of 1-5% then demands an absolute experimental resolution of  $\approx 10^{-12} \lesssim \Delta \mathcal{F}_p \lesssim 5 \times 10^{-12}$ .

Excluding systematic experimental errors,  $\Delta \mathcal{F}_p$  tends to be the standard deviation  $\sigma_N$  of the Gaussian distribution

$$n(\mathcal{F}_p^{\text{exp}}) = \frac{1}{\sigma_N \sqrt{2\pi}} \exp \left[ -\frac{1}{2\sigma_N^2} (\mathcal{F}_p^{\text{exp}} - \langle \mathcal{F}_p^{\text{exp}} \rangle)^2 \right] \quad (5.34)$$

for  $N \rightarrow \infty$  according to the central-limit theorem. It states that the relative fluctuations, i.e., the ratio of absolute fluctuations to the mean value of the measured quantity, scale as  $1/\sqrt{N}$  for  $N \rightarrow \infty$ . Here, the mean value  $\langle \mathcal{F}_p^{\text{exp}} \rangle$  is the expectation value that we want to determine from experimental outcomes  $\mathcal{F}_p^{\text{exp}}$ . The width of the distribution is  $\sigma_N = \sigma/\sqrt{N}$ , with  $\sigma = 1/2$  being the standard deviation for a single spin measurement of a spin-1/2-particle. In fact, the measurement of  $\mathcal{F}_p$ , i.e., the projection of a two-level system consisting of the two states  $|9\rangle$  and  $|11\rangle$  onto an analysing state  $|p\rangle$ , can be regarded as the pseudo-spin measurement of a pseudo-spin-1/2-particle. We will discuss this more detailed in Section 5.6. For now, we arrive at the requirement

$$\Delta \mathcal{F}_p = \sigma_N = \frac{1}{2} \frac{1}{\sqrt{N}} \approx 10^{-12} \Rightarrow N \approx \frac{1}{4} 10^{24} \quad (5.35)$$

i.e., a minimum number of analysing projections of about  $10^{24}$ , only taking into account a statistical measurement error. Supposing  $10^{10}$  projections per second, see Section 4.1, we arrive at a measurement time of about  $10^6$  years for one point of the spin echo curve. Clearly, this is not feasible. The above consideration provides a lower bound of required measurement time given the according magnitudes of PV effects and the mentioned experimental limitations. Obvious improvements would be a more powerful source of metastable hydrogen states and further enhancement of the PV phases. Another line of attack from the theoretical side could be the employment of entangled initial states of many hydrogen atoms instead of interferometry with single atoms. We will outline corresponding considerations in the next section.

## 5.6 Atom Interferometry Below the Standard Quantum Limit

Taking into account the size of the hitherto found PV signals, we argued in Section 5.5 that the precision requirements for the measurement of PV signatures with IABSE experiments call for further improvements, ideally from both experimental and theoretical side.

A straightforward approach is the more systematic search of PV Abelian Berry phases in the six-dimensional parameter space of electric and magnetic fields. That could reveal larger Berry phases than those found so far. In this section we want to present another idea to improve the precision of atomic beam interferometry experiments. We will consider squeezed many-particle states as input states instead of single atoms and discuss ways of how to adopt these considerations to IABSE experiments.

The usage of squeezed states for interferometry is known as Heisenberg-limited interferometry which exploits that entangled states can provide the possibility to decrease the variance of one observable  $A$ , compared to the case of product states, at the expense of increasing the variance of observable  $B$  while still obeying Heisenberg's uncertainty relation

$$\Delta A \Delta B \geq \frac{1}{2} | \langle [A, B] \rangle | . \quad (5.36)$$

This uncertainty relation does not forbid zero uncertainty for single measurements even for non-commuting observables. Taking for example the Pauli operators  $\sigma_z$  and  $\sigma_x$ , (5.36) reduces to  $0 \geq 0$  for an eigenstate of  $\sigma_z$ . That is, when talking about improvements of measurement uncertainties of  $N$  particles by introducing entanglement between them, we have to be cautious which uncertainties to consider. We will address this issue in Section 5.6.2.

The so-called standard quantum limit of quantum measurement errors, being proportional to  $1/\sqrt{N}$  for uncorrelated quanta, can be relaxed up to an additional factor of  $1/\sqrt{N}$  in the limit of large  $N$  via appropriately entangled states of  $N$  quanta, i.e., squeezed states. Interferometric phase sensitivity depending on squeezed input states is for instance discussed in [177, 178]. For certain entangled states and certain observables a  $1/N$ -scaling of the measurement uncertainty can be reached. An according example is given in [71], where the initial state  $|\psi\rangle = \{|N/2, N/2\rangle + |N/2, -N/2\rangle\} / \sqrt{2}$  of  $N$  two-level systems is used to measure the energy difference between ground state and excited state in a Ramsey-type spectroscopy scheme. See [69, 70] for an investigation of quantum projection noise and precision enhancement in Ramsey spectroscopy via squeezed atomic states.

Squeezed light states, see, for instance, [179], were first prepared and observed in 1985 [180]. So far, the creation of entangled states of many massive particles has been achieved with trapped ions, see, e.g., [72, 181]. To date, the controlled entanglement of 14 ions is reported [182]. Squeezing of neutral atoms may be provided by entanglement in a Bose Einstein Condensate (BEC), cf. for instance [74, 75, 183]. If and how BECs can

## 5.6. Atom Interferometry Below the Standard Quantum Limit

---

be a source of appropriately squeezed many-particle states for precision enhancement of IABSE experiments is beyond the scope of the present thesis, but may be a fruitful route of investigation due to the extensive knowledge of manipulating BECs which has been accumulated over the past years. In view of our two-level system, the analysis of two-mode BECs may prove valuable, see, for example, [76]. However, in the following, we want to outline a principle approach of how to adopt  $N = 2$  squeezed atomic states to the IABSE scheme presented in Chapter 4. This might be the first step to connect to high-precision IABSE experiments utilising an entangled BEC.

Before turning to the concept of spin squeezing, we note the formal equivalence of a two-level system, such as the subsystem of hydrogen states  $|9\rangle$  and  $|11\rangle$ , and a spin-1/2-system. Thereby, we can put spin squeezing into context with IABSE experiments.

### Formal Equivalence of a Two-Level Systems and a Spin-1/2-System

The state of a two-level system in the Hilbert space spanned by  $\{|A\rangle, |B\rangle\}$  can be written as

$$|\psi\rangle = \sqrt{\frac{1 - \cos\theta}{2}} e^{i\beta} |A\rangle + \sqrt{\frac{1 + \cos\theta}{2}} e^{i(\beta-\phi)} |B\rangle =: c_A |A\rangle + c_B |B\rangle . \quad (5.37)$$

Considering the spatial wave function, the two-component spinor (5.37) depends on the spatial coordinates  $\mathbf{x}$  and time  $t$ . Therefore, the angles  $\theta$ ,  $\phi$ , and  $\beta$  also depend on  $\mathbf{x}$  and  $t$ . But at any fixed position at a distinct time the coefficients  $c_A$  and  $c_B$  are fixed complex numbers.

At time  $t = 0$  we choose our system to be in a normalised state with basis vectors

$$\begin{aligned} |A\rangle &= \frac{1}{\sqrt{2}} (|9\rangle_{t=0} - |11\rangle_{t=0}) , \\ |B\rangle &= \frac{1}{\sqrt{2}} (|9\rangle_{t=0} + |11\rangle_{t=0}) . \end{aligned} \quad (5.38)$$

Due to the decay the state will end up with norm less than 1, but we will address this issue later in Section 5.6.2. Having defined the basis (5.38) of the two-dimensional Hilbert space, we introduce operators which obey the commutation relations  $[r_i, r_j] = i\epsilon_{ijk} r_k$  of angular momentum operators:

$$r_1 = \frac{1}{2} (|A\rangle\langle B| + |B\rangle\langle A|) , \quad (5.39)$$

$$r_2 = \frac{i}{2} (|A\rangle\langle B| - |B\rangle\langle A|) , \quad (5.40)$$

$$r_3 = \frac{1}{2} (|A\rangle\langle A| - |B\rangle\langle B|) , \quad (5.41)$$

with expectation values

$$\begin{pmatrix} \langle r_1 \rangle \\ \langle r_2 \rangle \\ \langle r_3 \rangle \end{pmatrix} = \begin{pmatrix} \frac{1}{2} \sin\theta \cos\phi \\ \frac{1}{2} \sin\theta \sin\phi \\ \frac{1}{2} \cos\theta \end{pmatrix} . \quad (5.42)$$

This gives a visualisation of the mean state vector in terms of a three-dimensional vector of length  $\frac{1}{2}$  pointing in the direction according to the spherical coordinates  $\theta$  and  $\phi$ . The parameter space of  $\theta$  and  $\phi$  makes up the Bloch sphere.

### 5.6.1 Spin Squeezing

We now consider the case of two spin-1/2-particles. To define our states, we employ the basis  $\{|1, 1\rangle, |1, 0\rangle, |1, -1\rangle, |0, 0\rangle\}$  of triplet and singlet states of two spin-1/2-particles with the  $z$ -axis as quantisation axis. The according coefficients are denoted as  $c_{1,1}$ ,  $c_{1,-1}$ ,  $c_{1,0}$ , and  $c_{0,0}$ . The product state

$$\begin{aligned} |\psi\rangle &= |j = \frac{1}{2}, m_j = \frac{1}{2}\rangle \otimes |j = \frac{1}{2}, m_j = \frac{1}{2}\rangle \\ &= |J = 1, M_J = 1\rangle \end{aligned} \quad (5.43)$$

leads to

$$\Delta J_x = \Delta J_y = \frac{1}{\sqrt{2}} \quad (5.44)$$

for the fluctuations of total-spin measurements in  $x$ - and  $y$ -direction, see Figure 5.10. For  $N$  uncorrelated particles one obtains  $\Delta J_x = \Delta J_y = \sqrt{N}/2$ .

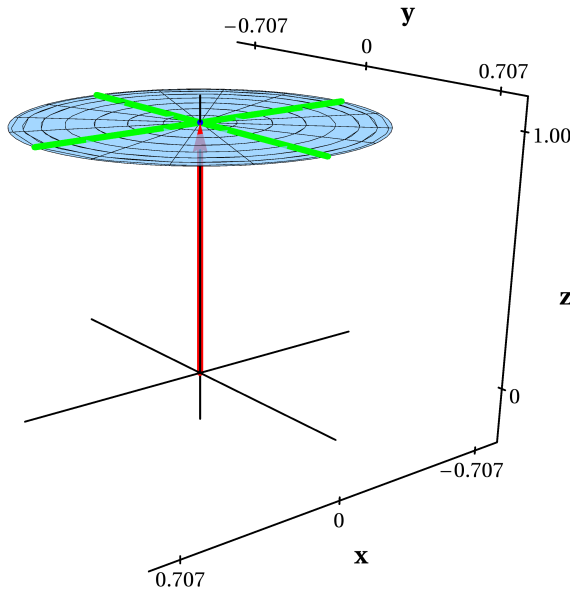


**Figure 5.10:** Illustration of the expectation value of the total spin  $\langle \mathbf{J} \rangle$  (red arrow) and its error ellipsoid representing the fluctuations. Here, the green lines correspond to  $\pm \Delta J_x$  and  $\pm \Delta J_y$ , respectively. We choose the coefficients  $c_{1,1} = 1$ ,  $c_{1,-1} = c_{1,0} = c_{0,0} = 0$ . The fluctuations  $1/\sqrt{2}$  in  $x$ - and  $y$ -direction as well as the components of  $\langle \mathbf{J} \rangle$  are marked on the axes.

Choosing entangled states, we obtain the possibility to decrease, e.g.,  $\Delta J_y$  at the cost of  $\Delta J_x$ , see Figure 5.11. The measurement error of the total spin in  $y$ -direction is decreased, compared to  $\Delta J_y = 1/\sqrt{2}$  in Figure 5.10. Note that the uncertainty ellipsoids in Figures 5.10 and 5.11 are merely a graphical representation of the fluctuations when measuring the respective spin components. Regarding for example Figure 5.10 it is of

## 5.6. Atom Interferometry Below the Standard Quantum Limit

course not possible to measure a total spin value  $|\langle \mathbf{J} \rangle| > 1$  although the uncertainty ellipse, which lies tangential to the Bloch sphere, might suggest so.

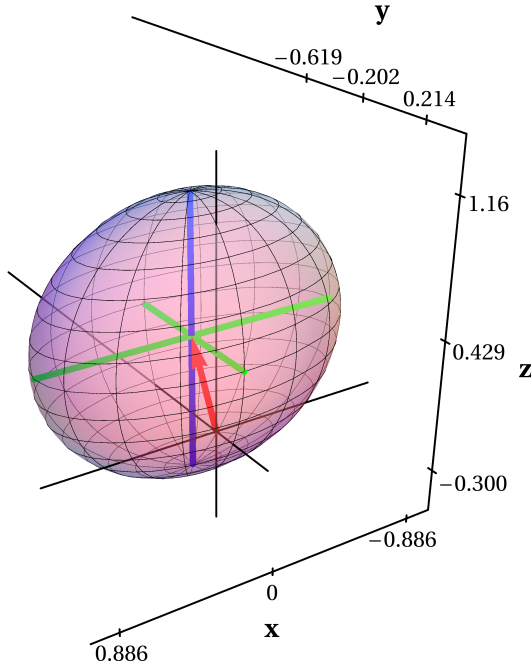


**Figure 5.11:** Illustration of the expectation value of the total spin  $\langle \mathbf{J} \rangle$  (red arrow) and its error ellipsoid representing the fluctuations, cf. Figure 5.10. Here, we choose the coefficients  $c_{1,1} = 2i/\sqrt{7}$ ,  $c_{1,-1} = i/\sqrt{7}$ ,  $c_{1,0} = c_{0,0} = 1/\sqrt{7}$ . Of course, the expectation value of the total spin and its direction are changed compared to the product state of Figure 5.10. But the variance in  $y$ -direction is decreased.

We emphasise that we do not want to squeeze states for their own sake but enlarge the precision of interferometry. In general, these are two different matters as we will see in the following section. There, our aim is to take advantage of spin-squeezed states regarding IABSE Experiments.

### 5.6.2 Applications for IABSE Experiments

Essentially, IABSE experiments measure the ratio of the numbers of initial and final states by counting atoms in the desired final state  $|p\rangle$ . A single atom accounts for the total integrated flux  $0 \leq \mathcal{F}_p \leq 1$  measuring the probability of finding the evolved state in the analysing state.  $N$  atoms yield the signal  $\mathcal{F}_{Np} = N \mathcal{F}_p$ . To be more precise, one obtains an experimental value<sup>7</sup>  $[\mathcal{F}_p]_N$  approaching the theoretical value  $\mathcal{F}_{Np}$ , i.e.,  $[\mathcal{F}_p]_N \rightarrow \mathcal{F}_{Np}$ , for  $N \rightarrow \infty$ , if systematic errors can be neglected. Analogously, measuring the spin  $S_z$  of a spin-1/2-system yields an expectation value  $-1/2 \leq \langle S_z \rangle \leq 1/2$ , or, equivalently,  $0 \leq \langle S_z \rangle + 1/2 \leq 1$ . The formal equivalence of a spin-1/2-system and a two level system such as  $\{|9\rangle, |11\rangle\}$  implies the correspondence  $\mathcal{F}_p \leftrightarrow \langle S_z \rangle + 1/2$ .

<sup>7</sup> $[\mathcal{F}_p]_N$  denotes the sum of  $N$  single-atom measurements of  $\mathcal{F}_p$ .

### Experimental Resolution

In Figure 5.12 we schematically show a spin echo signal  $[\mathcal{F}_p]_N(s)$ , depending on an effective parameter  $s$  which accounts for the variation of the external fields. It is immediately clear from Figure 5.12 that we may employ

$$\left| \frac{\partial \mathcal{F}_{Np}}{\partial s} \right| = \left| \frac{[\mathcal{F}_p]_N - \mathcal{F}_{Np}}{\Delta s_N} \right| \quad (5.45)$$

for an estimate of the 'frequency' uncertainty  $\Delta s_N$ .

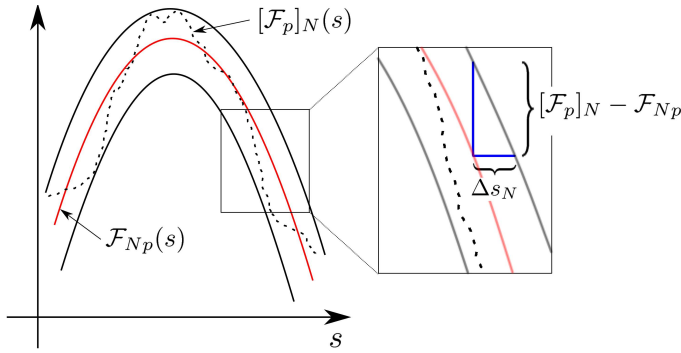


**Figure 5.12:** The envelope (black solid line) enclosing the fluctuations of the experimental data  $[\mathcal{F}_p]_N$  (black dashed line) around the theoretical prediction  $\mathcal{F}_{Np}$  (red solid line) yields an estimate for the experimental resolution  $\Delta s_N$  of  $s$ , directly related to the resolution of the interference pattern.

The experimental resolution of  $s$  for  $N$  independent measurements is then

$$|\Delta s_N| = \frac{|\Delta s_1|}{\sqrt{N}} = \sigma_N \left| \frac{\partial \mathcal{F}_{Np}}{\partial s} \right|^{-1} = \frac{1}{\sqrt{N}} \sigma \left| \frac{\partial \mathcal{F}_{Np}}{\partial s} \right|^{-1} \quad (5.46)$$

where  $\sigma = [\mathcal{F}_p]_1 - \mathcal{F}_p$  is the measurement error for a single atom. Phase shifts, for example due to Berry phases, show up in shifts and other modifications of the interference pattern  $\mathcal{F}_p$ . That makes a sufficiently small  $|\Delta s_N|$  vital for a successful experiment.

A single  $S_z$  measurement of one spin-1/2-system either yields  $+1/2$  or  $-1/2$ , but if the system is in the eigenstate with eigenvalue  $+1/2$ , the measurement yields  $+1/2$  with 100% certainty, i.e.,  $\sigma = 0$ . However, we are not interested in  $\sigma$  but in  $|\Delta s_1|$  which incorporates the slope of the  $\mathcal{F}_p$ -curve. In fact, in the just mentioned situation where  $\sigma = 0$  one finds  $|\partial \mathcal{F}_{Np}/\partial s| = 0$  and  $|\Delta s_1| = 1/2$ . Moreover, one can show that  $|\Delta s_1| \equiv 1/2$  for all final states, i.e., for all values of  $s$ . The goal is to obtain a higher signal-to-noise ratio by minimising (5.46).  $N$  atoms in a product state correspond to  $N$  independent measurements where (5.46) applies. Then, the quantum-mechanical measurement error scales like

$$\sigma_N \sim 1/\sqrt{N} . \quad (5.47)$$

In the following we discuss entangled states for which a  $1/N$ -scaling of  $\Delta s_N$  is in principle achievable regarding IABSE experiments.

## 5.6. Atom Interferometry Below the Standard Quantum Limit

---

Before considering the uncertainty minimisation, we present a procedure enabling the derivation of the appropriate initial state in the realm of our IABSE scheme, given an optimal<sup>8</sup> final state.

### Derivation of a Squeezed Initial State

Suppose, we have found an optimal final state  $|\psi_F(s_{\text{opt}})\rangle$  of a IABSE experiment for a given field configuration<sup>9</sup> via the minimisation of (5.46). This means that an entangled final state with appropriately small fluctuations  $\sigma_N$  is found at  $s_{\text{opt}}$ . Then, we have to infer the initial state that leads to the desired final state. This task can be carried out easily as follows.

We want to employ squeezing in spin space, which is the  $\{|9\rangle, |11\rangle\}$ -space in our case. For one atom we write its initial and final states as

$$|\psi_I(s)\rangle = c_9|9\rangle + c_{11}|11\rangle, \quad (5.48)$$

$$|\psi_F(s)\rangle = b_9|9\rangle + b_{11}|11\rangle, \quad (5.49)$$

respectively, with  $c_{9/11}$  and  $b_{9/11}$  being  $s$ -dependent. Then, the spin echo signal  $\mathcal{F}_p(s)$  is related to this two-dimensional representation such that  $\langle\psi_F(s)|\psi_I(s)\rangle = 1$  corresponds to maxima of  $\mathcal{F}_p(s)$ , whereas  $\langle\psi_F(s)|\psi_I(s)\rangle = 0$  corresponds to minima<sup>10</sup>. Thus, the values  $s$  of maximal slope coincide for  $\langle\psi_F(s)|\psi_I(s)\rangle$  and  $\mathcal{F}_p(s)$ . As a result, we may squeeze the fluctuations  $\sigma_N$  connected to the spin states while calculating  $|\partial\mathcal{F}_{Np}/\partial s|$  to minimise the overall uncertainty (5.46).

In the adiabatic limit the evolution of the two states  $|9\rangle$  and  $|11\rangle$  is decoupled. Therefore, the action of the IABSE experiment can effectively be written as

$$\begin{pmatrix} z_9 & 0 \\ 0 & z_{11} \end{pmatrix} \begin{pmatrix} c_9 \\ c_{11} \end{pmatrix} = \begin{pmatrix} b_9 \\ b_{11} \end{pmatrix} \Leftrightarrow \begin{pmatrix} c_9 \\ c_{11} \end{pmatrix} = \begin{pmatrix} 1/z_9 & 0 \\ 0 & 1/z_{11} \end{pmatrix} \begin{pmatrix} b_9 \\ b_{11} \end{pmatrix}. \quad (5.50)$$

For a given field configuration  $\text{FC}(s_{\text{opt}})$  the complex numbers  $z_9$  and  $z_{11}$  have to be calculated numerically without knowing anything about the initial state that we want to derive. This is simply done by considering an arbitrary initial state  $x|9\rangle + y|11\rangle$ , with  $x, y \neq 0$ , since

$$\begin{aligned} x|9\rangle + y|11\rangle &\xrightarrow{\text{FC}(s_{\text{opt}})} x'|9\rangle + y'|11\rangle \equiv z_9x|9\rangle + z_{11}y|11\rangle \\ &\Rightarrow z_9 = \frac{x'}{x}, \quad z_{11} = \frac{y'}{y}, \end{aligned} \quad (5.51)$$

---

<sup>8</sup>Optimal in the sense of (5.46) being minimal for that state.

<sup>9</sup>For a given field configuration  $\text{FC}(s)$  depending on  $s$  we assume the existence of a parameter value  $s_{\text{opt}}$  yielding minimal  $\Delta s_N$ .

<sup>10</sup>Due to the variation of  $s$  the final states circle the Bloch sphere. Of course, the full hydrogen wave packet within the  $n = 2$  shell decays, such that the global maximum  $\mathcal{F}_p(s_{\text{max}}) \neq 1$ , although  $\langle\psi_F(s_{\text{max}})|\psi_I(s)\rangle = 1$ . Moreover, the spatial separation of interfering wave packets at  $z_a$  leads to a decreased envelope amplitude for  $s \neq s_{\text{max}}$ . That is,  $\mathcal{F}_p$  does not reach zero even for  $\langle\psi_F(s)|\psi_I(s)\rangle = 0$ . See Figure 4.7 for the prime example illustrating those issues.

while we have numerical access to  $x'$  and  $y'$ . An arbitrary rescaling of the initial  $x$  and  $y$  yields the same rescaling of  $x'$  and  $y'$  such that  $z_9$  and  $z_{11}$  are unchanged for a fixed  $\text{FC}(s_{\text{opt}})$ . The same way the internal states |9) and |11), which are superimposed already for a single atom, evolve independently, we suppose the internal states  $|\alpha\rangle_i$ ,  $i = 1, \dots, N$ , of  $N$  entangled atoms to evolve independently in the adiabatic limit.

At this point the only missing ingredient is the minimisation of  $|\Delta s_N|$ . In the following, we will outline the necessary steps for the case  $N = 2$ . However, the concrete derivation and the extension to  $N > 2$  is left for future work.

### Uncertainty Minimisation

We want to find the global minimum of

$$|\Delta s_N| = \Delta J_z \left| \frac{\partial \mathcal{F}_{Np}}{\partial s} \right|^{-1}, \quad (5.52)$$

where  $\Delta J_z$  is the quantum mechanical measurement error of the total pseudo-spin in  $z$ -direction. Here, the  $z$ -direction can be defined by (5.41) or a similar observable. To minimise the uncertainty of a  $J_z$ -measurement for  $N = 2$  particles, we consider the most general analytical expression

$$\Delta J_z = \sqrt{w^2(x^2 + 3y^2 + z^2) - y^4 + y^2} \quad (5.53)$$

for the coefficients

$$\{c_{1,1}, c_{1,0}, c_{1,-1}, c_{0,0}\} = \{we^{i\varphi_w}, xe^{i\varphi_x}, ye^{i\varphi_y}, ze^{i\varphi_z}\}, \quad (5.54)$$

with real amplitudes and phases. These coefficients entirely determine that part of the total hydrogen state  $|\psi^{N=2}\rangle$  which lives in the pseudo-spin subspace of the total Hilbert space. The fluctuations (5.53) contribute four real parameters to the minimisation problem (5.52).

Furthermore, we need the derivative of  $\mathcal{F}_{Np}$  with respect to  $s$  or with respect to any parameter which is well accessible. For example, the variation of  $\mathcal{F}_{Np}$  could solely be due to a variation of the dynamic phase while the geometric phase is kept constant. Such a situation is considered in Section 5.4 for one atom, where  $\partial \mathcal{F}_p / \partial \phi_{\text{dyn}}$  could be calculated immediately, see (5.32). Of course, first we need  $\mathcal{F}_{Np}$  itself.

In analogy to Section 4.3, we can project a product state

$$|\Psi^{N=2}(\mathbf{x}, t)\rangle = |\Psi_1\rangle \otimes |\Psi_2\rangle \quad (5.55)$$

onto a two-atomic analysing state  $|P\rangle = |p_1\rangle \otimes |p_2\rangle$ , where  $|p_i\rangle = \sum_{\beta_i \in I} p_{\beta_i} |\beta_i(z_a)\rangle$ . Thereby, we obtain

$$\begin{aligned} |\Psi_P(\mathbf{x}, t)\rangle &= |P\rangle (\tilde{P} | \Psi^{N=2}(\mathbf{x}, t)\rangle) \\ &= |P\rangle (\tilde{p}_1 | \Psi_1(\mathbf{x}, t)\rangle) (\tilde{p}_2 | \Psi_2(\mathbf{x}, t)\rangle) \\ &= |P\rangle \Psi_{p_1}(\mathbf{x}, t) \Psi_{p_2}(\mathbf{x}, t) \\ &=: |P\rangle \Psi_P(\mathbf{x}, t). \end{aligned} \quad (5.56)$$

## 5.6. Atom Interferometry Below the Standard Quantum Limit

---

From the spatial wave function  $\Psi_P(\mathbf{x}, t)$  we can calculate the total integrated flux of the product state

$$\mathcal{F}_P = \int dt \int d^2x_T J_z(\mathbf{x}_T, z_a, t). \quad (5.57)$$

Here, the  $z$ -component of the probability current can be written in terms of single-particle currents:

$$\begin{aligned} J_z(\mathbf{x}_T, z, t) &= \frac{1}{2mi} \Psi_P^*(\mathbf{x}, t) \partial_z \Psi_P(\mathbf{x}, t) + \text{c.c.} \\ &= \frac{1}{2mi} \Psi_{p_1}^* \Psi_{p_2}^* [(\partial_z \Psi_{p_1}) \Psi_{p_2} + \Psi_{p_1} (\partial_z \Psi_{p_2})] + \text{c.c.} \\ &= \frac{1}{2mi} [\Psi_{p_2}^* (\Psi_{p_1}^* \partial_z \Psi_{p_1}) \Psi_{p_2} + \Psi_{p_1}^* (\Psi_{p_2}^* \partial_z \Psi_{p_2}) \Psi_{p_1}] + \text{c.c.} \\ &= |\Psi_{p_2}|^2 \left[ \frac{1}{2mi} (\Psi_{p_1}^* \partial_z \Psi_{p_1}) + \text{c.c.} \right] + |\Psi_{p_1}|^2 \left[ \frac{1}{2mi} (\Psi_{p_2}^* \partial_z \Psi_{p_2}) + \text{c.c.} \right] \\ &= |\Psi_{p_2}|^2 j_{z,1} + |\Psi_{p_1}|^2 j_{z,2}. \end{aligned} \quad (5.58)$$

With  $j_z(\mathbf{x}_T, z_a, t) = \frac{\bar{k}_m}{m} |\psi_p(\mathbf{x}_T, z_a, t)|^2$ , see Equation (97) of [32], we obtain

$$J_z(\mathbf{x}_T, z_a, t) = 2 \frac{\bar{k}_m}{m} |\psi_{p_1}(\mathbf{x}_T, z_a, t)|^2 |\psi_{p_2}(\mathbf{x}_T, z_a, t)|^2. \quad (5.59)$$

Inserting (5.59) into (5.57) and evaluating the integrals using the explicit functions (4.26) and (4.27), we would gain  $\mathcal{F}_{Np}$  for  $N = 2$  in the case of product states.

An analogous procedure has to be carried out for two entangled atoms in the state

$$\begin{aligned} |\Psi^{N=2}(\mathbf{x}, t)\rangle &= \sum_{i,j \in \{1,2\}} u_{ij} |\Psi_i \Psi_j\rangle \\ &= \sum_{i,j} u_{ij} |\Psi_i(\mathbf{x}, t)\rangle \otimes |\Psi_j(\mathbf{x}, t)\rangle. \end{aligned} \quad (5.60)$$

The projection of (5.60) onto

$$\begin{aligned} |P\rangle &= \sum_{i,j \in \{1,2\}} v_{ij} |p_i p_j\rangle \\ &= \sum_{i,j} v_{ij} |p_i\rangle \otimes |p_j\rangle, \end{aligned} \quad (5.61)$$

where  $|p_a\rangle = \sum_{\beta_a} p_{\beta_a} |\beta_a\rangle$ , yields

$$\begin{aligned} |\Psi_P(\mathbf{x}, t)\rangle &= |P\rangle (\tilde{P} | \Psi^{N=2}(\mathbf{x}, t)\rangle) \\ &= |P\rangle \sum_{i,j,k,l} v_{ij}^* u_{kl} \underbrace{(\tilde{p}_i \tilde{p}_j | \Psi_k \Psi_l\rangle)}_{=:(\tilde{p}_i | \Psi_k\rangle)(\tilde{p}_j | \Psi_l\rangle) =: \Psi_{ik} \Psi_{jl}} \\ &=: |P\rangle \Psi_P(\mathbf{x}, t). \end{aligned} \quad (5.62)$$

With (5.62) we have to calculate the probability current

$$\begin{aligned}
 J_z(\mathbf{x}_T, z, t) &= \frac{1}{2mi} \Psi_P^*(\mathbf{x}, t) \partial_z \Psi_P(\mathbf{x}, t) + \text{c.c.} \\
 &= \sum_{\substack{i,j,k,l, \\ q,r,s,t}} v_{ij} u_{kl}^* v_{qr}^* u_{st} \Psi_{ik}^* \Psi_{jl}^* [(\partial_z \Psi_{qr}) \Psi_{st} + (\partial_z \Psi_{st}) \Psi_{qr}] + \text{c.c.} \quad (5.63)
 \end{aligned}$$

explicitly and, using (4.26) and (4.27), integrate it according to

$$\mathcal{F}_P = \int dt \int d^2x_T J_z(\mathbf{x}_T, z_a, t) . \quad (5.64)$$

The pseudo-spin part of (5.60) is used to calculate the squeezed state according to (5.53). That is, we identify the amplitudes of the four coefficients  $u_{ij}$  with  $\{w, x, y, z\}$  of (5.53). The phases of the coefficients  $u_{ij}$  are not incorporated in (5.53) and are additional four free parameters to consider in the minimisation procedure. Furthermore, we have four effective complex coefficients  $v_{ij} p_{\beta_i} p_{\beta_j}$  from the analysing state. Hence, given a field configuration which determines the spatial wave functions including dynamic and geometric phases, (5.52) has to be minimised with respect to 14 real parameters<sup>11</sup>. At the end of this procedure we will have extracted an initially entangled state which enhances the experimental resolution by a factor close to  $\sqrt{N} = \sqrt{2}$ . For the extension to  $N > 2$  quantum field theoretical methods may be more useful to deal with the increasingly large Hilbert spaces. We leave this task for future work. As already mentioned before, the experimental implementation of controllable squeezing for states of many atoms is demanding at present. That may render the experimental realisation of the above scheme, which aims for significant improvements of the interferometric resolution, unlikely in the near future.

With these considerations we close our investigation of hydrogen in LABSE experiments and move over to Berry phases in helium which is presently used in the LABSE apparatus of M. DeKieviet and P. Augenstein.

---

<sup>11</sup>The normalisations of the sole ingredients  $|\Psi^{N=2}(\mathbf{x}, t)\rangle$  and  $|P\rangle$  reduce the number of 16 real parameters by two.

## 6 Berry Phases for Helium

The derivations for the geometric flux-density vector fields in Section 3.5 are not restricted to hydrogen but can be adopted for every system which is governed by a mass matrix of the form  $\underline{\mathcal{M}}(t) = \underline{\mathcal{M}}_0 - \underline{\mathbf{D}} \cdot \underline{\boldsymbol{\mathcal{E}}}(t) - \underline{\boldsymbol{\mu}} \cdot \underline{\boldsymbol{\mathcal{B}}}(t) + \delta \underline{\mathcal{M}}_{\text{PV}}$ . We therefore may use those derivations for helium. Since metastable  $^4\text{He}$  is currently used in the LABSE apparatus described in Section 4.1, the theoretical investigation of Berry phases for helium is worthwhile. Adapting the findings for hydrogen to the case of helium, a short term experimental verification of the predicted phenomena may be at hand.

An electronic structure of  $^4\text{He}$ , which has zero nuclear spin, similar to the  $n = 2$  states of hydrogen is provided by the  $n = 2$  states of helium. Instead of a nuclear-spin-1/2 the second electron accounts for the spin coupling of two spin-1/2 quanta, leading again to 16 states in the  $n = 2$  shell, see Table A.6 of Appendix A.3 for the according numbering scheme. As for hydrogen a PV part of the mass matrix is introduced via the couplings between 2S and 2P states. For the matrix representations of  $\underline{\mathcal{M}}_0 + \delta \underline{\mathcal{M}}_{\text{PV}}$ ,  $\underline{\mathbf{D}}$ , and  $\underline{\boldsymbol{\mu}}$  see Appendix A.3. They were calculated by Mariusz Puchalski from Adam Mickiewicz University, Poland, see Appendix A.3 for details.

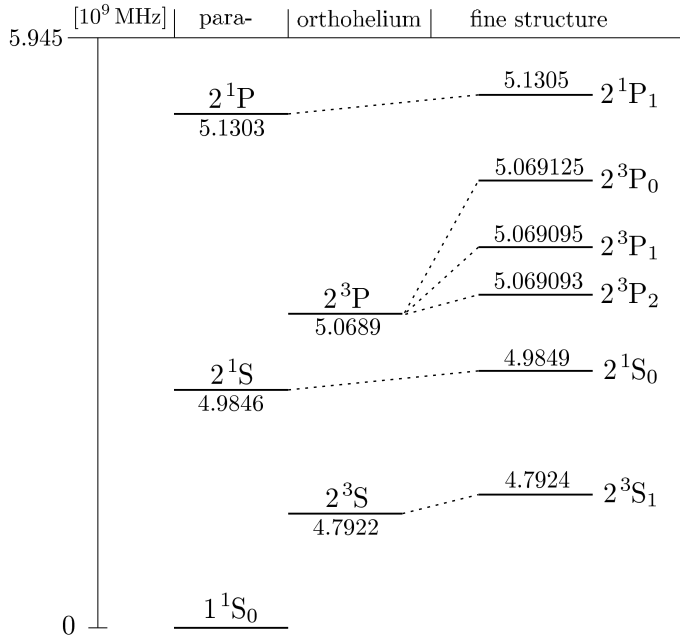
In order to obtain reliable results and find appropriate regions of parameter space for the calculation of Berry phases we numerically derive the Zeeman diagrams for the  $n = 2$  helium states as well as their decay rates in presence of an external electric field in Section 6.1. We want to emphasise that the results presented here should be considered as preliminary. Further cross-checks and verifications are needed.

In Section 6.2 we calculate PC Berry phases for metastable helium in magnetic field parameter space. These results can be immediately checked with the existing LABSE experiment.

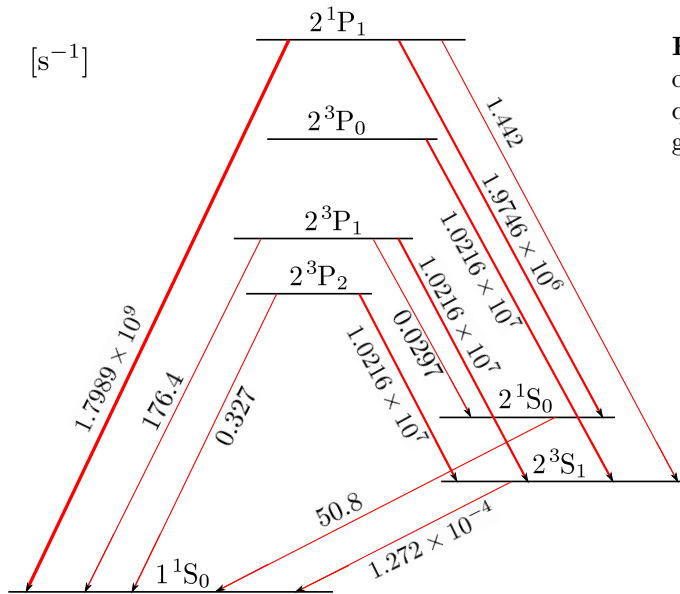
### 6.1 Energies and Decay Rates

Figure 6.1 shows the energy levels of the helium states with principal quantum number  $n = 2$  in vacuum. Para- and orthohelium denote the states with total electron Spin  $S = 0$  and  $S = 1$ , respectively. In Figure 6.2 we give the corresponding decay rates.

In Figures 6.3 and 6.4 we show the Zeeman diagrams for the triplet-2S states and the triplet-2P states, respectively.



**Figure 6.1:** Schematic illustration of the energy levels of the helium states for the principal quantum number  $n = 2$  in vacuum. The numerical values are given in units of  $10^9$  MHz, as cited in Table A.7 of Appendix A.3. The level notations are  $n^{2S+1}L_J$ , with principal quantum number  $n$ , total electron spin  $S$ , orbital angular momentum  $L$ , and total angular momentum  $J$ . The energy axis between the defined point of zero energy and the ionisation energy of  $5.945 \times 10^9$  MHz is not linearly scaled.



**Figure 6.2:** The vacuum decay rates of the helium states with principal quantum number  $n = 2$  in vacuum, given in  $s^{-1}$ .

## 6.1. Energies and Decay Rates

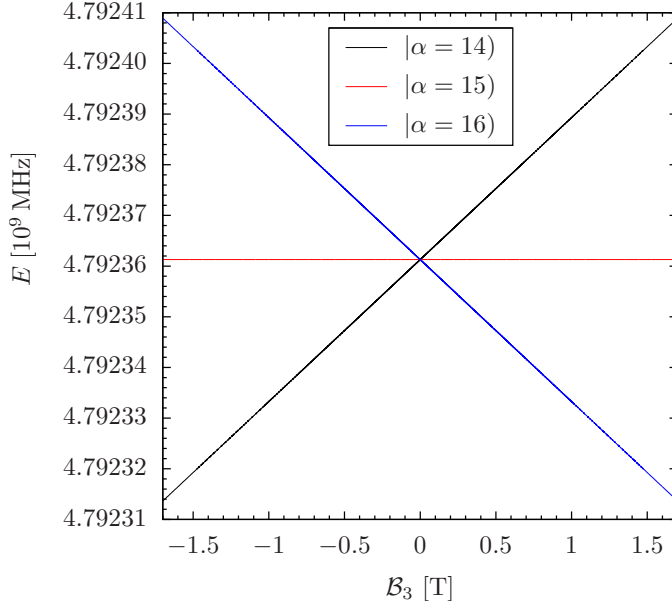


**Figure 6.3:** The Zeeman diagram for the triplet 2S states of helium for magnetic field strengths  $-1.7 \text{ T} \leq \mathcal{B}_3 \leq 1.7 \text{ T}$ . In that range the  $2^3\text{S}_1$  states do not have further crossings of the real energies with any other  $n = 2$  state.

The lifetime of the 2S state  $|2^3\text{S}_1, 1\rangle = |14\rangle$ , see Table A.6 of Appendix A.3, is shown in Figure 6.5. An electric field  $\mathcal{E} = \mathcal{E}_3 \mathbf{e}_3$  admixes 2P states to  $|14\rangle$  according to

$$\begin{aligned} |2^3\text{S}_1, 1, \mathcal{E}_3 \mathbf{e}_3, \mathbf{0}\rangle &:= |2^3\text{S}_1, 1\rangle' \\ &= a |2^3\text{S}_1, 1, \mathbf{0}, \mathbf{0}\rangle + b |2^3\text{P}_1, 1, \mathbf{0}, \mathbf{0}\rangle + c |2^3\text{P}_2, 1, \mathbf{0}, \mathbf{0}\rangle. \end{aligned} \quad (6.1)$$

However, the full decay rates of the 2P states also involves the fast decay into the  $|2^3\text{S}_1, 1\rangle$  state itself. The state  $|2^3\text{S}_1, 1\rangle'$  can decay only into states of lower energy, i.e., only into the  $n = 1$  ground state. We suppose the same consideration to hold for the small 2P-admixtures in  $|2^3\text{S}_1, 1\rangle'$ . As a first approach we therefore do not account for the full decay rates of the 2P states when calculating the decay rate of (6.1). We rather omit the decays of the 2P states into the  $|2^3\text{S}_1, 1\rangle$  state leading to an approximate decay rate

$$\Gamma_{2^3\text{S}'_1} = p_a |a|^2 \Gamma_{2^3\text{S}_1 \rightarrow 1^1\text{S}_0} + p_b |b|^2 \Gamma_{2^3\text{P}_1 \rightarrow 1^1\text{S}_0} + p_c |c|^2 \Gamma_{2^3\text{P}_2 \rightarrow 1^1\text{S}_0} \quad (6.2)$$

for state  $|14\rangle$  in an electric field  $\mathcal{E} = \mathcal{E}_3 \mathbf{e}_3$ . Here, the expression

$$p_a = (E_{3\text{S}'_1} - E_{1^1\text{S}_0})^3 / (E_{3\text{S}_1} - E_{1^1\text{S}_0})^3, \quad (6.3)$$

and analogously  $p_{b,c}$  for the  $^3\text{P}_{1,2}$ -terms, compensate for the phase space factors which are altered in the presence of external fields. The decay rates  $\Gamma_{A \rightarrow B}$  are those for the transition from level  $A$  to level  $B$  in vacuum. The red line in Figure 6.5 is the numerically evaluated lifetime of  $|14\rangle$ , i.e., the inverse of (6.2), as a function of electric field magnitude. The rate suggests substantially large lifetimes of  $|14\rangle$  even at very high electric field strengths.

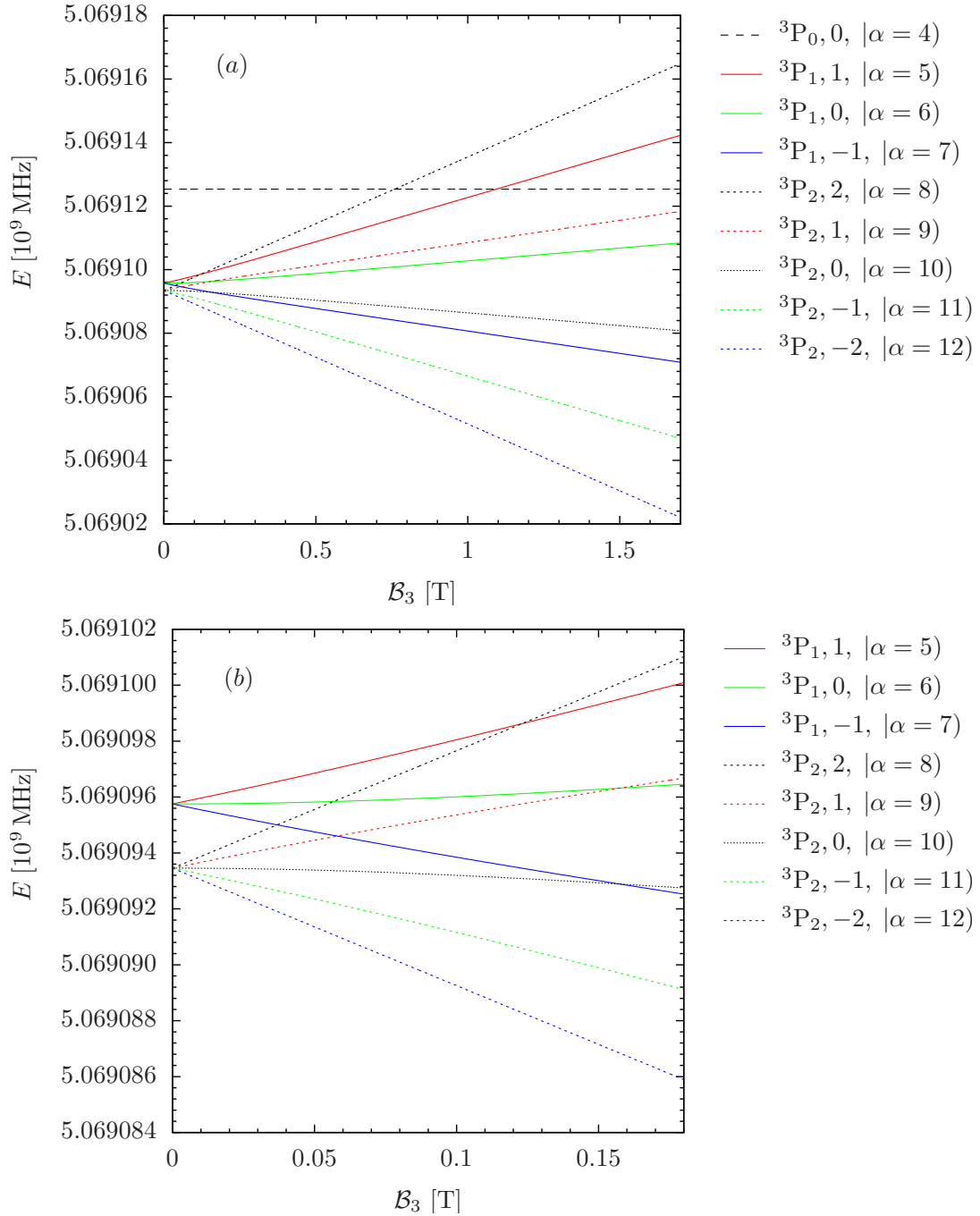


**Figure 6.4:** The Zeeman diagram for the triplet 2P states of helium in two different ranges of magnetic field strength  $B_3$ . Comparing Figure 6.4 (a) with Figure 1 (a) from [184], we find qualitative agreement. Figure (b) shows the low crossings in the real parts of the complex energies in more detail.

From an experimental point of view, the possibility to apply electric fields up to 100kV/cm without decreasing the lifetime more than by a factor of two could be promising when searching for large Berry Phases. Especially, the modification of lifetimes as discussed for hydrogen in Section 3.7 could benefit from strong electric fields. However, we have to point out that the large lifetimes of the triplet 2S states of helium can be difficult to measure when dealing with observation times of the order of milliseconds like for the atomic spin echo experiments described in Section 4. The measurement of decay rate differences is expected to be demanding as well [77]. One possibility to circumvent these difficulties could be the application of Lasers exciting transitions  $2^3S \rightarrow 2P$ , thereby manipulating the effective decay rate  $\Gamma_{2^3S'}$  [173]. That way, or with other means to get rid of the  $2^3S'$  states<sup>1</sup>, the decay rates could essentially be tuned at will. However, these considerations are beyond the scope of the present thesis and are left as a future project. For now, we proceed with the investigation of real PC Berry phases for helium.

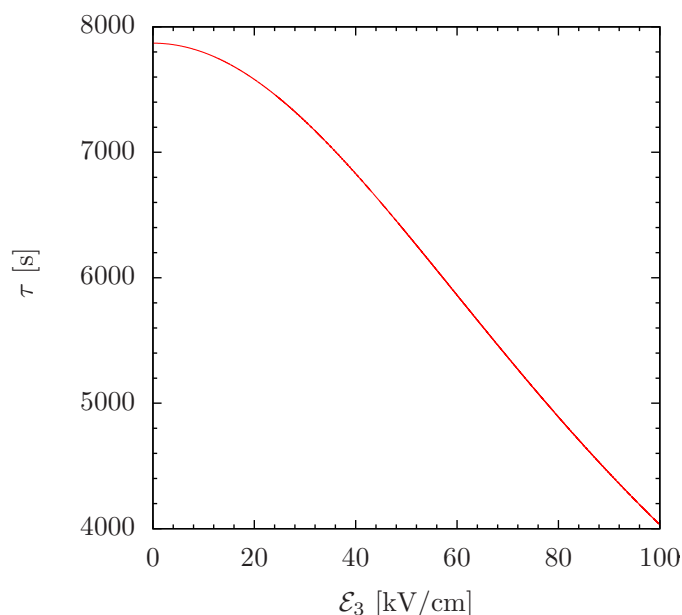


**Figure 6.5:** The lifetime of the helium state |14) according to (6.2) in an electric field  $\mathcal{E} = \mathcal{E}_3 \mathbf{e}_3$ .

## 6.2 Parity-Conserving Berry Phases

As for hydrogen we start our investigation with Berry phases in  $\mathcal{B}$ -space. Extending the QABSE software with the helium mass matrix, we are able to calculate Berry phases and flux-density vector fields in magnetic field space, where possible errors in the decay rates do not influence the results<sup>2</sup>.

<sup>1</sup>For example, by ionisation [173].

<sup>2</sup>Of course, the decay rates do matter when calculating spin echo signals.

### Berry Phases for the Magnetic Field Parameter Space

According to (2.89) for a Spin- $J$  particle in a magnetic field, we expect to find the Berry phase  $\gamma_\alpha(\mathcal{C}) = -J_{\alpha,3}\Omega(\mathcal{C})$  for a path  $\mathcal{C}$  and the vector field structure  $\hat{\mathbf{J}}_\alpha^{(L)\text{PC}}(\mathbf{B}) = -J_{\alpha,3}\mathbf{B}/|\mathbf{B}|^3$ . In  $\mathbf{B}$ -space with vanishing electric field we already derived the structure of geometric flux densities for hydrogen in Section 3.6.1. The path

$$\begin{aligned} \mathcal{C}: z \rightarrow \mathbf{L}(z) &= \mathbf{B}/B_0, \quad 0 \leq z \leq 1, \\ \mathcal{B}_1(z) &= -6.614378277661477 \sin(2\pi z) \text{ mT}, \\ \mathcal{B}_2(z) &= 6.614378277661477 \cos(2\pi z) \text{ mT}, \\ \mathcal{B}_3(z) &= 7.5 \text{ mT} \end{aligned} \quad (6.4)$$

encircles a solid angle of  $\pi/2$  with an accuracy of  $10^{-14}$ . A representative part of the P-conserving flux-density vector field  $\hat{\mathbf{J}}_{14}^{(L)\text{PC}}(\mathbf{B})$  is shown in Figure 6.6, indicating the expected monopole structure. Indeed, we obtain  $\hat{\mathbf{J}}_{14}^{(L)\text{PC}}(\mathbf{B}) = -\mathbf{B}/|\mathbf{B}|^3$  with an accuracy of  $10^{-11}$ , comparable with the accuracy found for hydrogen, see (3.119). Our numerical result for (6.4) is  $\gamma_{14}(\mathcal{C}) = -1.570796326789$ , corresponding to  $-1.570796326795(6) \approx -\pi/2 \pm 10^{-11}$ , adopting the accuracy estimate of  $10^{-11}$ . This result can be checked immediately with the IABSE apparatus built in the group of M. DeKieviet.

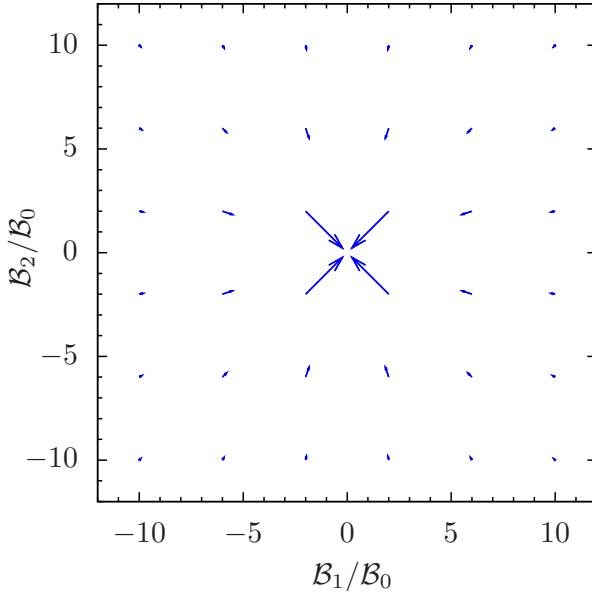


**Figure 6.6:** Visualisation of the real part of the P-conserving flux-density vector field  $\hat{\mathbf{J}}_{14}^{(L)\text{PC}}(\mathbf{B})$  at  $\mathcal{B}_3 = 0$  for the state  $|\alpha = 14\rangle$  of helium. The scaling factor is chosen as  $\eta_9 = 20$ .  $\hat{\mathbf{J}}_{14}^{(L)\text{PC}}(\mathbf{B})$  consistently leads to a negative Berry phase for the path (6.4) which encircles a surface oriented in positive  $z$ -direction.

The next tasks on the theoretical side are the correct implementation of the helium decay rates and the numerical routines for calculating spin echo signals. Finally, P-violating Berry phases for helium ought to be investigated. The according PV part of the mass matrix is given in Table A.8 of Appendix A.3.

## 7 Conclusions and Future Prospects

In this work we investigated parity-violating (PV) and parity-conserving (PC) Berry phases emerging for metastable states of hydrogen and helium in electromagnetic fields. The final goal was to identify PV Berry phases with enhanced magnitudes, possibly large enough to be detectable with a high-precision atomic beam spin echo experiment. We analysed the general structure of Berry phases and developed the theoretical formalism describing realistic spin echo signals. We applied our findings to hydrogen and helium, taking into account realistic experimental parameters in accordance with the Heidelberg spin echo experiment. In the course of that, we explored the parameter space of electromagnetic fields to obtain large PV effects as well as non-trivial PC phenomena. Eventually, we derived PV spin echo signals for specific electromagnetic field configurations, i.e., paths of the system's evolution in the parameter space. In view of an experimental determination of these PV effects, we discussed their impact on the electroweak mixing angle and on the proton's weak charges.

The P-violating mass matrix of hydrogen, incorporating the electroweak PV Hamiltonian and the dipole couplings to the external fields  $\mathcal{E}$  and  $\mathcal{B}$ , formed the basis of our analysis. The decay of the  $n = 2$  hydrogen states was included by means of the Wigner-Weisskopf approximation. We reviewed the conditions for adiabatic evolution of the metastable 2S states of hydrogen exposed to electromagnetic fields. These conditions, conveniently adaptable for all concrete situations which are addressed in this thesis, were provided in terms of relations for the electric field magnitudes, the rates of change of the external fields, and the energy separations between the 2S states. In view of the adiabaticity conditions, we numerically investigated the eigenenergies of the hydrogen mass matrix and found no complex degeneracies except at  $\mathcal{B} = \mathbf{0}$ . That is, excluding the origin of magnetic field space, the whole parameter space of electromagnetic fields is available for adiabatic cyclic paths yielding Berry phases.

To better understand the origin and the structure of Berry phases in atomic systems, we investigated the corresponding flux-density vector fields. More generally, we derived representations of these vector fields which hold for any system having metastable states and being governed by an effective Schrödinger equation with a mass matrix that depends on an arbitrary number of parameters. Making use of resolvent methods, we gained vector field representations in terms of complex integrals having a structural simplicity which is valuable for both analytical and numerical investigations. In particular, we obtained analytical expressions for the derivatives of the flux-density vector fields. We numerically implemented both the vector fields and their derivatives. The latter permit the analysis of the curl of the vector fields in case of three-dimensional parameter spaces as well as the divergence of the flux densities. Both are useful to

## Chapter 7. Conclusions and Future Prospects

---

clarify the vector field structures and provided further consistency checks of our numerical data. Specialising to hydrogen, we derived the behaviour of the flux-density vector fields under proper rotations  $R$  and improper rotations, represented by the parity transformation  $P$ . Thereby, we could establish expansions of the vector fields in terms of functions which are invariant under  $R$  and  $P$ . Apart from those invariant functions, the dependence on the external fields is explicitly revealed. With the vector field expansions we obtained a tool to test the numerically calculated structures of flux-density vector fields for specific parameter spaces. Analogous derivations can also be performed for atomic species other than hydrogen.

To illustrate our findings, we gave several examples of flux densities for metastable  $n = 2$  hydrogen states in three-dimensional parameter spaces. For a pure magnetic field we could derive the vector field structure analytically and found it to be that of a Dirac monopole, consistent with the known result for spin-1-particles in a magnetic field. Consequently, the Berry phases for any closed curve  $\mathcal{C}$  come out to be  $P$ -conserving and proportional to the solid angle spanned by  $\mathcal{C}$ . The degeneracy at  $\mathbf{B} = \mathbf{0}$  can be interpreted as the source of the vector field. However, degeneracies cannot be regarded as the only source of Berry phases. For example, in the electric field parameter space together with a constant magnetic field, we found no degeneracy but both  $PC$  and  $PV$  flux densities. In particular, we presented a  $PC$  vector field which exhibits a high sensitivity to the electric dipole operator. For atomic species other than hydrogen with less accurately known dipole operators, similar findings could prove valuable for cross-checking calculated representations of the dipole operators by measuring suitable Berry phases. For the parameter space of  $\mathcal{E}_1, \mathcal{E}_3, \mathcal{B}_3$ , together with a constant  $\mathcal{B}_2$ -field, we presented  $PC$  and  $PV$  flux densities, including both real and imaginary parts, and analysed their structure. For all considered parameter spaces we found our numerical results for the flux densities consistent with the analytical expressions of the vector field expansions. We observed relative discrepancies of the order of  $10^{-10}$  at most.

Based on the investigation of a variety of flux-density vector fields it became possible to preselect parameter spaces and parameter space regions which provide for tailored properties of Berry phases. For instance, there are parameter spaces which solely allow for  $PC$  Berry phases or  $PV$  Berry phases, respectively. After presenting a  $PC$  geometric phase with both real and imaginary parts, we focus on an intriguing phenomenon related to imaginary Berry phases. With these, the decay rates of atomic states can be modified through geometry, going beyond the usual modification via the magnitudes of electric fields. We demonstrate such a geometry-dependent effect by calculating the effective decay rate  $\Gamma_{\text{eff}}(\mathcal{C})$  of a  $2S$  hydrogen state for a closed path  $\mathcal{C}$  in the parameter space of  $\mathcal{E}_1, \mathcal{E}_3, \mathcal{B}_3$ , together with a constant  $\mathcal{B}_2$ -field. Reversing the cycling direction of the path, the magnitudes of the electromagnetic fields evolve the same way, whereas the Berry phase flips sign. This results in an effective decay rate  $\Gamma_{\text{eff}}(\bar{\mathcal{C}})$  for the reversed path  $\bar{\mathcal{C}}$ , differing from  $\Gamma_{\text{eff}}(\mathcal{C})$  by 1.9%. Such a modification of atomic lifetimes has not been observed experimentally to date. The present limit for the precision in phase measurements is expected to be  $10^{-5}$  rad [77]. Hence, the here mentioned  $PC$  effects

---

should be well within experimental reach. A more systematic search for imaginary parts of Berry phases may reveal even larger effects. We eventually provide a concrete field configuration leading to a PV Berry phase that consists of real and imaginary parts of both nuclear-spin dependent and nuclear-spin independent PV phases. The PV effects can be enlarged by multiple cyclings of the field configuration. The number of cyclings is, however, limited by the adiabaticity conditions. All the above mentioned types of Berry phases should, in principle, also be found for other atomic species.

We implemented the mass matrix of the  $n = 2$  states of  $^4\text{He}$  in our numerical software QABSE. Regarding a triplet 2S state of helium, we found the PC Berry phases in magnetic field space to be proportional to the solid angle spanned by a curve  $\mathcal{C}$ , in accordance with the known results of spin-1-particles in a magnetic field. The numerical implementation of spin echo signals for  $n = 2$  helium states is, in principle, a straightforward task. Then, a theoretical prediction of interference patterns in the case of pure magnetic fields is at hand. Furthermore, we hope that an experimentally feasible observation with the Heidelberg experiment could be the modification of decay rates due to imaginary parts of P-conserving Berry phases. To obtain reliable results for those Berry phases we have to implement the proper decay rates of the  $n = 2$  helium states. This is, of course, also necessary for reliable results of spin echo signals when electric fields are employed. Another goal is the computation of PV phases for helium. The required PV part of the mass matrix is available. The calculated mixings between 2S and 2P states due to  $H_{\text{PV}}$  turn out to be about twelve orders of magnitude smaller than the mixings in hydrogen. This suggests that helium is, generically, not a very suitable candidate for observing PV effects, although the applicability of large electric fields may prove beneficial for finding large PV Berry phases.

Regarding the simple electronic structure of hydrogen, hydrogen-like ions may as well be considered for determining PV effects with high accuracy. The ions can be trapped in storage rings and exposed to external fields. Then, multiple cyclings of the ion through an electromagnetic field configuration can be naturally achieved. Employing the scalings in Table 3 for, e.g., hydrogen-like  $^3\text{He}^+$  with nuclear spin-1/2 and one electron, the decay rates of metastable  $^3\text{He}^+$  are found to be larger than those of the hydrogen 2S states, which is a disadvantage for experiments. The PV mixing is, on the one hand, generically decreased due to the increased Lamb shift. On the other hand, the interaction between electron and the larger nucleus may eventually provide enhanced PV effects for feasible parameter regimes nonetheless. A quantitative analysis of these effects for  $^3\text{He}^+$  and other hydrogen-like ions could in principle be performed with the tools developed in this thesis.

We introduced the theoretical description of the Heidelberg longitudinal atomic beam spin echo (LABSE) experiment. Incorporating the experimental parameters, we obtained a realistic model of the interferometer for that part which is essential regarding the prediction of spin echo signals. We accomplished that by solving the effective Schrödinger equation in the adiabatic limit and employing a controllable expansion of the atomic wave function. The atoms propagate longitudinally through the external

## Chapter 7. Conclusions and Future Prospects

---

fields and accumulate dynamic as well as geometric phases. Being in a superposition of internal states, the atoms can interfere with themselves by external-field-induced spatial separation and recombination of the internal states. We calculated the interference signal in terms of the total integrated flux  $\mathcal{F}$  of one atom at the end of the interferometer. This observable is easily accessible in the experiment and includes the phase informations we are interested in. For the case of a spin echo field configuration the interference pattern is a spin echo signal. The interference signal is built up by modulating the field configuration and extracting  $\mathcal{F}$  for each setting of the field configuration.

In order to explicitly get numerical as well as analytical access to the small PV signatures which are hidden in the total spin echo signal, we provided for a perturbative expansion of  $\mathcal{F}$  in the PV parameters. This allowed us to cross-check numerically calculated interference patterns. In particular, we derived P-violating spin echo signals for a concrete chiral field configuration and its mirror-reflected version under realistic conditions while respecting the adiabaticity conditions. Adding both signals, this specific PV signature manifests itself on top of the PC signal as an oscillatory contribution which is damped as a function of the external field modulation. We found excellent agreement between the numerical data and the perturbative expansion. The amplitude of the PV part of the interference pattern is of the order of magnitude of the PV Berry phases whereas the total interference signal varies between zero and one. We obtained nuclear-spin dependent Berry phases of the order of  $10^{-10}$  for 1000 cyclings of the employed field configuration while still fulfilling the adiabaticity conditions. Reviewing the uncertainties for our calculations, we estimated that the total error of the predicted PV signals, being proportional to proton's weak charges, does not exceed the 1%-level. A determination of the nuclear-spin independent weak charge  $Q_W^{(1)} = 1 - 4 \sin^2 \theta_W$  with an error of 1% implies an error of 0.05% for  $\sin^2 \theta_W$ . The present Standard Model prediction for the electroweak mixing angle is  $\sin^2 \theta_W = 0.23867(16)$  with an uncertainty of 0.07%. Thus, our calculations do not impose additional errors to the weak charges larger than currently known theoretical errors. Moreover, an experimental determination of the nuclear-spin dependent weak charge  $Q_W^{(2)}$  with a 5% uncertainty would already improve the knowledge about the total  $s$ -quark polarisation  $\Delta s + \Delta \bar{s}$  of the proton. We also report a lower bound of about  $10^{24}$  single-atom measurements in the IABSE scheme required for a 1%-determination of  $Q_W^{(2)}$ , taking into account only statistical uncertainties and the magnitude of the so far derived PV signals.

In view of the small PV effects, further enhancement effects shall be needed for a feasible determination, given the current experimental constraints. Compared to the PV Berry phases discussed in [68] the investigation in the present thesis already revealed PV phases five orders of magnitude larger. A more systematic analysis of the full six-dimensional parameter space could yield even larger PV Berry phases.

Another route of investigation is offered by non-Abelian and non-adiabatic geometric phases, respectively. For the former, degeneracies encountered on a cyclic adiabatic path could reveal larger PV effects. In the present thesis we focused on Abelian Berry

---

phases, i.e., Berry phases emerging for adiabatic processes and non-degeneracy for the whole evolution. For non-adiabatic evolution the geometric phases are generically non-Abelian. Instead of diagonal matrices  $(U_{\alpha\beta}) \propto \delta_{\alpha\beta}$  in the effective Schrödinger equation  $i\partial_t\psi_\alpha = \sum_\beta U_{\alpha\beta}\psi_\beta$  non-diagonal matrices  $U$ , which in general do not commute, determine the evolution. Such couplings within Hilbert subspaces, that are decoupled in the case of Abelian phases, may also lead to interesting observable effects, possibly also in the realm of atomic parity violation. The foundations for non-Abelian Berry phases regarding metastable atomic states are laid in [67]. Furthermore, a non-adiabatic evolution of the atomic states may allow for advantageous field configurations which are not required to fulfil the adiabaticity conditions spelled out in this thesis.

We also outlined an idea of how to improve the interferometric resolution for the measurement of spin echo signals using squeezed many-particle states instead of single atoms. We transferred the concept of spin-squeezing to our situation of the atomic two-level systems used in the LABSE scheme employed in this thesis. For the case of two entangled atoms we formulated the necessary procedures to infer a suitable initial two-atom state. Although experimental difficulties can be expected, this approach offers a possibility for enhancing the measurement resolution of atom interferometry experiments up to a factor of  $\sqrt{N}$ , where  $N$  is the number of entangled atoms.



# A Notations and Definitions

In this appendix we collect the numerical values for the quantities entering our calculations for the hydrogen states with principal quantum number  $n = 2$ . We specify our numbering scheme for these states. The expressions for the mass matrix at zero external fields and for the electric and the magnetic dipole operators are given in Appendix A.2. The appendices A.1 and A.2 are adopted from [40].

Physical constants used throughout the present thesis are given in Table 1. If not indicated otherwise we use natural units which, in elementary particle physics, are commonly defined by  $\hbar = c = 1$ . We also set  $\epsilon_0 = 1$ . For the unit of energy we choose electron volt. In Table 2 we give useful conversion relations between physical quantities in natural units, based on the unit of energy, and SI units (S.I.). Here, we write  $[X]_S$  for the units of a physical quantity  $X$  in the unit system  $S$ .

All integrals in this thesis run from  $-\infty$  to  $+\infty$  if not explicitly noted otherwise.

physical constant	symbol	numerical value (in SI units)
speed of light	$c$	299792458 m/s
reduced Planck constant	$\hbar$	$1.054571726(47) \times 10^{-34}$ Js
electron charge	$e$	$1.602176565(35) \times 10^{-19}$ C
electron mass	$m_e$	$0.510998928(11)$ MeV/ $c^2$
vacuum permittivity	$\epsilon_0$	$8.854187817 \times 10^{-12}$ F/m
fine structure constant	$\alpha$	$1/137.035999074(44)$
Bohr radius	$r_B$	$0.52917721092(17) \times 10^{-10}$ m
Bohr magneton	$\mu_B$	$5.7883818066(38) \times 10^{-11}$ MeV/T
Rydberg constant	$R_\infty$	$13.60569253(30)$ eV/ $(\hbar c)$
Fermi's constant	$G$	$1.1663787(6) \times 10^{-5}$ GeV $^{-2}(\hbar c)^3$

**Table 1:** Frequently used physical constants, taken from [12]. The value of the fine structure constant is given for zero momentum transfer, that of the Bohr radius for infinite nucleus mass.

quantity	relation	in natural units	in SI units
energy $E$		1 eV	$1.602176565 \times 10^{-19}$ J
mass $m$	$[m] = [E]/c^2$	1 eV = 1 eV/ $c^2$	$1.782661845 \times 10^{-36}$ kg
time $t$	$[\hbar]_{\text{S.I.}} = \text{Js}$ $\Rightarrow [t] = [\hbar]/[E]$	$1 \text{ eV}^{-1} = \hbar \cdot 1 \text{ eV}^{-1}$	$6.582119281 \times 10^{-16}$ s
length $x$	$[c]_{\text{S.I.}} = \text{m/s} = \text{Jm}/[\hbar]_{\text{S.I.}}$ $\Rightarrow [x] = [\hbar] \cdot [c]/[E]$	$1 \text{ eV}^{-1} = \hbar c \cdot 1 \text{ eV}^{-1}$	$1.973269718 \times 10^{-7}$ m

**Table 2:** Conversions of basic physical quantities between natural and SI units. When noting energies in Hz, we adhere to the relation  $E = h\nu = \hbar \cdot 2\pi\nu$  between energy and frequency. For example, the hydrogen Lamb shift reads  $L/h = 1057.844$  MHz and  $L = 2\pi\hbar \cdot 1.057844 \times 10^9 \text{ s}^{-1} \hat{=} 2\pi \cdot 1.057844 \times 10^9 \cdot 6.582119281 \times 10^{-16} \text{ eV} = 4.3748911 \mu\text{eV}$ , respectively.

## A.1 Values for Quantities Related to $n = 2$ Hydrogen

### Notations and Numerical Values Related to the Mass Matrix

In Table A.1 we present parameter values for  ${}^1_1\text{H}$ , where the nuclear spin is  $I = 1/2$ , the numerical values for the weak charges  $Q_W^{(i)}$ ,  $i = 1, 2$ , the quantities  $\Delta q + \Delta\bar{q}$ , the Lamb shift  $L = E(2S_{1/2}) - E(2P_{1/2})$ , the fine structure splitting  $\Delta = E(2P_{3/2}) - E(2P_{1/2})$ , and the ground state hyperfine splitting energy  $\mathcal{A} = E(1S_{1/2}, F = 1) - E(1S_{1/2}, F = 0)$  for hydrogen. We define the weak charges as in Section 2 of [68] which gives for the proton in the SM:

$$Q_W^{(1)} = 1 - 4 \sin^2 \theta_W , \quad (\text{A.1})$$

$$Q_W^{(2)} = -2(1 - 4 \sin^2 \theta_W)(\Delta u + \Delta\bar{u} - \Delta d - \Delta\bar{d} - \Delta s - \Delta\bar{s}) . \quad (\text{A.2})$$

Here  $\theta_W$  is the weak mixing angle and  $\Delta q + \Delta\bar{q}$  denotes the total polarisation of the proton carried by the quarks and antiquarks of species  $q$  ( $q = u, d, s$ ). Note that in [68] and [80] the then usual notation of  $\Delta q$  was used for what is now denoted as  $\Delta q + \Delta\bar{q}$ . The quantity  $\Delta u + \Delta\bar{u} - \Delta d - \Delta\bar{d}$  is related to the ratio axial and vector couplings  $g_A/g_V$  from neutron  $\beta$  decay  $\Delta u + \Delta\bar{u} - \Delta d - \Delta\bar{d} = -g_A/g_V$ , cf. [12, 80]. The total polarisation of the proton carried by strange quarks,  $\Delta s + \Delta\bar{s}$ , is still only poorly known experimentally. One finds values of  $-0.12$  to very small and positive ones quoted in recent papers; see for instance [55–59]. Therefore, we assume for our purposes

$$-0.12 \leq \Delta s + \Delta\bar{s} \leq 0 . \quad (\text{A.3})$$

Of course, the dependence of  $Q_W^{(2)}$  on  $\Delta s + \Delta\bar{s}$  is, in principle, very interesting, since this quantity can be determined in atomic P violation experiments with hydrogen.

### A.1. Values for Quantities Related to $n = 2$ Hydrogen

	${}^1_1\text{H}$	Ref.
$L/h$	1057.8440(24) MHz	[185]
$\Delta/h$	10969.0416(48) MHz	[185]
$\mathcal{A}/h$	1420.405751768(1) MHz	[186]
$Q_W^{(1)}$	0.04532(64)	(11) of [68]
$\delta_1$	$-2.78(4) \times 10^{-13}$	(20) of [68]
$\Delta u + \Delta \bar{u}$ $-\Delta d - \Delta \bar{d}$	1.2701(25)	[12]
$\Delta s + \Delta \bar{s}$	-0.12	0.00
		(A.3)
$Q_W^{(2)}$	-0.1259(18)	-0.1151(16)
$\delta_2$	$7.74(11) \times 10^{-13}$	$7.07(10) \times 10^{-13}$
		(A.2)-(A.3),(2.52)

**Table A.1:** Values of parameters for  ${}^1_1\text{H}$  for numerical calculations. The weak mixing angle in the low-energy limit,  $\sin^2 \theta_W = 0.23867(16)$ , is taken from [43]. The uncertainty in  $\delta_1$  is dominated by the uncertainty of  $\sin^2 \theta_W$ . The uncertainties quoted for  $Q_W^{(2)}$  and  $\delta_2$  for hydrogen are resulting from the error of the weak mixing angle, whereas the variation of  $Q_W^{(2)}$  and  $\delta_2$  with  $(\Delta s + \Delta \bar{s})$  varying in the range (A.3) is given explicitly.

We see from Table A.1 that varying  $\Delta s + \Delta \bar{s}$  in the range (A.3) corresponds to a 10% shift in  $\delta_2$ . Thus, a percent-level measurement of  $\delta_2$  would be most welcome for a clarification of the role of strange quarks for the nucleon spin.

#### Eigenstates of the Mass Matrix

The  $n = 2$  states of hydrogen in the absence of P violation and for zero external fields are denoted by  $|2L_J, F, F_3\rangle$ , where  $L$ ,  $J$ ,  $F$ , and  $F_3$  are the quantum numbers of the electron's orbital angular momentum, its total angular momentum, the total atomic angular momentum and its third component, respectively. In the following, we discuss the properties, the ordering and the numbering of the eigenstates of  $\underline{\mathcal{M}}(\mathcal{E}, \mathcal{B})$  as given in (3.25). We investigated the eigenenergies of  $\underline{\mathcal{M}}(\mathcal{E}, \mathcal{B})$  already in Section 3.2.3.

The eigenstates of  $\underline{\mathcal{M}}$  (3.25) for electric field  $\mathcal{E}$  and magnetic field  $\mathcal{B}$  equal to zero are the free 2S and 2P states. The hat symbol on  $\hat{L}$ ,  $\hat{P}$ , and  $\hat{S}$  indicates that these states include the parity mixing due to  $H_{\text{PV}}$ . Thus, the eigenstates of the mass matrix (3.25), including the PV part but with electric and magnetic fields equal to zero, will be denoted by  $|2\hat{L}_J, F, F_3, \mathcal{E} = \mathbf{0}, \mathcal{B} = \mathbf{0}\rangle$ . The corresponding states for the mass matrix without the PV term, that is, with  $\underline{\mathcal{M}}_0$  replaced by  $\underline{\mathcal{M}}$  in (3.25), will be denoted by  $|2L_J, F, F_3, \mathcal{E} = \mathbf{0}, \mathcal{B} = \mathbf{0}\rangle$ . But it is not convenient to start a numbering scheme at the degeneracy point  $(\mathcal{E}, \mathcal{B}) = (\mathbf{0}, \mathbf{0})$ . Therefore, we consider first atoms in a constant

hydrogen	
$\alpha$	$ 2\hat{L}_J, F, F_3, \mathcal{E}, \mathcal{B})$
1	$ 2\hat{P}_{3/2}, 2, 2, \mathcal{E}, \mathcal{B})$
2	$ 2\hat{P}_{3/2}, 2, 1, \mathcal{E}, \mathcal{B})$
3	$ 2\hat{P}_{3/2}, 2, 0, \mathcal{E}, \mathcal{B})$
4	$ 2\hat{P}_{3/2}, 2, -1, \mathcal{E}, \mathcal{B})$
5	$ 2\hat{P}_{3/2}, 2, -2, \mathcal{E}, \mathcal{B})$
6	$ 2\hat{P}_{3/2}, 1, 1, \mathcal{E}, \mathcal{B})$
7	$ 2\hat{P}_{3/2}, 1, 0, \mathcal{E}, \mathcal{B})$
8	$ 2\hat{P}_{3/2}, 1, -1, \mathcal{E}, \mathcal{B})$
9	$ 2\hat{S}_{1/2}, 1, 1, \mathcal{E}, \mathcal{B})$
10	$ 2\hat{S}_{1/2}, 1, 0, \mathcal{E}, \mathcal{B})$
11	$ 2\hat{S}_{1/2}, 1, -1, \mathcal{E}, \mathcal{B})$
12	$ 2\hat{S}_{1/2}, 0, 0, \mathcal{E}, \mathcal{B})$
13	$ 2\hat{P}_{1/2}, 1, 1, \mathcal{E}, \mathcal{B})$
14	$ 2\hat{P}_{1/2}, 1, 0, \mathcal{E}, \mathcal{B})$
15	$ 2\hat{P}_{1/2}, 1, -1, \mathcal{E}, \mathcal{B})$
16	$ 2\hat{P}_{1/2}, 0, 0, \mathcal{E}, \mathcal{B})$

**Table A.2:** The numbering scheme for the atomic  $n = 2$  states of hydrogen.

$\mathcal{B}$ -field pointing in positive 3-direction,

$$\mathcal{B} = \mathcal{B}e_3, \quad \mathcal{B} > 0. \quad (\text{A.4})$$

The corresponding eigenstates, denoted by  $|2\hat{L}_J, F, F_3, 0, \mathcal{B}e_3)$ , and the corresponding quasi projectors (3.51) of  $\mathcal{M}$  in (3.25) are obtained from those at  $\mathcal{B} = 0$  by continuously turning on  $\mathcal{B}$  in the form (A.4). Of course, for  $\mathcal{B} > 0$ ,  $F_3$  still is a good quantum number but this is no longer true for  $F$ . The latter is merely a label for the states. We now choose a reference field  $\mathcal{B}_{\text{ref}} = \mathcal{B}_{\text{ref}}e_3$ ,  $\mathcal{B}_{\text{ref}} > 0$ , below the first crossings in the Breit-Rabi diagram, for instance  $\mathcal{B}_{\text{ref}} = 0.05$  mT. We are then at a no-degeneracy point and number the  $n = 2$  states and quasi projectors (3.51) with  $\alpha = 1, \dots, 16$  as shown in Table A.2 setting there  $(\mathcal{E}, \mathcal{B}) = (\mathbf{0}, \mathcal{B}_{\text{ref}})$ . In the next step we consider external fields of the form

$$\mathcal{E}' = \begin{pmatrix} \mathcal{E}_1 \\ 0 \\ \mathcal{E}_3 \end{pmatrix}, \quad \mathcal{B}' = \begin{pmatrix} 0 \\ 0 \\ \mathcal{B}' \end{pmatrix}, \quad \mathcal{B}' > 0, \quad (\text{A.5})$$

and a continuous path to these fields from the reference point  $(\mathcal{E}, \mathcal{B}) = (\mathbf{0}, \mathcal{B}_{\text{ref}})$ :

$$\begin{aligned} \mathcal{E}'(\lambda) &= \lambda \mathcal{E}', \\ \mathcal{B}'(\lambda) &= \mathcal{B}_{\text{ref}} + \lambda(\mathcal{B}' - \mathcal{B}_{\text{ref}}), \quad \lambda \in [0, 1]. \end{aligned} \quad (\text{A.6})$$

Since we encounter no degeneracies for  $\lambda \in [0, 1]$  the energy eigenvalues as well as the quasi projectors are continuous functions of  $\lambda$  there. This allows us to carry over the numbering of the quasi projectors from  $(\mathbf{0}, \mathcal{B}_{\text{ref}})$  to all fields of the form (A.5).

---

### A.1. Values for Quantities Related to $n = 2$ Hydrogen

---

Finally, we consider arbitrary fields  $(\mathcal{E}, \mathcal{B})$  with  $\mathcal{B} \neq \mathbf{0}$ . We can always find a proper rotation  $R$  such that

$$\begin{aligned} R\mathcal{E} &= \mathcal{E}' , \\ R\mathcal{B} &= \mathcal{B}' \end{aligned} \tag{A.7}$$

with  $(\mathcal{E}', \mathcal{B}')$  of the form (A.5). From the considerations of the resolvent in Section 3.5.2 we conclude that the eigenvalues of  $\underline{\mathcal{M}}(\mathcal{E}, \mathcal{B})$  and  $\underline{\mathcal{M}}(\mathcal{E}', \mathcal{B}')$  are equal. There are also no degeneracies here and, therefore, we can unambiguously carry over the numbering of eigenvalues and quasi projectors from the case  $(\mathcal{E}', \mathcal{B}')$  to the case  $(\mathcal{E}, \mathcal{B})$ . The labels  $\alpha = 1, \dots, 16$  in Table A.2 for arbitrary  $(\mathcal{E}, \mathcal{B})$  with  $\mathcal{B} \neq \mathbf{0}$  correspond to this identification procedure of eigenenergies and quasi projectors. The corresponding eigenstates  $|\alpha, \mathcal{E}, \mathcal{B}\rangle$  of  $\underline{\mathcal{M}}(\mathcal{E}, \mathcal{B})$  are defined as the eigenstates of the quasi projectors

$$\mathbb{P}_\alpha(\mathcal{E}, \mathcal{B})|\alpha, \mathcal{E}, \mathcal{B}\rangle = |\alpha, \mathcal{E}, \mathcal{B}\rangle , \tag{A.8}$$

where we also require (2.70) to hold. For given  $\alpha$ ,  $\mathcal{E}$ , and  $\mathcal{B}$  this fixes the state vector up to a phase factor. In all considerations of flux densities only the quasi projectors enter and thus, such a phase factor in the states is irrelevant. The choice of phase factor *is* relevant for the calculation of the geometric phases via the line integrals (3.42) and (3.56). Then, we always make sure to choose a phase factor being differentiable along the path considered.

Finally, we note that for the case of no P violation, that is for  $\delta = 0$ , the numbering of the quasi projectors and the states  $|2L_J, F, F_3, \mathcal{E}, \mathcal{B}\rangle$  is done in a completely analogous way.

#### Derivation of the Decay Matrix

As discussed in Section 3.1 the only non-diagonal matrix elements (3.11) of the decay matrix  $\underline{\Gamma}$  which could be non-zero are those for  $L = L' = 1$ ,  $F = F' = 1$ ,  $F_3 = F'_3$ , and  $(J', J) = (1/2, 3/2)$  or  $(J', J) = (3/2, 1/2)$ , respectively. In the following, we show that these off-diagonal matrix elements vanish and derive the decay rates of the states  $|2P_J, F = 1, F_3\rangle$  for a consistency check.

We consider the initial state  $|I\rangle = |t = -\infty\rangle = |\psi_I\rangle \otimes |\Omega_\gamma\rangle$  of an atom in the eigenstate  $|\psi_I\rangle$  with the vacuum state  $|\Omega_\gamma\rangle$  of photons and the transition to  $|\psi_F; \mathbf{p}, \epsilon_r\rangle$  at  $t = \infty$ , i.e., a final atomic eigenstate  $|\psi_F\rangle$  together with one photon having momentum  $\mathbf{p} = \hbar\mathbf{k}$  and polarisation  $\epsilon_r$  [173]. In the Born approximation, the according S-matrix element can be written as

$$\begin{aligned} \langle \psi_F; \mathbf{p}, \epsilon_r | S | \psi_I; \Omega_\gamma \rangle &= -2\pi i \delta(\hbar\omega + E_F - E_I) \mathcal{T}_{F,I} \\ &:= 2\pi i \delta(\hbar\omega + E_F - E_I) \frac{i}{\sqrt{\hbar}} \frac{E_F - E_I}{\sqrt{2\omega} (2\pi\hbar)^{3/2}} \langle \psi_F | \epsilon_r^*(\mathbf{k}) \cdot \mathbf{D} | \psi_I \rangle , \end{aligned} \tag{A.9}$$

where  $\mathbf{D} = e\mathbf{x}$  is the operator of the electric dipole moment at time  $t = 0$ , with  $\mathbf{x}$

## Chapter A. Notations and Definitions

---

being the position operator. Then, the total transition rate (3.11) becomes

$$\begin{aligned}
\langle 2L'_{J'}, F', F'_3 | \underline{\Gamma} | 2L_J, F, F_3 \rangle &= - \sum_{\text{1S states}} \int d^3p \sum_{r=\pm} \frac{2\pi}{\hbar\epsilon_0} \delta(\hbar\omega + E_F - E_I) \\
&\times \left( \frac{i}{\sqrt{\hbar}} \frac{E_F - E_I}{\sqrt{2\omega}(2\pi\hbar)^{3/2}} \right)^2 \langle 2L'_{J'}, F', F'_3 | \boldsymbol{\epsilon}_r(\mathbf{k}) \mathbf{D} | \text{1S} \rangle \\
&\times \langle \text{1S} | \boldsymbol{\epsilon}_r^*(\mathbf{k}) \mathbf{D} | 2L_J, F, F_3 \rangle . \tag{A.10}
\end{aligned}$$

Here,  $\epsilon_0 = 8.854187817 \times 10^{-12}$  F/m is the electric constant [187]. Using  $d^3k = d^3p/\hbar^3$ ,  $\omega = c|\mathbf{k}| = ck$ ,  $\mathbf{k} = k\hat{\mathbf{k}}$ , and  $\sum_{r=\pm} \epsilon_{r,j}(\mathbf{k})\epsilon_{r,i}^*(\mathbf{k}) = \delta_{ij} - \hat{k}_j\hat{k}_i$ , (A.10) reduces to

$$\begin{aligned}
\langle 2L'_{J'}, F', F'_3 | \underline{\Gamma} | 2L_J, F, F_3 \rangle &= \frac{e^2}{3\pi\hbar^4 c^3 \epsilon_0} \sum_{\text{1S states}} (E_I - E_F)^3 \\
&\times \sum_m \langle \text{1S} | \mathbf{e}_m^* \mathbf{x} | 2L'_{J'}, F', F'_3 \rangle^* \langle \text{1S} | \mathbf{e}_m^* \mathbf{x} | 2L_J, F, F_3 \rangle , \tag{A.11}
\end{aligned}$$

where  $m$  indexes the spherical unit vectors  $\mathbf{e}_0 = \mathbf{e}_3$ ,  $\mathbf{e}_{\pm} = \mp \frac{1}{\sqrt{2}}(\mathbf{e}_1 \pm i\mathbf{e}_2)$ .

The matrix elements of  $\mathbf{e}_m^* \mathbf{x}$  in the basis of total atomic angular momentum eigenstates  $|nL_J, F, F_3\rangle$  of hydrogen can be expanded using Clebsch-Gordan coefficients. Here, of course, we use that the transition matrix elements are diagonal in the nuclear quantum numbers. With the spherical harmonics  $Y_l^m$ ,

$$\mathbf{x} = r\hat{\mathbf{x}} = r \begin{pmatrix} \sin\theta \cos\varphi \\ \sin\theta \sin\varphi \\ \cos\theta \end{pmatrix} , \tag{A.12}$$

$\mathbf{e}_m^* \hat{\mathbf{x}} = \sqrt{\frac{4\pi}{3}} Y_1^m(\hat{\mathbf{x}})^*$ ,  $F = 1$ ,  $L = 1$ , and  $S = I = 1/2$  one then finds

$$\begin{aligned}
\langle \text{1S} | \mathbf{e}_m^* \mathbf{x} | 2L_J, F, F_3 \rangle &= \langle 1L''_{J''}, F'', F''_3 | r\mathbf{e}_m^* \hat{\mathbf{x}} | 2L_J, F, F_3 \rangle \\
&= \sum_{\substack{j \ i \ l \ s \\ j'' \ i'' \ l'' \ s''}} \delta_{II''} \delta_{ii''} \langle L'' l'' S'' s'' | J'' j'' \rangle \langle J'' j'' I'' i'' | F'' F''_3 \rangle \\
&\times \langle LlSs | Jj \rangle \langle JjIi | FF_3 \rangle \langle 1L'' l'' S'' s'' | r\mathbf{e}_m^* \hat{\mathbf{x}} | 2LlSs \rangle \\
&= \sum_{j \ i \ l \ s} \langle \frac{1}{2}s \frac{1}{2}i | F'' F''_3 \rangle \langle 1l \frac{1}{2}s | Jj \rangle \langle Jj \frac{1}{2}i | 1F_3 \rangle \frac{R}{\sqrt{3}} \delta_{ml} . \tag{A.13}
\end{aligned}$$

The quantum numbers of the 1S states are indicated with two primes. For the last step of (A.13) we used  $\langle 00 \frac{1}{2}s | \frac{1}{2}j'' \rangle = \delta_{sj''}$ . With  $\langle \frac{1}{2}s'' | \frac{1}{2}s \rangle = \delta_{ss''}$  we calculated

$$\langle 100 \frac{1}{2}s'' | r\mathbf{e}_m^* \hat{\mathbf{x}} | 21l \frac{1}{2}s \rangle = \int d^3x \chi_{1,0}^*(r) Y_0^0(\hat{\mathbf{x}}) r \sqrt{\frac{4\pi}{3}} Y_1^m(\hat{\mathbf{x}})^* \chi_{2,1}(r) Y_1^l(\hat{\mathbf{x}}) \langle \frac{1}{2}s'' | \frac{1}{2}s \rangle \tag{A.14}$$

---

## A.2. The Matrix Representations of $\tilde{\mathcal{M}}_0$ , $\underline{D}$ , and $\underline{\mu}$ for Hydrogen

---

with radial functions  $\chi_{n,l}$ ,  $\int d\Omega Y_1^{m*} Y_1^{m'} = \delta_{mm'}$ , and

$$R = \int dr r^3 \chi_{1,0}^*(r) \chi_{2,1}(r) = \frac{128}{81} \sqrt{\frac{2}{3}} r_B . \quad (\text{A.15})$$

With  $E_I - E_F = E_{2P} - E_{1S} = \frac{3}{4} R_\infty$ ,  $R_\infty$  being the Rydberg constant, and exploiting the orthogonality relations of the Clebsch-Gordan coefficients, we finally arrive at

$$\begin{aligned} (2P_{J',1}, F_3 | \underline{\Gamma} | 2P_{J,1}, F_3) &= \frac{512}{6561} \frac{r_B^2 e^2 R_\infty^3}{\hbar^4 c^3 \epsilon_0 \pi} \delta_{JJ'} \\ &= \begin{cases} 0 & , \quad J \neq J' \\ 6.26831 \times 10^8 \text{ s}^{-1} & , \quad J = J' \end{cases} . \end{aligned} \quad (\text{A.16})$$

Therefore, we can consider all off-diagonal matrix elements of  $\underline{\Gamma}$  to be zero.

## A.2 The Matrix Representations of $\tilde{\mathcal{M}}_0$ , $\underline{D}$ , and $\underline{\mu}$ for Hydrogen

Tables A.3, A.4, and A.5 show the mass matrix for zero external fields,  $\tilde{\mathcal{M}}_0$ , the electric dipole operator  $\underline{D}$  and the magnetic dipole operator  $\underline{\mu}$  for the  $n = 2$  states of hydrogen. We give all these matrices in the basis of the pure 2S and 2P states, that is, the states for zero external fields and without the P-violating mixing.

To calculate the matrices  $\mathcal{M}_{\text{PV}}^{(1)}$ ,  $\mathcal{M}_{\text{PV}}^{(2)}$ ,  $\underline{D}$ , and  $\underline{\mu}$  the standard Coulomb wave functions for hydrogen are employed. As in [80] (see Appendix B there) the phase conventions of [188] are used for these states, except for an overall sign change in all radial wave functions.

In Tables A.4 and A.5 we use the spherical unit vectors, which are defined as

$$\begin{aligned} \mathbf{e}_0 &= \mathbf{e}_3 , \\ \mathbf{e}_\pm &= \mp \frac{1}{\sqrt{2}} (\mathbf{e}_1 \pm i\mathbf{e}_2) , \end{aligned} \quad (\text{A.17})$$

where  $\mathbf{e}_i$  ( $i = 1, 2, 3$ ) are the Cartesian unit vectors. It is  $\mathbf{e}_\pm^* = -\mathbf{e}_\mp$ .

## Chapter A. Notations and Definitions

**Table A.3:** The mass matrix  $\tilde{\mathcal{M}}_0$  (3.24) for the  $n = 2$  states of hydrogen. For the quantities  $\Delta$ ,  $L$ ,  $\mathcal{A}$ , and  $\delta_{1,2}$  see Table A.1. For the lifetimes see (3.12).

	$2P_{3/2}, 2, 2$	$2P_{3/2}, 2, 1$	$2P_{3/2}, 1, 1$	$2P_{1/2}, 1, 1$	$2S_{1/2}, 1, 1$
$2P_{3/2}, 2, 2$	$\Delta + \frac{\mathcal{A}}{160}$ $-\frac{i}{2}\Gamma_P$	0	0	0	0
$2P_{3/2}, 2, 1$	0	$\Delta + \frac{\mathcal{A}}{160}$ $-\frac{i}{2}\Gamma_P$	0	0	0
$2P_{3/2}, 1, 1$	0	0	$\Delta - \frac{\mathcal{A}}{96}$ $-\frac{i}{2}\Gamma_P$	$-\frac{\mathcal{A}}{192\sqrt{2}}$	0
$2P_{1/2}, 1, 1$	0	0	$-\frac{\mathcal{A}}{192\sqrt{2}}$	$\frac{\mathcal{A}}{96} - \frac{i}{2}\Gamma_P$	$i\delta_1 L$ $+\frac{i}{2}\delta_2 L$
$2S_{1/2}, 1, 1$	0	0	0	$-i\delta_1 L$ $-\frac{i}{2}\delta_2 L$	$L + \frac{\mathcal{A}}{32}$ $-\frac{i}{2}\Gamma_S$

**Table A.3 (a)**

	$2P_{3/2}, 2, 0$	$2P_{3/2}, 1, 0$	$2P_{1/2}, 1, 0$	$2S_{1/2}, 1, 0$	$2P_{1/2}, 0, 0$	$2S_{1/2}, 0, 0$
$2P_{3/2}, 2, 0$	$\Delta + \frac{\mathcal{A}}{160}$ $-\frac{i}{2}\Gamma_P$	0	0	0	0	0
$2P_{3/2}, 1, 0$	0	$\Delta - \frac{\mathcal{A}}{96}$ $-\frac{i}{2}\Gamma_P$	$-\frac{\mathcal{A}}{192\sqrt{2}}$	0	0	0
$2P_{1/2}, 1, 0$	0	$-\frac{\mathcal{A}}{192\sqrt{2}}$	$\frac{\mathcal{A}}{96} - \frac{i}{2}\Gamma_P$	$i\delta_1 L$ $+\frac{i}{2}\delta_2 L$	0	0
$2S_{1/2}, 1, 0$	0	0	$-i\delta_1 L$ $-\frac{i}{2}\delta_2 L$	$L + \frac{\mathcal{A}}{32}$ $-\frac{i}{2}\Gamma_S$	0	0
$2P_{1/2}, 0, 0$	0	0	0	0	$-\frac{\mathcal{A}}{32} - \frac{i}{2}\Gamma_P$	$i\delta_1 L$ $+\frac{3}{2}i\delta_2 L$
$2S_{1/2}, 0, 0$	0	0	0	0	$-i\delta_1 L$ $-\frac{3}{2}i\delta_2 L$	$L - \frac{3\mathcal{A}}{32}$ $-\frac{i}{2}\Gamma_S$

**Table A.3 (b)**

## A.2. The Matrix Representations of $\tilde{\mathcal{M}}_0$ , $\underline{D}$ , and $\underline{\mu}$ for Hydrogen

	2P <sub>3/2</sub> , 2, -1	2P <sub>3/2</sub> , 1, -1	2P <sub>1/2</sub> , 1, -1	2S <sub>1/2</sub> , 1, -1	2P <sub>3/2</sub> , 2, -2
2P <sub>3/2</sub> , 2, -1	$\Delta + \frac{\mathcal{A}}{160}$ $-\frac{i}{2}\Gamma_P$	0	0	0	0
2P <sub>3/2</sub> , 1, -1	0	$\Delta - \frac{\mathcal{A}}{96}$ $-\frac{i}{2}\Gamma_P$	$-\frac{\mathcal{A}}{192\sqrt{2}}$	0	0
2P <sub>1/2</sub> , 1, -1	0	$-\frac{\mathcal{A}}{192\sqrt{2}}$	$\frac{\mathcal{A}}{96} - \frac{i}{2}\Gamma_P$	$i\delta_1 L$ $+\frac{i}{2}\delta_2 L$	0
2S <sub>1/2</sub> , 1, -1	0	0	$-i\delta_1 L$ $-\frac{i}{2}\delta_2 L$	$L + \frac{\mathcal{A}}{32}$ $-\frac{i}{2}\Gamma_S$	0
2P <sub>3/2</sub> , 2, -2	0	0	0	0	$\Delta + \frac{\mathcal{A}}{160}$ $-\frac{i}{2}\Gamma_P$

Table A.3 (c)

**Table A.4:** The suitably normalised electric dipole operator  $\underline{D}/(er_B)$  for the  $n = 2$  states of hydrogen where  $r_B$  is the Bohr radius for hydrogen.

	2P <sub>3/2</sub> , 2, 2	2P <sub>3/2</sub> , 2, 1	2P <sub>3/2</sub> , 1, 1	2P <sub>1/2</sub> , 1, 1	2S <sub>1/2</sub> , 1, 1
2P <sub>3/2</sub> , 2, 2	0	0	0	0	$-3e_-$
2P <sub>3/2</sub> , 2, 1	0	0	0	0	$\frac{3}{\sqrt{2}}e_0$
2P <sub>3/2</sub> , 1, 1	0	0	0	0	$-\sqrt{\frac{3}{2}}e_0$
2P <sub>1/2</sub> , 1, 1	0	0	0	0	$-\sqrt{3}e_0$
2S <sub>1/2</sub> , 1, 1	$3e_+$	$\frac{3}{\sqrt{2}}e_0$	$-\sqrt{\frac{3}{2}}e_0$	$-\sqrt{3}e_0$	0

Table A.4 (a)

	2P <sub>3/2</sub> , 2, 0	2P <sub>3/2</sub> , 1, 0	2P <sub>1/2</sub> , 1, 0	2S <sub>1/2</sub> , 1, 0	2P <sub>1/2</sub> , 0, 0	2S <sub>1/2</sub> , 0, 0
2P <sub>3/2</sub> , 2, 1	0	0	0	$-\frac{3}{\sqrt{2}}e_-$	0	0
2P <sub>3/2</sub> , 1, 1	0	0	0	$-\sqrt{\frac{3}{2}}e_-$	0	$-\sqrt{6}e_-$
2P <sub>1/2</sub> , 1, 1	0	0	0	$-\sqrt{3}e_-$	0	$\sqrt{3}e_-$
2S <sub>1/2</sub> , 1, 1	$\sqrt{\frac{3}{2}}e_-$	$-\sqrt{\frac{3}{2}}e_-$	$-\sqrt{3}e_-$	0	$\sqrt{3}e_-$	0

Table A.4 (b)

Chapter A. Notations and Definitions

---

	$2P_{3/2, 2, 1}$	$2P_{3/2, 1, 1}$	$2P_{1/2, 1, 1}$	$2S_{1/2, 1, 1}$
$2P_{3/2, 2, 0}$	0	0	0	$-\sqrt{\frac{3}{2}}e_+$
$2P_{3/2, 1, 0}$	0	0	0	$\sqrt{\frac{3}{2}}e_+$
$2P_{1/2, 1, 0}$	0	0	0	$\sqrt{3}e_+$
$2S_{1/2, 1, 0}$	$\frac{3}{\sqrt{2}}e_+$	$\sqrt{\frac{3}{2}}e_+$	$\sqrt{3}e_+$	0
$2P_{1/2, 0, 0}$	0	0	0	$-\sqrt{3}e_+$
$2S_{1/2, 0, 0}$	0	$\sqrt{6}e_+$	$-\sqrt{3}e_+$	0

Table A.4 (c)

	$2P_{3/2, 2, 0}$	$2P_{3/2, 1, 0}$	$2P_{1/2, 1, 0}$	$2S_{1/2, 1, 0}$	$2P_{1/2, 0, 0}$	$2S_{1/2, 0, 0}$
$2P_{3/2, 2, 0}$	0	0	0	$\sqrt{6}e_0$	0	0
$2P_{3/2, 1, 0}$	0	0	0	0	0	$\sqrt{6}e_0$
$2P_{1/2, 1, 0}$	0	0	0	0	0	$-\sqrt{3}e_0$
$2S_{1/2, 1, 0}$	$\sqrt{6}e_0$	0	0	0	$-\sqrt{3}e_0$	0
$2P_{1/2, 0, 0}$	0	0	0	$-\sqrt{3}e_0$	0	0
$2S_{1/2, 0, 0}$	0	$\sqrt{6}e_0$	$-\sqrt{3}e_0$	0	0	0

Table A.4 (d)

	$2P_{3/2, 2, -1}$	$2P_{3/2, 1, -1}$	$2P_{1/2, 1, -1}$	$2S_{1/2, 1, -1}$
$2P_{3/2, 2, 0}$	0	0	0	$-\sqrt{\frac{3}{2}}e_-$
$2P_{3/2, 1, 0}$	0	0	0	$-\sqrt{\frac{3}{2}}e_-$
$2P_{1/2, 1, 0}$	0	0	0	$-\sqrt{3}e_-$
$2S_{1/2, 1, 0}$	$\frac{3}{\sqrt{2}}e_-$	$-\sqrt{\frac{3}{2}}e_-$	$-\sqrt{3}e_-$	0
$2P_{1/2, 0, 0}$	0	0	0	$-\sqrt{3}e_-$
$2S_{1/2, 0, 0}$	0	$\sqrt{6}e_-$	$-\sqrt{3}e_-$	0

Table A.4 (e)

**A.2. The Matrix Representations of  $\tilde{\mathcal{M}}_0$ ,  $\underline{D}$ , and  $\underline{\mu}$  for Hydrogen**

	2P <sub>3/2</sub> , 2, 0	2P <sub>3/2</sub> , 1, 0	2P <sub>1/2</sub> , 1, 0	2S <sub>1/2</sub> , 1, 0	2P <sub>1/2</sub> , 0, 0	2S <sub>1/2</sub> , 0, 0
2P <sub>3/2</sub> , 2, -1	0	0	0	$-\frac{3}{\sqrt{2}}\mathbf{e}_+$	0	0
2P <sub>3/2</sub> , 1, -1	0	0	0	$\sqrt{\frac{3}{2}}\mathbf{e}_+$	0	$-\sqrt{6}\mathbf{e}_+$
2P <sub>1/2</sub> , 1, -1	0	0	0	$\sqrt{3}\mathbf{e}_+$	0	$\sqrt{3}\mathbf{e}_+$
2S <sub>1/2</sub> , 1, -1	$\sqrt{\frac{3}{2}}\mathbf{e}_+$	$\sqrt{\frac{3}{2}}\mathbf{e}_+$	$\sqrt{3}\mathbf{e}_+$	0	$\sqrt{3}\mathbf{e}_+$	0

Table A.4 (f)

	2P <sub>3/2</sub> , 2, -1	2P <sub>3/2</sub> , 1, -1	2P <sub>1/2</sub> , 1, -1	2S <sub>1/2</sub> , 1, -1	2P <sub>3/2</sub> , 2, -2
2P <sub>3/2</sub> , 2, -1	0	0	0	$\frac{3}{\sqrt{2}}\mathbf{e}_0$	0
2P <sub>3/2</sub> , 1, -1	0	0	0	$\sqrt{\frac{3}{2}}\mathbf{e}_0$	0
2P <sub>1/2</sub> , 1, -1	0	0	0	$\sqrt{3}\mathbf{e}_0$	0
2S <sub>1/2</sub> , 1, -1	$\frac{3}{\sqrt{2}}\mathbf{e}_0$	$\sqrt{\frac{3}{2}}\mathbf{e}_0$	$\sqrt{3}\mathbf{e}_0$	0	$3\mathbf{e}_-$
2P <sub>3/2</sub> , 2, -2	0	0	0	$-3\mathbf{e}_+$	0

Table A.4 (g)

**Table A.5:** The suitably normalised magnetic dipole operator  $\underline{\mu}/\mu_B$  for the  $n = 2$  states of hydrogen, where  $\mu_B = e\hbar/(2m_e)$  is the Bohr magneton and  $g = 2.00231930436153(53)$  is the Landé factor of the electron [187].

	2P <sub>3/2</sub> , 2, 2	2P <sub>3/2</sub> , 2, 1	2P <sub>3/2</sub> , 1, 1	2P <sub>1/2</sub> , 1, 1	2S <sub>1/2</sub> , 1, 1
2P <sub>3/2</sub> , 2, 2	$-\frac{g+2}{2}\mathbf{e}_0$	$-\frac{\sqrt{2}(g+2)}{4}\mathbf{e}_-$	$\frac{\sqrt{2}(g+2)}{4\sqrt{3}}\mathbf{e}_-$	$-\frac{g-1}{\sqrt{3}}\mathbf{e}_-$	0
2P <sub>3/2</sub> , 2, 1	$\frac{\sqrt{2}(g+2)}{4}\mathbf{e}_+$	$-\frac{g+2}{4}\mathbf{e}_0$	$-\frac{g+2}{4\sqrt{3}}\mathbf{e}_0$	$-\frac{g-1}{\sqrt{6}}\mathbf{e}_0$	0
2P <sub>3/2</sub> , 1, 1	$-\frac{\sqrt{2}(g+2)}{4\sqrt{3}}\mathbf{e}_+$	$-\frac{g+2}{4\sqrt{3}}\mathbf{e}_0$	$-\frac{5(g+2)}{12}\mathbf{e}_0$	$\frac{g-1}{3\sqrt{2}}\mathbf{e}_0$	0
2P <sub>1/2</sub> , 1, 1	$\frac{g-1}{\sqrt{3}}\mathbf{e}_+$	$-\frac{g-1}{\sqrt{6}}\mathbf{e}_0$	$\frac{g-1}{3\sqrt{2}}\mathbf{e}_0$	$\frac{g-4}{6}\mathbf{e}_0$	0
2S <sub>1/2</sub> , 1, 1	0	0	0	0	$-\frac{g}{2}\mathbf{e}_0$

Table A.5 (a)

Chapter A. Notations and Definitions

	$2P_{3/2}, 2, 0$	$2P_{3/2}, 1, 0$	$2P_{1/2}, 1, 0$	$2S_{1/2}, 1, 0$	$2P_{1/2}, 0, 0$	$2S_{1/2}, 0, 0$
$2P_{3/2}, 2, 1$	$-\frac{\sqrt{3}(g+2)}{4}e_-$	$\frac{g+2}{4\sqrt{3}}e_-$	$-\frac{g-1}{\sqrt{6}}e_-$	0	0	0
$2P_{3/2}, 1, 1$	$-\frac{g+2}{12}e_-$	$-\frac{5(g+2)}{12}e_-$	$-\frac{\sqrt{2}(g-1)}{6}e_-$	0	$-\frac{\sqrt{2}(g-1)}{3}e_-$	0
$2P_{1/2}, 1, 1$	$\frac{\sqrt{2}(g-1)}{6}e_-$	$-\frac{\sqrt{2}(g-1)}{6}e_-$	$\frac{g-4}{6}e_-$	0	$-\frac{g-4}{6}e_-$	0
$2S_{1/2}, 1, 1$	0	0	0	$-\frac{g}{2}e_-$	0	$\frac{g}{2}e_-$

Table A.5 (b)

	$2P_{3/2}, 2, 1$	$2P_{3/2}, 1, 1$	$2P_{1/2}, 1, 1$	$2S_{1/2}, 1, 1$
$2P_{3/2}, 2, 0$	$\frac{\sqrt{3}(g+2)}{4}e_+$	$\frac{g+2}{12}e_+$	$-\frac{\sqrt{2}(g-1)}{6}e_+$	0
$2P_{3/2}, 1, 0$	$-\frac{g+2}{4\sqrt{3}}e_+$	$\frac{5(g+2)}{12}e_+$	$\frac{\sqrt{2}(g-1)}{6}e_+$	0
$2P_{1/2}, 1, 0$	$\frac{g-1}{\sqrt{6}}e_+$	$\frac{\sqrt{2}(g-1)}{6}e_+$	$-\frac{g-4}{6}e_+$	0
$2S_{1/2}, 1, 0$	0	0	0	$\frac{g}{2}e_+$
$2P_{1/2}, 0, 0$	0	$\frac{\sqrt{2}(g-1)}{3}e_+$	$\frac{g-4}{6}e_+$	0
$2S_{1/2}, 0, 0$	0	0	0	$-\frac{g}{2}e_+$

Table A.5 (c)

	$2P_{3/2}, 2, 0$	$2P_{3/2}, 1, 0$	$2P_{1/2}, 1, 0$	$2S_{1/2}, 1, 0$	$2P_{1/2}, 0, 0$	$2S_{1/2}, 0, 0$
$2P_{3/2}, 2, 0$	0	$-\frac{g+2}{6}e_0$	$-\frac{\sqrt{2}(g-1)}{3}e_0$	0	0	0
$2P_{3/2}, 1, 0$	$-\frac{g+2}{6}e_0$	0	0	0	$-\frac{\sqrt{2}(g-1)}{3}e_0$	0
$2P_{1/2}, 1, 0$	$-\frac{\sqrt{2}(g-1)}{3}e_0$	0	0	0	$\frac{g-4}{6}e_0$	0
$2S_{1/2}, 1, 0$	0	0	0	0	0	$-\frac{g}{2}e_0$
$2P_{1/2}, 0, 0$	0	$-\frac{\sqrt{2}(g-1)}{3}e_0$	$\frac{g-4}{6}e_0$	0	0	0
$2S_{1/2}, 0, 0$	0	0	0	$-\frac{g}{2}e_0$	0	0

Table A.5 (d)

**A.2. The Matrix Representations of  $\tilde{\mathcal{M}}_0$ ,  $\underline{D}$ , and  $\underline{\mu}$  for Hydrogen**

	2P <sub>3/2</sub> , 2, -1	2P <sub>3/2</sub> , 1, -1	2P <sub>1/2</sub> , 1, -1	2S <sub>1/2</sub> , 1, -1
2P <sub>3/2</sub> , 2, 0	$-\frac{\sqrt{3}(g+2)}{4}e_-$	$\frac{g+2}{12}e_-$	$-\frac{\sqrt{2}(g-1)}{6}e_-$	0
2P <sub>3/2</sub> , 1, 0	$-\frac{g+2}{4\sqrt{3}}e_-$	$-\frac{5(g+2)}{12}e_-$	$-\frac{\sqrt{2}(g-1)}{6}e_-$	0
2P <sub>1/2</sub> , 1, 0	$\frac{g-1}{\sqrt{6}}e_-$	$-\frac{\sqrt{2}(g-1)}{6}e_-$	$\frac{g-4}{6}e_-$	0
2S <sub>1/2</sub> , 1, 0	0	0	0	$-\frac{g}{2}e_-$
2P <sub>1/2</sub> , 0, 0	0	$\frac{\sqrt{2}(g-1)}{3}e_-$	$\frac{g-4}{6}e_-$	0
2S <sub>1/2</sub> , 0, 0	0	0	0	$-\frac{g}{2}e_-$

Table A.5 (e)

	2P <sub>3/2</sub> , 2, 0	2P <sub>3/2</sub> , 1, 0	2P <sub>1/2</sub> , 1, 0	2S <sub>1/2</sub> , 1, 0	2P <sub>1/2</sub> , 0, 0	2S <sub>1/2</sub> , 0, 0
2P <sub>3/2</sub> , 2, -1	$\frac{\sqrt{3}(g+2)}{4}e_+$	$\frac{g+2}{4\sqrt{3}}e_+$	$-\frac{g-1}{\sqrt{6}}e_+$	0	0	0
2P <sub>3/2</sub> , 1, -1	$-\frac{g+2}{12}e_+$	$\frac{5(g+2)}{12}e_+$	$\frac{\sqrt{2}(g-1)}{6}e_+$	0	$-\frac{\sqrt{2}(g-1)}{3}e_+$	0
2P <sub>1/2</sub> , 1, -1	$\frac{\sqrt{2}(g-1)}{6}e_+$	$\frac{\sqrt{2}(g-1)}{6}e_+$	$-\frac{g-4}{6}e_+$	0	$-\frac{g-4}{6}e_+$	0
2S <sub>1/2</sub> , 1, -1	0	0	0	$\frac{g}{2}e_+$	0	$\frac{g}{2}e_+$

Table A.5 (f)

	2P <sub>3/2</sub> , 2, -1	2P <sub>3/2</sub> , 1, -1	2P <sub>1/2</sub> , 1, -1	2S <sub>1/2</sub> , 1, -1	2P <sub>3/2</sub> , 2, -2
2P <sub>3/2</sub> , 2, -1	$\frac{g+2}{4}e_0$	$-\frac{g+2}{4\sqrt{3}}e_0$	$-\frac{g-1}{\sqrt{6}}e_0$	0	$-\frac{\sqrt{2}(g+2)}{4}e_-$
2P <sub>3/2</sub> , 1, -1	$-\frac{g+2}{4\sqrt{3}}e_0$	$\frac{5(g+2)}{12}e_0$	$-\frac{g-1}{3\sqrt{2}}e_0$	0	$-\frac{\sqrt{2}(g+2)}{4\sqrt{3}}e_-$
2P <sub>1/2</sub> , 1, -1	$-\frac{g-1}{\sqrt{6}}e_0$	$-\frac{g-1}{3\sqrt{2}}e_0$	$-\frac{g-4}{6}e_0$	0	$\frac{g-1}{\sqrt{3}}e_-$
2S <sub>1/2</sub> , 1, -1	0	0	0	$\frac{g}{2}e_0$	0
2P <sub>3/2</sub> , 2, -2	$\frac{\sqrt{2}(g+2)}{4}e_+$	$\frac{\sqrt{2}(g+2)}{4\sqrt{3}}e_+$	$-\frac{g-1}{\sqrt{3}}e_+$	0	$\frac{2+g}{2}e_0$

Table A.5 (g)

### A.3 Notations and Matrix Representations of $\underline{\tilde{\mathcal{M}}}_0$ , $\underline{\mathcal{D}}$ , and $\underline{\boldsymbol{\mu}}$ for Helium

The numbering scheme of the  $n = 2$   $^4\text{He}$  states in Table A.6 can be put up with a procedure analogous to that of hydrogen in Appendix A.1.

helium	
$\alpha$	$ n^{2S+1}\hat{L}_J, J_3, \boldsymbol{\mathcal{E}}, \boldsymbol{\mathcal{B}}\rangle$
1	$ 2^1\hat{\text{P}}_1, 1, \boldsymbol{\mathcal{E}}, \boldsymbol{\mathcal{B}}\rangle$
2	$ 2^1\hat{\text{P}}_1, 0, \boldsymbol{\mathcal{E}}, \boldsymbol{\mathcal{B}}\rangle$
3	$ 2^1\hat{\text{P}}_1, -1, \boldsymbol{\mathcal{E}}, \boldsymbol{\mathcal{B}}\rangle$
4	$ 2^3\hat{\text{P}}_0, 0, \boldsymbol{\mathcal{E}}, \boldsymbol{\mathcal{B}}\rangle$
5	$ 2^3\hat{\text{P}}_1, 1, \boldsymbol{\mathcal{E}}, \boldsymbol{\mathcal{B}}\rangle$
6	$ 2^3\hat{\text{P}}_1, 0, \boldsymbol{\mathcal{E}}, \boldsymbol{\mathcal{B}}\rangle$
7	$ 2^3\hat{\text{P}}_1, -1, \boldsymbol{\mathcal{E}}, \boldsymbol{\mathcal{B}}\rangle$
8	$ 2^3\hat{\text{P}}_2, 2, \boldsymbol{\mathcal{E}}, \boldsymbol{\mathcal{B}}\rangle$
9	$ 2^3\hat{\text{P}}_2, 1, \boldsymbol{\mathcal{E}}, \boldsymbol{\mathcal{B}}\rangle$
10	$ 2^3\hat{\text{P}}_2, 0, \boldsymbol{\mathcal{E}}, \boldsymbol{\mathcal{B}}\rangle$
11	$ 2^3\hat{\text{P}}_2, -1, \boldsymbol{\mathcal{E}}, \boldsymbol{\mathcal{B}}\rangle$
12	$ 2^3\hat{\text{P}}_2, -2, \boldsymbol{\mathcal{E}}, \boldsymbol{\mathcal{B}}\rangle$
13	$ 2^1\hat{\text{S}}_0, 0, \boldsymbol{\mathcal{E}}, \boldsymbol{\mathcal{B}}\rangle$
14	$ 2^3\hat{\text{S}}_1, 1, \boldsymbol{\mathcal{E}}, \boldsymbol{\mathcal{B}}\rangle$
15	$ 2^3\hat{\text{S}}_1, 0, \boldsymbol{\mathcal{E}}, \boldsymbol{\mathcal{B}}\rangle$
16	$ 2^3\hat{\text{S}}_1, -1, \boldsymbol{\mathcal{E}}, \boldsymbol{\mathcal{B}}\rangle$

**Table A.6:** The numbering scheme for the atomic  $n = 2$  states of helium, with principal quantum number  $n$ , total electron spin  $S$ , orbital angular momentum  $L$ , total angular momentum  $J$ , and its third component  $J_3$ . The nomenclature of the states  $|n^{2S+1}\hat{L}_J, J_3, \boldsymbol{\mathcal{E}}, \boldsymbol{\mathcal{B}}\rangle$  is analogous to that of hydrogen exchanging  $J$  for  $F$ , see Appendix A.1.

Tables A.8, A.9, and A.10 show the mass matrix of helium for zero external fields,  $\underline{\tilde{\mathcal{M}}}_0 = \underline{\mathcal{M}}_0 + \underline{\mathcal{M}}_{\text{PV}}$ , the electric dipole operator  $\underline{\mathcal{D}}$ , and the magnetic dipole operator  $\underline{\boldsymbol{\mu}}$  for the  $n = 2$  states of  $^4\text{He}$ . We give all these matrices in the basis of the pure 2S and 2P states, that is, the states for zero external fields and without the P-violating mixing. The matrices  $\underline{\mathcal{M}}_{\text{PV}}$ ,  $\underline{\mathcal{D}}$ , and  $\underline{\boldsymbol{\mu}}$  were derived by M. Puchalski via a variational method utilising an optimised set of 600 basis functions, cf. [189–191]. Employing a simple approach with hydrogen-like wave functions for the two electrons [173], we could also calculate the third component of  $\underline{\boldsymbol{\mu}} = -\mu_B(\mathbf{L} + g\mathbf{S})$  and found exact agreement with the third component of the matrix A.10. In Tables A.9 and A.10 we use the spherical unit vectors defined in (A.17).

With  $m, n \in \{1, 3\}$  denoting singlet (1) or triplet (3) states, respectively, we have the following relations for the PV-admixture quantities  $pv(^m\text{P}, ^n\text{S})$  in Table A.7:

$$pv(^m\text{P}, ^n\text{S}) = \kappa(^m\text{P}, ^n\text{S})^{-1} \langle ^m\text{P} | \delta^3(\mathbf{x}) \boldsymbol{\sigma} \cdot \vec{\mathbf{p}} + \boldsymbol{\sigma} \cdot \overleftarrow{\mathbf{p}} \delta^3(\mathbf{x}) | ^n\text{S} \rangle, \quad (\text{A.18})$$

$$pv(^n\text{S}, ^m\text{P}) = -pv(^m\text{P}, ^n\text{S}), \quad (\text{A.19})$$

### A.3. Notations and Matrix Representations of $\tilde{\mathcal{M}}_0$ , $\underline{D}$ , and $\underline{\mu}$ for Helium

where  $\kappa(^m\text{P}, ^n\text{S}) = \kappa(^n\text{S}, ^m\text{P})$  is a suitable constant. According to (2.33) and (2.35) the matrix elements of  $H_{\text{PV}}^{(1)}$  read

$$\begin{aligned} \langle ^m\text{P} | H_{\text{PV}}^{(1)} | ^n\text{S} \rangle &= \frac{G}{4\sqrt{2}m_e} ((1 - 4 \sin^2 \theta_W) Z - N) \kappa(^m\text{P}, ^n\text{S}) pv(^m\text{P}, ^n\text{S}) \\ &=: -i \delta(^m\text{P}, ^n\text{S}) \Delta(^m\text{P}, ^n\text{S}) \end{aligned} \quad (\text{A.20})$$

and  $\langle ^n\text{S} | H_{\text{PV}}^{(1)} | ^m\text{P} \rangle = -\langle ^m\text{P} | H_{\text{PV}}^{(1)} | ^n\text{S} \rangle$ . In (A.20) we define

$$\delta(^m\text{P}, ^n\text{S}) = \frac{G}{4\sqrt{2}m_e} ((1 - 4 \sin^2 \theta_W) Z - N) \frac{i \kappa(^m\text{P}, ^n\text{S}) pv(^m\text{P}, ^n\text{S})}{\Delta(^m\text{P}, ^n\text{S})}, \quad (\text{A.21})$$

$$\Delta(^m\text{P}, ^n\text{S}) = |E(^m\text{P}) - E(^n\text{S})|. \quad (\text{A.22})$$

	$^4\text{He}$	Ref.
$E(^1\text{P}_1)$	$5.130495(5) \times 10^9 \text{ MHz}$	[192]
$E(^3\text{P}_0)$	$5.069125(5) \times 10^9 \text{ MHz}$	[193]
$E(^3\text{P}_1)$	$5.069095(5) \times 10^9 \text{ MHz}$	[193]
$E(^3\text{P}_2)$	$5.069093(5) \times 10^9 \text{ MHz}$	[193]
$E(^1\text{S}_0)$	$4.984872(5) \times 10^9 \text{ MHz}$	[192, 193]
$E(^3\text{S}_1)$	$4.792361(5) \times 10^9 \text{ MHz}$	[192, 193]
$\Gamma_{3\text{S}}$	$1.272(13) \times 10^{-4} \text{ s}^{-1}$	[194]
$\Gamma_{1\text{S}}$	$0.0508(26) \text{ s}^{-1}$	[195]
$\Gamma_{3\text{P}}$	$1.0216(31) \times 10^7 \text{ s}^{-1}$	[196–199]
$\Gamma_{1\text{P}}$	$1.80087(54) \times 10^9 \text{ s}^{-1}$	[196]
$^1d_e$	$2.6729737072(5) \times 10^{-10} \text{ eV}/(\text{V/m})$	[78]
$^3d_e$	$2.320141227(7) \times 10^{-10} \text{ eV}/(\text{V/m})$	[78]
$\kappa(^3\text{P}, ^1\text{S}) \times pv(^3\text{P}, ^1\text{S})$	$i \times 25810.8(2) \text{ eV}^4$	[78]
$\kappa(^1\text{P}, ^3\text{S}) \times pv(^1\text{P}, ^3\text{S})$	$\frac{i}{\sqrt{3}} \times 20073.2(4) \text{ eV}^4$	[78]
$\kappa(^3\text{P}, ^3\text{S}) \times pv(^3\text{P}, ^3\text{S})$	$i\sqrt{\frac{2}{3}} \times 68186.7(6) \text{ eV}^4$	[78]
$\delta_a = \delta(^3\text{P}_0, ^1\text{S}_0)$	$1.040926 \times 10^{-30}$	A.21
$\delta_b = \delta(^1\text{P}_1, ^3\text{S}_1)$	$1.164582 \times 10^{-31}$	A.21
$\delta_c = \delta(^3\text{P}_1, ^3\text{S}_1)$	$6.835910 \times 10^{-31}$	A.21
$\Delta_a = \Delta(^3\text{P}_0, ^1\text{S}_0)$	$0.084255 \times 10^9 \text{ MHz} = 0.348444 \text{ eV}$	A.22
$\Delta_b = \Delta(^1\text{P}_1, ^3\text{S}_1)$	$0.338134 \times 10^9 \text{ MHz} = 1.398408 \text{ eV}$	A.22
$\Delta_c = \Delta(^3\text{P}_1, ^3\text{S}_1)$	$0.276735 \times 10^9 \text{ MHz} = 1.144482 \text{ eV}$	A.22

**Table A.7:** Values of parameters and physical quantities for  $^4\text{He}$  as used in Tables A.8 and A.9. The energy values  $E(^{2S+1}L_J)$  are taken from NIST [200], the corresponding errors from [193], referring to [192]. The decay rates  $\Gamma_{2S+1L}$  are those in vacuum. The errors of the quantities  $pv(^3\text{P}, ^1\text{S})$  and  $^{2S+1}d_e$  are given according to [78].

## Chapter A. Notations and Definitions

---

**Table A.8:** The mass matrix  $\tilde{\mathcal{M}}_0$  for the  $n = 2$  states of  ${}^4\text{He}$ . The  $n = 2$  energies  $E({}^{2S+1}L_J)$  with respect to the  $n = 1$  ground state  $1{}^1\text{S}_0$  and the total decay rates  $\Gamma_{2S+1L}$  are given in Table A.7, cf. the NIST Atomic Spectra Database Lines Data [200].

	$2^3\text{P}_{2,2}$	$2^3\text{P}_{2,1}$	$2^3\text{P}_{1,1}$	$2^3\text{S}_{1,1}$	$2^1\text{P}_{1,1}$
$2^3\text{P}_{2,2}$	$E({}^3\text{P}_2)$ $-\frac{i}{2}\Gamma_{3\text{P}}$	0	0	0	0
$2^3\text{P}_{2,1}$	0	$E({}^3\text{P}_2)$ $-\frac{i}{2}\Gamma_{3\text{P}}$	0	0	0
$2^3\text{P}_{1,1}$	0	0	$E({}^3\text{P}_1)$ $-\frac{i}{2}\Gamma_{3\text{P}}$	$-i\delta_c\Delta_c$	0
$2^3\text{S}_{1,1}$	0	0	$i\delta_c\Delta_c$	$E({}^3\text{S}_1)$ $-\frac{i}{2}\Gamma_{3\text{S}}$	$-i\delta_b\Delta_b$
$2^1\text{P}_{1,1}$	0	0	0	$i\delta_b\Delta_b$	$E({}^1\text{P}_1)$ $-\frac{i}{2}\Gamma_{1\text{P}}$

Table A.8 (a)

	$2^3\text{P}_{2,0}$	$2^3\text{P}_{1,0}$	$2^3\text{S}_{1,0}$	$2^1\text{P}_{1,0}$	$2^3\text{P}_{0,0}$	$2^1\text{S}_{0,0}$
$2^3\text{P}_{2,0}$	$E({}^3\text{P}_2)$ $-\frac{i}{2}\Gamma_{3\text{P}}$	0	0	0	0	0
$2^3\text{P}_{1,0}$	0	$E({}^3\text{P}_1)$ $-\frac{i}{2}\Gamma_{3\text{P}}$	$-i\delta_c\Delta_c$	0	0	0
$2^3\text{S}_{1,0}$	0	$i\delta_c\Delta_c$	$E({}^3\text{S}_1)$ $-\frac{i}{2}\Gamma_{3\text{S}}$	$-i\delta_b\Delta_b$	0	0
$2^1\text{P}_{1,0}$	0	0	$i\delta_b\Delta_b$	$E({}^1\text{P}_1)$ $-\frac{i}{2}\Gamma_{1\text{P}}$	0	0
$2^3\text{P}_{0,0}$	0	0	0	0	$E({}^3\text{P}_0)$ $-\frac{i}{2}\Gamma_{3\text{P}}$	$-i\delta_a\Delta_a$
$2^1\text{S}_{0,0}$	0	0	0	0	$i\delta_a\Delta_a$	$E({}^1\text{S}_0)$ $-\frac{i}{2}\Gamma_{1\text{S}}$

Table A.8 (b)

A.3. Notations and Matrix Representations of  $\tilde{\mathcal{M}}_0$ ,  $\underline{D}$ , and  $\underline{\mu}$  for Helium

	$2^3P_{2,-1}$	$2^3P_{1,-1}$	$2^3S_{1,-1}$	$2^1P_{1,-1}$	$2^3P_{2,-2}$
$2^3P_{2,-1}$	$E(^3P_2)$ $-\frac{i}{2}\Gamma_{3P}$	0	0	0	0
$2^3P_{1,-1}$	0	$E(^3P_1)$ $-\frac{i}{2}\Gamma_{3P}$	$-i\delta_c\Delta_c$	0	0
$2^3S_{1,-1}$	0	$i\delta_c\Delta_c$	$E(^3S_1)$ $-\frac{i}{2}\Gamma_{3S}$	$-i\delta_b\Delta_b$	0
$2^1P_{1,-1}$	0	0	$i\delta_b\Delta_b$	$E(^1P_1)$ $-\frac{i}{2}\Gamma_{1P}$	0
$2^3P_{2,-2}$	0	0	0	0	$E(^3P_2)$ $-\frac{i}{2}\Gamma_{3P}$

Table A.8 (c)

Table A.9: The suitably normalised electric dipole operator  $\underline{D}/(e r_B)$  for the  $n = 2$  states of helium.

	$2^3P_{2,2}$	$2^3P_{2,1}$	$2^3P_{1,1}$	$2^3S_{1,1}$
$2^3P_{2,2}$	0	0	0	$-\frac{3d_e}{\sqrt{3}}e_-$
$2^3P_{2,1}$	0	0	0	$\frac{3d_e}{\sqrt{6}}e_0$
$2^3P_{1,1}$	0	0	0	$-\frac{3d_e}{\sqrt{6}}e_0$
$2^3S_{1,1}$	$\frac{3d_e}{\sqrt{3}}e_+$	$\frac{3d_e}{\sqrt{6}}e_0$	$-\frac{3d_e}{\sqrt{6}}e_0$	0

Table A.9 (a)

	$2^3P_{2,1}$	$2^3P_{1,1}$	$2^3S_{1,1}$	$2^1P_{1,1}$
$2^3P_{2,0}$	0	0	$-\frac{3d_e}{3\sqrt{2}}e_+$	0
$2^3P_{1,0}$	0	0	$\frac{3d_e}{\sqrt{6}}e_+$	0
$2^3S_{1,0}$	$\frac{3d_e}{\sqrt{6}}e_+$	$\frac{3d_e}{\sqrt{6}}e_+$	0	0
$2^1P_{1,0}$	0	0	0	0
$2^3P_{0,0}$	0	0	$-\frac{3d_e}{3}e_+$	0
$2^1S_{0,0}$	0	0	0	$\frac{1d_e}{\sqrt{3}}e_+$

Table A.9 (b)

	$2^3P_{2,0}$	$2^3P_{1,0}$	$2^3S_{1,0}$	$2^1P_{1,0}$	$2^3P_{0,0}$	$2^1S_{0,0}$
$2^3P_{2,1}$	0	0	$-\frac{3d_e}{\sqrt{6}}e_-$	0	0	0
$2^3P_{1,1}$	0	0	$-\frac{3d_e}{\sqrt{6}}e_-$	0	0	0
$2^3S_{1,1}$	$\frac{3d_e}{3\sqrt{2}}e_-$	$-\frac{3d_e}{\sqrt{6}}e_-$	0	0	$\frac{3d_e}{3}e_-$	0
$2^1P_{1,1}$	0	0	0	0	0	$-\frac{1d_e}{\sqrt{3}}e_-$

Table A.9 (c)

	$2^3P_{2,0}$	$2^3P_{1,0}$	$2^3S_{1,0}$	$2^1P_{1,0}$	$2^3P_{0,0}$	$2^1S_{0,0}$	$2^3P_{2,-1}$	$2^3P_{1,-1}$	$2^3S_{1,-1}$	$2^1P_{1,-1}$	$2^3P_{2,-2}$
$2^3P_{2,0}$	0	0	$\frac{3d_e\sqrt{2}}{3}e_0$	0	0	0	0	0	$-\frac{3d_e}{3\sqrt{2}}e_-$	0	0
$2^3P_{1,0}$	0	0	0	0	0	0	0	0	$-\frac{3d_e}{\sqrt{6}}e_-$	0	0
$2^3S_{1,0}$	$\frac{3d_e\sqrt{2}}{3}e_0$	0	0	0	$-\frac{3d_e}{3}e_0$	0	$\frac{3d_e}{\sqrt{6}}e_-$	$-\frac{3d_e}{\sqrt{6}}e_-$	0	0	0
$2^1P_{1,0}$	0	0	0	0	0	$\frac{1d_e}{\sqrt{3}}e_0$	0	0	0	0	0
$2^3P_{0,0}$	0	0	$-\frac{3d_e}{3}e_0$	0	0	0	0	0	$-\frac{3d_e}{3}e_-$	0	0
$2^1S_{0,0}$	0	0	0	$\frac{1d_e}{\sqrt{3}}e_0$	0	0	0	0	0	$\frac{1d_e}{\sqrt{3}}e_-$	0
$2^3P_{2,-1}$	0	0	$-\frac{3d_e}{\sqrt{6}}e_+$	0	0	0	0	0	$\frac{3d_e}{\sqrt{6}}e_0$	0	0
$2^3P_{1,-1}$	0	0	$\frac{3d_e}{\sqrt{6}}e_+$	0	0	0	0	0	$\frac{3d_e}{\sqrt{6}}e_0$	0	0
$2^3S_{1,-1}$	$\frac{3d_e}{3\sqrt{2}}e_+$	$\frac{3d_e}{\sqrt{6}}e_+$	0	0	$\frac{3d_e}{3}e_+$	0	$\frac{3d_e}{\sqrt{6}}e_0$	$\frac{3d_e}{\sqrt{6}}e_0$	0	0	$\frac{3d_e}{\sqrt{3}}e_-$
$2^1P_{1,-1}$	0	0	0	0	0	$-\frac{1d_e}{\sqrt{3}}e_+$	0	0	0	0	0
$2^3P_{2,-2}$	0	0	0	0	0	0	0	0	$-\frac{3d_e}{\sqrt{3}}e_+$	0	0

Table A.9 (d)

**Table A.10:** The suitably normalised magnetic dipole operator  $\underline{\mu}/\mu_B$  for the  $n = 2$  states of helium.

	$2^3P_{2,2}$	$2^3P_{2,1}$	$2^3P_{1,1}$	$2^3S_{1,1}$	$2^1P_{1,1}$	$2^3P_{2,0}$	$2^3P_{1,0}$	$2^3S_{1,0}$	$2^1P_{1,0}$	$2^3P_{0,0}$
$2^3P_{2,2}$	$-(g+1)e_0$	$-\frac{g+1}{\sqrt{2}}e_-$	$\frac{1-g}{\sqrt{2}}e_-$	0	0	0	0	0	0	0
$2^3P_{2,1}$	$\frac{g+1}{\sqrt{2}}e_+$	$-\frac{g+1}{2}e_0$	$\frac{g-1}{2}e_0$	0	0	$-\frac{\sqrt{3}(g+1)}{2}e_-$	$\frac{1-g}{2}e_-$	0	0	0
$2^3P_{1,1}$	$\frac{g-1}{\sqrt{2}}e_+$	$\frac{g-1}{2}e_0$	$-\frac{g+1}{2}e_0$	0	0	$\frac{g-1}{2\sqrt{3}}e_-$	$-\frac{g+1}{2}e_-$	0	0	$\frac{\sqrt{2}(1-g)}{\sqrt{3}}e_-$
$2^3S_{1,1}$	0	0	0	$-ge_0$	0	0	0	$-ge_-$	0	0
$2^1P_{1,1}$	0	0	0	0	$-e_0$	0	0	0	$-e_-$	0
$2^3P_{2,0}$	0	$\frac{g+1}{2}\sqrt{3}e_+$	$\frac{1-g}{2\sqrt{3}}e_+$	0	0	0	$\frac{g-1}{\sqrt{3}}e_0$	0	0	0
$2^3P_{1,0}$	0	$\frac{g-1}{2}e_+$	$\frac{g+1}{2}e_+$	0	0	$\frac{g-1}{\sqrt{3}}e_0$	0	0	0	$\frac{\sqrt{2}(g-1)}{\sqrt{3}}e_0$
$2^3S_{1,0}$	0	0	0	$ge_+$	0	0	0	0	0	0
$2^1P_{1,0}$	0	0	0	0	$e_+$	0	0	0	0	0
$2^3P_{0,0}$	0	0	$\frac{\sqrt{2}(g-1)}{\sqrt{3}}e_+$	0	0	0	$\frac{\sqrt{2}(g-1)}{\sqrt{3}}e_0$	0	0	0

**Table A.10 (a)**

A.3. Notations and Matrix Representations of  $\tilde{\mathcal{M}}_0$ ,  $\underline{D}$ , and  $\underline{\mu}$  for Helium

	$2^3P_{2,0}$	$2^3P_{1,0}$	$2^3S_{1,0}$	$2^1P_{1,0}$	$2^3P_{0,0}$
$2^3P_{2,-1}$	$\frac{\sqrt{3}(g+1)}{2}e_+$	$\frac{1-g}{2}e_+$	0	0	0
$2^3P_{1,-1}$	$\frac{g-1}{2\sqrt{3}}e_+$	$\frac{g+1}{2}e_+$	0	0	$\frac{\sqrt{2}(1-g)}{\sqrt{3}}e_+$
$2^3S_{1,-1}$	0	0	$ge_+$	0	0
$2^1P_{1,-1}$	0	0	0	$e_+$	0

Table A.10 (b)

	$2^3P_{2,-1}$	$2^3P_{1,-1}$	$2^3S_{1,-1}$	$2^1P_{1,-1}$
$2^3P_{2,0}$	$-\frac{\sqrt{3}(g+1)}{2}e_-$	$\frac{1-g}{2\sqrt{3}}e_-$	0	0
$2^3P_{1,0}$	$\frac{g-1}{2}e_-$	$-\frac{g+1}{2}e_-$	0	0
$2^3S_{1,0}$	0	0	$-ge_-$	0
$2^1P_{1,0}$	0	0	0	$-e_-$
$2^3P_{0,0}$	0	$\frac{\sqrt{2}(g-1)}{\sqrt{3}}e_-$	0	0

Table A.10 (c)

	$2^3P_{2,-1}$	$2^3P_{1,-1}$	$2^3S_{1,-1}$	$2^1P_{1,-1}$	$2^3P_{2,-2}$
$2^3P_{2,-1}$	$\frac{g+1}{2}e_0$	$\frac{g-1}{2}e_0$	0	0	$-\frac{g+1}{\sqrt{2}}e_-$
$2^3P_{1,-1}$	$\frac{g-1}{2}e_0$	$\frac{g+1}{2}e_0$	0	0	$\frac{g-1}{\sqrt{2}}e_-$
$2^3S_{1,-1}$	0	0	$ge_0$	0	0
$2^1P_{1,-1}$	0	0	0	$e_0$	0
$2^3P_{2,-2}$	$\frac{g+1}{\sqrt{2}}e_+$	$\frac{1-g}{\sqrt{2}}e_+$	0	0	$(g+1)e_0$

Table A.10 (d)



## B Flux-Density Vector Fields

We now present several relations and derivations for the flux-density vector fields discussed in Sections 3.5 and 3.6.1. The following derivations are taken from [40].

### B.1 Relations for the Geometric Flux Densities

In this appendix we derive the representations (3.66), (3.67), and (3.68) for  $Y_{\alpha,ab}(K)$  and its derivatives, respectively. In the following, we will omit the  $K$ -dependence of all quantities for abbreviation. We consider the expression

$$X_{\alpha,ab} := \frac{i}{2} \frac{1}{2\pi i} \sum_{\beta,\gamma} \oint_{S_\alpha} d\zeta \frac{\text{Tr} \left[ \mathbb{P}_\beta \frac{\partial \mathcal{M}}{\partial K_a} \mathbb{P}_\gamma \frac{\partial \mathcal{M}}{\partial K_b} \right]}{(\zeta - E_\beta)(\zeta - E_\gamma)^2}. \quad (\text{B.1})$$

According to the residue theorem the integral vanishes for  $\beta = \gamma = \alpha$  since a pole of third order at  $\zeta = E_\alpha$  gives a residual of zero

$$\oint_{S_\alpha} d\zeta \frac{1}{(\zeta - E_\alpha)^3} = 2\pi i \text{Res} \left( \frac{1}{(\zeta - E_\alpha)^3}; \zeta = E_\alpha \right) = 0. \quad (\text{B.2})$$

Let  $D \subset \mathbb{C}$  be a simply connected set with  $S_\alpha$  entirely inside  $D$  and  $E_\sigma \notin D$  for all  $\sigma \neq \alpha$ ; see Figure 3.6. Therefore, for  $\beta \neq \alpha$  and  $\gamma \neq \alpha$  the integrand in (B.1) is analytic on  $D$ , and the integral in (B.1) vanishes due to Cauchy's integral theorem. The only two remaining cases  $\beta = \alpha$  and  $\gamma \neq \alpha$  as well as  $\beta \neq \alpha$  and  $\gamma = \alpha$  can be treated using again the residue theorem. We find easily

$$\begin{aligned} X_{\alpha,ab} &= \frac{i}{2} \sum_{\gamma \neq \alpha} \frac{1}{(E_\alpha - E_\gamma)^2} \text{Tr} \left[ \mathbb{P}_\alpha \frac{\partial \mathcal{M}}{\partial K_a} \mathbb{P}_\gamma \frac{\partial \mathcal{M}}{\partial K_b} \right] + \frac{i}{2} \sum_{\beta \neq \alpha} \frac{-1}{(E_\alpha - E_\beta)^2} \text{Tr} \left[ \mathbb{P}_\beta \frac{\partial \mathcal{M}}{\partial K_a} \mathbb{P}_\alpha \frac{\partial \mathcal{M}}{\partial K_b} \right] \\ &= \frac{i}{2} \sum_{\beta \neq \alpha} \frac{1}{(E_\alpha - E_\beta)^2} \text{Tr} \left[ \mathbb{P}_\alpha \frac{\partial \mathcal{M}}{\partial K_a} \mathbb{P}_\beta \frac{\partial \mathcal{M}}{\partial K_b} \right] + \frac{i}{2} \sum_{\beta \neq \alpha} \frac{-1}{(E_\alpha - E_\beta)^2} \text{Tr} \left[ \mathbb{P}_\alpha \frac{\partial \mathcal{M}}{\partial K_b} \mathbb{P}_\beta \frac{\partial \mathcal{M}}{\partial K_a} \right] \\ &= \frac{i}{2} \sum_{\beta \neq \alpha} \frac{1}{(E_\alpha - E_\beta)^2} \text{Tr} \left[ \mathbb{P}_\alpha \frac{\partial \mathcal{M}}{\partial K_a} \mathbb{P}_\beta \frac{\partial \mathcal{M}}{\partial K_b} \right] - (a \leftrightarrow b) \end{aligned} \quad (\text{B.3})$$

which is exactly  $Y_{\alpha,ab}$ , see (3.65). Thus, we obtain the integral representation (3.66) for  $Y_{\alpha,ab}$

$$\begin{aligned} Y_{\alpha,ab} &= X_{\alpha,ab} = \frac{i}{2} \frac{1}{2\pi i} \oint_{S_\alpha} d\zeta \text{Tr} \left[ \left( \sum_\beta \frac{\mathbb{P}_\beta}{\zeta - E_\beta} \right) \frac{\partial \mathcal{M}}{\partial K_a} \left( \sum_\gamma \frac{\mathbb{P}_\gamma}{(\zeta - E_\gamma)^2} \right) \frac{\partial \mathcal{M}}{\partial K_b} \right] \\ &= \frac{i}{2} \frac{1}{2\pi i} \oint_{S_\alpha} d\zeta \text{Tr} \left[ \frac{1}{\zeta - \mathcal{M}} \frac{\partial \mathcal{M}}{\partial K_a} \frac{1}{(\zeta - \mathcal{M})^2} \frac{\partial \mathcal{M}}{\partial K_b} \right], \end{aligned} \quad (\text{B.4})$$

where we use the relation (3.54) for the quasi projectors in the last step.

In order to calculate the derivatives of  $Y_{\alpha,ab}$  we first derive some useful relations:

$$\begin{aligned}
 0 &= \frac{\partial}{\partial K_a} \mathbb{1} = \frac{\partial}{\partial K_a} [(\zeta - \underline{\mathcal{M}})^{-1}(\zeta - \underline{\mathcal{M}})] \\
 &= \frac{\partial}{\partial K_a} [(\zeta - \underline{\mathcal{M}})^{-1}] (\zeta - \underline{\mathcal{M}}) + (\zeta - \underline{\mathcal{M}})^{-1} \frac{\partial}{\partial K_a} [\zeta - \underline{\mathcal{M}}] \\
 \Leftrightarrow \frac{\partial}{\partial K_a} \frac{1}{\zeta - \underline{\mathcal{M}}} &= \frac{1}{\zeta - \underline{\mathcal{M}}} \frac{\partial \underline{\mathcal{M}}}{\partial K_a} \frac{1}{\zeta - \underline{\mathcal{M}}}, \tag{B.5}
 \end{aligned}$$

$$\begin{aligned}
 0 &= \frac{\partial}{\partial K_a} \mathbb{1} = \frac{\partial}{\partial K_a} [(\zeta - \underline{\mathcal{M}})^{-2}(\zeta - \underline{\mathcal{M}})^2] \\
 &= \frac{\partial}{\partial K_a} [(\zeta - \underline{\mathcal{M}})^{-2}] (\zeta - \underline{\mathcal{M}})^2 + (\zeta - \underline{\mathcal{M}})^{-2} \frac{\partial}{\partial K_a} [(\zeta - \underline{\mathcal{M}})^2] \\
 \Leftrightarrow \frac{\partial}{\partial K_a} [(\zeta - \underline{\mathcal{M}})^{-2}] &= (\zeta - \underline{\mathcal{M}})^{-2} \left( \frac{\partial \underline{\mathcal{M}}}{\partial K_a} (\zeta - \underline{\mathcal{M}}) + (\zeta - \underline{\mathcal{M}}) \frac{\partial \underline{\mathcal{M}}}{\partial K_a} \right) (\zeta - \underline{\mathcal{M}})^{-2} \\
 \Leftrightarrow \frac{\partial}{\partial K_a} \frac{1}{(\zeta - \underline{\mathcal{M}})^2} &= \frac{1}{(\zeta - \underline{\mathcal{M}})^2} \frac{\partial \underline{\mathcal{M}}}{\partial K_a} \frac{1}{\zeta - \underline{\mathcal{M}}} + \frac{1}{\zeta - \underline{\mathcal{M}}} \frac{\partial \underline{\mathcal{M}}}{\partial K_a} \frac{1}{(\zeta - \underline{\mathcal{M}})^2}. \tag{B.6}
 \end{aligned}$$

With (B.5) and (B.6) we obtain from (B.4)

$$\begin{aligned}
 \frac{\partial}{\partial K_a} Y_{\alpha,bc} &= \frac{i}{2} \frac{1}{2\pi i} \oint_{S_\alpha} d\zeta \left\{ \text{Tr} \left[ \frac{1}{\zeta - \underline{\mathcal{M}}} \frac{\partial^2 \underline{\mathcal{M}}}{\partial K_a \partial K_b} \frac{1}{(\zeta - \underline{\mathcal{M}})^2} \frac{\partial \underline{\mathcal{M}}}{\partial K_c} \right] \right. \\
 &\quad + \text{Tr} \left[ \frac{1}{\zeta - \underline{\mathcal{M}}} \frac{\partial \underline{\mathcal{M}}}{\partial K_b} \frac{1}{(\zeta - \underline{\mathcal{M}})^2} \frac{\partial^2 \underline{\mathcal{M}}}{\partial K_a \partial K_c} \right] \\
 &\quad + \text{Tr} \left[ \frac{1}{\zeta - \underline{\mathcal{M}}} \frac{\partial \underline{\mathcal{M}}}{\partial K_a} \frac{1}{\zeta - \underline{\mathcal{M}}} \frac{\partial \underline{\mathcal{M}}}{\partial K_b} \frac{1}{(\zeta - \underline{\mathcal{M}})^2} \frac{\partial \underline{\mathcal{M}}}{\partial K_c} \right] \\
 &\quad + \text{Tr} \left[ \frac{1}{\zeta - \underline{\mathcal{M}}} \frac{\partial \underline{\mathcal{M}}}{\partial K_b} \frac{1}{(\zeta - \underline{\mathcal{M}})^2} \frac{\partial \underline{\mathcal{M}}}{\partial K_a} \frac{1}{\zeta - \underline{\mathcal{M}}} \frac{\partial \underline{\mathcal{M}}}{\partial K_c} \right] \\
 &\quad \left. + \text{Tr} \left[ \frac{1}{\zeta - \underline{\mathcal{M}}} \frac{\partial \underline{\mathcal{M}}}{\partial K_b} \frac{1}{\zeta - \underline{\mathcal{M}}} \frac{\partial \underline{\mathcal{M}}}{\partial K_a} \frac{1}{(\zeta - \underline{\mathcal{M}})^2} \frac{\partial \underline{\mathcal{M}}}{\partial K_c} \right] \right\}. \tag{B.7}
 \end{aligned}$$

Using the cyclicity of the trace and performing partial integrations of the second and fourth summand in (B.7) we get

$$\begin{aligned}
 \frac{\partial}{\partial K_a} Y_{\alpha,bc} &= \frac{i}{2} \frac{1}{2\pi i} \oint_{S_\alpha} d\zeta \left\{ \text{Tr} \left[ \frac{1}{\zeta - \underline{\mathcal{M}}} \frac{\partial^2 \underline{\mathcal{M}}}{\partial K_a \partial K_b} \frac{1}{(\zeta - \underline{\mathcal{M}})^2} \frac{\partial \underline{\mathcal{M}}}{\partial K_c} \right] \right. \\
 &\quad - \text{Tr} \left[ \frac{1}{(\zeta - \underline{\mathcal{M}})^2} \frac{\partial \underline{\mathcal{M}}}{\partial K_b} \frac{1}{\zeta - \underline{\mathcal{M}}} \frac{\partial^2 \underline{\mathcal{M}}}{\partial K_a \partial K_c} \right] \\
 &\quad + \text{Tr} \left[ \frac{1}{\zeta - \underline{\mathcal{M}}} \frac{\partial \underline{\mathcal{M}}}{\partial K_a} \frac{1}{\zeta - \underline{\mathcal{M}}} \frac{\partial \underline{\mathcal{M}}}{\partial K_b} \frac{1}{(\zeta - \underline{\mathcal{M}})^2} \frac{\partial \underline{\mathcal{M}}}{\partial K_c} \right] \\
 &\quad - \text{Tr} \left[ \frac{1}{(\zeta - \underline{\mathcal{M}})^2} \frac{\partial \underline{\mathcal{M}}}{\partial K_c} \frac{1}{\zeta - \underline{\mathcal{M}}} \frac{\partial \underline{\mathcal{M}}}{\partial K_b} \frac{1}{\zeta - \underline{\mathcal{M}}} \frac{\partial \underline{\mathcal{M}}}{\partial K_a} \right] \\
 &\quad - \text{Tr} \left[ \frac{1}{\zeta - \underline{\mathcal{M}}} \frac{\partial \underline{\mathcal{M}}}{\partial K_c} \frac{1}{(\zeta - \underline{\mathcal{M}})^2} \frac{\partial \underline{\mathcal{M}}}{\partial K_b} \frac{1}{\zeta - \underline{\mathcal{M}}} \frac{\partial \underline{\mathcal{M}}}{\partial K_a} \right] \\
 &\quad \left. + \text{Tr} \left[ \frac{1}{\zeta - \underline{\mathcal{M}}} \frac{\partial \underline{\mathcal{M}}}{\partial K_b} \frac{1}{\zeta - \underline{\mathcal{M}}} \frac{\partial \underline{\mathcal{M}}}{\partial K_a} \frac{1}{(\zeta - \underline{\mathcal{M}})^2} \frac{\partial \underline{\mathcal{M}}}{\partial K_c} \right] \right\}. \tag{B.8}
 \end{aligned}$$

---

## B.1. Relations for the Geometric Flux Densities

---

Again, using the cyclicity of the trace this can be simplified to

$$\begin{aligned} \frac{\partial}{\partial K_a} Y_{\alpha,bc} = & \frac{i}{2} \frac{1}{2\pi i} \oint_{S_\alpha} d\zeta \left\{ \text{Tr} \left[ \frac{1}{\zeta - \underline{\mathcal{M}}} \frac{\partial^2 \underline{\mathcal{M}}}{\partial K_a \partial K_b} \frac{1}{(\zeta - \underline{\mathcal{M}})^2} \frac{\partial \underline{\mathcal{M}}}{\partial K_c} \right] \right. \\ & \left. + \text{Tr} \left[ \frac{1}{\zeta - \underline{\mathcal{M}}} \frac{\partial \underline{\mathcal{M}}}{\partial K_a} \frac{1}{\zeta - \underline{\mathcal{M}}} \frac{\partial \underline{\mathcal{M}}}{\partial K_b} \frac{1}{(\zeta - \underline{\mathcal{M}})^2} \frac{\partial \underline{\mathcal{M}}}{\partial K_c} \right] \right\} - (b \leftrightarrow c) , \end{aligned} \quad (\text{B.9})$$

which proves (3.67). With (3.54) we find

$$\begin{aligned} \frac{\partial}{\partial K_a} Y_{\alpha,bc} = & \frac{i}{2} \frac{1}{2\pi i} \left\{ \sum_{\beta,\gamma} \oint_{S_\alpha} d\zeta (\zeta - E_\beta)^{-1} (\zeta - E_\gamma)^{-2} \text{Tr} \left[ \mathbb{P}_\beta \frac{\partial^2 \underline{\mathcal{M}}}{\partial K_a \partial K_b} \mathbb{P}_\gamma \frac{\partial \underline{\mathcal{M}}}{\partial K_c} \right] \right. \\ & \left. + \sum_{\beta,\gamma,\sigma} \oint_{S_\alpha} d\zeta (\zeta - E_\beta)^{-1} (\zeta - E_\gamma)^{-1} (\zeta - E_\sigma)^{-2} \text{Tr} \left[ \mathbb{P}_\beta \frac{\partial \underline{\mathcal{M}}}{\partial K_a} \mathbb{P}_\gamma \frac{\partial \underline{\mathcal{M}}}{\partial K_b} \mathbb{P}_\sigma \frac{\partial \underline{\mathcal{M}}}{\partial K_c} \right] \right\} \\ & - (b \leftrightarrow c) . \end{aligned} \quad (\text{B.10})$$

The integrals in (B.10) are easily evaluated using Cauchy's theorems. With the short hand notations

$$\beta := \mathbb{P}_\beta , \quad (\text{B.11})$$

$$a := \frac{\partial \underline{\mathcal{M}}}{\partial K_a} , \quad (\text{B.12})$$

$$(ab) := \frac{\partial^2 \underline{\mathcal{M}}}{\partial K_a \partial K_b} \quad (\text{B.13})$$

we obtain

$$\begin{aligned} \frac{\partial}{\partial K_a} Y_{\alpha,bc} = & \frac{i}{2} \left\{ \sum_{\gamma \neq \alpha} (E_\alpha - E_\gamma)^{-2} \text{Tr}[\alpha(ab)\gamma c] + \sum_{\beta \neq \alpha} -(E_\alpha - E_\beta)^{-2} \text{Tr}[\beta(ab)\alpha c] \right. \\ & - 2 \sum_{\sigma \neq \alpha} (E_\alpha - E_\sigma)^{-3} \text{Tr}[\alpha a \alpha b \sigma c] + \sum_{\gamma \neq \alpha} (E_\alpha - E_\gamma)^{-3} \text{Tr}[\alpha a \gamma b \alpha c] \\ & + \sum_{\beta \neq \alpha} (E_\alpha - E_\beta)^{-3} \text{Tr}[\beta a \alpha b \alpha c] \\ & + \sum_{\gamma, \sigma \neq \alpha} (E_\alpha - E_\gamma)^{-1} (E_\alpha - E_\sigma)^{-2} \text{Tr}[\alpha a \gamma b \sigma c] \\ & + \sum_{\beta, \sigma \neq \alpha} (E_\alpha - E_\beta)^{-1} (E_\alpha - E_\sigma)^{-2} \text{Tr}[\beta a \alpha b \sigma c] \\ & - \sum_{\beta, \gamma \neq \alpha} (E_\alpha - E_\beta)^{-1} (E_\alpha - E_\gamma)^{-2} \text{Tr}[\beta a \gamma b \alpha c] \\ & \left. - \sum_{\beta, \gamma \neq \alpha} (E_\alpha - E_\gamma)^{-1} (E_\alpha - E_\beta)^{-2} \text{Tr}[\beta a \gamma b \alpha c] \right\} - (b \leftrightarrow c) . \end{aligned} \quad (\text{B.14})$$

This can be simplified to

$$\begin{aligned}
 \frac{\partial}{\partial K_a} Y_{\alpha,bc} &= \frac{i}{2} \left\{ \sum_{\beta \neq \alpha} (E_\alpha - E_\beta)^{-2} \text{Tr}[\alpha(ab)\beta c - \alpha c\beta(ab)] \right. \\
 &+ \sum_{\beta \neq \alpha} (E_\alpha - E_\beta)^{-3} \text{Tr}[-2\alpha aab\beta c + \alpha a\beta b\alpha c + \beta aab\alpha c] \\
 &+ \sum_{\beta, \gamma \neq \alpha} (E_\alpha - E_\beta)^{-1} (E_\alpha - E_\gamma)^{-2} \text{Tr}[\alpha a\beta b\gamma c + \beta a\alpha b\gamma c - \gamma a\beta b\alpha c - \beta a\gamma b\alpha c] \left. \right\} \\
 &- (b \leftrightarrow c)
 \end{aligned} \tag{B.15}$$

which proves (3.68).

## B.2 Useful Expressions for Parity-Violating Fluxes

In this appendix we derive the divergence condition (3.75), present several useful relations for the resolvent  $(\zeta - \mathcal{M})^{-1}$ , derive  $\mathcal{I}_{\alpha,jk}^{(\mathcal{E})\text{PV}}$  (3.108), and give the analogous expressions for  $\mathcal{I}_{\alpha,jk}^{(\mathcal{B})\text{PV}}$  and  $\mathcal{I}_{\alpha,jk}^{(\mathcal{E},\mathcal{B})\text{PV}}$ . With  $d = \sum_a dK_a \frac{\partial}{\partial K_a} = \sum_a dK_a \partial_a$  and the short-hand notation  $\Upsilon(abc) \kappa(abc) := \partial_a Y_{\alpha,bc} dK_a \wedge dK_b \wedge dK_c$  we have

$$\begin{aligned}
 0 &\stackrel{(3.74)}{=} d \sum_{bc} Y_{\alpha,bc} dK_b \wedge dK_c \\
 &= \sum_{abc} \partial_a Y_{\alpha,bc} dK_a \wedge dK_b \wedge dK_c \\
 &= \sum_{\substack{abc \\ (b < c)}} \Upsilon(abc) \kappa(abc) + \sum_{\substack{abc \\ (c < b)}} \Upsilon(abc) \kappa(abc) \\
 &= \sum_{\substack{abc \\ (a < b < c)}} \Upsilon(abc) \kappa(abc) + \sum_{\substack{abc \\ (b < a < c)}} \Upsilon(abc) \kappa(abc) + \sum_{\substack{abc \\ (b < c < a)}} \Upsilon(abc) \kappa(abc) \\
 &+ \sum_{\substack{abc \\ (a < c < b)}} \Upsilon(abc) \kappa(abc) + \sum_{\substack{abc \\ (c < a < b)}} \Upsilon(abc) \kappa(abc) + \sum_{\substack{abc \\ (c < b < a)}} \Upsilon(abc) \kappa(abc) \\
 &= \sum_{\substack{abc \\ (a < b < c)}} \Upsilon(abc) \kappa(abc) + \sum_{\substack{bac \\ (a < b < c)}} \Upsilon(bac) \kappa(bac) + \sum_{\substack{cab \\ (a < b < c)}} \Upsilon(cab) \kappa(cab) \\
 &+ \sum_{\substack{acb \\ (a < b < c)}} \Upsilon(acb) \kappa(acb) + \sum_{\substack{bca \\ (a < b < c)}} \Upsilon(bca) \kappa(bca) + \sum_{\substack{cba \\ (a < b < c)}} \Upsilon(cba) \kappa(cba) \\
 &= \sum_{\substack{abc \\ (a < b < c)}} \left( \Upsilon(abc) + \Upsilon(bca) + \Upsilon(cab) + \Upsilon(abc) + \Upsilon(bca) + \Upsilon(cab) \right) \kappa(abc) \\
 &= 2 \sum_{\substack{abc \\ (a < b < c)}} \left( \Upsilon(abc) + \Upsilon(bca) + \Upsilon(cab) \right) \kappa(abc) .
 \end{aligned} \tag{B.16}$$

## B.2. Useful Expressions for Parity-Violating Fluxes

Since (B.16) holds for arbitrary flux densities  $Y_\alpha$  we obtain (3.75). Calculating

$$\begin{aligned}
\left( \sum_{\beta} \frac{\mathbb{P}_{\beta}}{\zeta - E_{\beta}} \right) (\zeta - \underline{\mathcal{M}}) &= \sum_{\beta, \alpha} \frac{\mathbb{P}_{\beta}}{\zeta - E_{\beta}} (\mathbb{P}_{\alpha} \zeta - \mathbb{P}_{\alpha} \underline{\mathcal{M}}) \\
&= \sum_{\beta, \alpha} \frac{|\beta\rangle \langle \tilde{\beta}| \alpha\rangle \langle \tilde{\alpha}| \zeta - |\beta\rangle \langle \tilde{\beta}| \alpha\rangle \langle \tilde{\alpha}| E_{\alpha}}{\zeta - E_{\beta}} \\
&= \sum_{\beta, \alpha} |\beta\rangle \langle \tilde{\alpha}| \delta_{\alpha\beta} \frac{\zeta - E_{\alpha}}{\zeta - E_{\beta}} \\
&= \sum_{\beta} |\beta\rangle \langle \tilde{\beta}| = \mathbb{1} ,
\end{aligned} \tag{B.17}$$

the resolvent can be written as

$$(\zeta - \underline{\mathcal{M}}(K))^{-1} = \sum_{\beta} (\zeta - E_{\beta}(K))^{-1} \mathbb{P}_{\beta}(K) . \tag{B.18}$$

From that we find

$$\begin{aligned}
\frac{1}{(\zeta - \underline{\mathcal{M}})^2} &= \sum_{\beta} \frac{\mathbb{P}_{\beta}}{\zeta - E_{\beta}} \sum_{\gamma} \frac{\mathbb{P}_{\gamma}}{\zeta - E_{\gamma}} \\
&= \sum_{\beta, \gamma} \frac{|\beta\rangle \langle \tilde{\beta}| \gamma\rangle \langle \tilde{\gamma}|}{(\zeta - E_{\beta})(\zeta - E_{\gamma})} \\
&= \sum_{\beta} \frac{\mathbb{P}_{\beta}}{(\zeta - E_{\beta})^2} ,
\end{aligned} \tag{B.19}$$

immediately leading to (3.54) via complete induction.

Taking into account the mass matrix (3.25), (3.24), and (3.26) we first derive the expansion of  $(\zeta - \underline{\mathcal{M}}(K))^{-1}$  around  $\delta = 0$ . Analogously to (B.5) and (B.6) we find

$$\frac{\partial}{\partial \delta} \frac{1}{\zeta - \underline{\mathcal{M}}} = \frac{1}{\zeta - \underline{\mathcal{M}}} \frac{\partial \underline{\mathcal{M}}}{\partial \delta} \frac{1}{\zeta - \underline{\mathcal{M}}} \tag{B.20}$$

and

$$\frac{\partial}{\partial \delta} \frac{1}{(\zeta - \underline{\mathcal{M}})^2} = \frac{1}{(\zeta - \underline{\mathcal{M}})^2} \frac{\partial \underline{\mathcal{M}}}{\partial \delta} \frac{1}{\zeta - \underline{\mathcal{M}}} + \frac{1}{\zeta - \underline{\mathcal{M}}} \frac{\partial \underline{\mathcal{M}}}{\partial \delta} \frac{1}{(\zeta - \underline{\mathcal{M}})^2} . \tag{B.21}$$

With the short hand notation

$$z := \frac{1}{\zeta - \underline{\mathcal{M}}(\boldsymbol{\mathcal{E}}, \boldsymbol{\mathcal{B}})} \Big|_{\delta=0} = \frac{1}{\zeta - \underline{\mathcal{M}}^{(0)}(K)} \tag{B.22}$$

the expansion of the trace in (3.86) up to linear order in the PV parameter  $\delta$  reads

$$\begin{aligned}
&\text{Tr} \left[ \frac{1}{\zeta - \underline{\mathcal{M}}(\boldsymbol{\mathcal{E}}, \boldsymbol{\mathcal{B}})} \underline{D}_j \frac{1}{(\zeta - \underline{\mathcal{M}}(\boldsymbol{\mathcal{E}}, \boldsymbol{\mathcal{B}}))^2} \underline{D}_k \right] \\
&= \text{Tr} \left[ (z + z \delta \underline{\mathcal{M}}_{\text{PV}} z + \mathcal{O}(\delta^2)) \underline{D}_j (z^2 + z^2 \delta \underline{\mathcal{M}}_{\text{PV}} z + z \delta \underline{\mathcal{M}}_{\text{PV}} z^2 + \mathcal{O}(\delta^2)) \underline{D}_k \right] \\
&= \text{Tr} [z \underline{D}_j z^2 \underline{D}_k] + \delta \text{Tr} [z \underline{D}_j z^2 \underline{\mathcal{M}}_{\text{PV}} z \underline{D}_k + z \underline{D}_j z \underline{\mathcal{M}}_{\text{PV}} z^2 \underline{D}_k + z^2 \underline{D}_k z \underline{\mathcal{M}}_{\text{PV}} z \underline{D}_j] \\
&\quad + \mathcal{O}(\delta^2) .
\end{aligned} \tag{B.23}$$

Inserting (B.23) in (3.86) and performing a partial integration we obtain

$$\mathcal{I}_{\alpha,jk}^{(\mathcal{E})}(\boldsymbol{\mathcal{E}}, \boldsymbol{\mathcal{B}}) = \frac{i}{2} \frac{1}{2\pi i} \oint_{S_\alpha} d\zeta \operatorname{Tr} [z \underline{D}_j z^2 \underline{D}_k] + \delta \operatorname{Tr} [z \underline{\mathcal{M}}_{\text{PV}} z \underline{D}_j z^2 \underline{D}_k - (j \leftrightarrow k)] \quad (\text{B.24})$$

which proves (3.108). This derivation also holds for  $\mathcal{I}_{\alpha,jk}^{(\mathcal{B})\text{PV}}$  and  $\mathcal{I}_{\alpha,jk}^{(\mathcal{E},\mathcal{B})\text{PV}}$  where  $\underline{D}_j, \underline{D}_k$  are replaced by  $\underline{\mu}_j, \underline{\mu}_k$  and  $\underline{D}_j, \underline{\mu}_k$ , respectively. In this way we obtain from (3.87) and (3.88)

$$\begin{aligned} \mathcal{I}_{\alpha,jk}^{(\mathcal{B})\text{PV}}(\boldsymbol{\mathcal{E}}, \boldsymbol{\mathcal{B}}) &= \delta \frac{i}{2} \frac{1}{2\pi i} \oint_{S_\alpha} d\zeta \operatorname{Tr} \left[ \frac{1}{\zeta - \underline{\mathcal{M}}^{(0)}(\boldsymbol{\mathcal{E}}, \boldsymbol{\mathcal{B}})} \underline{\mathcal{M}}_{\text{PV}} \right. \\ &\quad \left. \times \frac{1}{\zeta - \underline{\mathcal{M}}^{(0)}(\boldsymbol{\mathcal{E}}, \boldsymbol{\mathcal{B}})} \underline{\mu}_j \frac{1}{(\zeta - \underline{\mathcal{M}}^{(0)}(\boldsymbol{\mathcal{E}}, \boldsymbol{\mathcal{B}}))^2} \underline{\mu}_k - (j \leftrightarrow k) \right] \end{aligned} \quad (\text{B.25})$$

and

$$\begin{aligned} \mathcal{I}_{\alpha,jk}^{(\mathcal{E},\mathcal{B})\text{PV}}(\boldsymbol{\mathcal{E}}, \boldsymbol{\mathcal{B}}) &= \delta i \frac{1}{2\pi i} \oint_{S_\alpha} d\zeta \operatorname{Tr} \left[ \frac{1}{\zeta - \underline{\mathcal{M}}^{(0)}(\boldsymbol{\mathcal{E}}, \boldsymbol{\mathcal{B}})} \underline{\mathcal{M}}_{\text{PV}} \right. \\ &\quad \left. \times \frac{1}{\zeta - \underline{\mathcal{M}}^{(0)}(\boldsymbol{\mathcal{E}}, \boldsymbol{\mathcal{B}})} \underline{D}_j \frac{1}{(\zeta - \underline{\mathcal{M}}^{(0)}(\boldsymbol{\mathcal{E}}, \boldsymbol{\mathcal{B}}))^2} \underline{\mu}_k - (\underline{D}_j \leftrightarrow \underline{\mu}_k) \right]. \end{aligned} \quad (\text{B.26})$$

### B.3 Detailed Calculations of Specific Flux-Density Vector Fields

In this appendix we calculate the constants  $a^\alpha$  of (3.117). From (3.105) we find the P-violating part  $\mathcal{J}_\alpha^{(\mathcal{B})\text{PV}}(\mathbf{0}, \boldsymbol{\mathcal{B}})$  of  $\mathcal{J}_\alpha^{(\mathcal{B})}(\mathbf{0}, \boldsymbol{\mathcal{B}})$  to vanish. Therefore, neglecting terms of second order in the small PV parameter  $\delta$ , we can calculate  $\mathcal{J}_\alpha^{(\mathcal{B})}(\mathbf{0}, \boldsymbol{\mathcal{B}})$  setting  $\delta = 0$ . Then, the 2S states decouple from the 2P states, and we may restrict ourselves to the submatrix  $\underline{\mathcal{M}}^{2\text{S},(0)}(\mathbf{0}, \boldsymbol{\mathcal{B}})$  of  $\underline{\mathcal{M}}^{(0)}(\mathbf{0}, \boldsymbol{\mathcal{B}})$  (3.25) with respect to the 2S states, see Tables A.3 and A.5 in Appendix A.2. The derivatives  $\partial_{B_i} \underline{\mathcal{M}}^{2\text{S},(0)}(\mathbf{0}, \boldsymbol{\mathcal{B}})$ ,  $i \in \{1, 2, 3\}$ , of this submatrix read in the basis  $|\alpha, \boldsymbol{\mathcal{E}} = \mathbf{0}, \boldsymbol{\mathcal{B}} = \mathbf{0}\rangle$  with  $\alpha = 9, \dots, 12$ :

$$\frac{\partial \underline{\mathcal{M}}^{2\text{S},(0)}}{\partial B_1} = \frac{g\mu_B}{2\sqrt{2}} \begin{pmatrix} 0 & 1 & 0 & -1 \\ 1 & 0 & 1 & 0 \\ 0 & 1 & 0 & 1 \\ -1 & 0 & 1 & 0 \end{pmatrix}, \quad (\text{B.27})$$

$$\frac{\partial \underline{\mathcal{M}}^{2\text{S},(0)}}{\partial B_2} = \frac{g\mu_B}{2\sqrt{2}} \begin{pmatrix} 0 & -i & 0 & i \\ i & 0 & -i & 0 \\ 0 & i & 0 & i \\ -i & 0 & -i & 0 \end{pmatrix}, \quad (\text{B.28})$$

$$\frac{\partial \underline{\mathcal{M}}^{2\text{S},(0)}}{\partial B_3} = \frac{g\mu_B}{2} \begin{pmatrix} 1 & 0 & 0 & 0 \\ 0 & 0 & 0 & 1 \\ 0 & 0 & -1 & 0 \\ 0 & 1 & 0 & 0 \end{pmatrix}. \quad (\text{B.29})$$

### B.3. Detailed Calculations of Specific Flux-Density Vector Fields

Due to rotational invariance of  $\mathbf{J}_\alpha^{\mathcal{B}}(\mathbf{0}, \mathcal{B})$ , see (3.117), we may specify  $\mathcal{B} = B_3 \mathbf{e}_3$  for the evaluation of  $a^\alpha$  in (3.118). This simplifies the calculation of the eigenvalues and of the right and left eigenvectors of  $\underline{\mathcal{M}}^{2S,(0)}(\mathbf{0}, \mathcal{B})$ . In this case we find

$$\underline{\mathcal{M}}^{2S,(0)}(\mathbf{0}, B_3 \mathbf{e}_3) = \begin{pmatrix} \chi_1 + \frac{g\mu_B}{2}\mathcal{B}_3 & 0 & 0 & 0 \\ 0 & \chi_1 & 0 & \frac{g\mu_B}{2}\mathcal{B}_3 \\ 0 & 0 & \chi_1 - \frac{g\mu_B}{2}\mathcal{B}_3 & 0 \\ 0 & \frac{g\mu_B}{2}\mathcal{B}_3 & 0 & \chi_2 \end{pmatrix} \quad (\text{B.30})$$

where  $\chi_1 = L + \mathcal{A}/32 - i\Gamma_S/2$  and  $\chi_2 = L - 3\mathcal{A}/32 - i\Gamma_S/2$ . The eigenvalues of the matrix in (B.30) are

$$E_9 = \chi_1 + \frac{g\mu_B}{2}\mathcal{B}_3, \quad (\text{B.31})$$

$$E_{10} = L - \frac{\mathcal{A}}{32} + \frac{\chi_3}{16} - i\Gamma_S/2, \quad (\text{B.32})$$

$$E_{11} = \chi_1 - \frac{g\mu_B}{2}\mathcal{B}_3, \quad (\text{B.33})$$

$$E_{12} = L - \frac{\mathcal{A}}{32} - \frac{\chi_3}{16} - i\Gamma_S/2 \quad (\text{B.34})$$

where  $\chi_3 = \sqrt{\mathcal{A}^2 + (8\mathcal{B}_3 g\mu_B)^2}$ . From the eigenvectors we calculate explicit representations of the projection operators  $\mathbb{P}_\alpha^{2S}$  for the 2S states and obtain

$$\mathbb{P}_9^{2S,(0)} = \begin{pmatrix} 1 & 0 & 0 & 0 \\ 0 & 0 & 0 & 0 \\ 0 & 0 & 0 & 0 \\ 0 & 0 & 0 & 0 \end{pmatrix}, \quad (\text{B.35})$$

$$\mathbb{P}_{10}^{2S,(0)} = \frac{1}{2\chi_3} \begin{pmatrix} 0 & 0 & 0 & 0 \\ 0 & \chi_3 + \mathcal{A} & 0 & 8\mathcal{B}_3 g\mu_B \\ 0 & 0 & 0 & 0 \\ 0 & 8\mathcal{B}_3 g\mu_B & 0 & \chi_3 - \mathcal{A} \end{pmatrix}, \quad (\text{B.36})$$

$$\mathbb{P}_{11}^{2S,(0)} = \begin{pmatrix} 0 & 0 & 0 & 0 \\ 0 & 0 & 0 & 0 \\ 0 & 0 & 1 & 0 \\ 0 & 0 & 0 & 0 \end{pmatrix}, \quad (\text{B.37})$$

$$\mathbb{P}_{12}^{2S,(0)} = \frac{1}{2\chi_3} \begin{pmatrix} 0 & 0 & 0 & 0 \\ 0 & \chi_3 - \mathcal{A} & 0 & -8\mathcal{B}_3 g\mu_B \\ 0 & 0 & 0 & 0 \\ 0 & -8\mathcal{B}_3 g\mu_B & 0 & \chi_3 + \mathcal{A} \end{pmatrix}. \quad (\text{B.38})$$

Now, all ingredients for (3.65) are available, and a straightforward calculation yields, with (3.71), (3.87), and (3.89), the P-conserving flux-density vector field

$$\mathbf{J}_\alpha^{\mathcal{B}}(\mathbf{0}, \mathcal{B} = B_3 \mathbf{e}_3) = \begin{cases} -\frac{B_3 \mathbf{e}_3}{|\mathcal{B}_3|^3}, & \text{for } \alpha = 9, \\ \frac{B_3 \mathbf{e}_3}{|\mathcal{B}_3|^3}, & \text{for } \alpha = 11, \\ 0, & \text{for } \alpha = 10, 12. \end{cases} \quad (\text{B.39})$$

Rotational invariance of  $\mathbf{J}_\alpha^{\mathcal{B}}(\mathbf{0}, \mathcal{B})$  then leads to (3.118).

We now give the relations between the functions  $g_r^\alpha$ ,  $h_r^\alpha$ ,  $r = 1, \dots, 15$ , see (3.110)-(3.112), and the functions  $\tilde{g}_i^\alpha$ ,  $\tilde{h}_i^\alpha$ ,  $i = 1, \dots, 6$ , introduced for (3.140) and (3.141) in Section 3.6.3:

$$\tilde{g}_1^\alpha = \mathcal{E}_0 \mathcal{B}_0 \left[ g_7^\alpha + \frac{1}{3}(2\mathcal{E}_3^2 - \mathcal{E}_1^2) g_8^\alpha + \frac{1}{3}(2\mathcal{B}_3^2 - \mathcal{B}_2^2) g_9^\alpha + \frac{4}{3} g_{10}^\alpha \right], \quad (\text{B.40})$$

$$\tilde{g}_2^\alpha = \mathcal{E}_0 \mathcal{B}_0 \left[ 2\mathcal{B}_2 \mathcal{E}_3^2 g_{11}^\alpha + 2\mathcal{B}_2 g_{12}^\alpha \right], \quad (\text{B.41})$$

$$\tilde{g}_3^\alpha = \mathcal{E}_0 \mathcal{B}_0 \left[ \frac{1}{2} \mathcal{B}_2 g_5^\alpha + \mathcal{B}_2 (\mathcal{E}_3^2 - \mathcal{E}_1^2) g_{11}^\alpha + \mathcal{B}_2 g_{12}^\alpha \right], \quad (\text{B.42})$$

$$\tilde{g}_4^\alpha = \mathcal{E}_0 \mathcal{B}_0 \left[ -\frac{1}{2} g_6^\alpha - \mathcal{E}_3^2 g_8^\alpha - g_{10}^\alpha \right], \quad (\text{B.43})$$

$$\tilde{g}_5^\alpha = -\mathcal{E}_0^2 \mathcal{B}_2 g_2^\alpha, \quad (\text{B.44})$$

$$\tilde{g}_6^\alpha = \mathcal{E}_0^2 \mathcal{B}_3^2 g_3^\alpha, \quad (\text{B.45})$$

$$\tilde{h}_1^\alpha = \mathcal{E}_0 \mathcal{B}_0 \left[ h_7^\alpha + \frac{1}{3}(2\mathcal{E}_3^2 - \mathcal{E}_1^2) h_8^\alpha + \frac{1}{3}(2\mathcal{B}_3^2 - \mathcal{B}_2^2) h_9^\alpha + \frac{4}{3} \mathcal{E}_3^2 \mathcal{B}_3^2 h_{10}^\alpha \right], \quad (\text{B.46})$$

$$\tilde{h}_2^\alpha = \mathcal{E}_0 \mathcal{B}_0 \left[ 2\mathcal{B}_2 h_{11}^\alpha + 2\mathcal{B}_2 \mathcal{B}_3^2 h_{12}^\alpha \right], \quad (\text{B.47})$$

$$\tilde{h}_3^\alpha = \mathcal{E}_0 \mathcal{B}_0 \left[ \frac{1}{2} \mathcal{B}_2 h_5^\alpha + \mathcal{B}_2 (\mathcal{E}_3^2 - \mathcal{E}_1^2) h_{11}^\alpha + \mathcal{B}_2 \mathcal{E}_3^2 \mathcal{B}_3^2 h_{12}^\alpha \right], \quad (\text{B.48})$$

$$\tilde{h}_4^\alpha = \mathcal{E}_0 \mathcal{B}_0 \left[ -\frac{1}{2} \mathcal{B}_3^2 h_6^\alpha - h_8^\alpha - \mathcal{B}_3^2 h_{10}^\alpha \right], \quad (\text{B.49})$$

$$\tilde{h}_5^\alpha = -\mathcal{E}_0^2 \mathcal{B}_2 h_2^\alpha, \quad (\text{B.50})$$

$$\tilde{h}_6^\alpha = \mathcal{E}_0^2 h_3^\alpha. \quad (\text{B.51})$$

# C Derivation of the Non-Relativistic Parity-Violating Hamiltonian

We outlined the derivation of the non-relativistic PV Hamiltonian in Section 2.2. In the following, we present the details of this calculation [93, 201].

## The Lagrangian of Quantum Flavor Dynamics

First, we introduce the Lagrangian  $\mathcal{L}_{\text{QFD}}$  of quantum flavour dynamics incorporating the neutral currents which are the first-principle reason for the emergence of PV in atoms. To motivate those terms of  $\mathcal{L}_{\text{QFD}}$  which are closely related to the present thesis, we start with

$$\mathcal{L}_0(x) = (\bar{\nu}_{\text{eL}}(x), \bar{\mathbf{e}}_{\text{L}}(x)) (i\gamma^\lambda \partial_\lambda) \begin{pmatrix} \nu_{\text{eL}}(x) \\ \mathbf{e}_{\text{L}}(x) \end{pmatrix} + \bar{\mathbf{e}}_{\text{R}}(x) i\gamma^\lambda \partial_\lambda \mathbf{e}_{\text{R}}(x), \quad (\text{C.1})$$

$\lambda \in \{0, 1, 2, 3\}$ , as an ansatz for a Lagrangian of a theory including free Dirac fields of electrons and electron-neutrinos. Here, we introduce the decomposition of the spinors  $\mathbf{e}$  into their left- and right-handed parts according to

$$\psi = \psi_{\text{L}} + \psi_{\text{R}}, \quad \psi_{\text{L}} = \frac{1}{2}(1 - \gamma_5)\psi, \quad \psi_{\text{R}} = \frac{1}{2}(1 + \gamma_5)\psi. \quad (\text{C.2})$$

The wave functions depend on the four-vector coordinate  $x$ . We define the Dirac matrices  $\gamma^\mu = g^{\mu\nu}\gamma_\nu = \{\gamma_0, -\gamma_1, -\gamma_2, -\gamma_3\}$  as

$$\gamma^0 = \begin{pmatrix} \mathbb{1} & 0 \\ 0 & -\mathbb{1} \end{pmatrix}, \quad \gamma^i = \begin{pmatrix} 0 & \sigma^i \\ -\sigma^i & 0 \end{pmatrix}, \quad \gamma_i = \begin{pmatrix} 0 & -\sigma^i \\ \sigma^i & 0 \end{pmatrix}, \quad \gamma_5 = \begin{pmatrix} 0 & \mathbb{1} \\ \mathbb{1} & 0 \end{pmatrix}, \quad (\text{C.3})$$

with the Pauli matrices  $\sigma_i$ ,  $i \in \{1, 2, 3\}$ . The adjoint Dirac spinors are denoted as  $\bar{\psi} = \psi^\dagger \gamma_0$ .

The Lagrangian (C.1) is not invariant under local SU(2)-transformations

$$\begin{pmatrix} \nu_{\text{eL}}(x) \\ \mathbf{e}_{\text{L}}(x) \end{pmatrix} \longrightarrow U(x) \begin{pmatrix} \nu_{\text{eL}}(x) \\ \mathbf{e}_{\text{L}}(x) \end{pmatrix}. \quad (\text{C.4})$$

But by introducing three real vector fields  $\mathbf{W}_\lambda^a(x)$ , summarised in the matrix  $\mathbf{W}_\lambda(x) = g \mathbf{W}_\lambda^a(x) \sigma_a / 2$ , we can re-establish SU(2)-invariance since the Pauli matrices are the generators of the fundamental representation of SU(2). The fields  $\mathbf{W}_\lambda^a(x)$  are chosen to

## Chapter C. Derivation of the Non-Relativistic PV Hamiltonian

---

be accompanied by a coupling constant  $g$ . We further demand invariance of the theory under local U(1)-transformations

$$\psi(x) = \begin{pmatrix} \nu_{e_L}(x) \\ \mathbf{e}_L(x) \\ \mathbf{e}_R(x) \end{pmatrix} \longrightarrow \exp^{i\chi(x)\mathbf{Y}} \psi(x) \quad , \quad \mathbf{Y} = \begin{pmatrix} y_L & 0 & 0 \\ 0 & y_L & 0 \\ 0 & 0 & y_R \end{pmatrix} \quad , \quad (\text{C.5})$$

with an arbitrary scalar function  $\chi(x)$  and the weak hypercharge  $\mathbf{Y}$ , which are chosen as  $y_L := -1/2$  and  $y_R := -1$  in order to end up with the correct charges of the fundamental fermions. The matrices  $\mathbf{Y}$  and

$$\mathbf{T}_a = \left( \begin{array}{c|c} \frac{1}{2}\sigma_a & 0 \\ \hline 0 & 0 \end{array} \right) \quad (\text{C.6})$$

are the representations of the generators of  $SU(2) \times U(1)$  for the vector space associated with  $\psi$ . Analogously to the vector fields  $\mathbf{W}_\lambda^a(x)$  with coupling  $g$ , related to the generators  $\mathbf{T}_a$  of  $SU(2)$ , we introduce a vector field  $\mathbf{B}_\lambda$  with coupling  $g'$ , related to the generator  $\mathbf{Y}$  of  $U(1)$ . From  $\mathbf{W}_\lambda^3$  and  $\mathbf{B}_\lambda$  we build up the linear combinations

$$\begin{aligned} \mathbf{Z}_\lambda &= \cos \theta_W \mathbf{W}_\lambda^3 - \sin \theta_W \mathbf{B}_\lambda \quad , \\ \mathbf{A}_\lambda &= \sin \theta_W \mathbf{W}_\lambda^3 + \cos \theta_W \mathbf{B}_\lambda \quad , \end{aligned} \quad (\text{C.7})$$

constituting the Z-boson field  $\mathbf{Z}_\lambda$  and the photon field  $\mathbf{A}_\lambda$ , respectively.

We define the electromagnetic Lagrangian

$$\begin{aligned} \mathcal{L}'_{\text{em}} &= e \{ \bar{\mathbf{e}}_L \gamma^\lambda \mathbf{e}_L + \bar{\mathbf{e}}_R \gamma^\lambda \mathbf{e}_R \} \mathbf{A}_\lambda \\ &= e \{ \bar{\mathbf{e}} \gamma^\lambda \mathbf{e} \} \mathbf{A}_\lambda \\ &= -e \mathcal{J}_{\text{em}}^\lambda \mathbf{A}_\lambda \end{aligned} \quad (\text{C.8})$$

with the electromagnetic current  $\mathcal{J}_{\text{em}}^\lambda$ . It is included in the Lagrangian

$$\begin{aligned} \mathcal{L}'_{\text{Int}} &= -e \left\{ \mathbf{A}_\lambda \mathcal{J}_{\text{em}}^\lambda + \frac{1}{\sqrt{2} \sin \theta_W} (\mathbf{W}_\lambda^+ \bar{\nu}_{e_L} \gamma^\lambda \mathbf{e}_L + \mathbf{W}_\lambda^- \bar{\mathbf{e}}_L \gamma^\lambda \nu_{e_L}) \right. \\ &\quad \left. + \frac{1}{\sin \theta_W \cos \theta_W} \mathbf{Z}_\lambda \mathcal{J}_{NC}^\lambda \right\} \quad , \end{aligned} \quad (\text{C.9})$$

describing the interaction between the gauge bosons and the fundamental fermions. At this point, the particle masses and the fermion couplings to the Higgs field are not included yet. In (C.9), we have the neutral current

$$\mathcal{J}_{NC}^\lambda = \frac{1}{2} \bar{\nu}_{e_L} \gamma^\lambda \nu_{e_L} - \frac{1}{2} \bar{\mathbf{e}}_L \gamma^\lambda \mathbf{e}_L - \sin^2 \theta_W \mathcal{J}_{\text{em}}^\lambda \quad . \quad (\text{C.10})$$

$\mathcal{L}'_{\text{Int}}$  incorporates the four boson fields  $\mathbf{W}_\lambda^\pm = \frac{1}{\sqrt{2}}(\mathbf{W}_\lambda^1 \mp i \mathbf{W}_\lambda^2)$ ,  $\mathbf{Z}_\lambda$ , and  $\mathbf{A}_\lambda$ , all of which are massless at this point.

---

The inclusion of explicit mass terms in the Lagrangian (C.9) for the  $W^\pm$ - and  $Z$ -bosons violate the demanded gauge invariance. In the SM the masses of these gauge bosons are generated by a spontaneously broken Higgs field

$$\phi(x) = \begin{pmatrix} \phi_1(x) \\ \phi_2(x) \end{pmatrix}, \quad (\text{C.11})$$

with complex scalar fields  $\phi_{1/2}(x)$ . A symmetry of the fundamental equations of a theory is said to be spontaneously broken if the ground state does not possess this symmetry anymore. In the case of the Higgs field, the Lagrangian

$$\begin{aligned} \mathcal{L}_\phi &= (\partial_\mu \phi^\dagger)(\partial^\mu \phi) - V(\phi) \\ &= (\partial_\mu \phi^\dagger)(\partial^\mu \phi) - (\kappa \phi^\dagger \phi + \lambda(\phi^\dagger \phi)^2), \end{aligned} \quad (\text{C.12})$$

with  $\kappa < 0$  and  $\lambda > 0$ , is invariant under local  $SU(2)$ -transformations  $\phi(x) \rightarrow U(x)\phi(x)$ . But the (degenerate) ground states, for example  $\phi_0$  with

$$\langle 0|\phi_0|0\rangle = \begin{pmatrix} 0 \\ \sqrt{-\kappa/\lambda} \end{pmatrix} =: \begin{pmatrix} 0 \\ \frac{1}{\sqrt{2}}\rho_0 \end{pmatrix}, \quad (\text{C.13})$$

are not. The interaction of the Higgs field with the gauge bosons and the fermions is introduced through the Yukawa-Lagrangian

$$\begin{aligned} \mathcal{L}_{\text{Yuk}} &= -c_e \bar{\mathbf{e}}_R \phi^\dagger \begin{pmatrix} \nu_{eL} \\ \mathbf{e}_L \end{pmatrix} + h.c. \\ &= -c_e (\phi_1^\dagger \bar{\mathbf{e}}_R \nu_{eL} + \phi_2^\dagger \bar{\mathbf{e}}_R \mathbf{e}_L) + h.c. \end{aligned} \quad (\text{C.14})$$

with coupling constant  $c_e$ . In order to achieve gauge invariance, the derivatives  $\partial_\lambda$  have to be replaced by suitable covariant derivatives  $\mathbf{D}_\lambda$  according to

$$\partial_\lambda \psi \longrightarrow \mathbf{D}_\lambda \psi = (\partial_\lambda + i g \mathbf{W}_\lambda^a \mathbf{T}_a + i g' \mathbf{B}_\lambda \mathbf{Y}) \psi, \quad (\text{C.15})$$

$$\partial_\lambda \phi \longrightarrow \mathbf{D}_\lambda \phi = \left( \partial_\lambda + i g \mathbf{W}_\lambda^a \frac{\sigma_a}{2} + i g' \mathbf{B}_\lambda y_H \right) \phi. \quad (\text{C.16})$$

The hypercharge of the Higgs field is  $y_H = y_L - y_R = \frac{1}{2}$ . We define then the  $SU(2) \times U(1)$ -invariant Lagrangian

$$\begin{aligned} \mathcal{L} &= -\frac{1}{2} \text{Tr}(\mathbf{W}_{\lambda\rho} \mathbf{W}^{\lambda\rho}) - \frac{1}{4} \mathbf{B}_{\lambda\rho} \mathbf{B}^{\lambda\rho} + (\bar{\nu}_{eL}, \bar{\mathbf{e}}_L) (i \gamma^\lambda \mathbf{D}_\lambda) \begin{pmatrix} \nu_{eL} \\ \mathbf{e}_L \end{pmatrix} + \bar{\mathbf{e}}_R i \gamma^\lambda \mathbf{D}_\lambda \mathbf{e}_R \\ &\quad - c_e \bar{\mathbf{e}}_R \phi^\dagger \begin{pmatrix} \nu_{eL} \\ \mathbf{e}_L \end{pmatrix} - c_e^* (\bar{\nu}_{eL}, \bar{\mathbf{e}}_L) \phi \mathbf{e}_R + (\mathbf{D}_\lambda \phi^\dagger) (\mathbf{D}^\lambda \phi) - V(\phi), \end{aligned} \quad (\text{C.17})$$

where  $\mathbf{W}_{\lambda\rho} = \partial_\lambda \mathbf{W}_\rho - \partial_\rho \mathbf{W}_\lambda$  and  $\mathbf{B}_{\lambda\rho} = \partial_\lambda \mathbf{B}_\rho - \partial_\rho \mathbf{B}_\lambda$ . The gauge transformations for (C.17) are given explicitly in [93].

## Chapter C. Derivation of the Non-Relativistic PV Hamiltonian

---

The gauge freedom of the Higgs field under  $SU(2)$  allows us to set

$$\phi(x) = \begin{pmatrix} 0 \\ \frac{1}{\sqrt{2}}\rho(x) \end{pmatrix}, \quad (\text{C.18})$$

with

$$\langle 0|\phi(x)|0\rangle = \begin{pmatrix} 0 \\ \frac{1}{\sqrt{2}}\langle 0|\rho(x)|0\rangle \end{pmatrix} =: \begin{pmatrix} 0 \\ \frac{1}{\sqrt{2}}\rho_0 \end{pmatrix}. \quad (\text{C.19})$$

Now, rewriting (C.17) in terms of the shifted field  $\rho'(x) = \rho(x) - \rho_0$ , which is the physical Higgs field, we arrive at the desired Lagrangian for the theory of electron and electron neutrino with mass terms for the  $W^\pm$ - and Z-bosons as well as for the electron. It reads

$$\begin{aligned} \mathcal{L} = & -\frac{1}{2}\text{Tr}(\mathbf{W}_{\lambda\rho}\mathbf{W}^{\lambda\rho}) - \frac{1}{4}\mathbf{B}_{\lambda\rho}\mathbf{B}^{\lambda\rho} + \bar{\nu}_{eL}(i\gamma^\lambda\partial_\lambda)\nu_{eL} + \bar{\mathbf{e}}(i\gamma^\lambda\partial_\lambda)\mathbf{e} \\ & + \mathbf{W}_\lambda^+\mathbf{W}^{-\lambda}m_W^2\left(1 + \frac{\rho'}{\rho_0}\right)^2 + \frac{1}{2}\mathbf{Z}_\lambda\mathbf{Z}^\lambda m_Z^2\left(1 + \frac{\rho'}{\rho_0}\right)^2 - m_e\bar{\mathbf{e}}\mathbf{e}\left(1 + \frac{\rho'}{\rho_0}\right) \\ & + \frac{1}{2}(\partial_\lambda\rho')(\partial^\lambda\rho') - \frac{1}{2}m_{\rho'}^2\rho'^2\left[1 + \frac{\rho'}{\rho_0} + \frac{1}{4}\left(\frac{\rho'}{\rho_0}\right)^2\right] + \mathcal{L}'_{\text{Int}}, \end{aligned} \quad (\text{C.20})$$

with  $\mathcal{L}'_{\text{Int}}$  from (C.9). As parameters of the model given by (C.20) one may choose

$$e, \sin\theta_W, m_e, m_W^2, m_{\rho'}^2. \quad (\text{C.21})$$

The remaining parameters in (C.20) are related to (C.21) via

$$g^2 = \frac{e^2}{\sin^2\theta_W}, \quad g'^2 + g^2 = \frac{e^2}{\sin^2\theta_W \cos^2\theta_W}, \quad (\text{C.22})$$

$$m_Z^2 = \frac{m_W^2}{\cos^2\theta_W}, \quad \rho_0 = 2m_W\sqrt{\frac{\sin^2\theta_W}{e^2}}, \quad c_e\rho_0 = \sqrt{2}m_e. \quad (\text{C.23})$$

Analogously to the procedure given so far, all other fundamental fermions of the SM can be introduced and summarised in the spinor

$$\psi = \begin{pmatrix} \nu_{eL} \\ \mathbf{e}_L \\ \mathbf{e}_R \\ \mathbf{u}_L \\ \mathbf{d}'_L \\ \vdots \\ \mathbf{b}_R \end{pmatrix}. \quad (\text{C.24})$$

			$T$	$T_3$	$Y$	$Q$
$\begin{pmatrix} \nu_{eL} \\ \mathbf{e}_L \end{pmatrix}$	$\begin{pmatrix} \nu_{\mu L} \\ \boldsymbol{\mu}_L \end{pmatrix}$	$\begin{pmatrix} \nu_{\tau L} \\ \boldsymbol{\tau}_L \end{pmatrix}$	1/2	1/2	-1/2	0
$\mathbf{e}_R$	$\boldsymbol{\mu}_R$	$\boldsymbol{\tau}_R$	1/2	-1/2	-1/2	-1
$\mathbf{e}_R$	$\boldsymbol{\mu}_R$	$\boldsymbol{\tau}_R$	0	0	-1	-1
$\begin{pmatrix} \mathbf{u}_L \\ \mathbf{d}'_L \end{pmatrix}$	$\begin{pmatrix} \mathbf{c}_L \\ \mathbf{s}'_L \end{pmatrix}$	$\begin{pmatrix} \mathbf{t}_L \\ \mathbf{b}'_L \end{pmatrix}$	1/2	1/2	1/6	2/3
$\mathbf{u}_R$	$\mathbf{c}_R$	$\mathbf{t}_R$	1/2	-1/2	1/6	-1/3
$\mathbf{u}_R$	$\mathbf{c}_R$	$\mathbf{t}_R$	0	0	2/3	2/3
$\mathbf{d}_R$	$\mathbf{s}_R$	$\mathbf{b}_R$	0	0	-1/3	-1/3

**Table C.1:** The flavour quantum numbers of leptons and quarks. We give the weak isospin  $T$ , its third component  $T_3$ , the weak hypercharge  $Y$ , and the electric charge  $Q = T_3 + Y$ .

The flavour quantum numbers for the leptons and quarks are given in Table C.1. The fields  $\mathbf{d}'$ ,  $\mathbf{s}'$ , and  $\mathbf{b}'$  are the isospin partners of the fields  $\mathbf{u}$ ,  $\mathbf{c}$ , and  $\mathbf{t}$ , respectively. The former do not have a defined mass – in contrast to  $\mathbf{d}$ ,  $\mathbf{s}$ , and  $\mathbf{b}$ , but both sets of fields are related via the CKM-Matrix  $V$  according to

$$\begin{pmatrix} \mathbf{d} \\ \mathbf{s} \\ \mathbf{b} \end{pmatrix} = V^\dagger \begin{pmatrix} \mathbf{d}' \\ \mathbf{s}' \\ \mathbf{b}' \end{pmatrix}. \quad (\text{C.25})$$

All fermion masses  $m_e$ ,  $m_u$ , etc. can then be effectively summarised in the matrix  $\mathbf{M}$ . With this preceding preparatory work we can write down the Lagrangian of quantum flavour dynamics (2.14).

### Low Energy Limit for Atomic Physics

The S-matrix elements of the second order diagrams in Figure 2.3 can be deduced from  $\mathcal{L}_{\text{int,eff}}^Z$  in (2.20) as first-order perturbation of the S-operator

$$S = 1 + i \int dx \mathcal{L}_{\text{int,eff}}^Z(x). \quad (\text{C.26})$$

So, we take a closer look at

$$\begin{aligned} \mathcal{L}_{\text{int,eff}}^Z &= -\frac{e^2}{2m_W^2 \sin^2 \theta_W} \left( \mathcal{J}_{\text{NC}}^\lambda \Big|_{\text{lepton}} g_{\lambda\rho} \mathcal{J}_{\text{NC}}^\rho \Big|_{\text{quark}} + \mathcal{J}_{\text{NC}}^\lambda \Big|_{\text{quark}} g_{\lambda\rho} \mathcal{J}_{\text{NC}}^\rho \Big|_{\text{lepton}} \right) \\ &= -\frac{8G}{\sqrt{2}} \left( \mathcal{J}_{\text{NC}}^\lambda \Big|_{\text{lepton}} g_{\lambda\rho} \mathcal{J}_{\text{NC}}^\rho \Big|_{\text{quark}} \right), \end{aligned} \quad (\text{C.27})$$

where  $G = \sqrt{2} e^2 / (8 m_W^2 \sin^2 \theta_W)$  is Fermi's constant. We can use (2.17) and Table C.1 to evaluate (C.27) for electron-quark interaction. With  $\mathbf{Q} = \mathbf{T}_3 + \mathbf{Y}$  this yields

$$\begin{aligned} \mathcal{J}_{\text{NC}}^\lambda \Big|_{\text{electron}} &= \bar{\mathbf{e}} \gamma^\lambda \mathbf{T}_3 \mathbf{e} - \sin^2 \theta_W \bar{\mathbf{e}} \gamma^\lambda \mathbf{Q} \mathbf{e} \\ &= \bar{\mathbf{e}}_L \gamma^\lambda \left( -\frac{1}{2} \right) \mathbf{e}_L + 0 - \sin^2 \theta_W \bar{\mathbf{e}}_L \gamma^\lambda (-1) \mathbf{e}_L - \sin^2 \theta_W \bar{\mathbf{e}}_R \gamma^\lambda (-1) \mathbf{e}_R \\ &= \bar{\mathbf{e}}_L \gamma^\lambda \left( -\frac{1}{2} + \sin^2 \theta_W \right) \mathbf{e}_L + \bar{\mathbf{e}}_R \gamma^\lambda \sin^2 \theta_W \mathbf{e}_R \end{aligned}$$

$$\begin{aligned}
&= \left( -\frac{1}{4} + \frac{1}{2} \sin^2 \theta_W \right) (\bar{\mathbf{e}} \gamma^\lambda \mathbf{e} - \bar{\mathbf{e}} \gamma^\lambda \gamma_5 \mathbf{e}) + \frac{1}{2} \sin^2 \theta_W (\bar{\mathbf{e}} \gamma^\lambda \mathbf{e} + \bar{\mathbf{e}} \gamma^\lambda \gamma_5 \mathbf{e}) \\
&= \left( -\frac{1}{4} + \sin^2 \theta_W \right) \bar{\mathbf{e}} \gamma^\lambda \mathbf{e} + \frac{1}{4} \bar{\mathbf{e}} \gamma^\lambda \gamma_5 \mathbf{e} , \tag{C.28}
\end{aligned}$$

using  $a \bar{\psi}_{L/R} \gamma^\lambda \psi_{L/R} = \frac{a}{2} (\bar{\psi} \gamma^\lambda \psi \mp \bar{\psi} \gamma^\lambda \gamma_5 \psi)$  in the last step.

Analogously, we can calculate the neutral current for the  $u$ -quark and obtain

$$\begin{aligned}
\mathcal{J}_{\text{NC}}^\lambda \Big|_{\mathbf{u}} &= \bar{\mathbf{u}}_L \gamma^\lambda \left( \frac{1}{2} - \frac{2}{3} \sin^2 \theta_W \right) \mathbf{u}_L + \bar{\mathbf{u}}_R \gamma^\lambda \left( -\frac{2}{3} \sin^2 \theta_W \right) \mathbf{u}_R \\
&= \left( \frac{1}{4} - \frac{2}{3} \sin^2 \theta_W \right) \bar{\mathbf{u}} \gamma^\lambda \mathbf{u} - \frac{1}{4} \bar{\mathbf{u}} \gamma^\lambda \gamma_5 \mathbf{u} . \tag{C.29}
\end{aligned}$$

The neutral current for  $d'$ - and  $s'$ -quarks can be calculated in terms of the  $d$ - and  $s$ -quarks using the unitarity of the CKM-matrix

$$\begin{aligned}
(\bar{\mathbf{d}}', \bar{\mathbf{s}}', \bar{\mathbf{b}}') \gamma^\lambda \begin{pmatrix} \mathbf{d}' \\ \mathbf{s}' \\ \mathbf{b}' \end{pmatrix} &= (\bar{\mathbf{d}}', \bar{\mathbf{s}}', \bar{\mathbf{b}}') \gamma^\lambda V V^\dagger \begin{pmatrix} \mathbf{d}' \\ \mathbf{s}' \\ \mathbf{b}' \end{pmatrix} \\
&= (\bar{\mathbf{d}}', \bar{\mathbf{s}}', \bar{\mathbf{b}}') V \gamma^\lambda V^\dagger \begin{pmatrix} \mathbf{d}' \\ \mathbf{s}' \\ \mathbf{b}' \end{pmatrix} \\
&= \bar{\mathbf{d}} \gamma^\lambda \mathbf{d} + \bar{\mathbf{s}} \gamma^\lambda \mathbf{s} + \bar{\mathbf{b}} \gamma^\lambda \mathbf{b} . \tag{C.30}
\end{aligned}$$

We then obtain

$$\begin{aligned}
\mathcal{J}_{\text{NC}}^\lambda \Big|_{\mathbf{d}} &= \bar{\mathbf{d}} \gamma^\lambda \mathbf{T}_3 \mathbf{d} - \sin^2 \theta_W \bar{\mathbf{d}} \gamma^\lambda \mathbf{Q} \mathbf{d} \\
&\equiv \bar{\mathbf{d}}' \gamma^\lambda \mathbf{T}_3 \mathbf{d}' - \sin^2 \theta_W \bar{\mathbf{d}}' \gamma^\lambda \mathbf{Q} \mathbf{d}' \\
&= \bar{\mathbf{d}}_L \gamma^\lambda \left( -\frac{1}{2} + \frac{1}{3} \sin^2 \theta_W \right) \mathbf{d}_L + \bar{\mathbf{d}}_R \gamma^\lambda \left( \frac{1}{3} \sin^2 \theta_W \right) \mathbf{d}_R \\
&= \left( -\frac{1}{4} + \frac{1}{3} \sin^2 \theta_W \right) \bar{\mathbf{d}} \gamma^\lambda \mathbf{d} + \frac{1}{4} \bar{\mathbf{d}} \gamma^\lambda \gamma_5 \mathbf{d} \tag{C.31}
\end{aligned}$$

and

$$\mathcal{J}_{\text{NC}}^\lambda \Big|_{\mathbf{s}} = \left( -\frac{1}{4} + \frac{1}{3} \sin^2 \theta_W \right) \bar{\mathbf{s}} \gamma^\lambda \mathbf{s} + \frac{1}{4} \bar{\mathbf{s}} \gamma^\lambda \gamma_5 \mathbf{s} . \tag{C.32}$$

For the effective Lagrangian (C.27) we obtain (2.21).

---

## Non-Relativistic Reduction of the P-violating Hamiltonian

We neglect PV in the nucleus<sup>1</sup>. Therefore, the matrix elements  $\langle I, I'_3 | \bar{q}\gamma q | I, I_3 \rangle$ , with  $\gamma = (\gamma_1, \gamma_2, \gamma_3)$ , and  $\langle I, I'_3 | \bar{q}\gamma_0\gamma_5 q | I, I_3 \rangle$  of the quark currents in (2.28) have to vanish due to

$$P\bar{\psi}(\mathbf{x}, t)\gamma\psi(\mathbf{x}, t)P = -\bar{\psi}(-\mathbf{x}, t)\gamma\psi(-\mathbf{x}, t) , \quad (\text{C.33})$$

$$P\bar{\psi}(\mathbf{x}, t)\gamma_0\gamma_5\psi(\mathbf{x}, t)P = -\bar{\psi}(-\mathbf{x}, t)\gamma_0\gamma_5\psi(-\mathbf{x}, t) . \quad (\text{C.34})$$

In the limit of vanishing momentum transfers between electrons and nucleus we found the Z-boson propagator in (2.19) described by a  $\delta$ -distribution in spatial space. With the approximation of an infinitely heavy nucleus at the origin  $\mathbf{x} = 0$ , i.e., neglecting recoil effects, we can therefore write the matrix elements of the number operators of the quarks with flavour  $q$  as

$$\langle Z, N, I, I'_3 | \bar{\mathbf{q}}\gamma_0\mathbf{q} | Z, N, I, I_3 \rangle = \delta^3(\mathbf{x})\delta_{I'_3 I_3} \begin{cases} 2Z + N & (q = u) \\ Z + 2N & (q = d) \\ 0 & (q = s) \end{cases} , \quad (\text{C.35})$$

see [80]. The matrix elements of the axial-vector operator  $\bar{q}\gamma\gamma_5 q$  have to be proportional to the matrix elements of the only axial vector at hand, namely the nuclear-spin operator  $\mathbf{I}$ . Thereby, the proportionality constants are defined as the so-called axial form factors  $G_A^{(q)}(Z, N)$  of the nucleus for the quark species  $q$ . This yields

$$\langle I, I'_3 | \bar{\mathbf{q}}\gamma\gamma_5\mathbf{q} | I, I_3 \rangle = G_A^{(q)}(Z, N) \delta^3(\mathbf{x}) \langle I, I'_3 | \mathbf{I} | I, I_3 \rangle , \quad (\text{C.36})$$

see [80].

We calculate the matrix elements corresponding to the currents involving the electron in (2.28). Employing normal ordering of the annihilation and creation operators and using (2.30), (2.31), and Wick's theorem, we calculate the matrix elements

$$\begin{aligned} & \langle \psi'_e | : \bar{\mathbf{e}}\gamma^\mu\gamma_5\mathbf{e} : | \psi_e \rangle \\ &= \int \frac{d^3p d^3p'}{(2\pi)^6 \sqrt{4p_0 p'_0}} \int \frac{d^3k d^3k'}{(2\pi)^6 4k_0 k'_0} \sum_{s_1, s_2, s_3, s_4} \langle 0 | a_{s_1}(\mathbf{p}') \\ & \times \tilde{\psi}_{s_1}^{\prime*}(\mathbf{p}') : \left\{ e^{-ik'x} \bar{v}_{s_2}(k') b_{s_2}(\mathbf{k}') + e^{ik'x} \bar{u}_{s_2}(k') a_{s_2}^\dagger(\mathbf{k}') \right\} \gamma^\mu \gamma_5 \\ & \times \left\{ e^{ikx} v_{s_3}(k) b_{s_3}^\dagger(\mathbf{k}) + e^{-ikx} u_{s_3}(k) a_{s_3}(\mathbf{k}) \right\} : \tilde{\psi}_{s_4}(\mathbf{p}) a_{s_4}^\dagger(\mathbf{p}) | 0 \rangle \end{aligned}$$

---

<sup>1</sup>The main nuclear PV effect is expected to emerge due to the so-called anapole moment, a PV effect involving nucleon-nucleon-interactions. Classically, it arises from a higher-order term in the multipole expansion of the electromagnetic vector potential. It can be regarded as generated by a P-odd and T-even toroidal current distribution, see, e.g., [202, 203] for details. The orbital motions of the nucleons form an effective current while the Z-boson exchange between nucleons accounts for an additional toroidal current distribution associated with the anapole moment. It involves a  $\delta$ -distribution at the nucleus, rendering the interaction with an atomic electron point-like. A successful measurement had been accomplished with caesium [47] by measuring the discrepancy of the PV effect between two different parity-violating hyperfine transitions, see Section 2.4.

$$\begin{aligned}
 &= \int \frac{d^3p d^3p'}{(2\pi)^6 \sqrt{4p_0 p'_0}} \int \frac{d^3k d^3k'}{(2\pi)^6 4k_0 k'_0} \\
 &\times \sum_{s_1, s_2, s_3, s_4} \langle 0 | a_{s_1}(\mathbf{p}') \tilde{\psi}'_{s_1*}(\mathbf{p}') e^{ik'x} \bar{u}_{s_2}(k') a_{s_2}^\dagger(\mathbf{k}') \gamma^\mu \gamma_5 e^{-ikx} u_{s_3}(k) \tilde{\psi}_{s_4}(\mathbf{p}) | 0 \rangle \\
 &\times \langle 0 | a_{s_3}(\mathbf{k}) a_{s_4}^\dagger(\mathbf{p}) | 0 \rangle . \tag{C.37}
 \end{aligned}$$

With the anticommutation relation

$$\begin{aligned}
 2p^0 (2\pi)^3 \delta_{rs} \delta^3(\mathbf{p} - \mathbf{p}') &= \{a_r(\mathbf{p}), a_s^\dagger(\mathbf{p}')\} \\
 &= \{a_r(\mathbf{p}), a_s^\dagger(\mathbf{p}')\} \langle 0 | 0 \rangle \\
 &= \langle 0 | \{a_r(\mathbf{p}), a_s^\dagger(\mathbf{p}')\} | 0 \rangle \\
 &= \langle 0 | a_r(\mathbf{p}) a_s^\dagger(\mathbf{p}') | 0 \rangle \tag{C.38}
 \end{aligned}$$

we obtain

$$\begin{aligned}
 &\langle \psi'_e | : \bar{\mathbf{e}} \gamma^\mu \gamma_5 \mathbf{e} : | \psi_e \rangle \\
 &= \int \frac{d^3p d^3p'}{(2\pi)^6 \sqrt{4p_0 p'_0}} \int d^3k d^3k' \sum_{s_1, s_2, s_3, s_4} \delta_{s_1 s_2} \delta_{s_3 s_4} \delta^3(\mathbf{p}' - \mathbf{k}') \delta^3(\mathbf{p} - \mathbf{k}) \\
 &\times \tilde{\psi}'_{s_1*}(\mathbf{p}') e^{ik'x} \langle 0 | \bar{u}_{s_2}(k') \gamma^\mu \gamma_5 u_{s_3}(k) | 0 \rangle e^{-ikx} \tilde{\psi}_{s_4}(\mathbf{p}) \\
 &= \int \frac{d^3p d^3p'}{(2\pi)^6 \sqrt{4p_0 p'_0}} \sum_{s, s'} \tilde{\psi}'_{s'*}(\mathbf{p}') e^{ip'x} \langle 0 | \bar{u}_{s'}(p') \gamma^\mu \gamma_5 u_s(p) | 0 \rangle e^{-ipx} \tilde{\psi}_s(\mathbf{p}) , \tag{C.39}
 \end{aligned}$$

noting that  $k_0 = +\sqrt{m^2 + \mathbf{k}^2}$  and  $p_0 = +\sqrt{m^2 + \mathbf{p}^2}$  for the last step.

So far, we have only incorporated the approximation of low momentum transfers, leading to a 4-fermion-interaction. The expression (C.39) is still relativistic. Using (2.29) the general expressions of Dirac spinors (2.32) can be approximated by

$$u_s(p) = \sqrt{2m_e} \begin{pmatrix} \chi_s \\ \frac{\boldsymbol{\sigma} \cdot \mathbf{p}}{2m_e} \chi_s \end{pmatrix} \tag{C.40}$$

and  $\bar{u}_{s'}(p') = \sqrt{2m_e} \left( \chi_{s'}^*, \chi_{s'}^* \frac{\boldsymbol{\sigma} \cdot \mathbf{p}'}{2m_e} \right) \gamma^0$ . With the Dirac matrices (C.3) we get

$$\gamma^0 \gamma^\mu \gamma_5 = \left( \gamma_5 , \begin{pmatrix} \boldsymbol{\sigma} & 0 \\ 0 & \boldsymbol{\sigma} \end{pmatrix} \right) . \tag{C.41}$$

Because of  $\langle I, I_3 | \bar{\mathbf{q}} \boldsymbol{\gamma} \mathbf{q} | I, I_3 \rangle = 0$  we consider only  $\mu = 0$  for the vacuum expectation value in (C.39) in the NR limit

$$\begin{aligned}
 \langle 0 | \bar{u}_{s'}(p') \gamma^0 \gamma_5 u_s(p) | 0 \rangle &= 2m_e \left( \chi_{s'}^*, \chi_{s'}^* \frac{\boldsymbol{\sigma} \cdot \mathbf{p}'}{2m_e} \right) \gamma_5 \begin{pmatrix} \chi_s \\ \frac{\boldsymbol{\sigma} \cdot \mathbf{p}}{2m_e} \chi_s \end{pmatrix} \\
 &= 2m_e \left( \chi_{s'}^*, \chi_{s'}^* \frac{\boldsymbol{\sigma} \cdot \mathbf{p}'}{2m_e} \right) \cdot \begin{pmatrix} \frac{\boldsymbol{\sigma} \cdot \mathbf{p}}{2m_e} \chi_s \\ \chi_s \end{pmatrix} . \tag{C.42}
 \end{aligned}$$

We evaluate the integral in (C.39) using the Fourier transformations

$$\psi_s(\mathbf{x}) = \int \frac{d^3p}{(2\pi)^3} e^{i\mathbf{p}\mathbf{x}} \tilde{\psi}_s(\mathbf{p}) \quad \Rightarrow \quad \int \frac{d^3p}{(2\pi)^3} e^{-i\mathbf{p}\mathbf{x}} \tilde{\psi}_s(\mathbf{p}) = e^{-ip_0 t} \psi_s(\mathbf{x}) \quad (\text{C.43})$$

and

$$\begin{aligned} \int_{-\infty}^{\infty} \frac{d^3p'}{(2\pi)^3} \tilde{\psi}'_{s'}(\mathbf{p}') e^{ip'x} &= e^{ip'_0 t} \left( \int_{-\infty}^{\infty} \frac{d^3p'}{(2\pi)^3} \tilde{\psi}'_{s'}(\mathbf{p}') e^{i\mathbf{p}'\mathbf{x}} \right)^* \\ &= e^{ip'_0 t} (\psi'_{s'}(\mathbf{x}))^* = e^{ip'_0 t} \psi'^*_{s'}(\mathbf{x}). \end{aligned} \quad (\text{C.44})$$

With  $p_0 = p'_0 = m_e$  in the NR limit this leads to

$$\begin{aligned} &\langle \psi'_e | : \bar{\mathbf{e}}\gamma^0\gamma_5\mathbf{e} : | \psi_e \rangle \\ &\stackrel{\text{NR}}{=} \sum_{s,s'} \int \frac{d^3p'}{(2\pi)^3} \int \frac{d^3p}{(2\pi)^3} \tilde{\psi}'_{s'}(\mathbf{p}') e^{ip'x} \left( \chi_{s'}^*, \chi_{s'}^* \frac{\boldsymbol{\sigma} \cdot \mathbf{p}'}{2m_e} \right) \cdot \left( \frac{\boldsymbol{\sigma} \cdot \mathbf{p}}{2m_e} \chi_s \right) e^{-i\mathbf{p}\mathbf{x}} \tilde{\psi}_s(\mathbf{p}) \\ &= \sum_{s,s'} \int \frac{d^3p}{(2\pi)^3} \left\{ \chi_{s'}^* \frac{\boldsymbol{\sigma} \cdot \mathbf{p}}{2m_e} \chi_s e^{-i\mathbf{p}\mathbf{x}} \tilde{\psi}_s(\mathbf{p}) \right\} \int \frac{d^3p'}{(2\pi)^3} \tilde{\psi}'_{s'}(\mathbf{p}') e^{ip'x} \\ &\quad + \sum_{s,s'} \int \frac{d^3p'}{(2\pi)^3} \left\{ \tilde{\psi}'_{s'}(\mathbf{p}') e^{ip'x} \chi_{s'}^* \frac{\boldsymbol{\sigma} \cdot \mathbf{p}'}{2m_e} \chi_s \right\} \int \frac{d^3p}{(2\pi)^3} e^{-i\mathbf{p}\mathbf{x}} \tilde{\psi}_s(\mathbf{p}) \\ &= \sum_{s,s'} e^{-ip_0 t} e^{ip'_0 t} \int \frac{d^3p}{(2\pi)^3} \left\{ \chi_{s'}^* \frac{\boldsymbol{\sigma} \cdot \mathbf{p}}{2m_e} \chi_s e^{i\mathbf{p}\mathbf{x}} \tilde{\psi}_s(\mathbf{p}) \right\} \psi'^*_{s'}(\mathbf{x}) \\ &\quad + \sum_{s,s'} e^{-ip_0 t} e^{ip'_0 t} \int \frac{d^3p'}{(2\pi)^3} \left\{ \tilde{\psi}'_{s'}(\mathbf{p}') e^{-i\mathbf{p}'\mathbf{x}} \chi_{s'}^* \frac{\boldsymbol{\sigma} \cdot \mathbf{p}'}{2m_e} \chi_s \right\} \psi_s(\mathbf{x}) \\ &= \sum_{s,s'} \chi_{s'}^* \int \frac{d^3p}{(2\pi)^3} \left\{ \frac{\boldsymbol{\sigma} \cdot \mathbf{p}}{2m_e} e^{i\mathbf{p}\mathbf{x}} \tilde{\psi}_s(\mathbf{p}) \right\} \psi'^*_{s'}(\mathbf{x}) \chi_s \\ &\quad + \sum_{s,s'} \chi_{s'}^* \int \frac{d^3p'}{(2\pi)^3} \left\{ \frac{\boldsymbol{\sigma} \cdot \mathbf{p}'}{2m_e} e^{-i\mathbf{p}'\mathbf{x}} \tilde{\psi}'_{s'}(\mathbf{p}') \right\} \psi_s(\mathbf{x}) \chi_s. \end{aligned} \quad (\text{C.45})$$

We then find

$$\begin{aligned} \int \frac{d^3p}{(2\pi)^3} \boldsymbol{\sigma} \cdot \mathbf{p} e^{i\mathbf{p}\mathbf{x}} \tilde{\psi}_s(\mathbf{p}) &= \sum_j \sigma_j \int \frac{d^3p}{(2\pi)^3} p_j e^{i\mathbf{p}\mathbf{x}} \tilde{\psi}_s(\mathbf{p}) = -i \sum_j \sigma_j \partial_j \int \frac{d^3p}{(2\pi)^3} e^{i\mathbf{p}\mathbf{x}} \tilde{\psi}_s(\mathbf{p}) \\ &= -i(\boldsymbol{\sigma} \cdot \nabla) \psi_s(\mathbf{x}) \end{aligned} \quad (\text{C.46})$$

and

$$\begin{aligned} \int \frac{d^3p'}{(2\pi)^3} \boldsymbol{\sigma} \cdot \mathbf{p}' e^{-i\mathbf{p}'\mathbf{x}} \tilde{\psi}'_{s'}(\mathbf{p}') &= \sum_j \sigma_j \int \frac{d^3p'}{(2\pi)^3} p'_j e^{-i\mathbf{p}'\mathbf{x}} \tilde{\psi}'_{s'}(\mathbf{p}') \\ &= i \sum_j \sigma_j \partial_j \left( \int \frac{d^3p'}{(2\pi)^3} e^{i\mathbf{p}'\mathbf{x}} \tilde{\psi}'_{s'}(\mathbf{p}') \right)^* \\ &= i(\boldsymbol{\sigma} \cdot \nabla) \psi'^*_{s'}(\mathbf{x}) \end{aligned} \quad (\text{C.47})$$

yielding

$$\begin{aligned} & \langle \psi'_e | : \bar{\mathbf{e}} \gamma^0 \gamma_5 \mathbf{e} : | \psi_e \rangle \\ & \stackrel{\text{NR}}{=} \frac{1}{2m_e} \sum_{s,s'} \{ \chi_{s'}^* \psi'_{s'}(\mathbf{x}) \boldsymbol{\sigma} \cdot (-i \nabla \psi_s(\mathbf{x})) \chi_s + \chi_{s'}^* (\boldsymbol{\sigma} \cdot i \nabla \psi'_{s'}(\mathbf{x})) \psi_s(\mathbf{x}) \chi_s \} . \end{aligned} \quad (\text{C.48})$$

Thus, we obtain, with (C.35) and (C.48), the matrix elements of  $H_{\text{PV}}^{(1)}$

$$\begin{aligned} & \langle \psi'_e, I, I'_3 | H_{\text{PV}}^{(1)} | \psi_e, I, I_3 \rangle \\ & = -\frac{G}{\sqrt{2}} \int d^3x 2g_A^e \langle \psi'_e | : \bar{\mathbf{e}} \gamma^0 \gamma_5 \mathbf{e} : | \psi_e \rangle \left( \sum_{q=u,d,s} g_V^q \langle I, I'_3 | \bar{\mathbf{q}} \gamma_0 \mathbf{q} | I, I_3 \rangle \right) \\ & \stackrel{\text{NR}}{=} -\frac{G}{\sqrt{2}} \frac{2g_A^e}{2m_e} \boldsymbol{\sigma} \cdot \sum_{s,s'} \chi_{s'}^* \left\{ \int d^3x \psi'_{s'}(\mathbf{x}) (-i \nabla \psi_s(\mathbf{x})) + \int d^3x (i \nabla \psi'_{s'}(\mathbf{x})) \psi_s(\mathbf{x}) \right\} \chi_s \\ & \quad \times \delta^3(\mathbf{x}) \delta_{I'_3 I_3} \left\{ g_V^u (2Z + N) + g_V^d (Z + 2N) \right\} \\ & = \frac{G}{4\sqrt{2} m_e} Q_W^{(1)} \delta_{I'_3 I_3} \sum_{s,s'} \chi_{s'}^* \int d^3x \{ \psi'_{s'}(\mathbf{x}) \delta^3(\mathbf{x}) \boldsymbol{\sigma} \cdot (-i \nabla \psi_s(\mathbf{x})) \\ & \quad + \boldsymbol{\sigma} \cdot (i \nabla \psi'_{s'}(\mathbf{x})) \delta^3(\mathbf{x}) \psi_s(\mathbf{x}) \} \chi_s \end{aligned} \quad (\text{C.49})$$

where we introduced the nuclear-spin independent weak charge (2.34) of an atomic nucleus. With the spatial representation of the momentum operator  $\hat{\mathbf{p}}$  we have

$$\begin{aligned} \langle \mathbf{x} | \hat{\mathbf{p}} | \psi \rangle & = -i \nabla \psi(\mathbf{x}) , \\ \langle \psi | \hat{\mathbf{p}} | \mathbf{x} \rangle & = i \nabla \psi^*(\mathbf{x}) , \\ \langle \phi | \hat{\mathbf{p}} | \psi \rangle & = \int d^3x \langle \phi | \mathbf{x} \rangle \langle \mathbf{x} | \hat{\mathbf{p}} | \psi \rangle = \int d^3x \phi^*(\mathbf{x}) (-i \nabla \psi(\mathbf{x})) =: \langle \phi | \overleftarrow{\hat{\mathbf{p}}} | \psi \rangle , \\ \langle \phi | \hat{\mathbf{p}} | \psi \rangle & = \int d^3x \langle \phi | \hat{\mathbf{p}} | \mathbf{x} \rangle \langle \mathbf{x} | \psi \rangle = \int d^3x (i \nabla \phi^*(\mathbf{x})) \psi(\mathbf{x}) =: \langle \phi | \overleftarrow{\hat{\mathbf{p}}} | \psi \rangle . \end{aligned} \quad (\text{C.50})$$

With (C.50) we can conclude that the matrix elements (C.49) correspond to the operator (2.33).

The next task is the calculation of  $H_{\text{PV}}^{(2)}$ . The nuclear part of the according matrix element is given in (C.36). Since  $\langle I, I'_3 | \bar{q} \gamma_0 \gamma_5 q | I, I_3 \rangle = 0$  we have only to consider  $\mu = 1, 2, 3$  for the calculation of the NR reduction of  $\langle \psi'_e | : \bar{\mathbf{e}} \gamma^\mu \mathbf{e} : | \psi_e \rangle$ . The derivation is analogous to that of  $H_{\text{PV}}^{(1)}$  yielding (2.36).

## D The Numerical Software QABSE

In this appendix we briefly want to describe the global structure of implemented algorithms of the numerical QABSE (Qt Atomic Beam Spin Echo) software written in C++ and utilising it++ numerical routines. It is endowed with a Qt graphical user interface and was originally developed by Dr. Timo Bergmann [39]. QABSE provides for the computation of geometric flux densities and Berry phases of hydrogen ( $n = 1, 2$ ), deuterium ( $n = 2$ ), and  $^4\text{He}$  ( $n = 2$ ). It can be easily extended to other atomic species.

The software has the following features and numerical routines:

- Computation of Berry phases and dynamical phases for all field configurations that do not include degeneracies<sup>1</sup>. Here, the line-integral representation according to Section 3.4 is employed.
- Computation of flux-density vector fields in arbitrary three-dimensional parameter spaces. Divergence and curl of PC vector fields can also be calculated. The implementation for the PV vector fields is straightforward.
- Decomposition of the geometric phases and their flux densities in P-conserving and P-violating parts, where the P-violating contribution is broken down in the nuclear-spin dependent and the nuclear-spin independent contribution.
- Providing data for time-table plots, Zeeman diagrams, decay rates as function of the external fields, evolution of the eigenstates, their complex energies and  $F_3$  quantum numbers.
- Computation of spin echo signals based on the total integrated flux, parallelised using OpenMP<sup>®</sup>.

The implementation of these features is given as a pseudocode below. Its main parts have already been described in [83]. To entirely understand the procedures, studying the commented source code is advisable.

---

<sup>1</sup>Path sections of pure  $\mathcal{B}_3$ -fields may cross  $\mathcal{B}_3 = 0$ . For that situation the consistent labelling of states is described in Section 5.3.

```

IMPORT UserSpecifiedParameters{
  IMPORT AccuracyForAdaptiveStepping2
  IMPORT OMLIMIT3
  IMPORT MinimumAAS4
  IMPORT MultiplyPV5
}
IMPORT UserOptions{
  SET UsePerturbationTheory6
  SET IGNORE7
  CREATE SecondaryDataFileHandling8
  IMPORT SpinEchoSettings{
    IMPORT InitialState9
    IMPORT AnalysingState10
    IMPORT AverageMomentumScale11
    IMPORT WavePacketsWidths12
    IMPORT S_MIN and S_MAX13
    IMPORT SPINECHOSTART and SPINECHOEND14
    IMPORT SS_STEPS15
  }
}
INITIALIZE FieldConfiguration{
  PARSE AnalyticFieldExpression16
  IMPORT BaseSteps17
  IMPORT InterferometerLength
}
INITIALIZE AtomicSystem{

```

---

<sup>2</sup>The maximal value of the minimised norm used for the difference quotient approach, approximating the line integral representation of Berry phases.

<sup>3</sup>A parameter for the accuracy employed in the routines checking the continuity of energy eigenvalues and  $F_3$  quantum numbers, where appropriate and/or user-specified.

<sup>4</sup>Threshold (optional) up to which AccuracyForAdaptiveStepping is weakened for nasty field configurations.

<sup>5</sup>MultiplyPV1 and MultiplyPV2: Values with which the PV Berry phases are multiplied manually. Default is 1.

<sup>6</sup>For the decomposition of Berry phases into P-conserving and P-violating contributions.

<sup>7</sup>If true, alignment failures of non-metastable states are ignored.

<sup>8</sup>Eigenvalues, eigenvectors, scalar products, accumulated phases, data for time-table plots, data for total integrated flux, etc.

<sup>9</sup>The initial superposition of metastable eigenstates.

<sup>10</sup>The superposition of metastable eigenstates used for projection onto the evolved state at the end of the interferometer.

<sup>11</sup>Connected to the average velocity of the atoms in  $z$ -direction.

<sup>12</sup> $\sigma_L, \sigma_k$ .

<sup>13</sup>Range of the spin echo parameter  $s$  modulating the (user-specified) field components.

<sup>14</sup>The  $z$ -axis values between  $s$  is applied.

<sup>15</sup>Number of base points for the  $\mathcal{F}_p$ -curve.

<sup>16</sup>The math parser 'muparser' from SOURCEFORGE.NET<sup>®</sup> parses the  $z$ -parametrised field configuration.

<sup>17</sup>The number of points where the field configuration and the eigensystem is evaluated if an adaptive stepping is not needed due to the physical situation. Otherwise, the number of points will be increased as needed to reach the user-specified accuracy.

---

```

    IMPORT AtomicSpecies18
    IMPORT NumberingScheme19
    INITIALIZE MassMatrix20
}
CREATE MainDataFileHandling

BEGIN MAINROUTINE
  BEGIN WALRUS21
    'The time has come', the Walrus said,
    'To talk of many things:
    Of shoes – and ships – and sealing-wax –
    Of cabbages and kings...'
  END OF WALRUS
  MOVE_FIELDCONFIGURATION22
  SOLVE EigenProblem at first point of the FieldConfiguration23
  SYNCHRONISE NumberingScheme with the reference numbering scheme
  BEGIN WHILE ( FieldNotAtEnd OR ( FieldAtEnd AND AlignmentFailed ) )
    MOVE_FIELDCONFIGURATION to next point of field configuration24{
      IF ( AlignmentOk AND CurrentStepSize < BaseStepSize )
        THEN double CurrentStepSize
      ELSE IF ( AlignmentFailed )
        THEN halve CurrentStepSize
    }
    MOVE_EIGENSYSTEM to current point of field configuration25
    CHECK continuity26 of energies and  $F_3$ .
    ALIGN current RKets2 at the previous RKets
    BEGIN IF ( AlignmentFailed AND ( DeltaZ > MinimalDeltaZ27 ) )
      THEN skip the following code of the while-loop28
    ELSE IF ( AlignmentFailed AND ( DeltaZ ≤ MinimalDeltaZ ) )
      THEN{
        soften the alignment criteria29

```

---

<sup>18</sup>For example  $H(n = 2)$ .

<sup>19</sup>The label order of the eigenstates obtained by a reference field  $\mathcal{B} = (0, 0, 10)\mu\text{T}$ ,  $\mathcal{E} = \mathbf{0}$ .

<sup>20</sup>Depending on FieldConfiguration.

<sup>21</sup>Lewis Carroll, *Through the Looking-Glass and What Alice Found There*, 1872. In honour of the tradition to hide Easter eggs.

<sup>22</sup>From the reference field to the first point of the FieldConfiguration. Continuity of the energies (and of  $F_3$  for pure  $\mathcal{B}_3$ -fields) is ensured with a precision set by OMLIMIT.

<sup>23</sup>The according data are stored as reference eigenvectors in order to obtain the phases at the end of the interferometer, cf. [83].

<sup>24</sup>Using BaseStepSize computed from BaseSteps and InterferometerLength.

<sup>25</sup>That is, compute eigenvalues and eigenvectors at the current position on the z-axis and use the reference numbering scheme to label the new eigenvectors.

<sup>26</sup>In case the user-specified criteria are violated, MOVE\_FIELDCONFIGURATION will reverse the actual stepping and move forward half the distance instead.

<sup>27</sup>MinimalDeltaZ is at least machine precision, i.e.  $10^{-16}$  since DeltaZ is the difference of two numbers of type double. Actually, we define MinimalDeltaZ =  $10^{-13}$  m.

<sup>28</sup>MOVE\_FIELDCONFIGURATION will reverse the actual stepping and move forward half the distance instead.

<sup>29</sup>Increase the AccuracyForAdaptiveStepping up to the predefined value WeakenAAS.

```

        IF ( AlignmentFailed ) THEN break down the computation30
    }
ELSE IF ( AlignmentOk31 )
    COMPUTE left eigenvectors
    IF ( UsePerturbationTheory )
        THEN compute P-conserving and P-violating contributions
            separately32
    ELSE compute total geometric phase contribution33
    COMPUTE the effective potential
    COMPUTE the reduced arrival times
    STORE the current position  $z$ 34
    STORE the current left and right eigenvectors35
    EXPORT data36
END IF
END OF WHILE
END MAINROUTINE
COMPUTE relative phases between last and first right eigenvectors37
COMPUTE the total integrated flux
EXPORT data38
CLEANUP

COMPUTE FluxDensityVectorFields39
COMPUTE Divergence and curl of PC FluxDensityVectorFields40
COMPUTE SpinEchoSignal41

```

---

<sup>30</sup>This severe case cannot be handled with the present software.

<sup>31</sup>Now we have the right eigenvectors RKets2 at the current position on the  $z$ -axis suitably aligned with the right eigenvectors RKets at the previous (appropriate) position on the  $z$ -axis.

<sup>33</sup>The contributions to the geometric phase are local contributions that are accumulated additively.

<sup>34</sup>As the starting position for the next MOVE\_FIELDCONFIGURATION routine.

<sup>35</sup>As reference eigensystem for the next point in the field configuration.

<sup>36</sup>All data that evolves while the field configuration is stepped forward.

<sup>37</sup>This relative phases are added to the total accumulated geometric phases.

<sup>38</sup>Export all data that is calculated after the end of the field configuration is reached, e.g., geometric phases and total integrated flux. The latter is also exported to the 'SpinEcho' tab within the user interface.

<sup>39</sup>A separate procedure which, however, uses large parts of the MAINROUTINE. For each parameter space point of the user-specified grid, the procedure starts from the reference field and reaches the parameter point with a straight line. Thereby, the degeneracy at  $\mathbf{B} = \mathbf{0}$  has to be avoided when defining the grid.

<sup>40</sup>Both are calculated automatically when computing FluxDensityVectorFields.

<sup>41</sup>Using OpenMP<sup>®</sup> parallel computing (optional). Therefore, the *make*-file has to be modified: The flag *-fopenmp* has to be used for *gcc*, *g++*, *CFLAGS*, *CXXFLAGS*, and *LINK*. Otherwise *#pragma omp* source code will be omitted. Then type in console: *export OMP\_NUM\_THREADS=X*, where *X* is the number of CPUs which ought to be utilised. Then, execute QABSE.

# Bibliography

- [1] G. Lüders, *On the Equivalence of Invariance under Time Reversal and under Particle-Antiparticle Conjugation for Relativistic Field Theories*, Dan. Mat. Fys. Medd. **28**, no. 5 (1954).
- [2] G. Lüders, *Proof of the TCP Theorem*, Ann. Phys. **2**, 1 (1957).
- [3] O. W. Greenberg, *CPT Violation Implies Violation of Lorentz Invariance*, Phys. Rev. Lett. **89**, 231602 (2002).
- [4] T.-D. Lee and C. G. Yang, *Question of Parity Conservation in Weak Interactions*, Phys. Rev. **104**, 254 (1956).
- [5] C. S. Wu, E. Ambler, R. W. Hayward, D. D. Hoppes and R. P. Hudson, *Experimental Test of Parity Conservation in Beta Decay*, Phys. Rev. **105**, 1413 (1957).
- [6] E. G. Adelberger and W. C. Haxton, *Parity Violation in the Nucleon-Nucleon Interaction*, Ann. Rev. Nucl. Part. Sci. **35**, 501 (1985).
- [7] I. B. Khriplovich, *Parity Nonconservation in Atomic Phenomena*, (Gordon and Breach, Philadelphia, 1991).
- [8] M.-A. Bouchiat and C. Bouchiat, *Parity Violation in Atoms*, Rep. Prog. Phys. **60**, 1351 (1997).
- [9] B. Desplanques, *Parity-non-conservation in nuclear forces at low energy: phenomenology and questions*, Phys. Rep. **297**, 1 (1998).
- [10] J. Guena, M. Lintz and M.-A. Bouchiat, *Atomic Parity Violation: Principles, Recent Results, Present Motivations*, Mod. Phys. Lett. A **20**, 375 (2005).
- [11] M.-A. Bouchiat, *Atomic Parity Violation. Early days, present results, prospects*, Nuovo Cimento C **35**, 78 (2012).
- [12] J. Beringer et al., Particle Data Group, *Review of particle physics*, Phys. Rev. D **86**, 010001 (2012).
- [13] A. Guijarro and M. Yus, *The Origin of Chirality in the Molecules of Life*, (The Royal Society of Chemistry, 2009).
- [14] V. A. Avetisov, V. I. Goldanskii and V. V. Kuz'min, *Handedness, Origin of Life and Evolution*, Phys. Today **44**, 33 (1991).
- [15] S. L. Glashow, *Partial-Symmetries of Weak Interactions*, Nucl. Phys. **22**, 579 (1961).

## Bibliography

---

- [16] S. Weinberg, *A Model of Leptons*, Phys. Rev. Lett. **19**, 1264 (1967).
- [17] A. Salam, *Weak and Electromagnetic Interactions*, in Elementary Particle Theory, Proceedings Of The Nobel Symposium Held 1968 At Lerum, Sweden, edited by N. Svartholm (Almqvist & Wiksell, Stockholm, 1968).
- [18] F. J. Hasert et al., *Observation of neutrino-like interactions without muon or electron in the Gargamelle neutrino experiment*, Phys. Lett. B **46**, 138 (1973).
- [19] Y. B. Zel'dovich, *Parity nonconservation in the first order in the weak-interaction constant in electron scattering and other effects*, Sov. Phys. JETP **9**, 682 (1959).
- [20] F. C. Michel, *Neutral Weak Interaction Currents*, Phys. Rev. **138**, B408 (1965).
- [21] L. M. Barkov and M. S. Zolotarev, *Parity violation in atomic bismuth*, Phys. Lett. B **85**, 308 (1979).
- [22] M. V. Berry, *Quantal phase factors accompanying adiabatic changes*, Proc. R. Soc. Lond. A **392**, 45 (1984).
- [23] Y. Aharonov and D. Bohm, *Significance of Electromagnetic Potentials in the Quantum Theory*, Phys. Rev. **115**, 485 (1959).
- [24] *Geometric Phases in Physics*, edited by A. Shapere and F. Wilczek, Vol. 5 of Advanced Series in Mathematical Physics (World Scientific, Singapore, 1989).
- [25] J. W. Zwanziger, M. Koenig and A. Pines, *Berry's Phase*, Annu. Rev. Phys. Chem. **41**, 601 (1990).
- [26] S.-Y. Xu et al., *Experimental observation of the quantum Hall effect and Berry's phase in graphene*, Nature **438**, 201 (2005).
- [27] K. S. Novoselov et al., *Unconventional quantum Hall effect and Berry's phase of  $2\pi$  in bilayer graphene*, Nature Physics **2**, 177 (2006).
- [28] S.-Y. Xu et al., *Hedgehog spin texture and Berry's phase tuning in a magnetic topological insulator*, Nature Physics **8**, 616 (2012).
- [29] B. Simon, *Holonomy, the quantum adiabatic theorem, and Berry's phase*, Phys. Rev. Lett. **51**, 2167 (1983).
- [30] M. Nakahara, *Geometry, Topology and Physics*, Graduate student series in physics (Adam Hilger, Bristol and New York, 1990).
- [31] P. J. Leek et al., *Observation of Berry's Phase in a Solid-State Qubit*, Science **318**, 1889 (2007).
- [32] T. Bergmann, M. DeKieviet, T. Gasenzer, O. Nachtmann and M.-I. Trappe, *Parity Violation in Hydrogen and Longitudinal Atomic Beam Spin Echo I*, Eur. Phys. J. D **54**, 551 (2009).
- [33] M. DeKieviet, T. Gasenzer, O. Nachtmann and M.-I. Trappe, *Longitudinal atomic beam spin echo experiments: a possible way to study parity violation in hydrogen*, Hyperfine Interact. **200**, 35 (2011).

- 
- [34] E. L. Hahn, *Spin Echoes*, Phys. Rev. **80**, 580 (1950).
- [35] M. DeKieviet, D. Dubbers, C. Schmidt, D. Scholz and U. Spinola,  *$^3\text{He}$  spin echo: A new atomic beam technique for probing phenomena in the neV range*, Phys. Rev. Lett. **75**, 1919 (1995).
- [36] C. Schmidt and D. Dubbers, *Spin-echo Experiments with Neutrons and with Atomic Beams*, in Atomic Physics Methods in Modern Research, Lecture Notes in Physics, edited by K. P. Jungmann, J. Kowalski, I. Reinhard and F. Träger (Springer, Berlin, Heidelberg, 1997).
- [37] C.-E. Roux, *Dimensionierung eines Spinecho-Systems zur Messung von geometrischen Phasen in Wasserstoff*, diploma thesis (unpublished), Ruprecht-Karls-Universität, Heidelberg (2007).
- [38] A. Reiner, *Aufbau und Test einer Wasserstoff- und Deuteriumstrahl- spinecho-maschine*, PhD thesis, Ruprecht-Karls-Universität, Heidelberg (1998).
- [39] T. Bergmann, *Theorie des longitudinalen Atomstrahl-Spinechos und paritätsverletzende Berry-Phasen in Atomen*, PhD thesis, Ruprecht-Karls-Universität, Heidelberg (2006).
- [40] T. Gasenzer, O. Nachtmann and M.-I. Trappe, *Metastable states of hydrogen: their geometric phases and flux densities*, Eur. Phys. J. D **66**, 1 (2012).
- [41] K. Abe et al., SLD Collaboration, *High-Precision Measurement of the Left-Right Z Boson Cross-Section Asymmetry*, Phys. Rev. Lett. **84**, 5945 (2000).
- [42] The ALEPH Collaboration, The DELPHI Collaboration, The L3 Collaboration, The OPAL Collaboration, The SLD Collaboration, The LEP Electroweak Working Group and The SLD Electroweak and Heavy Flavour Groups, *Precision electroweak measurements on the Z resonance*, Phys. Rep. **427**, 257 (2006).
- [43] J. Erler and M. J. Ramsey-Musolf, *The weak mixing angle at low energies*, Phys. Rev. D **72**, 073003 (2005).
- [44] M.-A. Bouchiat and C. Bouchiat, *Weak neutral currents in atomic physics*, Phys. Lett. B **48**, 111 (1974).
- [45] M.-A. Bouchiat and C. Bouchiat, *Parity Violation Induced by Weak Neutral Currents in Atomic Physics*, J. Phys. France **35**, 899 (1974).
- [46] M.-A. Bouchiat and C. Bouchiat, *Parity Violation Induced by Weak Neutral Currents in Atomic Physics. Part II*, J. Phys. France **36**, 493 (1975).
- [47] C. S. Wood, S. C. Bennett, D. Cho, B. P. Masterson, J. L. Roberts, C. E. Tanner and C. E. Wieman, *Measurement of Parity Nonconservation and an Anapole Moment in Cesium*, Science **275**, 1759 (1997).
- [48] R. W. Dunford and R. J. Holt, *Parity violation in hydrogen revisited*, J. Phys. G: Nucl. Part. Phys. **34**, 2099 (2007).

## Bibliography

---

- [49] R. W. Dunford and R. J. Holt, *Parity nonconservation in hydrogen*, *Hyperfine Interact.* **200**, 45 (2011).
- [50] R. W. Dunford and T. Stöhlker, *PNC in hydrogen. Different prospects using heliumlike ions*, *Parity Violation in Atoms and Polarized Electron Scattering* (World Scientific, Singapore, 1999).
- [51] C. C. W. Fehrenbach, *An experimental limit on parity mixing in atomic hydrogen*, PhD thesis, University of Michigan, Ann Arbor (1993).
- [52] J. Ashman et al., European Muon Collaboration, *A measurement of the spin asymmetry and determination of the structure function  $g_1$  in deep inelastic muon-proton scattering*, *Phys. Lett. B* **206**, 364 (1988).
- [53] J. Ashman et al., *An investigation of the spin structure of the proton in deep inelastic scattering of polarised muons on polarised protons*, *Nucl. Phys. B* **328**, 1 (1989).
- [54] E. Leader and M. Anselmino, *A crisis in the parton model: where, oh where is the proton's spin?*, *Z. Phys. C* **41**, 239 (1988).
- [55] S. F. Pate, D. W. McKee and V. Papavassiliou, *Strange quark contribution to the vector and axial form factors of the nucleon: Combined analysis of data from the G0, HAPPEX, and Brookhaven E734 experiments*, *Phys. Rev. C* **78**, 015207 (2008).
- [56] D. Florian, R. Sassot, M. Stratmann and W. Vogelsang, *Global Analysis of Helicity Parton Densities and their Uncertainties*, *Phys. Rev. Lett.* **101**, 072001 (2008).
- [57] D. Florian, R. Sassot, M. Stratmann and W. Vogelsang, *Extraction of spin-dependent parton densities and their uncertainties*, *Phys. Rev. D* **80**, 034030 (2009).
- [58] M. G. Alekseev et al., COMPASS Collaboration, *Quark helicity distributions from longitudinal spin asymmetries in muon-proton and muon-deuteron scattering*, *Physics Letters B* **693**, 227 (2010).
- [59] E. Leader, A. V. Sidorov and D. B. Stamenov, *A Possible Resolution of the Strange Quark Polarization Puzzle?*, [hep-ph] arXiv:1103.5979v2 (2011).
- [60] J. C. Garrison and E. M. Wright, *Complex geometrical phases for dissipative systems*, *Phys. Lett. A* **128**, 177 (1988).
- [61] Ch. Miniatura, C. Sire, J. Baudon and J. Bellissard, *Geometrical Phase Factor for a Non-Hermitian Hamiltonian*, *Europhys. Lett.* **13**, 199 (1990), Correction: *Europhys. Lett.* **14**, 91 (1991).
- [62] S. Massar, *Applications of the complex geometric phase for metastable systems*, *Phys. Rev. A* **54**, 4770 (1996).
- [63] F. Keck, H. J. Korsch and S. Mossmann, *Unfolding a diabolic point: a generalized crossing scenario*, *J. Phys. A: Mathematical and General* **36**, 2125 (2003).
- [64] M. V. Berry, *Physics of Nonhermitian Degeneracies*, *Czech. J. Phys.* **54**, 1039 (2004).

- 
- [65] W. D. Heiss, *Exceptional Points – Their Universal Occurrence and Their Physical Significance*, Czech. J. Phys. **54**, 1091 (2004).
- [66] A. I. Nesterov and F. Aceves de la Cruz, *Complex magnetic monopoles, geometric phases and quantum evolution in the vicinity of diabolic and exceptional points*, J. Phys. A: Mathematical and Theoretical **41**, 485304 (2008).
- [67] T. Bergmann, T. Gasenzer and O. Nachtmann, *Metastable states, the adiabatic theorem and parity violating geometric phases I*, Eur. Phys. J. D **45**, 197 (2007).
- [68] T. Bergmann, T. Gasenzer and O. Nachtmann, *Metastable states, the adiabatic theorem and parity violating geometric phases II*, Eur. Phys. J. D **45**, 211 (2007).
- [69] D. J. Wineland, J. J. Bollinger, W. M. Itano and D. J. Heinzen, *Squeezed atomic states and projection noise in spectroscopy*, Phys. Rev. A **50**, 67 (1994).
- [70] W. M. Itano et al., *Quantum projection noise: Population fluctuations in two-level systems*, Phys. Rev. A **47**, 3554 (1993).
- [71] J. J. Bollinger, W. M. Itano, D. J. Wineland and D. J. Heinzen, *Optimal frequency measurements with maximally correlated states*, Phys. Rev. A **54**, R4649 (1996).
- [72] D. Leibfried et al., *Toward Heisenberg-Limited Spectroscopy with Multiparticle Entangled States*, Science **304**, 1476 (2004).
- [73] H. Uys and P. Meystre, *Quantum states for Heisenberg-limited interferometry*, Phys. Rev. A **76**, 013804 (2007).
- [74] A. Sørensen, L.-M. Duan, J. I. Cirac and P. Zoller, *Many-particle entanglement with Bose-Einstein condensates*, Nature **409**, 63 (2001).
- [75] J. Estève, C. Gross, A. Weller, S. Giovanazzi and M. K. Oberthaler, *Squeezing and entanglement in a Bose-Einstein condensate*, Nature **455**, 1216 (2008).
- [76] C. Bodet, J. Estève, M. K. Oberthaler and T. Gasenzer, *Two-mode Bose gas: Beyond classical squeezing*, Phys. Rev. A **81**, 063605 (2010).
- [77] Maarten DeKieviet, *private communication*.
- [78] Mariusz Puchalski, *private communication*.
- [79] W. Bernreuther and O. Nachtmann, *A New Way to Measure Parity Violating Effects in Atomic Systems*, Z. Phys. A **309**, 197 (1983).
- [80] G. W. Botz, D. Bruß and O. Nachtmann, *Polarization Rotation Effects due to Parity Violation in Atoms*, Ann. Phys. (NY) **240**, 107 (1995).
- [81] T. Gasenzer, *Paritätsverletzende Energieverschiebungen und Berry-Phasen in Atomen*, PhD thesis, Ruprecht-Karls-Universität, Heidelberg (1998).
- [82] D. Bruß, T. Gasenzer and O. Nachtmann, *Parity violating energy shifts and Berry phases in atoms. I*, Eur. Phys. J. direct **D2**, 1 (1999).

## Bibliography

---

- [83] M.-I. Trappe, *Parity Violating Berry Phases for Hydrogen in an Atom Interferometer*, diploma thesis (unpublished), Ruprecht-Karls-Universität, Heidelberg (2008).
- [84] R. W. Dunford, R. R. Lewis and W. L. Williams, *Parity nonconservation in the hydrogen atom. II*, Phys. Rev. A **18**, 2421 (1978).
- [85] M.-A. Bouchiat and L. Pottier, *Optical Experiments and Weak Interactions*, Science **234**, 1203 (1986).
- [86] L. Pasteur, *Sur les relations qui peuvent exister entre la forme cristalline, la composition chimique et le sens de la polarisation rotatoire*, Annales de Chimie et de Physique **24**, 442 (1848).
- [87] P. Bargueño, I. Gonzalo and R. Tudela, *Detection of parity violation in chiral molecules by external tuning of electroweak optical activity*, Phys. Rev. A **80**, 012110 (2009).
- [88] M. Ziskind, C. Daussy, T. Marrel and Ch. Chardonnet, *Improved sensitivity in the search for a parity-violating energy difference in the vibrational spectrum of the enantiomers of CHFClBr*, Eur. Phys. J. D **20**, 219 (2002).
- [89] A. J. MacDermott and R. A. Hegstrom, *A proposed experiment to measure the parity-violating energy difference between enantiomers from the optical rotation of chiral ammonia-like 'cat' molecules*, Chem. Phys. **305**, 55 (2004).
- [90] C. Bouchiat and C. A. Piketty, *Nuclear spin dependent atomic parity violation, nuclear anapole moments and the hadronic axial neutral current*, Z. Phys. C **49**, 91 (1991).
- [91] J. S. M. Ginges and V. V. Flambaum, *Violations of fundamental symmetries in atoms and tests of unification theories of elementary particles*, Phys. Rep. **397**, 63 (2004).
- [92] N. Cabibbo, *Unitary Symmetry and Leptonic Decays*, Phys. Rev. Lett. **10**, 531 (1963).
- [93] O. Nachtmann, *Elementary Particle Physics, Concepts and Phenomena*, (Springer, Berlin, 1990).
- [94] M. E. Peskin and D. V. Schröder, *An Introduction to Quantum Field Theory*, (Perseus Books Publishing, Reading, Massachusetts, 1995).
- [95] E. D. Commins and P. H. Bucksbaum, *The Parity Non-Conserving Electron-Nucleon Interaction*, Ann. Rev. Nucl. Part. Sci. **30**, 1 (1980).
- [96] C. Bouchiat and C. A. Piketty, *Parity violation in atomic cesium and alternatives to the standard model of electroweak interactions*, Phys. Lett. B **128**, 73 (1983).
- [97] K. Nakamura et al., Particle Data Group, *Review of particle physics*, J. Phys. G **37**, 075021 (2010).

- 
- [98] D. Acosta et al., CDF Collaboration, *Measurement of the forward-backward charge asymmetry of electron-positron pairs in  $\bar{p}p$  collisions at  $\sqrt{s} = 1.96$  TeV*, Phys. Rev. D **71**, 052002 (2005).
- [99] V. M. Abazov et al., D0 Collaboration, *Measurement of the W Boson Mass*, Phys. Rev. Lett. **103**, 141801 (2009).
- [100] J. M. Conrad, M. H. Shaevitz and T. Bolton, *Precision measurements with high-energy neutrino beams*, Rev. Mod. Phys. **70**, 1341 (1998).
- [101] G. P. Zeller et al., NuTeV Collaboration, *Precise Determination of Electroweak Parameters in Neutrino-Nucleon Scattering*, Phys. Rev. Lett. **88**, 091802 (2002).
- [102] P. L. Anthony et al., SLAC E158 Collaboration, *Observation of Parity Nonconservation in Møller Scattering*, Phys. Rev. Lett. **92**, 181602 (2004).
- [103] R. D. Carlini, J. M. Finn, S. Kowalski, S. A. Page and others, *The Qweak Experiment: A Search for New Physics at the TeV Scale via a Measurement of the Proton's Weak Charge*, [physics.ins-det] arXiv:1202.1255v2 (2012).
- [104] J. Guéna, M. Lintz and M.-A. Bouchiat, *Measurement of the parity violating 6S-7S transition amplitude in cesium achieved within  $2 \times 10^{-13}$  atomic-unit accuracy by stimulated-emission detection*, Phys. Rev. A **71**, 042108 (2005).
- [105] S. G. Porsev, K. Beloy and A. Derevianko, *Precision Determination of Electroweak Coupling from Atomic Parity Violation and Implications for Particle Physics*, Phys. Rev. Lett. **102**, 181601 (2009).
- [106] P. Fayet, *Light spin- $\frac{1}{2}$  or spin-0 dark matter particles*, Phys. Rev. D **70**, 023514 (2004).
- [107] C. Bouchiat and P. Fayet, *Constraints on the parity-violating couplings of a new gauge boson*, Phys. Lett. B **608**, 87 (2005).
- [108] R. E. Lingenfelter, J. C. Higdon and R. E. Rothschild, *Is There a Dark Matter Signal in the Galactic Positron Annihilation Radiation?*, Phys. Rev. Lett. **103**, 031301 (2009).
- [109] M.-A. Bouchiat, J. Guéna, L. Hunter and L. Pottier, *Observation of a parity violation in cesium*, Phys. Lett. B **117**, 358 (1982).
- [110] M.-A. Bouchiat, J. Guéna, L. Pottier and L. Hunter, *New observation of a parity violation in cesium*, Phys. Lett. B **134**, 463 (1984).
- [111] S. C. Bennett and C. E. Wieman, *Measurement of the 6S  $\rightarrow$  7S Transition Polarizability in Atomic Cesium and an Improved Test of the Standard Model*, Phys. Rev. Lett. **82**, 2484 (1999).
- [112] K. Tsigutkin, D. Dounas-Frazer, A. Family, J. E. Stalnaker, V. V. Yashchuk and D. Budker, *Observation of a Large Atomic Parity Violation Effect in Ytterbium*, Phys. Rev. Lett. **103**, 071601 (2009).

## Bibliography

---

- [113] N. H. Edwards, S. J. Phipp, P. E. G. Baird and S. Nakayama, *Precise Measurement of Parity Nonconserving Optical Rotation in Atomic Thallium*, Phys. Rev. Lett. **74**, 2654 (1995).
- [114] P. A. Vetter, D. M. Meekhof, P. K. Majumder, S. K. Lamoreaux and E. N. Fortson, *Precise Test of Electroweak Theory from a New Measurement of Parity Nonconservation in Atomic Thallium*, Phys. Rev. Lett. **74**, 2658 (1995).
- [115] M. J. D. Macpherson, K. P. Zetie, R. B. Warrington, D. N. Stacey and J. P. Hoare, *Precise measurement of parity nonconserving optical rotation at 876 nm in atomic bismuth*, Phys. Rev. Lett. **67**, 2784 (1991).
- [116] D. M. Meekhof, P. Vetter, P. K. Majumder, S. K. Lamoreaux and E. N. Fortson, *High-precision measurement of parity nonconserving optical rotation in atomic lead*, Phys. Rev. Lett. **71**, 3442 (1993).
- [117] V. A. Dzuba, V. V. Flambaum, P. G. Silvestrov and O. P. Sushkov, *Calculation of parity non-conservation in thallium*, J. Phys. B: At. Mol. Phys. **20**, 3297 (1987).
- [118] V. A. Dzuba, V. V. Flambaum and I. B. Khriplovich, *Enhancement of P- and T-nonconserving effects in rare-earth atoms*, Z. Phys. D: Atoms, Molecules and Clusters **1**, 243 (1986).
- [119] A. Derevianko and S. G. Porsev, *Reevaluation of the role of nuclear uncertainties in experiments on atomic parity violation with isotopic chains*, Phys. Rev. A **65**, 052115 (2002).
- [120] K. Tsigutkin, D. Dounas-Frazer, A. Family, J. E. Stalnaker, V. V. Yashchuk and D. Budker, *Parity violation in atomic ytterbium: Experimental sensitivity and systematics*, Phys. Rev. A **81**, 032114 (2010).
- [121] E. N. Fortson, *Possibility of measuring parity nonconservation with a single trapped atomic ion*, Phys. Rev. Lett. **70**, 2383 (1993).
- [122] L. W. Wansbeek, B. K. Sahoo, R. G. E. Timmermans, K. Jungmann, B. P. Das and D. Mukherjee, *Atomic parity nonconservation in  $\text{Ra}^+$* , Phys. Rev. A **78**, 050501 (2008).
- [123] B. K. Sahoo and B. P. Das, *Parity nonconservation in ytterbium ion*, Phys. Rev. A **84**, 010502 (2011).
- [124] V. A. Dzuba and V. V. Flambaum, *Calculation of nuclear-spin-dependent parity nonconservation in s-d transitions of  $\text{Ba}^+$ ,  $\text{Yb}^+$ , and  $\text{Ra}^+$  ions*, Phys. Rev. A **83**, 052513 (2011).
- [125] A. Schäfer, G. Soff, P. Indelicato, B. Müller and W. Greiner, *Prospects for an atomic parity-violation experiment in  $\text{U}^{90+}$* , Phys. Rev. A **40**, 7362 (1989).
- [126] L. N. Labzowsky, A. V. Nefiodov, G. Plunien, G. Soff, R. Marrus and D. Liesen, *Parity-violation effect in heliumlike gadolinium and europium*, Phys. Rev. A **63**, 054105 (2001).

- 
- [127] V. M. Shabaev, A. V. Volotka, C. Kozhuharov, G. Plunien and T. Stöhlker, *Parity-nonconservation effect with the laser-induced  $2\ ^3S_1-2\ ^1S_0$  transition in heavy heliumlike ions*, Phys. Rev. A **81**, 052102 (2010).
- [128] F. Ferro, A. Artemyev, T. Stöhlker and A. Surzhykov, *Isotope shift of the  $1s2p\ ^3P_0-1s2s\ ^1S_0$  level splitting in heavy He-like ions: Implications for atomic parity-nonconservation studies*, Phys. Rev. A **81**, 062503 (2010).
- [129] F. Ferro, A. Surzhykov and T. Stöhlker, *Hyperfine transitions in He-like ions as a tool for nuclear-spin-dependent parity-nonconservation studies*, Phys. Rev. A **83**, 052518 (2011).
- [130] J. R. Sapirstein and D. R. Yennie, *Theory of Hydrogenic Bound States*, in Quantum Electrodynamics, Advanced Series on Directions in High Energy Physics, Vol. 7, edited by T. Kinoshita (World Scientific, Singapore, 1990).
- [131] T. Bergmann, *Paritätsverletzende Polarisations-Rotationen von Deuterium in elektrischen Feldern*, diploma thesis (unpublished), Ruprecht-Karls-Universität, Heidelberg (2003).
- [132] E. A. Hinds, *Sensitivity and the Role of Level Crossings in Measurements of Parity Nonconservation using Metastable Atoms*, Phys. Rev. Lett. **44**, 374 (1980).
- [133] G. Feinberg and M. Y. Chen, *Hyperfine effects in parity-violating muonic-atom decays*, Phys. Rev. D **10**, 3789 (1974).
- [134] R. D. Young, R. D. Carlini, A. W. Thomas and J. Roche, *Testing the Standard Model by Precision Measurement of the Weak Charges of Quarks*, Phys. Rev. Lett. **99**, 122003 (2007).
- [135] C. Y. Prescott et al., *Parity Non-Conservation in Inelastic Electron Scattering*, Phys. Lett. B **77**, 347 (1978).
- [136] C. Y. Prescott et al., *Further Measurements of Parity Non-Conservation in Inelastic Electron Scattering*, Phys. Lett. B **84**, 524 (1979).
- [137] W. Heil et al., *Improved limits on the weak, neutral, hadronic axial vector coupling constants from quasielastic scattering of polarized electrons*, Nuclear Physics B **327**, 1 (1989).
- [138] P. A. Souder et al., *Measurement of parity violation in the elastic scattering of polarized electrons from  $^{12}\text{C}$* , Phys. Rev. Lett. **65**, 694 (1990).
- [139] L. P. Lévy and W. L. Williams, *Experimental Test of Laporte's Rule In Atomic Hydrogen*, Phys. Rev. Lett. **48**, 607 (1982).
- [140] L. P. Lévy and W. L. Williams, *Parity nonconservation in the hydrogen atom. III*, Phys. Rev. A **30**, 220 (1984).
- [141] E. A. Hinds and V. W. Hughes, *Parity Nonconservation in Hydrogen Involving Magnetic/Electric Resonance*, Phys. Lett. B **67**, 487 (1977).

## Bibliography

---

- [142] E. A. Hinds, *Experiments to measure parity violation*, The Spectrum of Atomic Hydrogen - Advances (World Scientific, Singapore, 1988).
- [143] E. G. Adelberger, T. A. Trainor, E. N. Fortson, T. E. Chupp, D. Holmgren, M. Z. Iqbal and H. E. Swanson, *A Technique for Measuring Parity Nonconservation in Hydrogenic Atoms*, Nucl. Instrum. Meth. **179**, 181 (1981).
- [144] Y. Aharonov and J. Anandan, *Phase Change during a Cyclic Quantum Evolution*, Phys. Rev. Lett. **58**, 1593 (1986).
- [145] S. Pancharatnam, *Generalized Theory of Interference and its Applications*, Proc. Indian Acad. Sci. A **44**, 247 (1956).
- [146] S. Ramaseshan and R. Nityananda, *The interference of polarized light as an early example of Berry's phase*, Curr. Sci. **55**, 1225 (1986).
- [147] M. V. Berry, *The Adiabatic Phase and Pancharatnam's Phase for Polarized Light*, J. Mod. Opt. **34**, 1401 (1987).
- [148] J. Samuel and R. Bhandari, *General Setting for Berry's Phase*, Phys. Rev. Lett. **60**, 2339 (1988).
- [149] F. Wilczek and A. Zee, *Appearance of Gauge Structure in Simple Dynamical Systems*, Phys. Rev. Lett. **52**, 2111 (1984).
- [150] J. Anandan and Y. Aharonov, *Geometric quantum phase and angles*, Phys. Rev. D **38**, 1863 (1988).
- [151] A. Messiah, *Quantum Mechanics*, 6th ed., (North Holland, Amsterdam, 1970).
- [152] D. J. Griffiths, *Introduction to Quantum Mechanics*, (Pearson Prentice Hall, New Jersey, 2005).
- [153] T. Bitter and D. Dubbers, *Manifestation of Berry's Topological Phase in Neutron Spin Rotation*, Phys. Rev. Lett. **59**, 251 (1987).
- [154] D. Dubbers, *Measurement of the Berry Phase with Polarized Neutrons*, Physica B **151**, 93 (1988).
- [155] D. Suter, G. C. Chingas, R. A. Harris and A. Pines, *Berry's phase in magnetic resonance*, Mol. Phys. **61**, 1327 (1987).
- [156] R. G. Chambers, *Shift of an Electron Interference Pattern by Enclosed Magnetic Flux*, Phys. Rev. Lett. **5**, 3 (1960).
- [157] D. H. Kobe, *Berry phase, Aharonov-Bohm effect and topology*, J. Phys. A: Mathematical and General **24**, 3551 (1991).
- [158] A. Tomita and R. Y. Chiao, *Observation of Berry's Topological Phase by Use of an Optical Fiber*, Phys. Rev. Lett. **57**, 937 (1986).
- [159] R. Y. Chiao and Y.-S. Wu, *Manifestations of Berry's Topological Phase for the Photon*, Phys. Rev. Lett. **57**, 933 (1986).

- 
- [160] T. H. Chyba, L. J. Wang, L. Mandel and R. Simon, *Manifestations of Berry's Topological Phase for the Photon*, Opt. Lett. **13**, 562 (1988).
- [161] Ch. Miniatura, J. Robert, O. Gorceix, V. Lorent, S. Le Boiteux, J. Reinhardt and J. Baudon, *Atomic Interferences and the Topological Phase*, Phys. Rev. Lett. **69**, 261 (1992).
- [162] C. L. Webb, R. M. Godun, G. S. Summy, M. K. Oberthaler, P. D. Featonby, C. J. Foot and K. Burnett, *Measurement of Berry's phase using an atom interferometer*, Phys. Rev. A **60**, R1783 (1999).
- [163] Y. Hasegawa, R. Loidl, M. Baron, G. Badurek and H. Rauch, *Off-Diagonal Geometric Phase in a Neutron Interferometer Experiment*, Phys. Rev. Lett. **87**, 070401 (2001).
- [164] V. F. Weisskopf and E. P. Wigner, *Über die natürliche Linienbreite in der Strahlung des harmonischen Oszillators*, Z. Phys. **65**, 18 (1930).
- [165] L. Mandel and E. Wolf, *Optical coherence and quantum optics*, (Cambridge University Press, Cambridge, 1995).
- [166] S. M. Barnett and P. M. Radmore, *Methods in Theoretical Quantum Optics*, (Oxford University Press Inc., New York, 1997).
- [167] P. L. Knight and L. Allen, *The ladder approximation in quantum optics and the Wigner-Weisskopf theory*, Phys. Lett. A **38**, 99 (1972).
- [168] Y. K. Wang and I. C. Khoo, *On the Wigner-Weisskopf approximation in quantum optics*, Opt. Comm. **11**, 323 (1974).
- [169] R. Jacob and R. G. Sachs, *Mass and Lifetime of Unstable Particles*, Phys. Rev. **121**, 350 (1961).
- [170] R. G. Sachs, *Interference phenomena of neutral K mesons*, Ann. Phys. **22**, 239 - 262 (1963).
- [171] L. N. Labzowsky, A. V. Shonin and D. A. Solovyev, *QED calculation of  $E 1 M 1$  and  $E 1 E 2$  transition probabilities in one-electron ions with arbitrary nuclear charge*, J. Phys. B: At. Mol. Opt. Phys. **38**, 265 (2005).
- [172] J. Sapirstein, K. Pachucki and K. T. Cheng, *Radiative corrections to one-photon decays of hydrogenic ions*, Phys. Rev. A **69**, 022113 (2004).
- [173] Otto Nachtmann, *private communication*.
- [174] H. Flanders, *Differential Forms*, Vol. 11 of Mathematics in Science and Engineering (Academic Press, New York, 1963).
- [175] C. E. Loving and P. G. H. Sandars, *On the feasibility of an atomic-beam resonance experiment sensitive to the nuclear-spin-dependent weak neutral current interaction*, J. Phys. B: At. Mol. Phys. **10**, 2755 (1977).

## Bibliography

---

- [176] Peter Augenstein, *private communication*.
- [177] L. Pezzé and A. Smerzi, *Phase sensitivity of a Mach-Zehnder interferometer*, Phys. Rev. A **73**, 011801 (2006).
- [178] H. Uys and P. Meystre, *Quantum states for Heisenberg-limited interferometry*, Phys. Rev. A **76**, 013804 (2007).
- [179] D. F. Walls, *Squeezed states of light*, Nature **306**, 141 (1983).
- [180] R. E. Slusher, L. W. Hollberg, B. Yurke, J. C. Mertz and J. F. Valley, *Observation of Squeezed States Generated by Four-Wave Mixing in an Optical Cavity*, Phys. Rev. Lett. **55**, 2409 (1985).
- [181] C. A. Sackett et al., *Experimental entanglement of four particles*, Nature **404**, 256 (2000).
- [182] T. Monz et al., *14-Qubit Entanglement: Creation and Coherence*, Phys. Rev. Lett. **106**, 130506 (2011).
- [183] C. Simon, *Natural entanglement in Bose-Einstein condensates*, Phys. Rev. A. **66**, 052323 (2002).
- [184] R. I. Semenov and V. I. Tuchkin, *Features of the Zeeman Splitting of Levels of the  $1snp$  Configurations of Helium*, Opt. Spectrosc. **88**, 147 (2000).
- [185] U. D. Jentschura, S. A. Kotochigova, E. LeBigot, P. J. Mohr and B. N. Taylor, *The Energy Levels of Hydrogen and Deuterium*, (National Institute of Standards and Technology, Gaithersburg, Maryland, 2005).
- [186] S. G. Karshenboim, *Precision physics of simple atoms: QED tests, nuclear structure and fundamental constants*, Phys. Rep. **422**, 1 (2005).
- [187] P. J. Mohr, B. N. Taylor and D. B. Newell, National Institute of Standards and Technology, *CODATA Recommended Values of the Fundamental Physical Constants: 2006*, Rev. Mod. Phys. **80**, 633 (2008).
- [188] E. U. Condon and G. H. Shortley, *The Theory of Atomic Spectra*, (Cambridge University Press, 1963).
- [189] M. Puchalski, U. D. Jentschura and P. J. Mohr, *Blackbody-radiation correction to the polarizability of helium*, Phys. Rev. A **83**, 042508 (2011).
- [190] V. I. Korobov, *Coulomb three-body bound-state problem: Variational calculations of nonrelativistic energies*, Phys. Rev. A **61**, 064503 (2000).
- [191] V. I. Korobov, *Nonrelativistic ionization energy for the helium ground state*, Phys. Rev. A **66**, 024501 (2002).
- [192] G. Herzberg, *Ionization Potentials and Lamb Shifts of the Ground States of  $^4\text{He}$  and  $^3\text{He}$* , Proc. R. Soc. London, Ser. A **248**, 309 (1958).

- 
- [193] W. C. Martin, *Energy Levels and Spectrum of Neutral Helium ( $^4\text{He I}$ )*, J. Res. Nat. Bur. Stand., Sect. A **64**, 19 (1960).
- [194] G. W. F. Drake, *Theory of relativistic magnetic dipole transitions: lifetime of the metastable  $2^3\text{S}$  state of the helium-like ions*, Phys. Rev. A **3**, 908 (1971).
- [195] R. S. Van Dyck, C. E. Johnson and H. A. Shugart, *Radiative Lifetime of the  $2^1\text{S}_0$  Metastable State of Helium*, Phys. Rev. A **4**, 1327 (1971).
- [196] G. W. F. Drake, *High precision calculations for helium*, in Springer Handbook of Atomic, Molecular, and Optical Physics, edited by G. W. F. Drake (Springer Science+Business Media, Inc., New York, 2006).
- [197] G. W. F. Drake, *Unified relativistic theory for  $1s2p^3\text{P}_1$ - $1s^2^1\text{S}_0$  and  $1s2p^1\text{P}_1$ - $1s^2^1\text{S}_0$  frequencies and transition rates in helium-like ions*, Phys. Rev. A **19**, 1387 (1979).
- [198] G. W. F. Drake, *The  $n^3\text{P}_2$ - $1^1\text{S}_0$  magnetic-quadrupole transitions of the helium sequence*, Astrophys. J. **158**, 1199 (1969).
- [199] G. W. F. Drake, *Erratum: The  $n^3\text{P}_2$ - $1^1\text{S}_0$  magnetic-quadrupole transitions of the helium sequence*, Astrophys. J. **163**, 439 (1971).
- [200] Y. Ralchenko, A. E. Kramida, J. Reader and NIST ASD Team (2011), *NIST Atomic Spectra Database*, (National Institute of Standards and Technology, Gaithersburg, Maryland, 2012).
- [201] Thomas Gasenzer, *private communication*.
- [202] W. C. Haxton, C.-P. Liu and M. J. Ramsey-Musolf, *Nuclear anapole moments*, Phys. Rev. C **65**, 045502 (2002).
- [203] W. C. Haxton and C. E. Wieman, *Atomic Parity Nonconservation and Nuclear Anapolemoments*, Annu. Rev. Nucl. Part. Sci. **51**, 261 (2001).



## Danksagung

Meinen herzlichsten Dank möchte ich Prof. Dr. Thomas Gasenzer für die hervorragende Betreuung während meiner Dissertation und für das Erstgutachten meiner Arbeit aussprechen. Seine fortwährende Unterstützung, sein immer offenes Ohr und das durchgehend äußerst angenehme Arbeitsklima in der Gruppe haben wesentlich zum Gelingen der Doktorarbeit beigetragen.

Ohne die vielen richtungsweisenden Ideen, die Denkanstöße und die tatkräftige Unterstützung von Prof. Dr. Otto Nachtmann wäre meine Doktorarbeit nicht möglich gewesen. Die unzähligen fruchtbaren und tiefgehenden Diskussionen sowie seine beständige und herzliche Betreuung werden mir stets in bester Erinnerung bleiben. Für all dies möchte ich mich nachdrücklich bedanken.

Für die Übernahme des Zweitgutachtens und die Teilnahme an meiner Prüfungskommission bedanke ich mich sehr bei Prof. Dr. Dirk Dubbers. Ebenso gilt mein Dank PD Dr. Jörg Evers für dessen Teilnahme an der Prüfungskommission.

Mein Dank gilt auch Dr. Maarten DeKieviet und Peter Augenstein für zahlreiche Diskussionen und Erläuterungen zum Heidelberger Spin-Echo-Experiment. Des Weiteren möchte ich mich bei Dr. Mariusz Puchalski für die angenehme und wertvolle Kooperation bedanken, die das Helium-Kapitel dieser Arbeit möglich machte.

Ein besonderes Dankeschön sei auch der gesamten Arbeitsgruppe Gasenzer, inklusive ihrer inoffiziellen Erweiterungen, für die schöne Zeit in Heidelberg gezollt. Darüber hinaus möchte ich mich zuvorderst bei Boris Nowak, Dr. Konrad Schade, Dr. Dénes Sexty und Martin Gärttner für das Korrekturlesen meiner Doktorarbeit bedanken, ebenso wie bei David Mesterhazy, Tobias Pfrommer, Lilian Kramer und Sabrina Kellner.

An dieser Stelle sei der Klaus Tschira Stiftung, der Heidelberg Graduate School of Fundamental Physics und nicht zuletzt dem Institut für Theoretische Physik der Universität Heidelberg für die finanzielle und infrastrukturelle Förderung meiner Arbeit ausdrücklich gedankt.

Zu guter Letzt möchte ich besonders meinen Eltern sowie Wilma Petzig danken, ohne deren stete und uneingeschränkte Unterstützung ich mein Studium in Heidelberg nicht derlei sorgenfrei hätte gestalten können.



**Erklärung:**

Ich versichere, dass ich diese Arbeit selbständig verfasst und keine anderen als die angegebenen Quellen und Hilfsmittel benutzt habe.

Heidelberg, 2. November 2012 .....

